Computational and Theoretical Contact Modelling of Hip Implant Devices with the Application of Wear Simulations

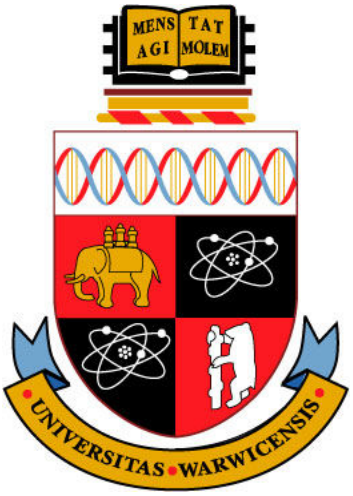

Murat Ali

A thesis submitted for the degree of
Doctor of Philosophy

University of Warwick
School of Engineering

May 2013

Contents

List of Figures

List of Tables

Acknowledgements

I would like to express sincere appreciation and gratitude to many people who made it possible for me to start and complete this project. Firstly, my thanks go out to Dr Ken Mao, for allowing me the opportunity to work on this topic along with his patience, kindness and support throughout. I would also like to thank Professor Derek Chetwynd for providing me with the extra inspiration I needed to study the subject of tribology and Dr Peter Jones for encouraging me to pursue my ambitions throughout the project. I would like to show my appreciation to Dr Glen Turley for his intellectual conversations and support, especially in using the gait lab.

My appreciation must be shown to all the engineers, scientists, mathematicians, computer scientists and programmers around the world who have helped me and provided much needed advice.

My thanks go out to all the researchers, academics and support staff at the School of Engineering and those within the University of Warwick as a whole, who supported me during this project. I would especially like to thank Kerrie Hatton for providing continued support throughout the project.

I would like to show my appreciation and gratitude to the EPSRC (Engineering and Physical Sciences Research Council) for supporting this research.

Finally, I would like to thank my family and friends for their continued support and patience throughout the challenges of this project.

Declarations

Statement of Originality

The work presented in this thesis is my own work, except where noted. This material has not been previously submitted for another degree at a degree granting institution.

Contributions to Knowledge

Peer reviewed conference papers and presentations

- M. Ali and K. Mao, "Modelling of Hip Resurfacing Device Contact under Central and Edge Loading Conditions", Lecture Notes in Engineering and Computer Science: Proceedings of The World Congress on Engineering 2012, 4-6 July, London, U.K. pp. 2054-2059, 2012. (*Awarded "Best Paper Award of The 2012 International Conference of Mechanical Engineering").*
- M. Ali and K. Mao, "Mechanical and Tribological Study of Hip Resurfacing Devices", Book of Abstracts, International Conference of the Polish Society of Biomechanics: Biomechanics 2012, Bialystok 2012. pp. 19-20. *(Conference travel fund 2012 award from the EPSRC and The University of Warwick School of Engineering).*

Peer reviewed journal papers

- M. Ali and K. Mao, "Contact Analysis of Hip Resurfacing Devices Under Normal and Edge Loading Conditions", IAENG Special Issue Journal, Engineering Letters, Volume 20 Issue 4, Pages 317-329. *(Accepted and published).*
- M. Ali and K. Mao, "Contact Mechanics of Wear Simulations of Hip Resurfacing Devices using Computational Methods", Acta of Bioengineering and Biomechanics, 2013. (*Provisionally accepted).*

Contribution to book chapter

- M. Ali and K. Mao, "Computational Contact Modelling of Hip Resurfacing Devices", Chapter 14, IAENG Transaction on Engineering Technologies – Special Issue of the World Congress on Engineering 2012. (*Accepted and published).*

Academic posters, conference proceedings, reports and seminars

- M. Ali and K. Mao, "The Use of Computational and Theoretical Methods to Study Edge Loading of Hip Resurfacing Devices", Institute of Digital Healthcare: Digital Innovation and Technology for Patient Benefit, The University of Warwick. November, 2011.
- M. Ali and K. Mao, "Hip resurfacing device analysis using the finite element method and the application of shakedown theory", School of Engineering, The University of Warwick, Progress Panel Poster, May 2011.
- M. Ali, C. Li, A. Kamali, K. Mao, "Fatigue assessments of hip resurfacing devices under normal gait and microseperation conditions leading to edge loading", School of Engineering, The University of Warwick, Progress Panel Paper, May 2011.
- M. Ali and K. Mao, "Hip resurfacing device analysis using the finite element method", University of Warwick Postgraduate Research Poster Competition, May 2011.
- M. Ali and K. Mao, "Mechanical and Tribological study of Orthopedic Devices for Articulating Joints", Café Scientifique, The University of Warwick, April 2010.

Abstract

Contact mechanics, wear and tribology of hip implant devices have been studied since early implantations and the performance of the devices are becoming increasingly important. Wear and surface damage of these bearing surfaces occur through normal gait loading conditions. However, in addition to this, stripe wear patterns are observed on patient implant retrievals and following hip simulator studies. Novel computational and theoretical methods were used and developed based on advanced computer aided engineering techniques and the finite element method. Hip joint modelling and numerical methodologies of mechanical wear simulations were studied through a newly proposed scripting method. Shakedown theory and maps were referred to for studying the biotribology and contact mechanics of hip resurfacing devices under cyclic normal, severe and edge loading conditions. Through implicit and explicit finite element modelling lateral displacement and laxity based microseparation models were developed. The contact pressure under edge loading conditions was at least a factor of 2 larger than under normal loading conditions. The wear rates of both the femoral head and acetabular cup during the bedding-in period were between 1-3 mm^3/mc (million cycles) and 80-110 mm^3/mc based on a steady-state wear coefficient. Results showed that modelling and verifying the contact and stress results under edge loading conditions required more careful computational modelling than for normal loading conditions. The high contact pressures observed during simulations of microseparation models were consistent with the high level of wear and surface damage observed in experimental simulator studies and from patient retrievals. These methods can therefore be used as a technique to simulate wear of hip implant devices. Shakedown assessments showed that under normal, as well as edge loading and severe loading conditions the hip device remained below the elastic shakedown region of a rolling and sliding shakedown map, which is ideal for minimal surface contact and subsurface damage.

Nomenclature

a	Contact pressure profile along x-axis
a_a	Circular micro contact radius
a_b	Gradient of ρ_b
a_c	Arc length
a_d	Debris minor axis length
a_e	Contact radius along x axis
a_n	Contact radius under normal loading conditions
A_i	Asperity contact area
B	Contact pressure profile along y-axis
b_b	Intercept of ρ_b
b_d	Debris major axis length
b_e	Contact radius along y axis
C	Radial clearance (between femoral head and acetabular cup)
c_d	Contact distance
c_m	Point of microseparation rim contact
c_t	General two body contact variable
C	Damping matrix
C_p	Plane of femoral head and acetabular cup contact
d	Depth of abrasive wear indentation
d_a	$= z_a - \delta_a$
d_c	Chord length
d_t	General two body contact variable
D_1	Diameter of body 1
D_2	Diameter of body 2
D_c	Diameter of acetabular cup bearing
D_h	Diameter of femoral head bearing
D_I	Inferior displacement
D_M	Medial displacement
D_{rp}	Hip replacement bearing diameter
D_{rs}	Hip resurfacing bearing diameter
DP_I	Distance from the acetabulum centre to inferior end point
DP_S	Distance from the acetabulum centre to superior end point
E	Elastic modulus
E_1	Elastic modulus of body 1
E_2	Elastic modulus of body 2
E^*	Equivalent modulus of elasticity for material pair
E_c	Elastic modulus of the acetabular cup
E_b	Elastic modulus of bone
E_h	Elastic modulus of the femoral head
E_{BF}	Equivalent femur bone elastic modulus
E_{BP}	Equivalent pelvis bone elastic modulus
E_T	Total Energy
F	Force
F_I	ISO vertical hip load
F_y	Normal vertical hip load
F_s	Stumbling vertical hip load
G	Shear modulus (modulus of rigidity)

GS	Element parent voxel greyscale
h	Wear depth
h_a	Implant section height for asperity contact model
h_I	Total wear depth calculated over the total number of increments
h_{min}	Minimum film thickness
h_s	Heal Strike
h_T	Total volumetric wear over the testing period
H_s	Hersey number
H_v	Material hardness
H_{VP}	Hardness of deforming material
HU	Hounsfield unit
i	Finite element analysis increment
I	Internal force
I_h	Upper integral limit (asperity probability density function)
I_d	Lower integral limit (asperity probability density function)
J_2	von Mises yield criterion
k_w	Dimensional wear coefficient
k	Material shear yield strength in simple shear
K	Stiffness
K_D	Ball-in-socket equivalent diameter
l	Length of cylinder under contact
L	Load
L_a	Asperity load
L_t	Total load of asperities
L_{o-c_2}	Distance from 0 to c_2 in the microseparation model
L_E	Externally applied load
L_F	Total femur length
L_{SF}	Segmented femur superior-inferior length
l_d	Distance travelled by cone
m	Total number of operating cycles
M	Mass
M_I	Contact area under ISO loading with microseparation
M_p	Contact area under peak loading with microseparation
n	Total number of increments
n_c	Nodal position
N	Number of cycles
N_a	Total number of asperities
N_I	Contact area under ISO loading without microseparation
N_p	Contact area under peak loading without microseparation
p	Pressure
p_s	Asperity shakedown pressure
p_o	Maximum contact pressure
$p_{o,c}$	Maximum contact pressure for a cylinder in cylindrical socket
$p_{o,e}$	Maximum finite element edge loading contact pressure
$p_{o,n}$	Maximum finite element normal loading contact pressure
$p_{o,s}$	Maximum contact pressure for a sphere in spherical socket
P_s	Shakedown pressure (shakedown limit)
P	Contact pressure distribution (contact stress)
P'	Infinitesimal volume
Pel_{h1}	Distance from acetabulum centroid to superior pelvis section cut

Pel_{h2}	Distance from acetabulum centroid to inferior pelvis section cut
Pel_L	Total inferior-superior length of pelvis
P_E	Contact pressure under edge loading
P_N	Contact pressure under normal loading
r	Radius
r_a	Reduced asperity radius
r_n	Distance from centre of contact under normal loading conditions
r_{GW}	Asperity radius for plasticity index
r_{acetab}	Radius of acetabulum
R_1	Radius of body 1
R_2	Radius of body 2
R'	Composite rotation matrix
R_a	Surface roughness
R_{ac}	Surface roughness of acetabular cup
R_{ah}	Surface roughness of femoral head
R_c	Acetabular cup radius
R_e	Effective radius
R_h	Femoral head radius
R_p	Maximum surface profile peak
R_{sk}	Surface skewness
R_x	Rotation matrix about x-axis
R_y	Rotation matrix about y-axis
R_z	Rotation matrix about z-axis
s	Sliding distance
s_r	Distance for onset of rim contact (along coronal plane)
s_s	Distance for onset of rim contact (along sagital plane)
s_t	Distance for onset of rim contact (along traverse plane)
s_L	Displacement of femoral head along medial-lateral axis
S_m	Allowable contact area between implant components
t	Time
t_o	Toe off
T	Temperature
u	Displacement
u_v	Entraining velocity
u'	Sliding distance in x direction
v	Sliding velocity
v'	Sliding distance in y direction
w'	Sliding distance in z direction
W	Wear depth distribution matrix
W_i	Load on asperity
x_h	Horizontal distance from centre of femoral head
Y	Tensile yield point (used in von Mises stress criterion)
z	Asperity height
α_c	General two body contact variable
β_c	General two body contact variable
γ_{ij}	Shear Strain
δ_a	Overlap distance between two asperity profiles
ε_{ij}	Strain
ε^{pl}	Work equivalent plastic strain

η	Viscosity
θ	Polar angle
θ_a	Chord central angle
θ_A	Cup version angle
θ_f	Femoral head inclination angle
θ_i	Acetabular cup inclination angle
θ_m	Angular displacement (normal to edge loading transition)
κ_r	Nodal rotation angle about the z-axis
λ	Dimensional scale parameter
λ_c	General two body contact variable
λ_l	Lambda ratio for lubrication calculation
λ_s	Dimensional scale parameter for shakedown
μ	Coefficient of friction
μ_{water}	Linear attenuation of water
μ_x	Linear attenuation of scanned data
ν	Poisson's ratio
ν_1	Poisson's ratio of body 1
ν_2	Poisson's ratio of body 2
ν_b	Poisson's ratio power law
ν_c	Poisson's ratio of acetabular cup
ν_h	Poisson's ratio of femoral head
ρ	Residual Stress
ρ_{ap}	Apparent density
ρ_b	Density of bone
σ^0	Equivalent uniaxial stress
σ_a	RMS height of asperities (standard deviation)
σ_{ij}	Stress
σ^e_{ij}	Elastic field stress (Melan's theorem)
ς_{ij}	Self-equilibrated residual stress field (Melan's theorem)
$\sigma_{c,max}$	Maximum contact pressure for load intensity calculation
σ_m	Mean hertzian micro contact pressure
σ_Y	Yield stress
τ_{ij}	Shear stress
φ	Angle between the plane of curvatures and azimuthal angle
φ_r	Nodal rotation angle about the y-axis
Φ	Surface element height
ϕ_c	Angle between R_1 plane and R_2 plane
ϕ_h	Gaussian distribution asperity heights
ϕ_{FE_S}	Flexion-extension angular displacement (start point)
ϕ_{FE_I}	Flexion-extension angular displacement (end point)
ϕ_{IO_S}	Inward-outward angular displacement (start point)
ϕ_{IO_I}	Inward-outward angular displacement (end point)
Ψ_{GW}	Greenwood and William's plasticity index
Ψ_s	Shakedown plasticity index
ω	Rotational speed
ω_r	Nodal rotation angle about the x-axis

Chapter 1 – Introduction

Following a brief background to the subject of biomedical engineering, a platform will be provided for the research needs and justifications to be made. The problem itself will be described with clarification on how this problem is going to be studied and the scope which is defined by the project.

1.1. Brief History of Biomechanical Engineering

In order to make progress in this field of research, the historical progress must be understood. Nebeker [1] provides a very comprehensive historical account for the biomedical engineering subject which is summarised within this section. Although the discipline of engineering has been around for many years, the field of biomedical engineering failed to exist before 1952. The subject initially seemed to be dominated by electrical engineering; however both mechanical and chemical engineering have made huge contributions to developments within the field. The need for mechanical engineers was firmly established following the introduction of heart valves in the 1960's. During this period computers were becoming prominent, and despite facing criticism for increasing health care expenses, the technology offered new opportunity for research. Any work within this field needed to be conducted with strict regulations in mind, enforced by the 'U.S. Food and Drug Administration' and the 'Medicines and Healthcare products Regulatory Agency'. Growth in orthopaedics knowledge and research was aided by the advances in medical imaging in the 1970's, which was also supported by the introduction of the Rehabilitation Act in 1973. Surprisingly, it was not until the mid 1990's that millions of patients globally were receiving artificial implants. Engineers have provided significant

contribution to this field by carrying out research for understanding and solving complex problems of hip resurfacing and replacement devices. Many solutions have been provided, some of which have been successful and some which have not be so successful.

With increasing health care demands and the use of medical devices such as hip replacement and resurfacing devices, it is as important as ever for mechanical engineers to remain involved in the biomedical field. One of the great challenges for engineers within the medical devices industry continues to be providing device solutions which can perform and function as well as the body part which is being replaced or modified. Some of the great feats in human engineering includes the low friction coefficient of a synovial joint ($\mu = 0.02$) with an overall joint wear factor as low as 10^{-9} mm^3/Nm [2], which currently outperforms the operating life of any hip replacement or resurfacing device.

Despite these challenges and high expectations, engineers have provided the medical industry with solutions to medical problems; therefore, morally it is the engineer's responsibility to deal with the issues that now exist from offering these solutions. This formed the basis of motivation for this research to be carried out.

Researchers within this field should continue to solve problems which currently hinder the progress of medical device improvements. In order to achieve this, not only should previous research successes and failures be studied, but also existing theories and methodologies should be challenged. By making use of accurate and well studied standards and methodologies, the engineering community can be guided with the most appropriate processes for problem solving and decision making in this area of research.

1.2. Research Needs and Justification

From a market's perspective a press release [3] provided a prediction of the significant growth expected for artificial joints and resurfacing operations in the future. In 2008 the artificial joints market as a whole was valued at $12.2 billion globally, which was expected to grow by

more than 9% annually to $17.4 billion by 2012. The key drivers are gender specific knee implants, hip and knee resurfacing devices, along with increased demands for spinal replacement products [3]. Based on past trends and the current understanding of the market, it would not be unreasonable to assume the demand for orthopaedic implant devices would increase even further in the future. For hip implant devices alone, a market forecast report predicts a global compound annual growth rate of 5% to reach $8.6 billion in 2017 [4].

This study will focus on the hip joint which is the area of the body that statistically receives the most number of orthopaedic implants over anywhere else in the body. The two main types of orthopaedic devices for the hip joint are the 'hip replacement' and 'hip resurfacing' devices. Both types of devices along with the advantages and disadvantages of each based on previous research and literature will be explained in the following chapters. It is important to note that both types of hip implants are still widely used today, and often choice of either option depends on many factors. From an engineering perspective, the benefits of using resurfacing devices rather than total joint replacements are theoretically justified. A study has shown a decrease in contact pressure and increase in contact area by using a hip resurfacing approach rather than a total hip replacement [5], further literature into the performances of these devices are discussed within this thesis. Although further studies indicate the need to model more realistic contact mechanics as well as lubrication, the reduction in contact area and pressure provides positive results for younger patients who require bone joint surgical intervention [5]. As the average age of patients opting for joint replacements and resurfacing products decreases, the hip implant devices are currently being pushed to their functional limits and longevity of the devices is more important than ever before.

1.3. Description of the Problem

The understanding of the contact mechanics as well as the wear modes and mechanisms is crucial in helping to minimise the wear debris of these devices *in vivo* (implanted within the

patient). The use of the computer aided engineering (CAE) and experimental simulator testing has provided device designers and manufacturers opportunities to develop wear resistant biomaterials for orthopaedic products. Along with normal wear patterns observed on hip implant devices, stripe wear and severe wear are observed from both *in vivo* and *in vitro* (experimental simulator tests) retrievals. Therefore, the occurrence of these wear modes have most recently received much attention from orthopaedic device companies, medical professionals and research communities. The purpose of this study was to use and develop computational and theoretical models to study the contact mechanics of normal, severe and edge loading of hip implant devices, and then assess the factors which impact on hip replacement and resurfacing device wear, surface damage and subsurface damage.

1.4. Project Scope

The research is limited to the human hip joint. Due to the specific medical subject expertise and access to specific equipment required, *in vivo* studies are not conducted. Therefore, the main focus is placed upon computational, theoretical and engineering experimental methods, including the study of hip simulators. The problems dealt with within this project are common to both hip resurfacing and hip replacement devices, and therefore both have been included within the scope of the literature review and the project as a whole. However, the analysis of hip resurfacing devices is the primary focus in terms of methodology and results due to the lesser amount of research compared with hip replacement devices.

In order to narrow down the modelling scope and keep within allocated time constraints, metal-on-metal ASTM F75 cobalt chromium molybdenum (CoCrMo) grade hip resurfacing modelling is of the highest priority. No coatings or surface engineering are include within the modelling or simulations. Only one side of the hip is modelled due to the symmetry of the body with negligible differences in loading and boundary conditions assumed between the left and right hip.

Computer aided engineering techniques are used to study and develop solutions to the problems discussed above. Finite element analysis methods form the basis of problem solving within this project along with computer aided design and relevant programming languages. Although gait loading conditions and angular displacements are based on ISO standards, other loading and boundary conditions are also considered to ensure that a range of realistic conditions will be covered within the study. Normal loading, edge loading and stumbling loads are the primary loading conditions considered within the scope of the project. Although covered in the literature review due to its importance in understanding the subject of tribology, no complex lubrication numerical models are included within the contact simulations. Finally, a limited amount of experimental work is conducted to focus on the primary aims and objectives of the study.

1.5. Aims and Objectives

The three key aims and objectives of this research are as follows:

- Develop contact models of hip implant devices under normal, edge loading and severe stumbling conditions, using computational, numerical and theoretical methods. These contact models would then be used to carry out mechanical wear simulations, especially for assessing the wear of both the acetabular cup and femoral head simultaneously from the contact analysis.
- Propose and use modelling methodologies to assess affects of loading profiles, material properties and boundary conditions to the hip implant contact results. This includes theoretical microseparation models to assess the impact of edge loaded hip resurfacing devices.
- Assess the application of shakedown principles to hip implant contact problems on the global and asperity level.

From the aims and objectives defined above, the solution based techniques covered in the project can be amalgamated. This method of amalgamation has not been covered in the past, and it offers an advantageous engineering solution and strong opportunity to promote further research opportunities.

The project is structured to meet these objectives and present the research clearly and logically. Firstly, the literature review was carried out which will be covered in chapter 2. From this, the methodology was developed, refined and this will be presented in chapter 3. Following on from this, the results were obtained, presented in chapter 4 and discussed in chapter 5. Finally, the conclusions and further work suggestions will be covered within chapter 6 and chapter 7.

1.6. Project and Literature Review Topics

The purpose of an orthopaedic device such as a total joint replacement or resurfacing device is to restore function in the body by replacing or modifying parts of the body which have lost the ability to fulfil their original function. Suitable engineering processes are available [6] which can be applied to many types of components, and form a basis for design, analysis and manufacture of orthopaedic devices. To design successful devices, the biomechanical loads and stresses must be understood; in summary these are: compressive force**,** sliding shear**,** tensile stretching on the surface**,** cyclic compressive load**,** fatigue stress and contact stress. Although predictions show an increased demand for total joint replacement devices [3], there still remain lots of challenges and problems to solve. The issues are mainly mechanical leading to biological failures. Today's designs are required to provide improved functional performance and a longer operating life. Historically, most joint replacement and resurfacing devices fail due to wear and debris, leading to joint loosening and ultimately failure of the device [7].

In many engineering applications there exists an optimised design in terms of weight and geometry. In some engineering applications, excess weight and strength does not pose a major performance concern, however, stress shielding (also known as osteopenia) has been identified as a problem with implanted total knee replacements [8] as well as other orthopaedic implanted devices. Due to an implanted device withstanding stresses that would normally have been the function of the bone, it is expected that there will be a reduction in patient bone density. This is an important example of how the engineering of implanted devices can adversely affect the normal functioning of the human body.

Within the current literature, computational methods are used to assess deformation of hip implants under load for elastohydrodynamic lubrication (EHL) calculations, calculating volumetric wear under gait loading with comparisons made to *in vitro* experimental work, determining the plastic strain of third body abrasive wear and predicting the contact mechanics of joint implants. To achieve this, a number of three dimensional (3D), two dimensional (2D) and two dimensional axisymmetric finite element models have been developed. In addition to this, the finite difference method (FDM) is used for solving the Reynolds equation for lubrication analysis.

All of the finite element wear simulations in current literature are developed based on the Archard adhesive/abrasive linear wear model. Although wear is a significant topic within this project, edge loading, stripe wear and third body abrasive wear have not been studied extensively. The topic of wear modes occur in more than just one part of the body, however the problem of edge loading and stripe wear has only been reported to occur on hip implant devices. The topic of fluid surface interaction (FSI) have applications within biomedical engineering, however it could not be found in any literature related to joint replacements. Following the literature review and developing an understanding of the specific subject

knowledge required, it was deemed that the subject of FSI would be beyond the scope of this research.

Experimental *in vitro* methods have been used extensively for assessing the wear rates in total hip replacements and resurfacing devices based on International Organization of Standardization (ISO) standards. These ISO standards have more recently covered guidelines to include microseparation conditions to simulate edge loading conditions and form stripe wear patterns on hip implant devices [9]. As experimental methods are time and cost intensive, it may be more feasible to run long term wear simulations using computational methods [10].

As previously mentioned, no study has considered or made an assessment of the application of shakedown theory both globally and at an asperity level for hip replacement and resurfacing devices. Shakedown research was pioneered by the group at the University of Cambridge, therefore this was the starting point for studying the subject and contemplating its application to solving the problems covered and dealt with in this project.

Chapter 2 - Literature Review and Theory

The research needs, description of the problem, project scope, aims and objectives determined the requirements and searching strategies for the literature review. Based on the literature search the majority of papers consisted of using computational, experimental (*in vitro*) and theoretical methods. Loading conditions are referred to as two separate entities for simplicity in writing. The first entity is "edge loading" and all other possible types of loading conditions are referred to as "normal" or "central" loading conditions unless stated otherwise. In addition, both hip resurfacing devices and hip replacement devices may be referred to as hip implant devices, as there are cases where the discussion relates to both types of devices.

2.1. Biomechanics of the Hip Joint

In order to appropriately model the contact mechanics of hip implant devices using computational and numerical methods, the biomechanics of the hip and experimental testing methods must be understood. The biomechanics of a human differ from person to person and change throughout a lifetime. By introducing a device into the body, the biomechanics are changed even further. To define the conventions used, the anatomical directions, body planes and load vectors are shown in Figure 2.1a and Figure 2.1b [11]. Current literature and the gait force analysis using the gait laboratory, show that the vertical load (F_z) is the dominate force, especially during normal walking, jogging and running. Coordinates of the implant devices are defined using a spherical coordinate system where the angles (r,θ,φ) represent the radial distance, polar angle (or inclination angle) and azimuthual angle respectively, as shown in Figure 2.2a.

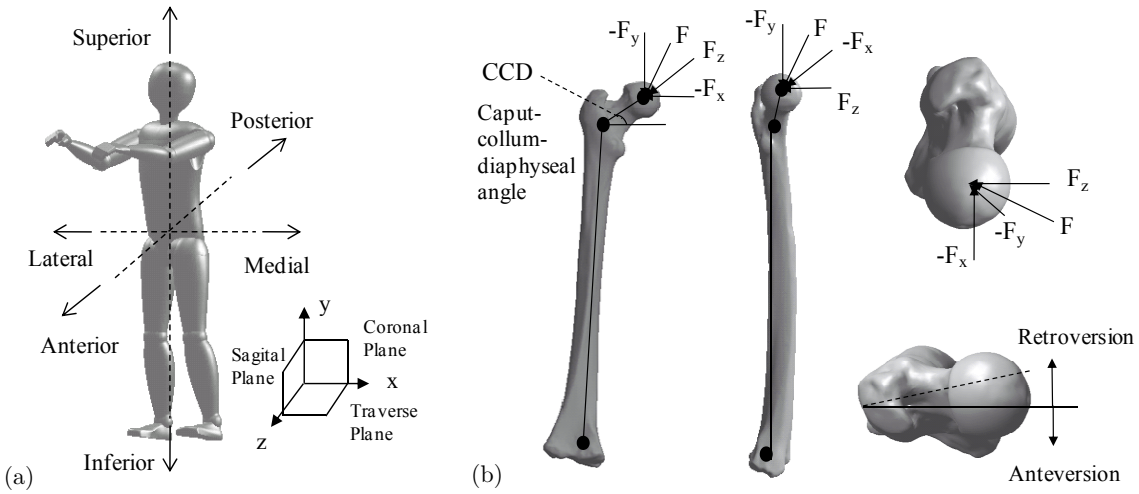

Figure 2.1. (a) Anatomical directions and body planes (b) load vectors on hip joint

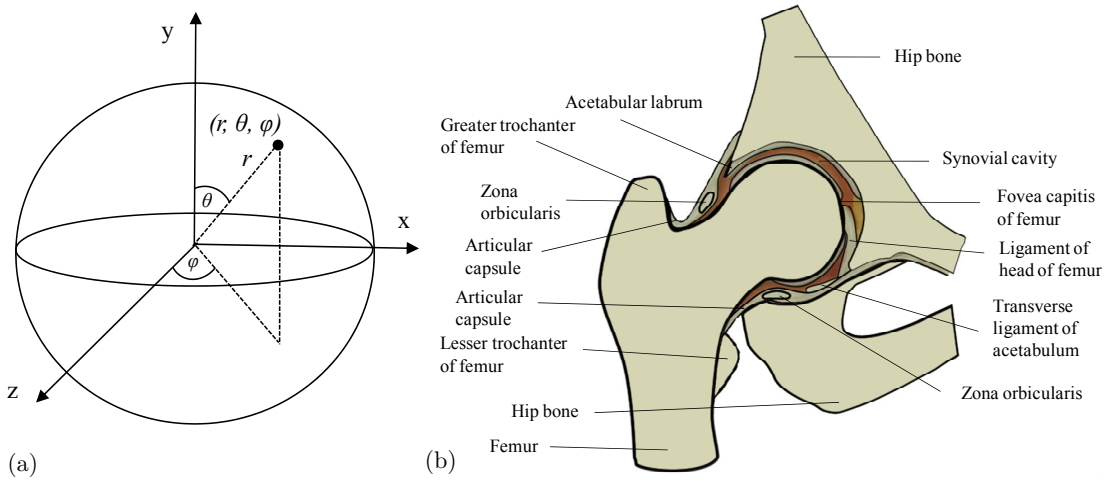

Figure 2.2. (a) Spherical coordinates system for hip implant components (b) frontal section (right hip)

2.1.1. Function of the Hip

The hip joint is defined as "*a ball-and-socket joint formed by the head of the femur and acetabulum of the hip joint*" [12]. The hip joint structure is made up of the femur and hip bone connected by ligaments and surrounded by muscles. The joint synovial cavity allows for flexion, extension, abduction, adduction, circumduction, medial rotation, and lateral rotation of the hip. The range of hip motion is limited by surface contact, impingement and maximum ligament tension [12]. Joint stability is not a problem for a healthy hip joint (Figure 2.2b) due to a well functioning system of ligament connections around the joint. The muscles surrounding the joint also offer dynamic stability, and together with ligaments they ensure close contact is maintained between the femoral head and joint socket. Unfortunately, during

hip replacement or resurfacing surgery, the joint structure is damaged and joint laxity and structural integrity of the joint area can become a problem.

The range of hip joint motion also varies between patients, who are advised not to extend the range of motion beyond a certain point (i.e. 90° in flexion) as this can lead to impingement, edge loading and the possibility of prosthesis or bone fracture. As mentioned, the biomechanics of the hip can change following a implantation of a hip joint replacement (Figure 2.3a) or resurfacing (Figure 2.3b) device. This topic is discussed by Sariali et al. [13] where important theoretical knowledge is covered, it has been noted that tight ligament tension can cause wear of the implant and affect the joint lubrication.

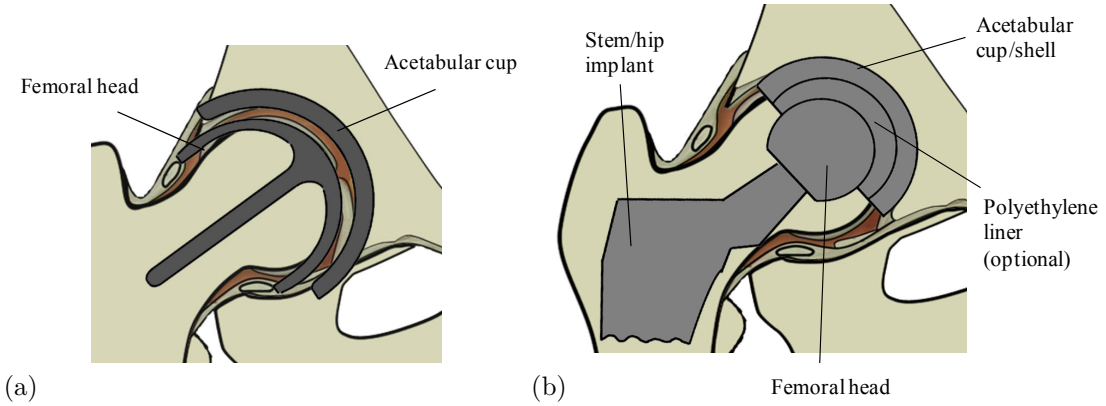

Figure 2.3. Orthopaedic implants (a) hip resurfacing (b) hip replacement

2.1.2. Mechanical Properties of Bone

The structure of bone is very complex relative to that of engineering materials. Bones in the body are anisotropic, where the properties of the material are dependent on orientation. Biological materials can be viscoelastic (time dependent) and poroelastic, which allows fluid to flow through the material (permeable properties). Cartilage on the end of bones and between the articulating joints in the body are viscoelastic, non-linear and inhomogeneous. However the properties of cartilage can be ignored in this project as this surface is removed during the implantation of the orthopaedic implant device. One of the questions to be addressed within this project is how the structure of bone models can be simplified for the purpose of mechanical contact modelling. From the literature, Udofia et al. [14] simplifies the bone

material complexity by modelling the mechanical properties of cortical bone and cancellous bone. The larger elastic modulus section of the cortical bone encapsulates the lower elastic modulus section of cancellous bone. The material properties of cortical and cancellous bone were calculated by Taylor et al. [15] from experimental data obtained by Linde et al. [16]. The values for the mechanical properties of cortical and cancellous bone used within the literature are provided in Table 2.1. The properties are also consistent with those used by Yew et al. [17] who reference these values from Dalstra et al. [18].

Table 2.1. Properties of bone sections

Section of bone	**Elastic modulus (GPa)**	**Poisson's ratio**
Cortical Bone	17	0.3
Cancellous Bone	0.8	0.2

For the dynamic analysis, which considers inertia effects, the bone material density must be defined. The current literature provides a range of bone density values ranging from 1000 kg/m^3 to 1900 kg/m^3. This large range of values can be explained by the difficulty in determining a bone density value. For this reason bone mineral density (BMD) is often obtained, which can also be used to estimate the strength of bones. Both the bone density and BMD values reduce as the age of the patient increases under normal circumstances.

2.1.3. Static and Dynamic Loading of Hip Joints

On a basic level, static equilibrium, Newton's laws of motion, Euler's equations of motion and moments of inertia can all be applied to understand the mechanics of the human body [8]. Clinical gait analysis is required to understand the kinematics of hip joint motion as this dictates the motion of the joint in the human body. Along with modelling and simulating joint kinematics, the kinetic data can be obtained from assessing the loads acting on the hip joint. The human kinematics and kinetics are shown diagrammatically in Figure 2.4a, with the implementation of this into experimental simulator testing (Figure 2.4b). Compared with a dynamic loading profile of a dynamic load, we can consider a static load to be applied during a stationary standing, sitting or lying position where no movement of the body is expected,

therefore loads can be assumed to remain constant for a duration of time. Dynamic loading would occur during brisk walking, running, jumping or any other movement of the body [19].

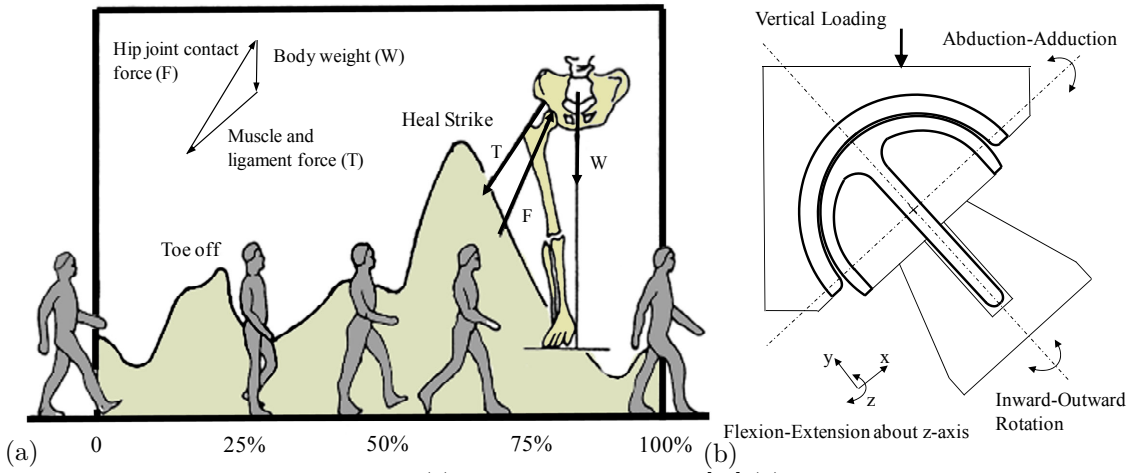

Figure 2.4. Kinematics and kinetics (a) during a walking cycle [20] (b) implemented into experimental simulator testing

The principle of a quasi-static analysis assumes that inertial effects are negligible and that the moments and forces of joints in the body can be approximated by a static load, where static loads in the body consider the gravitational and external reactions [21]. For static and quasi-static loading to be applied, the body must be in static equilibrium. It is important not to confuse a dynamic analysis with a quasi-static analysis. A dynamic analysis would include the inertial effects on the joints, where as a quasi-static analysis would not, unless the inertial effects were added to the body weight as suggested by Rybicki et al. [22]. In addition to this, impact (or shock) loading can occur when the one body (i.e. the femoral component) hits another object (i.e. the acetabular cup) with a high force over a short time period, inducing a stress in both objects where the bodies will vibrate and eventually come to a rest [23]. Although severe hip joint loading conditions such as edge loading has not been associated or described as 'impact loading' in current literature, no assessment has been conducted to study and clarify this.

2.1.4. Hip Joint Kinematics and Kinetics

A severe case of dislocation is shown by Bowsher et al. [24] where the retrieved metal-on-metal prosthesis had shown all forms of wear modes, including scratching caused by 3rd body wear

and stripe wear. The typical stripe wear patterns are affected by the geometrical positioning and loading conditions of artificial components implanted into the body, and these wear patterns were observed from patient implant retrievals and hip devices tested using experimental simulators (Figure 2.5).

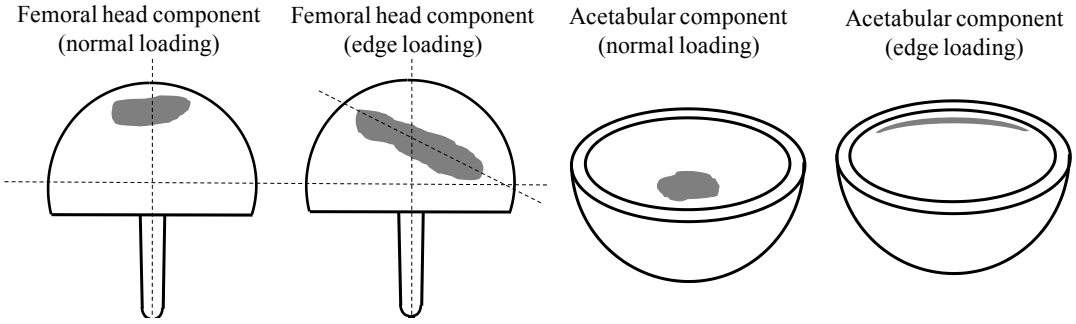

Figure 2.5. Schematic of normal and edge loading wear on the femoral head and acetabular cup ([25-27])

A stripe wear tilt angle on the femoral head component occurs due to the anteversion of the acetabular cup positioned inside the pelvis. General wear and stripe wear patterns are more clearly observed on ceramic-on-ceramic (CoC) hip joint implants. Positioning of stripe wear patterns on retrieval ceramic-on-ceramic cup and heads were recorded by Walter et al. [27], where the latitude of the scars centre on the femoral head were 30° north of the equator and the stripe wear on the cup were located superiorly above the cup radius. Although many studies have presented the occurrence of stripe wear, very few studies have used finite element analysis to study edge loading of the hip joint, the most recent concluded that no edge loading was observed. Whilst considering severe loading conditions, it should be noted that surface or fatigue cracking are not identified to be a consequence of normal/central loading, edge loading or severe loading such as stumbling of metal-on-metal hip implants although this has been noted to be a problem for UHMWPE cups.

Following the installation of the hip implant there are a number of biomechanical and anatomical advantages to restoring the hip joint centre of rotation which is defined as the geometrical centre of the femoral head [13]. One study had shown how deviation from the normal anatomical hip centre of rotation results in larger rate of aseptic loosening [28]. In the

natural hip, the centre of rotation is set, however for a hip prosthesis the centre of rotation can be adjusted by the geometrical design and positioning of the cup in the body. Positioning the cup and femoral component with the appropriate amount of anteversion should ensure anatomical revision for the patient, however retroversion could lead to impingement (potentially causing edge loading) during inward rotation [13]. Short offset distances are associated with increased reaction force and wear, and are also linked to the onset of edge loading due to microseparation. Serali et al. [13] also explain that correct leg length establishment is one of the most important aspects of hip joint restoration.

The cup inclination angle is reported to affect the wear rate of hip joint implants. A cup inclination angle of 60° without the inclusion of microseparation kinematics, and a cup inclination angle of 60° with the inclusion of microseparation kinematics, led to a 9 and 17 fold increase in wear rate respectively [29]. On the contrary, a further assessment for the wear of alumina ceramic bearing surfaces at 45° and 60° cup inclinations angles reports no significant increase in wear when cup angle increased from 45° to 60°. In addition to this, an increase of radial clearance from 20 μm to 30 μm did not show an increase in wear rate [30]. A separate study showed that an increase in cup inclination angle and lateral head position both increased the wear of metal-on-metal total hip replacements [31].

The laxity of the hip joint is known to lead to microseparation during the gait cycle, and fluoroscopy studies have revealed how edge loading of the hip joint is caused by lateral sliding of the femoral component [29]. The subluxation and microsperation is also concluded as the contributor of stripe wear due to edge loading [32]. The severity of rim contact caused by microseparation could depend on position, alignment, muscle force and soft tissue tension [33]. Further factors have been defined in Appendix A – Normal and Edge Loading Factors.

Impingement has been a cause of concern for many years. There appears to be no benefit of its occurrence and it can increase the likelihood of stripe wear due to edge contact between the

acetabular cup and femoral head. There are ways to avoid hip impingement through designing and implementing methods to overcome the problem, including increasing the femoral head size [34] and optimisation of acetabular cup rim geometry [35].

Experimental simulators are currently the most relied upon method of implant device testing and validation. One study shows the wear rate to be significantly affected by experimental simulator kinematics [36]. The motions from the two-axis simulator study by Firkins et al. [37] were flexion-extension and internal-external rotation. The motions from the three-axis simulator included flexion-extension, internal-external rotation and adduction-abduction. The two motion input rig shows wear rates ten times higher than for the three input motion rig. Computational methods in the future could bridge the gaps and uncertainties of experimental simulator methodologies.

2.1.4.1. Cyclic Loading and Activities

Along with understanding adverse kinematic effects such as microseparation and impingement leading to edge loaded hip implants, cyclic loading and patient activities would help to explain this further. Firstly, just the weight of the patient alone will have an effect on the wear of the device implanted into the body. The body weight of patients over 91Kg have been shown to be over four times more likely to have ceramic liner failure than patients who weighed less than 91Kg [32].

Even before the subject of 'tribology' existed it was observed that sliding distance, along with load and material wear coefficient was linearly proportional to the volumetric wear [38]. Therefore to obtain true performance data from the devices *in vitro*, the walking load path and number of cycles must be realised. From the literature one million cycles is assumed to equate to one year of implant usage [39], typically a total of 5×10^6 cycles are used as a standard for implant testing [40] where studies refer to ISO standards to establish the geometric and/or gravimetric wear rates. The differences in cyclic loading, lubrication,

frequencies and specimen orientation would be expected to lead to differing volumetric wear rates as observed in [41]. Interestingly, Affatato et al. [41] explains that some groups did not fully follow the international standards for the testing and methodology of wear assessment. This is understandable when literature such as that published by Kinkel et al. [37] reports a large discrepancy between ISO standards and patient recorded data. The number of walking cycles per year recorded during a study of over 100 patients of different age groups who had a well functioning total hip replacement, reports that the average number of walking cycles per year is 2.24 million cycles [37]. Younger and more active patients could place even more demand onto the devices meaning a larger number of intensive cycles per year. As previously mentioned, a more excessive range of motion can lead to impingement and increased risk of microseparation of the joint. It should be noted that many of the studies discussed within chapter 2, confirm the dominance of flexion-extension over internal-external rotation and adduction-abduction. Activities such as rising from the seating position and heal strike can also lead to microseparation of the femoral head and acetabular cup resulting in stripe wear caused by edge loading. By rising from a chair seated position, the flexion (and abduction) of the femur could lead to a high stress concentration between the head and acetabular cup rim, leading to edge loading and stripe wear. This could also occur during the normal walking gait cycle [42]. As previously discussed, this is not only a problem for ceramic-on-ceramic bearing surfaces, but also with metal-on-metal hip replacement and resurfacing devices *in vivo.* In addition to stripe wear, backside wear and contamination damage were observed in cases where a patient had multiple dislocations [24]. To study this phenomenon further, gait data can be analysed to assess the possible occurrences of edge loading and stripe wear [19]. This assessment is made through definition of the loading magnitudes (F_x, F_y and F_z) over the activity cycle, especially loading in the medial-lateral direction based edge loading, F_x. The variation of the loading profiles throughout a range of patient activities including walking

(Figure 2.6a), rising from a chair (Figure 2.6b), running (Figure 2.6c) and stair climb (Figure 2.6d) is shown. These profiles also show the complex variations of loading on the hip joint occurring *in vivo*, compared with the more simplistic vertical loading conditions applied through ISO standards.

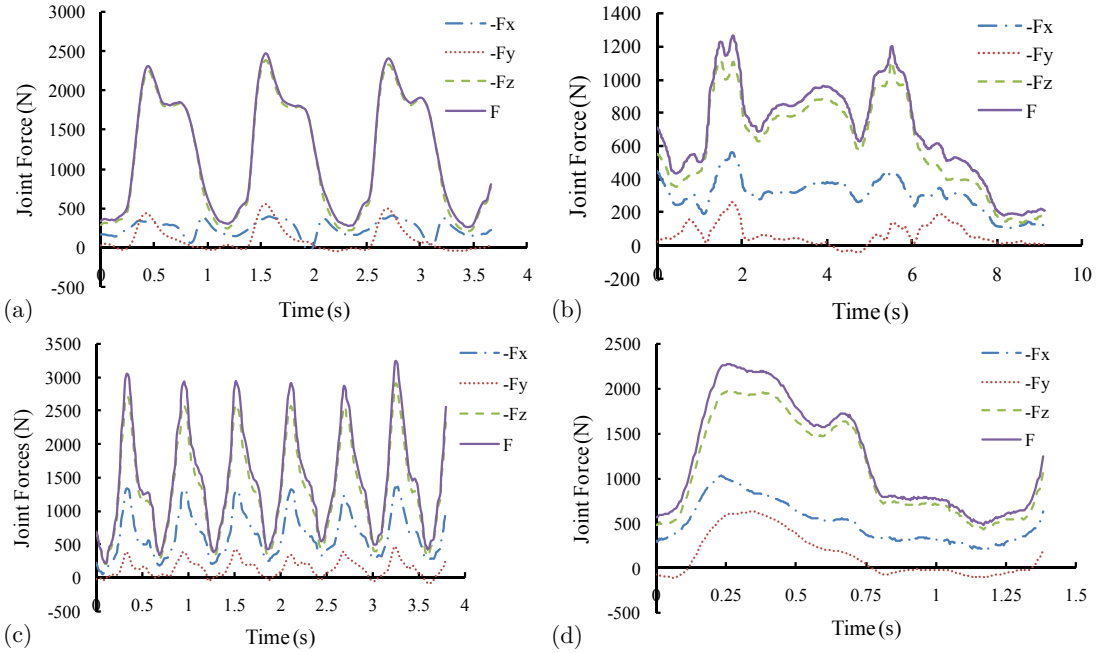

Figure 2.6. Loading curves for various patient activities (a) free walking at normal velocity (b) rise from a chair (c) 8 Km/h run (d) stair climb

The need to consider realistic patient gait data has been mentioned and also been supported by Dowson et al. [39]. The human activity extends beyond just running and walking, causing unexpected stress and strain states. For example, a severely fractured ceramic-on-ceramic femoral head and acetabular cup was caused by a car accident, which was a rare case as only 1 out of 100 hip arthroplasties showed this level of failure [43], such a severe amount of fracture was not observed for metal-on-metal devices. By investigating how microseparation and edge loading are considered in experimental studies, testing methods include a swing phase load which leads to an increase in steady state wear and elevation in surface friction [44]. For patients, soft tissue reconstruction following joint implantation will have an impact on the swing phase load and microseparation during *in vivo* activity. From experimental *in vitro* testing, the effect of different swing phase loads were assessed, and as expected when the swing

phase load was increased from 100N to 280N, the wear rate increased along with the presence of stripe wear. However, and interestingly from a tribological point of view this does not affect the debris particle size [45]. From a separate study, ceramic-on-ceramic retrievals report different dimensions, latitudes and tilt angles of stripe wear, which suggests different edge loading conditions that lead to different stripe wear patterns. This could be caused by polar and equatorial contact [46] leading to wear in these specific regions.

The effect of frequency on testing and computational simulations should be reviewed, as this is an important consideration when running experimental tests and computational models. The hip simulator testing ISO standard currently suggests the tests to be run at a frequency of 1 Hz ± 0.1 Hz [40], which is a standard followed by certain groups [41]. The review by Affatato et al. [41] provides a clear comparison of testing methodologies between research groups, however it does not discuss the justifications of cyclic frequencies used by those groups. From examining contact loading frequency, the effect is an important consideration for fretting wear. It is understood that low and high amplitude fretting leads to a difference in wear observed. For low amplitude fretting, fatigue and cracking becomes more critical than wear due to the increase in temperature and strain rate as the frequency increases. For high amplitude fretting, frequency is shown to have minimal impact to the wear, even for frequencies as high as 20,000 Hz [47]. An importance of amplitude on wear rates can be explained by the 'sticking' of surfaces at low amplitudes and 'gross slip' at high amplitudes. This observation is supported by Stachowiak et al. [48] when discussing environmental effects on fretting wear. The author explains how beyond a certain frequency, wear is no longer dependent on frequency. For materials reacting to oxygen and depending on the materials and environment, oxidative surfaces develop at a certain rate. The fretting frequency would affect the build up of a surface film, so by increasing the frequency a lower amount of oxidation occurs between cycles, therefore leading to a lower wear rate. The fretting wear mechanism is discussed further within

this chapter, however it should be noted at this stage that stripe wear lengths have been recorded from retrieved implants and simulator tests to be between 5 to 56 mm, and stripe wear is not expected to be caused by fretting due to the nature of its occurrence and retrieval surface assessments.

Temperature is considered to impact the abrasive wear of contact surfaces in two ways; the first being the impact of ambient temperature (i.e. temperature surrounding the hip joint) and the second being impact of temperature rises caused by plastic deformation of surfaces [48]. For hip joint implant devices, temperatures are not expected to exceed 50 °C and the lowest joint temperatures are expected to be consistent with body temperature [49]. A separate study by Neville et al. [50] states lower temperatures than those observed by Bergmann et al. [49], the temperature of joints were stated to range between 25-40 °C. The rise of temperature is due to the frictional heating of the components in contact. These temperature ranges would be considered as being very low for engineering materials and therefore, it is un-reasonable to assume that hip replacement or resurfacing device environmental temperatures would impact normal and stripe wear. Similarly, it is not expected that the sliding velocities of surfaces in contact is sufficient to cause a large temperature rise. From the point of lubrication, keeping the temperatures to a minimum can be advantageous as frictional heating can lead to disintegration of the synovial fluid. It has been suggested that the temperature within the lubricating environment (i.e. between articulating joints) should also not exceed 40 °C to ensure integrity of the synovial fluid [51].

2.1.5. Engineering and Testing of Hip Implant Devices

The use of experimental testing in orthopaedic devices is extensive, and although numerical methods such as finite element analysis has shown to reduce the time taken to solve certain problems, the primary chosen method by top researchers and orthopaedic device companies is experimental simulator testing. This choice is of course dependent upon time constraints,

financial position and availability of facilities. Through studying wear theory, it has become apparent that the process is directly affected by the particular application i.e. the occurrence of wear for a hip joint differs to that of a knee joint. Therefore different simulators have been developed for specific orthopaedic device applications, where the primary aim of the simulator testing has been to assess the wear rates of the devices. This finding led to the study of hip kinematics and kinetics. Experimental measurements of wear during testing can be obtained gravimetrically or geometrically [7]. There are advantages and disadvantages to both methods, and case studies in literature have been provided for both.

Although experimental simulator testing to study tribology for wear problems of orthopaedics is appreciated amongst the engineering and biomedical communities [41], less appreciation has been given for the use of numerical and computational methods in this field. Within the literature a number of comparisons have been made of different hip simulators; interestingly, although all the simulators have been designed to represent the human gait, they all adopt different degrees of freedom, load conditions, and lubrication types. This is due to differing theories and opinions of different research groups. It is expected that these differing methodologies may continue in the near future. The need to increase knowledge and understanding of testing strategies at hip bearing surface interaction such as lubrication for use in artificial joint simulation has been stated in [52]. The need for further work is also justified as measured volumetric wear rates show varying results for the same orthopaedic devices by using different testing methods. A major challenge for *in vitro* testing is to obtain long term (i.e. 10-25 year duration test results) in a short time scale (i.e. 1-2 months) and these short time scales can be achieved using numerical methods. To understand the potential for using computational methods alongside experimental methods, a comparison in the literature is made between total knee replacement wear simulator tests and finite element predictions [53]. Both forms of testing consisted of simulating five million gait cycles, and

surprisingly Knight et al. [53] has commented on this being only the second study of its nature being published for total knee replacements. This demonstrates how much work is still required to increase the knowledge within this subject area and it one of the key objectives of this project.

Due to its simplicity of application, the Archard wear model [54] has been used for surface wear calculations, although models such as this do not consider complex, random and changing characteristics such as surface friction [55]. However despite this limitation, the wear model is still widely used.

2.1.5.1. Component Design and Manufacture

The bearing design and diameters will have an impact on edge loading, due to a bearing relocation or dislocation distance [13]. Increasing the bearing diameter decreases the occurrence of dislocation and therefore reduces the likely occurrence of edge loading and stripe wear. Bearing diameters dictating the diametral clearance is a key area of design for metal-on-metal hip replacement and resurfacing devices. The bearing diameters of hip replacement and hip resurfacing devices can range between 16-54mm [56] and typical clearances for hip resurfacing devices are between 80-150μm [14, 57]. The debate of hip replacement against resurfacing devices continues to inspire comparative research with a number of advantages and disadvantages being presented for both options. A study into the comparison of friction between traditional 28mm hip replacements and 55mm resurfacing devices shows that the large diameter bearing leads to a lower friction factor than the small diameter bearing, also increasing the swing phase load increases the friction factor for both bearing sizes [58]. Through a combination of increased elasticity and bearing size, the finite element method was used to show that a hip resurfacing arrangement offers a reduction in contact pressure (over 53%) and a corresponding increase in contact area (220%) [5]. Further information on the history and comparisons between hip replacement and resurfacing products along with a clear

description of the evolution of hip implant designs have been provided by Grigoris et al. [59] and Roberts et al. [60].

The friction factor between 28mm replacement and 55mm resurfacing devices is compared by Brockett et al. [58]. The friction factor increases with a larger swing phase load which has provided a better understanding of friction and lubricating regimes of larger diameter bearings such as those of the resurfacing kind. All of these diameters and clearances are of course design and manufactured dimensions which may be changed following implantation, due to many factors. The effect of an interference fit between the cup and pelvis was studied using experimental methods by Jin et al. [61] and numerically by Yew et al. [17] using the finite element method. Experimentally a radial interference of 0.5mm led to a maximum diametral cup deflection of 60μm. The finite element study concludes that the wall thickness is a major contributing factor to influencing the magnitude of cup deformation. It is stated that the foam used in part 1 of the study did not have viscoelastic material properties such as that of cortical bone. In addition to this, the finite element analysis does not consider the pelvic bone to be non-linear or have viscoelastic material properties and 'bounce back' is not considered in the experimental methodology. A separate study [62] covers the initial stability of a hip resurfacing device as well as the contact mechanics at the articulating surfaces and impacts of cup interference.

To understand if there is any way of eliminating the problem of stripe wear completely, an innovative product was developed by Lazennec et al [63]. The device is a self adjusting acetabular cup component which shows high resistance to wear and stripe wear. However further in-depth assessments and testing of the design were not carried out. In addition to this research, wear rates for the tri-polar ceramic hip prosthesis are discussed and wear rates again are reported to be reduced under microseparation tests due to the elimination of stripe wear [64]. Although these products were developed to solve specific problems associated with hip

implant devices, the self adjusting cup or tri-polar hip prosthesis are not considered further in this thesis. The research focused on the modelling of the most widely used types of hip implants, which are hip replacement and resurfacing devices.

An equation for representing microseparation was published by Mak et al. [65] and following on from this, the use of finite element analysis was useful in assessing the contact mechanics for hip replacements under microseparation conditions. A three-dimensional model was developed based on a simpler two-dimensional axisymmetric model developed previously by Mak et al. [66]. It was found that for edge contact to occur, a microseparation distance above 120 µm was required for a cup inclination angle of 45° and radial clearance of 40 µm. Model sensitivity studies were not conducted due to the computational cost and memory space required. From the study by Mak et al. [67] the contact pressure and stress results before and during edge loading are summarised in Figure 2.7. The three acetabular cup rim conditions included in the study are new, worn and chamfered. The contact pressure results of normal loading occurred before 120 µm as highlighted. Overall, the results show the increase in contact pressure as the microseparation distance increases, leading to acetabular cup rim contact.

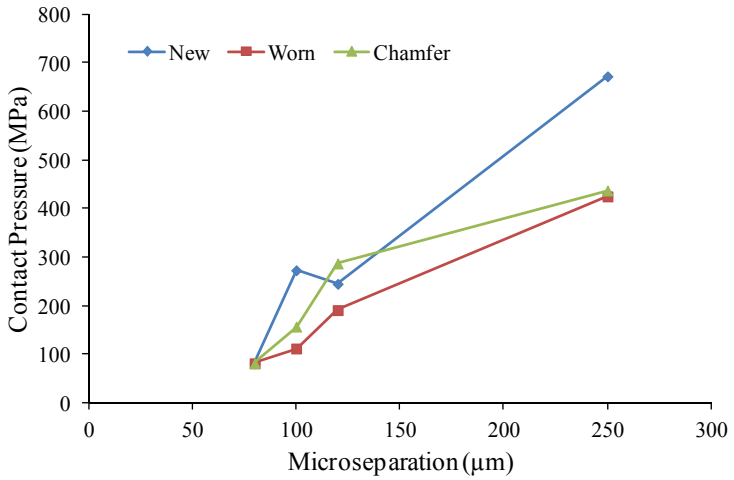

Figure 2.7. Contact pressure against microseparation for new, worn and chamferedacetabular cup rim conditions

To understand the high level of manufacturing quality and product consistency, the worlds best orthopaedic hip implant devices companies have ISO 9001 certification. The remarkable

surface finish on hip implant devices and a roundness tolerances of less than 2 µm mean that devices are produced as close to design specification as possible under current engineering technology and manufacturing practices.

2.1.5.2. Biomaterials and Tribology

Key topics related to this research project are biomaterials and tribology. These topics are important to improving the performance of orthopaedic devices. Certain metal, polymer and ceramic materials remain a common choice due to their biocompatibility and proven success rate. Although certain materials have been used for many years such as Stainless Steel 316L and UHMWPE, due to advancements in material technology new options have become available to use, such as ASTM F75 Cobalt Chrome Molybdenum (CoCrMo).

By establishing an understanding of wear mechanisms [41], [68] and wear modes [69] models can be delivered to solve these problems. Unfortunately, realistic and application specific solutions do not lie in the form of simple analytical forms, and the understanding of wear is arguably at a much earlier stage to that of friction, especially for biomedical applications. The following statement provides an example of the complexity of wear, *"There has been controversy concerning wear theory for over a century and it is improbable that a single governing equation will be established to cover all eventualities"* [70]. Many publications on wear modelling follow the basic governing equation of wear as previously defined [70]. In terms of wear modes the complexity becomes even greater when trying to model third body contact (i.e. mode 3).

Currently within the literature it seems that the particle influence of third body wear is less understood than other modes [7]. It has also been stated that the common mechanisms of wear in articulating joints are abrasion, adhesion and fatigue [69], although in other publications others have been stated for general wear. I do agree with McKellop [69] that the terminology of 'damage' needs to be clarified to ensure appropriate conclusions are reached when assessing

the wear of contact surfaces. This particular publication by McKellop [69] highlights other important challenges pertaining to measuring the wear of implanted devices *in vivo* (rather than assessment after retrieving the implants) and explaining causes for damage modes. To appreciate the amount of work published on 'wear', Meng and Ludema [71] reported over five thousand papers from two leading wear journals published from 1957 to 1992. Meng and Ludema [71] comment on current wear equations and models being very impractical and perplexing to engineers. Although the publication comes across as rather negative, this perhaps reflects the frustration of those whose study the topic and try to solve problems using numerical or analytical methods. There are one hundred different variables and constants used in general sliding wear equations [71], which is understandable based on the large number of equations available for general wear.

Despite the advancements in biomaterials this problem still poses a risk to patients in many areas of the body [72]. By reducing the wear of materials inside the human body, the risk of device loosening can be lowered. As a result the biological process of aseptic loosening is currently one of the most common causes of long term hip implant failure. A modified *in vitro* test demonstrates that a combination of MoM and CoC hip implants produces stripe wear caused by contact of the femoral head with the rim of the acetabular cup during the simulation cycle. This same observation was not present on the CoM (ceramic-on-metal) implant [9]. It is possible that the stripe wear pattern could have been removed by the polished surface of the softer metal and polyethylene material. The same study by Williams et al. [9] reports higher mean wear rates and friction factors for the MoM implant than for the CoM and CoC implants. It is important to note that microseparation has not always shown to result in a surface wear increase. Interestingly, for a CoP (ceramic-on-polyethylene) hip implant the volumetric wear was four times less during an experimental simulator test which included microseparation than for a testing procedure only based on standard conditions [73].

This finding is unique and the only material combination and test cited where this holds true. Stripe wear appears to be less of a problem for polyethylene materials due to the softer material properties. The advantages of a ceramic-on-metal configuration is presented in a particular study showing the CoM combination provides a wear rate of one hundred times less than that of a MoM configuration. Ceramic-on-metal can ensure a lower volume of wear over the MoM due to a reduction in corrosive wear, which is a point not often covered in the literature [74]. A bedding-in period wear rate for the first million cycles for MoM was measured at 3.09 ± 0.46 $mm^3/10^6$ cycles, which lowered to 1.23 ± 0.5 $mm^3/10^6$ cycles following the bedding-in period. However for the CoM combinations a very low wear rate of 0.01 $mm^3/10^6$ cycles is reported [75].

Further attention was given to a specific grade of metal bearing material known as cobalt chromium molybdenum (CoCrMo). For this material Cawley et al. [76] used microabrasion wear testing to establish the mechanical properties of the material under different conditions such as 'as-cast' and heat treated. Some orthopaedic device manufactures opt for the 'as-cast' form of Cobalt Chrome (i.e. 'BHR' by Smith and Nephew and 'Recap' by Zimmer), while some select the HIPed (hot isostatically pressed) option (i.e. Corin for the 'Cormet' and Weight Medical Technologies for the 'Conserve Plus'), there are even those who opt for the wrought form of the material (i.e. for the Zimmer 'Durom') [60]. Establishing the ideal form for the application of hip resurfacing is a topic of ongoing research. The study by Roberts et al. [60] highlights contradicting results by presenting superior wear resistance of the as-cast material over the wrought material and the study by Cawley et al. [76] presents the opposite finding. For the HIPed and as-cast wear performances, results are shown for the as-cast form of the material outperforming the HIPed form of the material in terms of wear coefficient [76], this finding is also backed up by a further reference showing lower wear rates at 2 million cycles [77].

Even though surface coating was not considered within the scope of modelling in this project, the motivation behind the application of surface engineering to hip implants is discussed along with its potential to reduce the problems. A high carbon CoCrMo hip implant device with engineered surfaces such as the application of CrN (chromium nitride) using arc evaporative physical vapour deposition, provided superior tribological performance in terms of wear rates against an equivalent hip prosthesis without any surface engineering [78]. The positive finding from this study means that opportunities exist to lower the wear rates of articulating hip joint implants using coating methods. It should be noted that only short term cyclic studies were conducted, therefore long term performance results must be obtained. A separate study reports that CrN coated hip bearing surfaces reduces the wear rates during *in vitro* testing, which is a positive solution to improving the tribological performance of MoM bearing surfaces, however it should be noted that no microseparation or other harsh conditions were considered [79].

2.1.5.3. Experimental Methods and Inspection

The Archard wear models were developed as a result of using pin-on-disc tests. However, these methods fail to simulate the complex wear and damage mechanisms experienced in human articulating joints. The inspiration behind the development of many wear models used today in computational wear simulations are based on the use of friction and wear testing machines. It was indeed a friction wear testing unit that Archard had used in 1953 to determine the volumetric wear rates of different material pins [54]. These testing methods as studied in this project and shown in Figure 2.8, can also contribute to useful research within this field. The equipment works by the lower disc being driven by an AC motor which also drives the upper disc through a gearing arrangement, this allows for a controlled amount of slip between the discs. To record the wear, a linear variable differential transducer measures the displacement which is then sent to a software controlled data logger. Such tests lead to calculations of gravimetric wear and wear rates for comparisons against different materials. Although this

type of test can be used to compare the wear rates of different biomaterials used for total joint replacements, it cannot directly compare the wear rates of specific hip implant designs. Therefore many research groups use *in vitro* testing equipment which are specific to assessing the wear of implant devices [80]. The experimental set-up (Phoenix tribology Ltd, Hampshire, UK) shown in Figure 2.8 provides a disc-on-disc configuration, however, a pin-on-disc configuration can also be used. Due to the limitations of the experimental methods discussed above, in this project the testing equipment was used for study and learning purposes only.

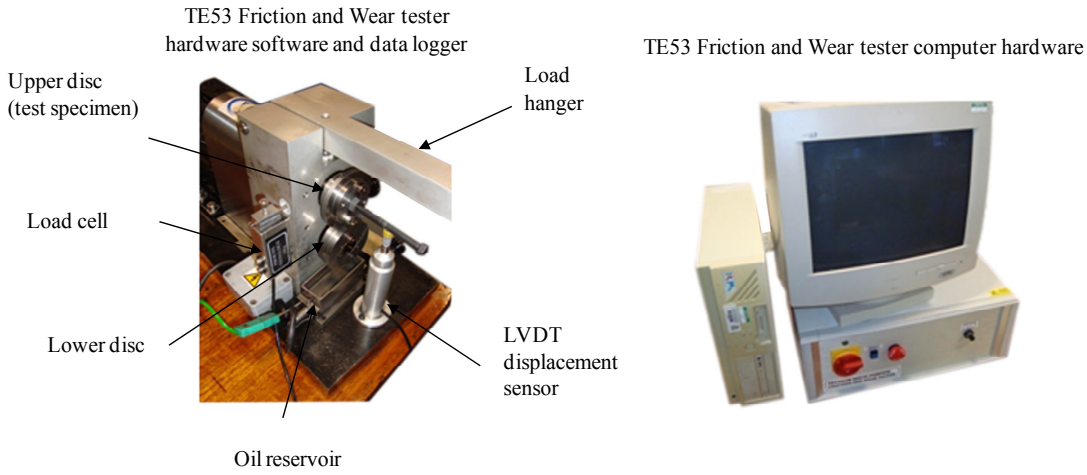

Figure 2.8. TE53 Friction and wear testing equipment and set-up (Precision Mechanics Laboratory, The University of Warwick)

Some studies have made specific reference to the use of pin-on-disc experiments in the aim to improve the performance of implant devices. The effect of pin geometry misalignment between a pin and plate was assessed with focus being placed on contact pressure using the finite element method. For soft-on-hard bearings geometrical discontinuity of pin misalignment did not cause a significant increase in contact pressure, however for hard-on-hard bearings with a misalignment of 0.5° the contact pressure increased by 10 times. This study is useful for understanding and justifying the benefits of pin-on-plate testing for studying the tribology of joint implant materials [81].

Another study describes the use of a pin-on-plate testing unit with an integrated electrochemical cell in 25% bovine serum to determine the effects of pin rotation on the wear and metal ion release of two different combinations (metal pins and metal plates, metal pins

and alumina plates). Important conclusions are drawn from the study [82]. In a separate study, electrochemical measurements were made. The aim was to determine the corrosion and corrosion enhanced wear and surface damage on high carbon CoCrMo and low carbon CoCrMo [83]. Finally, a pin-on-plate experimental test was useful for assessing the contact mechanics for a spherical and flat ended pin, which compares well to the theory [84].

An example of surface wear results obtained using a disc-on-disc experimental wear testing unit is shown in Figure 2.9a. Following any friction wear testing and depending on the geometry of the test specimen, a number of techniques can be used to assess the wear on the material surfaces. The most commonly used are microscope and imaging equipment such as: the optical microscope, scanning electron microscope (SEM) and transmission electron microscope (TEM).

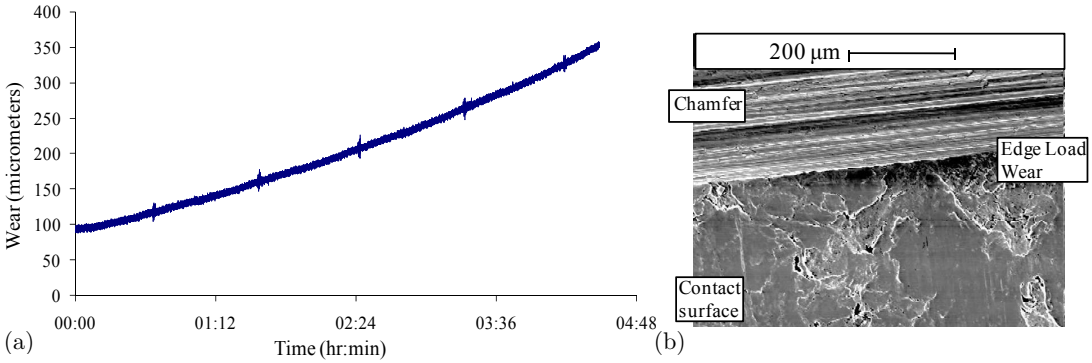

Figure 2.9. (a) TE53 wear test results for carbon steel (b) SEM inspection following friction and wear testing

Conducing SEM inspection before the test can be useful in understanding the relative affect of sliding and rolling contact under load following the friction and wear testing, as shown in Figure 2.9b. The figure shows the use of SEM techniques to assess the edge of the disc's contact surface.

2.2. Contact Mechanics

To establish an understanding of surface damage, wear and shakedown analysis associated with implanted hip devices, the contact mechanics between components must be considered.

The tribological performance of any component will be affected by the contact mechanics between two or more material bodies. Shigley et al. provides a clear explanation of the contact mechanics between two bodies [85] which has become a widely used reference in stress and strain calculations [86]. Roark and Shigley et al. [85, 86] make reference to "Hertzian stresses" between two spheres and two cylinders in contact. These geometric cases are typical of many engineering problems, with the two spheres being analogous and adaptable to a hip ball-in-socket type joint. The stress and pressure distributions will depend upon the geometry of the bodies and the load cases. For a simplistic view of the problem, the stress and pressure distribution (i.e. for uniaxially loaded cylinders or spheres in contact) is shown in Figure 2.10a. By knowing the following information for body 1 and body 2, the contact radius (c_d) can be obtained [85],

$$c_d = \sqrt[3]{\frac{3L}{8}\frac{(1-\nu_1^2)/E_1 + (1-\nu_2^2)/E_2}{1/D_1 + 1/D_2}} \tag{2.1}$$

where L is the applied load, ν_1 and ν_2 are the Poisson's ratio's of body 1 and body 2, E_1 and E_2 are the elastic modulus of body 1 and body 2, and D_1 and D_2 are the diameters of body 1 and body 2.

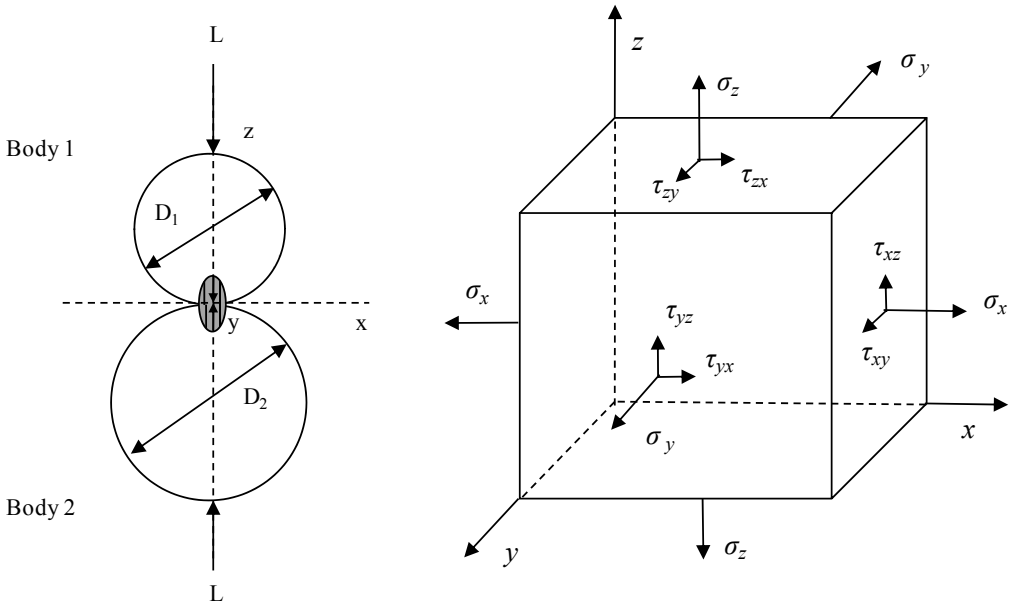

Figure 2.10. (a) Contact stress between two spheres and cylinders [85] (b) three-dimensional volume [87]

The maximum pressure (p_o) can be obtained from the following equation [85]

$$p_o = \frac{3L}{2\pi {c_d}^2} \tag{2.2}$$

Following calculation of the maximum contact pressure, the stress values can be obtained from [85],

$$\sigma_x = \sigma_y = -p_o \left[\left(1 - \frac{z}{c_d} \tan^{-1} \frac{1}{\frac{z}{c_d}} \right) (1+\nu) - \frac{1}{2\left(1 + \frac{z^2}{{c_d}^2}\right)} \right] \tag{2.3}$$

$$\sigma_z = \frac{-p_o}{1 + \frac{z^2}{{c_d}^2}} \tag{2.4}$$

where z (on the z-axis) is the radial distance from the point of contact between body 1 and body 2, and σ_x, σ_y and σ_z are the principal stresses in the x, y and z directions. From the equations above and knowing that σ_x (stress in the x direction) equals σ_y (stress in the y direction) and $\tau_{xy} = 0$, follows onto the following equation [85],

$$\tau_{yz} = \tau_{xz} = \frac{\sigma_y - \sigma_z}{2} = \frac{\sigma_x - \sigma_z}{2} \tag{2.5}$$

where τ is the shear stress. To understand the directions of these stresses, by taking an infinitesimal volume from one of the material bodies, the normal and shear stresses can be shown (Figure 2.10b). The maximum value of normal stress is found to be at the surface contact, however the maximum shear stress is below the surface contact. Although the Hertzian contact theory is applied to many simple geometric applications the limitations should not be ignored. The conditions of contact between joints in the body require more complex analysis for accurate solutions to be obtained, which includes non-linear material properties and irregular geometries. Nonetheless, this forms the basis of understanding contact between articulating joints for both natural and artificial joints.

2.2.1. Contact Pressure and Stresses of Hip Joints

For spherical bodies in contact, a circular contact patch will be observed as expressed by the following equation and shown in Figure 2.11a,

$$p(r) = p_o\left(1 - \frac{r^2}{a^2}\right)^{1/2} \tag{2.6}$$

where p is the pressure distribution, r is the radial distance from the centre of contact and a is the maximum contact radius. The contact area will be elliptical when the bodies in contact are non-conforming as expressed by the following equation and shown in Figure 2.11b,

$$p(x,y) = p_o\left(1 - \left(\frac{x}{a}\right)^2 - \left(\frac{y}{b}\right)^2\right)^{1/2} \tag{2.7}$$

where x and y is the radial distance from the centre of contact along the major and minor axes respectively. The maximum contact radius along the major and minor axes is given by a and b respectively.

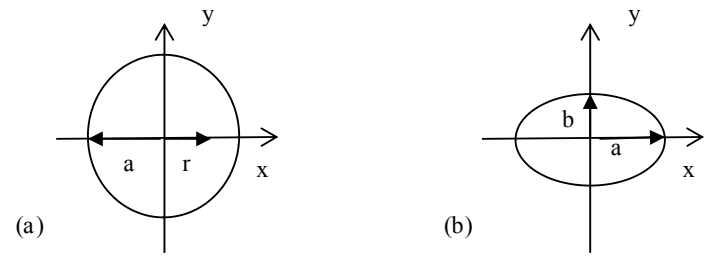

Figure 2.11. Contact area for (a) circular contact (b) elliptical contact

The principle of conforming and non-conforming contact should be carefully understood. Two bodies contacting each other at multiple points before any deformation takes place is known as conforming contact. Two bodies contacting at one point (elastic half space), is typical of non-conforming contact and is the basis of Hertzian contact theory. To ensure the theory is applicable to hip joints (ball-in-socket joints), the formulation is extended to consider angular coordinates [88].

Developing Hertzian contact theory further has provided a form of validation for finite element analysis of hip implant device analysis. The ball-on-plane theory has been presented by Mak et al. [89]. In order for comparisons to be made to a ball-in-socket joint, angular coordinates are used. To calculate the contact radius, a, the effective radius R_e is required,

$$R_e = \frac{R_c R_h}{c} \tag{2.8}$$

where the cup radius is R_c, femoral head radius is R_h and the radial clearnce c is between the acetabular cup and femoral head. The contact radius can be calculated,

$$a = \left\{ \frac{3LR_e\left(1-\nu^2\right)}{2E} \right\}^{1/3} \tag{2.9}$$

where E and v are the Poisson's ratio and elastic modulus respectively. The maximum contact pressure, p_o,

$$p_o = \frac{3L}{2\pi a^2} \tag{2.10}$$

can be obtained, along with the contact pressure distribution, P,

$$P = p_o\left[1-\left(\frac{x_h}{a}\right)^2\right]^{1/2} \tag{2.11}$$

where x_h is the x coordinate along the x-axis from the centre of contact.

An alternative approach by Young et al. [86] provides a more direct approach to determining the contact pressure between a ball-in socket joint. The contact pressure, p_o,

$$p_o = 0.616 \cdot \sqrt[3]{\frac{LE^2}{{K_D}^2}} \tag{2.12}$$

is calculated by establishing the constant, K_D,

$$K_D = \frac{D_c D_h}{D_c - D_h} \tag{2.13}$$

from the diameters D_c and D_h, which are the diameters of the cup and head respectively.

Whilst Hertzian contact theory provides suitable analytical solutions to determine the contact area, pressure and stress, the limitations and assumptions must be understood. Strains must be small as well as within the elastic limit of the material and the area of contact must be small compared with the body radius of the elastic half space, the surfaces must also be continuous and frictionless.

2.2.2. Contact Conditions and Modelling Simulations

The main types of contact arising from normal gait patterns and patient activities occurring within hip implants are briefly summarised by Buford, Goswami [90] and Cornwall et al. [91], which are sliding (or gliding) and rolling. Contact, wear and shakedown theory has been based on these two types of contact within the literature. For normal and edge loaded hip joints caused by microseparation it is expected that both rolling and sliding motion will occur due to the highly varied and complex kinematics of the human hip joint during its operating duration.

Contact mechanics is widely simulated using the finite element method (FEM), where both the contact area and contact pressure distribution can be determined. By simply decreasing the acetabular cup thickness from 4.5 mm to 1.5 mm the contact pressure reduces from 55 MPa to 20 MPa [92]. This is just one example of how efficient and effective FEM can be used as a tool for parametric studies of hip implant device design. A complex model of a hip implant contact problem using the finite element method is not always required. A comparison was conducted by Jin et al. between a 3D model and 2D axisymmetric model with good agreement of results [93]. The study claims how simplified models can be used to replace more complex ones, as long as the simplifications are valid and justifiable. The modelling strategies for various loading conditions are studied further and discussed in this thesis.

2.2.3. Contact, Subsurface Stresses and Edge Loading Contact Theory

So far all equations and theories discussed have only considered the contact mechanics under loading without any tangential or sliding contact. Therefore, in order to further understand the contact mechanics and tribology of hip resurfacing devices, both these occurrences must be studied. Theoretical equations have been derived for surface and subsurface stresses, which lead to the graphs plotted in Figure 2.12. Figure 2.12a provides a plot of the stresses σ_r/p_o, σ_θ/p_o, and σ_z/p_o in the directions based on a standard cylindrical coordinate system, as well as

the shear stress τ_1/p_o. The contact stresses on the body surface can also be plotted (Figure 2.12b). These plots can be extended further to include residual stresses and stresses after shakedown (Figure 2.12c), where σ_{xx} and σ_{yy} are the stresses in the x and y direction, σ_{xz} is the shear stress, ρ_{xx} and ρ_{yy} are the residual stresses in the x and y direction.

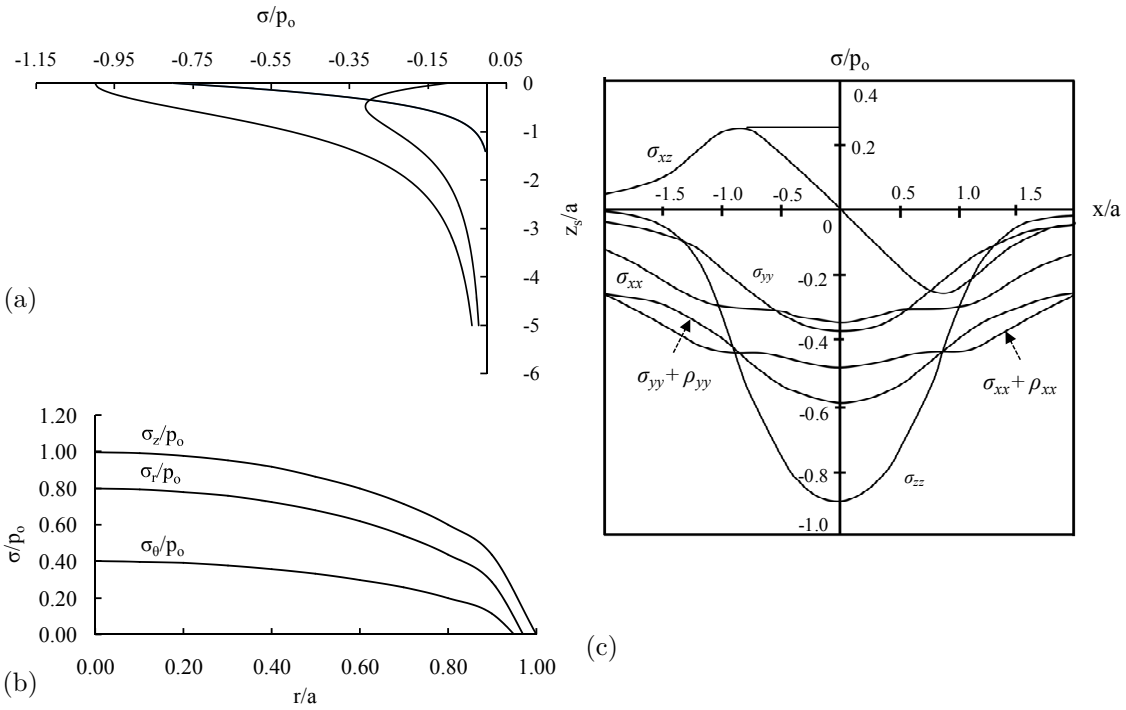

Figure 2.12. Contact theory (a) subsurface stresses and shear stress [94] (b) surface contact stresses [94] (c) internal stresses, shear stress, residual stresses (after shakedown) [95]

Non-Hertzian contact is observed close to the edge of contact due to the non-parabolic profiles of contact pressure. A theoretical model which considers the contact pressure distribution at the edge of contact, is known as the "roller end effect" as discussed by Johnson (Figure 2.13) [94].

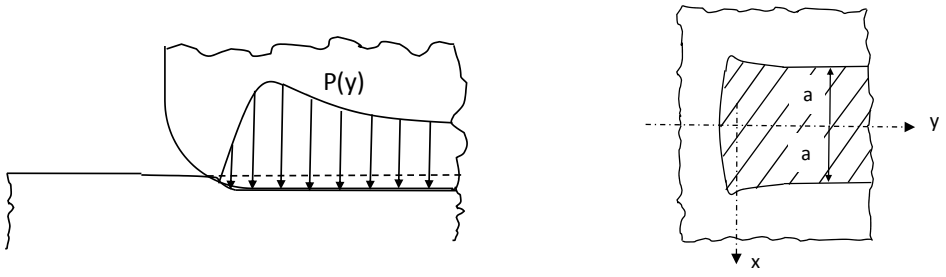

Figure 2.13. Cylindrical roller edge contact pressure distribution

The cylindrical roller ball bearing is discussed, where the Hertzian contact pressure distribution is given by

$$p(x,y) = \frac{P}{\pi a l}\left\{1-\left(\frac{x}{a}\right)^2\right\}^{1/2} \tag{2.14}$$

where corrections have also been discussed to form a more accurate expression at the ends of the rollers, the length of the roller is l and E^* is the effective modulus of the two bodies in contact

$$E^* = \frac{1-\nu_1^2}{E_1} + \frac{1-\nu_2^2}{E_2} \tag{2.15}$$

From the theoretical contact model presented by Young, Budynas [86] and Stolarski [96], the maximum and minimum radius of curvature for each body along with the principal curvature are shown in Figure 2.14a.

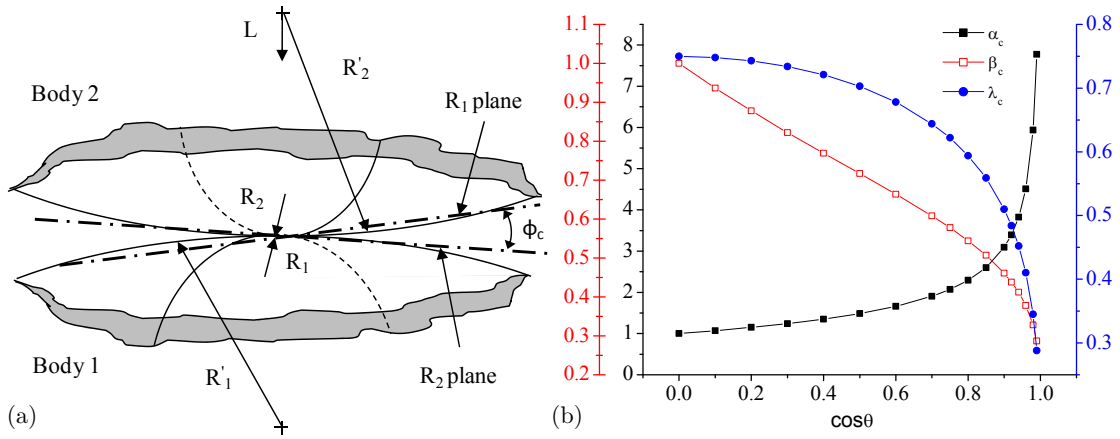

Figure 2.14. (a) General case of bodies in contact (b) α_c, β_c and λ_c values for general case contact

This theoretical model can be applied to both normal and edge loading conditions, however as theoretical models have already been developed and defined for normal loading contact, this section will only consider the theoretical model development to cover other possibilities of contact conditions occurring between the femoral head and acetabular cup. This model provides an equation for contact pressure, p_o,

$$p_o = \frac{1.5L}{\pi c_t d_t} \tag{2.16}$$

and the variables c_t, d_t and K_D are the calculated from:

$$c_t = \alpha_c \sqrt[3]{LK_D C_E} \tag{2.17}$$

$$d_t = \beta_c \sqrt[3]{LK_D C_E} \tag{2.18}$$

$$K_D = \frac{1.5}{1/R_1 + 1/R_2 + 1/R'_1 + 1/R'_2} \tag{2.19}$$

where α_c, β_c and λ_c can be determined from the data plotted in Figure 2.14b. To determine the variables above cosθ must be determined,

$$\cos\theta = \frac{K_D}{1.5} + \sqrt[3]{\left(\frac{1}{R_1} - \frac{1}{R'_1}\right) + \left(\frac{1}{R_2} - \frac{1}{R'_2}\right)^2 + 2\left(\frac{1}{R_1} - \frac{1}{R'_1}\right)\left(\frac{1}{R_1} - \frac{1}{R'_2}\right)\cos 2\phi_c} \tag{2.20}$$

where the angle between the R_1 plane and R_2 plane is denoted by, ϕ_c (Figure 2.14a).

2.3. Computational and Numerical Methods

Following on from discussing contact mechanics in section 2.2, the methods to study the contact mechanics and tribology of hip implant devices are discussed within this section.

While completing the literature review no study was found to cover the effect of bone models on the contact mechanics and wear of finite element models. From publications and implantation statistics, the femur and hip joint were the most commonly analysed areas of biomechanics. Therefore, hip orthopaedic devices are in many ways the most understood and developed devices. Despite early developments of finite element models being focused on the methodology rather than the result, axisymmetric studies of custom fit implants have been cited by Huiskes and Chao [97]. Based on unique patient specific factors such as: geometry, age and general health, FEM was used extensively and efficiently to study custom-design implants [98]. The demands for custom implants further justify the need for research in computational and numerical methods to ensure that such products would be successful and commercially viable. In addition, the use of finite element analysis in design optimisation is also a valuable tool for biomedical engineering [99].

The knowledge and application of wear simulations using finite element methods is not as extensive as that of conventional structural analysis. Currently, no commercial finite element package includes wear simulations as a standard application for solving wear problems.

McKellop [69] explains the methods to model the changes in contact surface geometry as a result of wear, which is achieved by moving nodal positions in the FE model using an explicit Euler Integration method. This is crucial because changes in contact geometry lead to changes in contact pressure. The author has cited five papers using three basic steps for wear simulations using finite element analysis. Perhaps this is the start of standardising these methods for the future, however, a method to assess the error introduced by extrapolations still requires development [100].

A recent paper by Kluess et al. describes a suitable approach of using finite element analysis to assess orthopaedic implants, which explains how finite element approaches are still developing in the field of biomedical engineering [101]. This methodology involves bone segmentation and computer aided design following on to pre-processing and post-processing. From this study it has been understood that the additional difficulty with modelling human bone is due to its varying properties, which require complex material model definitions. The author has avoided modelling the complexity of trabecular bone directly by defining different values of Young's modulus and using temperature dependent material models with Hounsfield units (also termed 'CT numbers'). This represents the attenuation coefficient of tissues in computer tomography. Dar et al. [102] comments on how the majority of analyses within biomechanics fail to consider the broad variation of material properties that can occur in human tissue or manufacturing deficiency of materials. The subject of model complexity and sensitivity remains open and has been studied in this thesis. It is important to understand how much the complexity and validity of the analysis is compromised based on this research aiming to solve contact problems of hip implant devices. Up to this point, a concerning factor throughout the literature review was the lack of consistency of finite element methodology and modelling techniques, which could make comparative work difficult. Nevertheless, for

experimental testing, standardisation has been set in the form of international standards which is also discussed in this chapter.

2.3.1. Finite Element Analysis

Finite element wear simulation studies have been published for total joint replacements [103], [10] although the validity and accuracy of the results are under great scrutiny. The primary FEA software package used within this project was Abaqus (Dassault Systèmes Simulia Corp.) which is widely used. This software has been developed for over 30 years and is used to solve many complex engineering problems within industry and academic research. It is designed to interact efficiently with other computer aided engineering software, and this has been explored within the scope of this project. There are examples within the literature showing how Abaqus has been used as a tool to model the contact between joints in the body as well as predict mechanical wear [104].

The importance of verification and validation of the finite element method was discussed by Jones and Wilcox [105]. A method of assessing the validity of the finite element results for a hip implantation was completed and the deformation of the finite element model was within 7.1% difference of mechanical testing of the component. For contact area validation, a study by Jin et al. [106] was conducted to assess the displacement and contact area comparison between the finite element analysis results and experimental work with very good agreement reached between results. A method was described by D'Lima et al. [107] who used pressure transducers to compare experimental peak contact stress and contact areas against results obtained from finite element analysis.

2.3.1.1. Analysis Types and Options

The different types of finite element analysis are clearly and concisely summarised by Heisler [108], as the understanding of this is important to ensure the problem is modelled with

appropriate solvers. As a starting point, linear analysis assumes that the material properties and displacement responses are linear. This offers a chance to assess the model at a less computationally intensive level than considering non-linearity. In terms of hip implant contact problems, it may be reasonable to assume linearity if the predicted contact stresses are not large enough to cause plastic deformation [109]. The complexity of the analysis would be increased when including non-linear effects. Non-linearity occurs when the stiffness of a material changes as the force exerted on it increases (i.e. the material deforms). The types of non-linearity to consider in tribological problems are contact, geometry and material. Non-linearity becomes increasingly important to consider when modelling non-linear materials with large deformations [87].

2.3.1.2. Finite Element Analysis with Wear Simulations

A combination of Lagrangian and Eulerian formulations allows for adaptive meshing techniques to be used for user defined mesh customisation and this technique has been formulated to be used to model specific finite element analysis problems [110]. The Arbitrary Lagragian Eulerian adaptive meshing techniques can be used to deal with large deformations or material loses (i.e. material wear). This can be achieved by a technique allowing the mesh to move independently to the material, therefore moving only the nodes. There are limitations of using adaptive meshing, including the restrictions of element types and contact interaction properties, therefore compromises may be required when using these techniques. The use of adaptive meshing has become an important part of conducting wear simulations for orthopaedic devices, and this methodology has been applied and published in [111]. This technique should not to be confused with adaptive 'remeshing' techniques which are used to refine the mesh of a model in areas which require high accuracy.

The need to study artificial joints in terms of its long term performance has been stated [39], and the drive to minimise wear even at the nanoscale is an ongoing ambition of many

engineers. A method of a contact-coupled wear simulation is carried out without the use of the FEM in [109] and good agreement was obtained against results from using the FEM [112]. Jin et al. [109] have criticised the use of a finite element model to study wear due to the amount of time required to build and refine the models, they also argue that this problem can be overcome by using simple equation based methods. It should be noted that as research continues in this field, flexibility, customisation and solving time will continue to improve. By assuming an Archard abrasive wear model [54], the following relationship can be used to simulate the wear between two surfaces in contact using finite element analysis. The following formulation is adapted from [113] to obtain the wear depth, h,

$$h = k_w ps \tag{2.21}$$

which is also used by Kurtz et al. [114], where the material and surface dependent dimensional wear coefficient k_w has units of mm^3/Nmm. The contact stress p and sliding distance s are obtained directly from the finite element post-processing solver. From (2.21), the wear depth, h, is calculated, however within hip implant contact problems, both the sliding distance and contact pressures vary during cyclic loading and angular displacement. Therefore, an equation to cover one complete patient walking gait cycle has been provided [113] for the wear depth distribution matrix $W(\theta,\varphi)$ as an integral with respect to time t from the limits of heal strike h_s to toe off t_o, where θ and φ are the polar angle and azimuthal angle respectively,

$$W(\theta,\varphi) = \int_{h_s}^{t_o} k_w \times P(\theta,\varphi,t) \times v(\theta,\varphi,t) dt \tag{2.22}$$

This equation is formulated to include the point location on the contact surface in terms of spherical co-ordinates (θ,φ), the distribution of normal stress components $P(\theta,\varphi,t)$ and the instantaneous sliding velocity at the contact surface $v(\theta,\varphi,t)$. In its temporally discretized form this equation becomes [113],

$$W(\theta,\varphi)=\sum_{i=1}^{n}k_w\times P_i(\theta,\varphi,t)\times s_i(\theta,\varphi,t) \tag{2.23}$$

where $P_i(\theta,\varphi,t)$ is the contact stress distribution, $s_i(\theta,\varphi,t)$ is the incremental sliding distance and n is the number of increments during the gait cycle. Along with the inclusion of hip joint angular displacement, this is in a form that can be utilised in combination with the finite element method along with the inclusion of hip joint angular displacement.

A similar approach was taken in a separate study which was a 10 year wear simulation of a UHMWPE (ultra high molecular weight polyethylene) patellofemoral joint [103]. The wear rates are comparable to that observed for the hip joint; however, the wear model does not consider wear such as delamination or pitting which are known to be factors from these types of retrieved joints and polyethylene joint implant materials. Although abrasive wear is a major contributing factor to the wear, it is not the only type of wear to be considered (as will be discussed further in this chapter) and it may not be safe to assume a constant wear coefficient. Ong et al. [115] also used a very similar methodology, by applying Archard's Law and using finite element analysis to determine the contact stress in combination with the sliding distance and wear coefficient. From this, the wear depth under component loading was obtained. Throughout this type of implicit finite element analysis, equilibrium requires establishment as demonstrated by Maxian et al. [116] where, once the contact is established, the displacement control can be replaced by load control.

To provide confidence and further validation of using an adaptively-meshed sliding-distance-coupled finite element model for predicting wear simulations for orthopaedic implants, Callaghan et al. [117] published volumetric wear results which compared within 4.1% of the gravimetric results from experimental testing. By extending the literature review outside of the wear of just orthopaedic device implants, wear simulations have been conducted based on more traditional applications. The work published by Kim et al. [100] presents a good agreement between the results obtained from finite element wear simulation and pin-on-disc

tests. The paper does highlight and confirm the lack of a standardised model for wear simulations within finite element analysis. The advantages of using computational methods over experimental methods can be seen from the simulations published by Lui et al. [10] where a long term wear simulation of a metal-on-metal hip resurfacing device was conducted, although no edge contact was observed.

2.4. Tribology and Biotribology

As discussed, wear and surface damage are a prominent problem with total joint implants and therefore tribology in the future will need to play a major role in solving these problems at all scales, especially as the behaviour of materials differ depending on the scale. As mentioned within this section, traditional friction wear testing equipment can not simulate the complex kinematics and loading conditions experienced by hip implants *in vivo*, therefore experimental hip simulators are used.

2.4.1. Friction and Lubrication

In order to consider the tribology of the hip bearing surfaces both friction and lubrication must be studied. A friction study of total hip replacements (THR) with 28mm bearing diameters was carried out [118] to assess the influence of material combinations, lubricant and swing phase load using a combination of theoretical and experimental methods. Unfortunately the study only considers 28mm diameter bearings, however it shows that CoC bearings had a lower friction factor compared with MoM bearings and by increasing the swing phase load the friction factor also increases. Specifically, the coefficient of friction between CoCrMo and CoCrMo in synovial fluid or bovine fluid can be represented by a friction factor of 0.16 [119], this value can be used as the coefficient of friction at the interface for finite element modelling. As well as ensuring a low coefficient of friction between the bearing surfaces, effective bio-lubrication plays a key role in reducing the wear of hip joint implant devices. This is an area

that engineers and surgeons have less control over than other aspects such as material properties, device design and manufacture. It is important to appreciate that the implants are being placed into a physiological environment. Lubrication regimes in both natural and implanted hip joints have improved our understanding of articulating joints and the causes of problems faced by patients, surgeons and engineers [120-122]. From 1932 to 1998 there were 40 examples of suggested mechanisms and investigations of synovial joint lubrication, which highlights the complexity of the subject and one which was described as *"far from being understood"* [123]. This statement is supported by Katta et al. [122], who summarise that no single theoretical model can provide a complete explanation of joint lubrication. Understanding the lubrication regimes will help to make appropriate assumptions of the contact conditions between bearing surfaces using the finite element method.

The most widely used expression for predicting the minimum film thickness h_{min} between hip bearing surfaces is the Hamrock-Dowson formula [58], [124],

$$h_{\min} = 2.798\left(\frac{\eta u_v}{E^* R_e}\right)^{0.65}\left(\frac{L}{E^* R_e{}^2}\right)^{0.21} \tag{2.24}$$

where u_v is the entraining velocity, E^* is the equivalent elastic modulus, η is the lubricant viscosity and L is the load. The effective radius R_e is calculated from

$$\frac{1}{R_e} = \frac{1}{R_c}\frac{1}{R_h} \tag{2.25}$$

by knowing the radius of the femoral head R_c and acetabular cup R_h respectively.

From understanding the presence of hip joint lubrication, the occurrence of hip squeaking can be discussed. If there is any link between hip squeaking and edge loading, then the mechanics of hip squeaking should be understood in detail. Brockett et al. [125] concludes that reducing the lubricant film thickness and increasing the friction leads to a greater chance of hip squeaking, which is more likely through increasing the bearing clearance. It was suggested by Chevillotte et al. [126] that when the fluid film between two surfaces is disturbed in

combination with metal particles that this leads to the problem of hip squeaking. The observation of hip squeaking and occurrence of stripe wear patterns from *in vivo* patient studies and retrievals (Figure 2.15) led to the investigation of determining the cause of these problems by Restrepo et al. [127]. Unlike the majority of studies reviewed, Figure 2.15 shows clear stripe wear occurring significantly above the rim radius of the acetabular cup. Even though the exact cause of stripe wear and edge loading could not be determined, there were suggestions of a link between hip squeaking, stripe wear and edge loading.

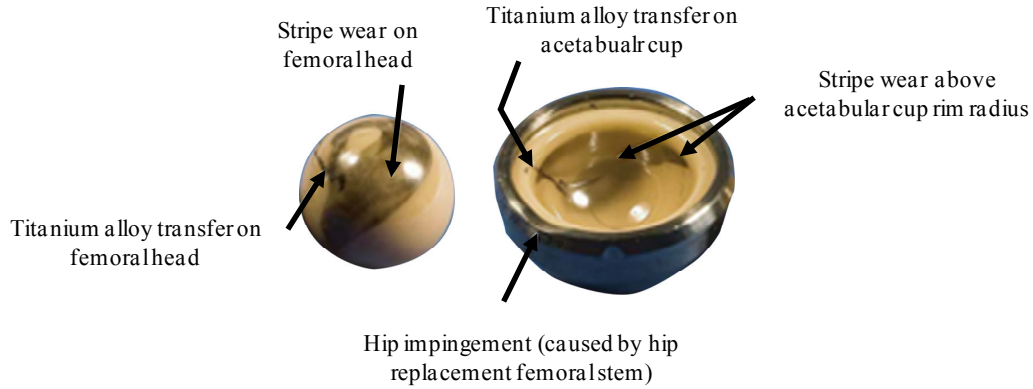

Figure 2.15. Stripe wear observed on CoC bearing surfaces [127]

The study of bio-lubrication helps to improve the understanding of wear associated with natural and artificial human joints as well as leads to the design of better performing implant devices. This philosophy is also supported by Neville et al. [50] who state that the main difference between artificial joints and natural joints is that the artificial joints are lubricated by oil (plus additives) and the natural joints are lubricated by water (plus other components). Further research into the lubrication of hip implant devices is provided in Appendix C – Lubrication of Hip Implant Devices.

2.4.2. Wear Mechanisms

Although wear itself is a process of material displacement from one material caused by the action of another material i.e. contact, there are many wear mechanisms (Figure 2.16) and they must all be considered to understand which are applicable to the hip joint implant devices and which contribute to normal and edge loading conditions.

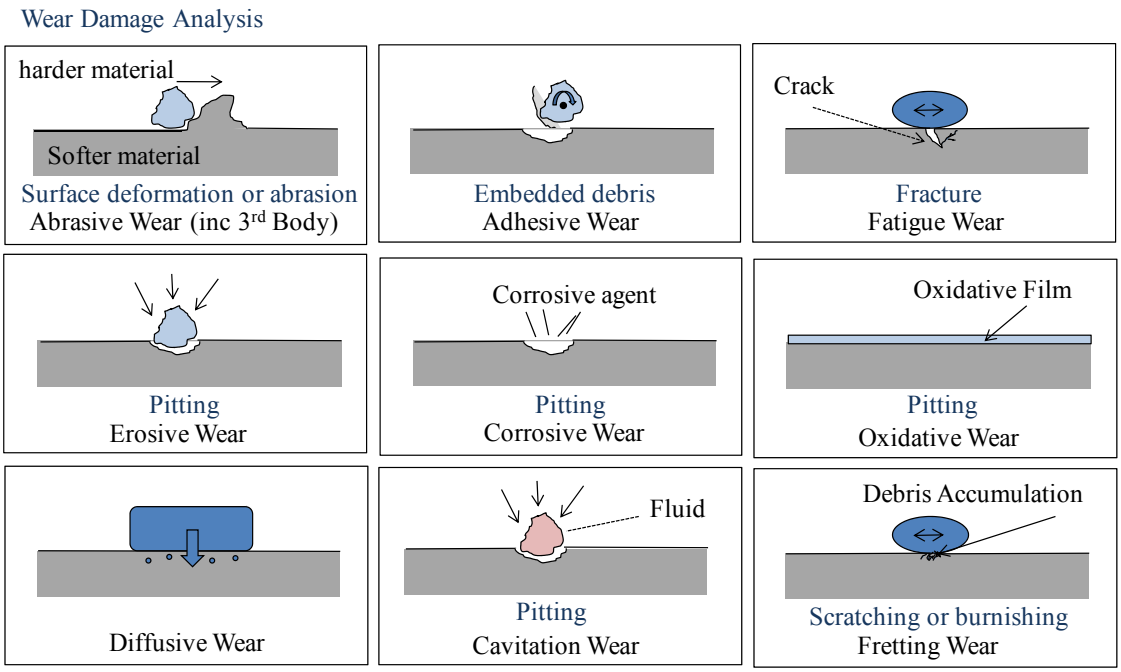

Figure 2.16. Wear mechanisms

Studying the wear data obtained directly from experimental simulators is a very challenging task [128]. Before discussing each wear mechanism, it is useful to discuss research previously conducted which indicate the relevant types of wear mechanisms specific to hip implant devices. Although specific to UHWMPE, both the hip and knee explants showed surface wear caused by adhesion, abrasion and micro-asperity contact [129]. Research has shown that it is also possible to specifically assess experimentally and theoretically the micro-asperity contact mechanics for metallic surfaces. A study by Jin et al. [130] concluded that micro asperity contact had a crucial role in the understanding of bearing device wear. This research provided part of the inspiration to study the application of shakedown in this problem. Retrieval devices have been compared to those from experimental simulator studies with microseparation modes and evidence of stripe wear were found on acetabular cups and femoral heads [9, 25, 26, 131].

The study completed by Manaka et al. provides evidence to two stripe wear patterns on the ceramic femoral head, which is also replicated in simulator testing [131]. This was caused by the femoral head centre displacing inferiorly which led to an inferior peripheral wear scar on the femoral head during swing phase. Then at heal strike the contact between the head and

cup caused a superior wear scar on the femoral head before full relocation between the cup and head was achieved. There is currently no literature which reports stripe wear occurring as a result of standard experimental simulator testing [132], however all *in vitro* studies which include microseparation report cases of stripe wear [133].

2.4.2.1. Abrasive and Adhesive Wear

By definition abrasive wear occurs when hard material particles or asperities move across a surface causing a loss of material [48]. This is one of the most important forms of wear to be considered for joint implant devices. During initial contact of the femoral head and acetabular cup, no third body particles are expected to be present between the surfaces. This is of course assuming that no debris exists from tooling or ground bone or human tissue. During the operating life of the components third-body mode abrasive wear (Figure 2.17) is a possibility. Within the hip articulating joints, the potential for 3rd body wear could however be lower than for an enclosed contact surface due to a separation of the device leading to the debris being carried away from the wear zones by synovial fluid. Two-body mode abrasive wear could also be significant to the wear of the device in the wear zones, which means that the surface damage and wear is caused by the contacting surface. By using electron microscope techniques, implant retrieval studies show evidence of abrasive wear following cyclic loading of the devices, including in the region of stripe wear [32, 134]. Fisher et al. [135] reports scratches on femoral heads and therefore used the finite element method to model third body debris in total joint replacements which highlights damage to the articulating surfaces. There appears to be no study using the finite element method to assess the combined effects of edge loading and third body interaction. From the review of current literature there is still much deliberation on the kinematics and wear modes which cause stripe wear, therefore more asperity contact modelling research could lead to a solution to the problem. The challenge of reducing the surface stress and wear loss as a result of abrasive wear is appreciated when observing the

simplicity of a theoretical model, as developed by Pourzal et al. [136]. Despite the additional complexity, these theoretical models can be cumbersome and only provide very specific assessments in dealing with the problem of abrasive wear.

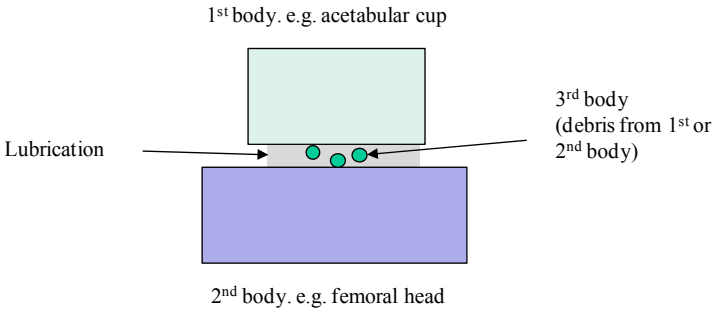

Figure 2.17. Third body abrasive wear

To understand abrasive wear further it is imperative to examine the shape of debris or grit between articulating surfaces. This can determine the resulting wear mechanism i.e. blunt debris leading to ploughing and sharp debris leading to scratching of the articulating surface with further debris particles being released. If debris particles are carried away from the bearing surface, then it is possible that they can be carried back there. By using computational fluid dynamic techniques it has been shown that a larger diameter bearing surface can lead to a high velocity influx of synovial fluid, which is ideal for improving the lubrication of the joint [117]. However, this could increase the amount of wear debris being transmitted back to the articulating surfaces, potentially leading to third body abrasive wear. An experimental study investigated 'foreign' body material leading to wear and damage of the articulating hip joint prosthesis caused by third body abrasive wear. Through the use of a scanning electron microscope, images of the surface and roughness from surface profiles revealed the severity and consequences of the problem [137, 138]. Unfortunately, this problem does not only occur on the softer bearing surface such as a UHMWPE, but also on a hard bearing surface such as CoCrMo. A study by Que and Topoleski [139] reports third-body wear on ASTM-F75 and ASTM-F799 CoCrMo material caused by poly-methyl methacrylate (PMMA) and bone particle surface ploughing. Therefore, ignoring the contributing factor of bone and other

foreign particles may not be a wise decision as this could account for a large amount of the total wear. More specifically a subjective study reports that 56.5% and 42% of the total wear debris collected after patients implantation surgery were bone fragments and cement fragments respectively, metal debris only account for the other 1.5% [140]. Past studies have also used chemical analysis techniques to observe debris from implantation tooling materials remaining within the implantation area.

For abrasive and debris modelling, the finite element method was used by Mirghany and Jin [141] in which a two dimensional axisymmetric finite element model was developed to simulate the entrapment of a 3rd body wear particle between polyethylene and CoCrMo alloy surfaces. The aim was to study the effects of the debris size on von Mises stress and deformation. The von Mises stresses could be used as a comparison to the materials yield strength and provide an indication of potential plastic deformation or scratching of the surface. The limitation of the study is that it only considers spherical wear particle morphology; also the study does not consider the effects of scratching through the increased number of wear particles between the bearing surfaces. One further study by McNie et al. presents results of the wear debris and near surface strain fields for UHMWPE using experimental and finite element methods, which also covers the assessment of scratch lip geometry on wear rate and debris morphology in UHMWPE. Although this is valuable research, not all causes of surfaces scratches were identified [135].

By reviewing the research carried out by Fisher et al. [75], for MoM and CoM bearing surfaces, a large portion of the wear debris assessed were *"oval to round in shape"*. Although the size of scratching within the contact area was between 0.5 µm to 5 µm and size of craters caused by pitting or carbide pullout, were between 0.7 µm and 3.5 µm, the size range of wear debris were in the nanometer scale. The mean maximum diameter for CoM and MoM debris were 18 nm and 30 nm respectively. The difficultly in assessing the ceramic debris was realised

due to the low wear debris quantities and accuracy at the nanoscale. A separate study by Shishido et al. [142] reports the use of a scanning electron microscope to determine the wear debris size and morphology to be 3 µm to 4 µm in size and polygon in shape for ceramic-on-ceramic bearing surfaces. The study is based on a retrieval Mittelmier type prosthesis with stripe wear observed during inspection of the device. Shishido et al. [142] concludes this type of prosthesis to be a poor design concept even though the device is shown to have excellent wear resistance.

For assessing hip implant bearing surfaces at this level, it is clear that the method of inspection used has a major role to play in determining the classification of micro and even nano sized particles. Nano sized alumina wear debris between 5-90 nm were recorded through the use of a transmission electron microscope (TEM) and larger particle sizes between 0.05-3.2 µm were observed using a lower resolution scanning electron microscope [33]. Although this study by Ingham et al. [33] is based only on the Mittelmeier and Charnley hip replacements, the study concludes that the wear debris morphology of particles released during standard kinematic conditions is smaller than that released during rim contact due to microseparation and heal strike [33]. A continuation of this study offers further research into the effects of abrasive wear and debris within the stripe wear zone specifically. By using both the SEM (scanning electron microscope) and TEM (transmission electron microscope) techniques the shape of the debris were found to be mostly oval to round in shape, however some were polygonic [143]. For the larger particles, it is shown that high local stresses during rim contact formed stripe wear patterns by trans-granular fracture. Specifically for metal-on-metal contact, Brown et al. [144] used TEM equipment and observed nano sized particles which ranged in size from 51-116 nm with a mean of 81 nm, and were mostly round in shape. However, a very small portion were characterised as “needle like”. The wear debris assessments from standard and microseparation based experimental simulator testing could provide further information

regarding the causes of stripe wear. Research carried out using a field emission gun scanning electron microscope (FEGSEM) found that both MoM and CoC wear particles were round and irregular in shape under standard and microseparation tests. No major differences in shape or size were found between particles from each test and the mean particle size was 50 nm [145]. By using the same inspection techniques Leslie et al. [146] reports that particles from a MoM 15 million cycle (mc) hip simulator study were oval or round in shape within a size range of 8-108 nm, and no sharp particles were found. Energy dispersive X-ray equipment was used to confirm the presence of cobalt chrome wear debris. Even more interestingly for the purpose of this project, Leslie et al. [146] noted that an increased bearing surface size led to a decrease in volumetric bedding in wear and overall wear. However the bearing diameter did not affect wear debris profile or magnitude.

The form of adhesive wear is determined by many factors and it is known to be one of the most common forms of wear [136]. When describing the wear mechanisms of stripe wear caused by edge loading adhesive wear is sometimes described and referred to as “grain pull out” [27, 32].

2.4.2.2. Additional Wear Mechanisms

Following a discussion of abrasive and adhesive wear, other forms of wear which have been stated within published tribology research, are covered within this section. The following wear mechanisms will be discussed within this section: fatigue, erosion, oxidation, corrosion, diffusion, cavitation and fretting.

Fatigue wear occurs due to cyclic stresses of asperities leading to crack propagation. Research for this particular wear mechanism could help to increase the longevity of the implant devices, as hip replacement and resurfacing devices are typically designed and expected to operate successfully for many millions of cycles. Therefore the problem of fatigue wear should not be ignored. The nature of cyclic loading means that crack initiation is likely to occur due to cyclic

surface fatigue. Although no deformation may be observed in the bulk material, surface assessments can show significant deformation and moderate sub-surface deformation. More detailed explanations of fatigue wear are provided by Stachowiak and Batchelor [48].

Erosive wear is defined as wear caused by the impact of a liquid or solid particle against a surface of a material [48, 136, 147, 148]. This form of wear mechanism is not stated as a form of wear which affects artificial joint implants. This project assumes that even low speed erosive wear models along with its governing equations and theory would not apply to the problems covered within the scope of this project.

As previously mentioned, materials such as metals implanted into the human body are classed as non-biological materials and therefore considered as a 'foreign' object to the body. For metals within the body, a thin oxidative layer occurs to protect the surface once the hip device has been implanted into the body [90]. The oxidative layer thickness has been noted to be within 5 nm [149]. After the oxidative coating is present, contact between the surfaces damages this layer causing it to dissipate [90], which means that metal ions and particulates would be released in the body. Although this should be considered for metal implantations, all ceramic materials do not react to oxygen like metals [149]. As oxygen will always be present in the human body, coating metallic implants such as diamond like coating (DLC) can reduce the occurrence of oxidation.

Corrosive wear is associated with surface damage caused by a chemical interaction with the surface, with the possibility of creating a film on the surface. Following the presence of a surface film, Stachowiak and Batchelor [48] explain that a combination of adhesive wear, corrosive wear, chemical damage, corrosive damage and 'pitting' could occur as a result.

In situations of high interface temperatures chemical diffusion can occur from one body to the other. The process of diffusion itself has been used as a method for coating joint implant surfaces, such as oxygen diffusion-hardening Ti-6Al-4V (Titanium alloy) [150]. In terms of

causing adverse tribological performance effects for metal or ceramic hip bearing surfaces, no literature or research has indicated such problems. However, diffusion wear is more of a consideration for UHMWPE bearing surfaces. A study observed that certain components of synovial fluid could diffuse into the material, causing alterations to the mechanical properties at the materials surface [151].

Cavitation wear is often observed in high speed engineering components such as propellers or turbine blades, and is not associated with a wear mechanism of joint implants. Therefore, this wear mechanism will not be considered to have any contributions to normal or stripe wear.

The mechanism of fretting is present when small amplitude reciprocating sliding occurs between surfaces in contact over a significant number of cycles. Fretting wear has received attention when assessing the wear between the bone and orthopaedic device interface, particularly the contact between the femoral stem and bone in hip replacements [152]. The micromotion between such surfaces were observed to be as small as 40 μm [153], and the wear debris could migrate to the bearing surface [154], leading to 3rd body abrasive wear. Fretting wear has also been observed between interfaces of modular implants, plates and screws [155]. It seems that fretting between the bearing surfaces directly is unlikely to occur, and therefore is not considered to occur during normal and edge loading.

Increasing the frequency of cyclic loading during experimental simulator studies can reduce testing times and allow more time for product development. International standards have long been the basis for setting such frequencies. In order to justify the frequency set during testing and wear simulations the effect of contact sliding velocity on wear must be understood. Assuming smooth surfaces, sliding velocity has only a very small effect on the wear factor, also the coefficient of friction was not dependent upon sliding velocity [156]. The paper by Fisher et al. [156] summarises this by suggesting that reducing experimental work durations of the

tri-pin-on-disc tests through increasing the velocity within a specific range is reasonable. However, the bearing surface topographies must be controlled.

2.4.2.3. Summary of Wear Mechanisms for Hip Implants

The review and study of wear mechanisms associated with hip implant devices has highlighted the complexity of explaining the subject specific wear results and analysing experimental data. The challenge becomes even greater when trying to use computational and numerical methods to solve these problems. When trying to separate the factors which affect the wear of hip implants and those which do not, Buford and Goswami [90] have provided a comprehensive review with twenty six citations. The factors affecting wear have been stated as the following: type of material, contact stress, surface hardness, roughness, type of articulation due to motion, number of cycles (i.e. sliding distance), solution particle count and distribution, oxidation of materials leading to oxidative wear, surface abrasions of particulates and manufacturing processes. The wear mechanisms for hip replacement devices are summarised as being abrasion, adhesion and fatigue (the presence of oxidative wear depends on the bearing material). An in-depth review of wear modes and mechanisms of polyethylene artificial joints is provided by McKellop [69]. From the literature review and especially the research published by Meng and Ludema [71, 157], it is clear to see why simplistic models such as the Archard wear law is still one of the most widely used wear models for numerical modelling and simulations of wear. Many of the coefficient based theoretical wear models by Holm, Archard, Kragelsky, Rabinowicz and Harricks are similar in form. All of the these models contain the parameters of contact pressure, sliding velocity, hardness and a wear coefficient to represent adhesive, abrasive, fatigue and fretting wear [158].

2.5. Shakedown Theory and Cyclic Analysis

Before summarising the literature review, this section builds on the research and theory

discussed within previous sections. It is therefore logical to study and explain shakedown theory and cyclic analysis at this stage of the literature review.

The use of shakedown theory has played an important part in improving the performance of designs within the tooling and rail industry where high cyclic loading is very common. The aim of the theory is to determine the material response as a result of cyclic loading. For a component under cyclic loading the residual stress can act to protect the component from plastic deformation by ensuring that purely elastic material behaviour is reached in the longer term. It is possible that shakedown of contact surfaces can be assessed, even at the asperity level [95]. The asperity level is relevant for hip implant devices because during the period of bedding-in wear, local asperities plastically deform, leading to a loss of material. To justify the application of shakedown to artificial hip joints, numerical finite element and analytical methods have been used based on Melan and Koiter theoretical theorems. Two components in contact can be modelled using finite element analysis, for a single load pass i.e. 1st cycle, then the residual stress and sub-surface stress, deformation and strain hardening can be determined. In the 2nd cycle the residual stress is also considered, and the process continues until a steady state has been reached. At this stage an elastic state may be reached depending on the loading conditions and the material's response to the load [159].

The shakedown theory has already been introduced as a method for studying the changes in surface topography and plastic deformation of asperities. The application for assessing and predicting the mild wear between rolling and sliding contacts is discussed within this section. Under repeated walking motion and edge loading of the hip joint, rolling and sliding contact is present. This is one of the first indications that shakedown theory can be applied to study hip implant joint contact. However, there are many other aspects to consider. The materials used for metallic hip joint implants are ductile and can be assumed as elastic-perfectly plastic. The literature review thus far has highlighted examples where material yield strength had been

exceeded, which is possible during a shakedown analysis. Under cyclic loading conditions plastic deformation must occur to initiate residual stresses. This can lead to a purely elastic steady material state [94]. In other words, yield strength must be exceeded for the residual stresses to be present following the load removal. The connection between elastic and residual stresses is understood further from the fundamental principle explained from Melan's theorem. This principle by Melan is used to determine if shakedown will occur or not. If no plastic deformation or residual stresses are present during the cyclic loading then shakedown will not occur as explained by Johnson [94].

As previously mentioned, for the inclusion of edge loading test conditions, microseparation occurs during each load cycle and the magnitude of microseparation is kept constant throughout the test. Shakedown not being reached could be caused by a lack of compatibility between the load and residual stresses [160]. Therefore, the application of shakedown theory should be applied to edge loaded hip joints under the assumption that the load condition for each cycle is constant. Currently, all experimental simulator studies of hip joints with the inclusion of edge loading consider a constant and repetitive microseparation condition for each and every cycle during the test.

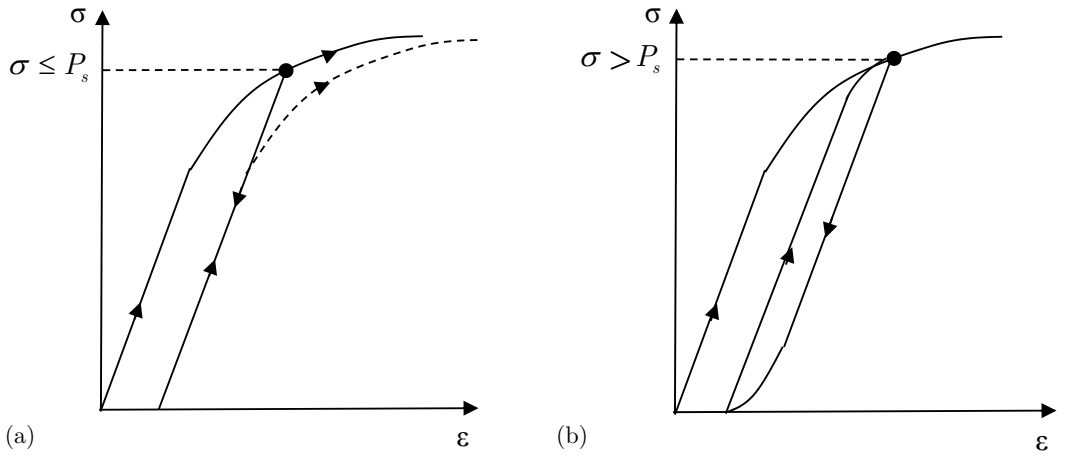

Figure 2.18. Typical stress-strain curves for ductile materials including (a) shakedown of cavity undercyclic loading (b) non-shakedown [161]

Before continuing on further with the discussion of shakedown and rachetting behaviour, the basic concepts of a stress-strain curve must be understood. Obtaining the stress-strain curve of

the materials such as a CoCrMo can be achieved by using experimental testing methods i.e. a tensile testing machine. The progress from a standard stress-strain curve to representing the idea of shakedown can be achieved by referring to a simple practical application of shakedown, as presented by Yu [161]. The example is of a cavity which is loaded below or equal to the shakedown pressure, P_s, therefore under cyclic loading elastic shakedown is obtained (Figure 2.18a). If the shakedown pressure is exceeded during the loading cycle then elastic shakedown would not be obtained (Figure 2.18b).

The stress-strain curve data is required for modelling appropriate material properties using the finite element method. On a schematic and theoretical level (Figure 2.19a), the linear region of the stress-curve provides the material's modulus of elasticity, i.e. the region between the true elastic limit and proportionality limit (between points A and B). The elastic limit provides the region of the loading curve where the material would no longer behave linear elastically (point C) and finally, the offset yield strength is highlighted at a 0.2% offset (point D). For ferrous materials, which are dealt in greater detail during numerical modelling within this project, the material stress-strain curves have different characteristics to the theoretical curve. Less ductile materials such as a high carbon content (max. 0.35%) ASTM-F75 [162] means that the material's yield strength is determined by the 0.2% offset yield method.

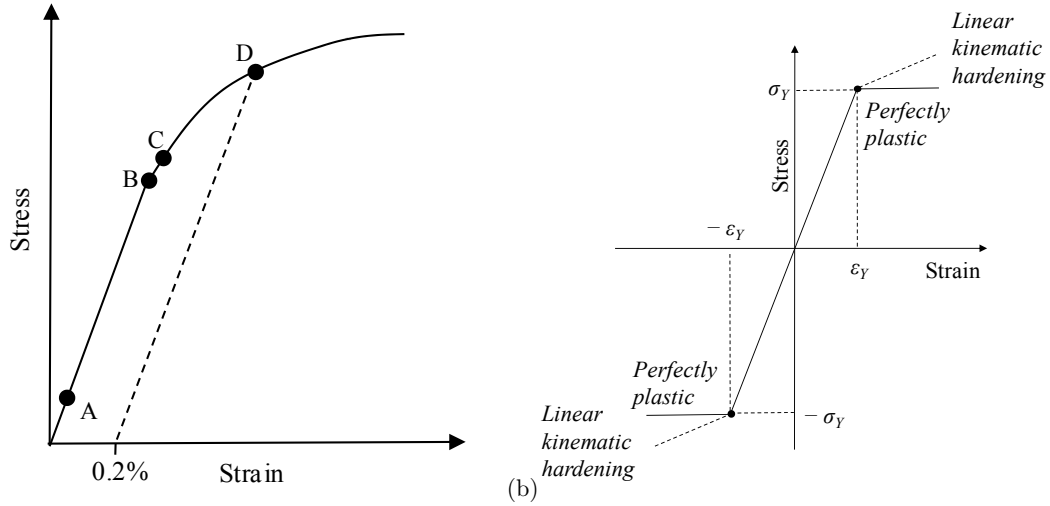

Figure 2.19. (a) Schematic theoretical stress-strain curve (b) elastic-perfectly plastic material model and kinematic hardening

The theory discussed above considers the strain hardening of a material (Figure 2.19b). However, if the model were to be simplified such that strain hardening were not taken into account, then the material model would be considered as an elastic-perfectly plastic material. In this material model, the material behaves linear elastically and at the point of yield the stress remains constant as the strain increases.

2.5.1 Shakedown Analysis with Cyclic Analysis

The practical application of shakedown to solving the problems discussed in this thesis has been inspired from the following statement,

> *"The practical importance of shakedown can now be readily appreciated by comparing the pressures, and hence the loads, for first yield to those required in the steady-state when the residual stress field has become established."* [95].

As hip devices undergo a very high number of cycles of loading under transient conditions, it is sensible to consider a direct cyclic analysis. For elastic-plastic material properties under loading fluctuations variations in stress and strain will occur. If plastic deformation occurs during the early loading cycles, the consequences are the occurrences of residual stresses, strain hardening and geometry changes. These three outcomes all affect the shakedown of the body. For structures in contact under cyclic loading, the material can behave in four different ways, assuming that the material is not rate dependent (Figure 2.20) [163, 164]:

(a) Perfectly elastic: No point of the material reaches the elastic limit under loading.

(b) Elastic shakedown: The elastic limit of the material is reached within the first few cycles of loading, however under further cycles of loading the material behaves in a steady state and linearly elastically. The elastic shakedown limit is defined as the maximum load where elastic shakedown is achieved.

(c) Plastic shakedown: This is also known as “cyclic plasticity” and involves the structure undergoing closed cycles of plastic deformation. The profile is repetitive and behaves in a steady state.

(d) Rachetting: This is also known as “incremental collapse” where there is an accumulation of plastic strain. These increments of plastic strain are unidirectional.

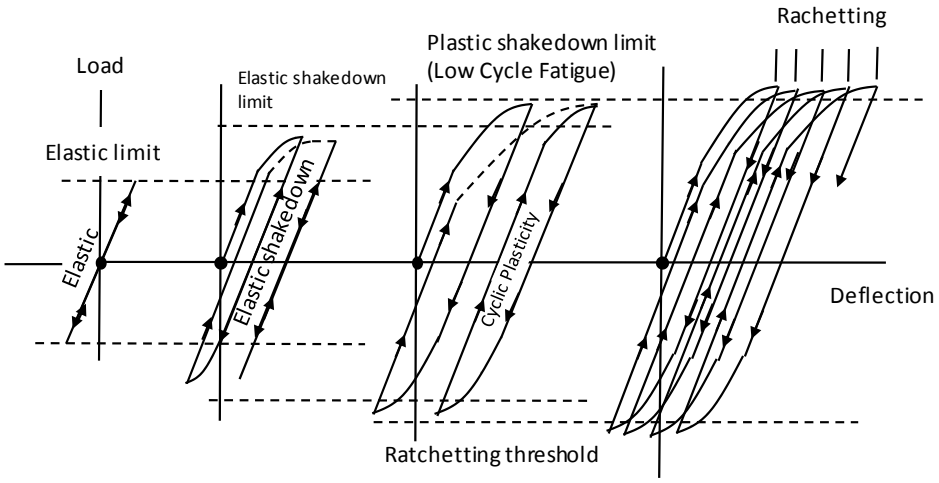

Figure 2.20. Response to cyclic loading

2.5.2. Shakedown Theorems

There are two shakedown theorems which define the lower and upper bounds of the shakedown limit. These theorems are essential for using shakedown concepts for practical engineering and design. Yu and Williams [161] have provided clear explanation of shakedown theorems which will be summarised within this chapter.

Before discussing the shakedown theorems it is important to understand the von Mises and Tresca yield criterions of ductile materials. These criterions form the basis for shakedown maps as well as important stress results using the finite element method. The von Mises stress yield criterion J_2 provides a shear strain energy criterion

$$J_2 \equiv \frac{1}{6}\left[(\sigma_1-\sigma_2)^2+(\sigma_2-\sigma_3)^2+(\sigma_1-\sigma_3)^2\right]=k^2=\frac{Y^2}{3} \tag{2.26}$$

where σ_1, σ_2, and σ_3 are principal stresses, k is the material shear yield in simple shear and Y is the tensile yield. The Tresca equation provides a maximum shear stress criterion

$$\max\left\{|\sigma_1-\sigma_2|,|\sigma_2-\sigma_3|,|\sigma_3-\sigma_1|\right\}=2k=Y \tag{2.27}$$

where it is found that both criteria provide similar results.

Following on from this, ***Melan's theorem*** (1938) provides the lower bound shakedown limit and static shakedown theorem. The theorem is best explained using a mathematical formula

with the consideration of an elastic-plastic structure. The requirement for Melan's lower bound theorem to hold true is stated,

$$f(\lambda\sigma_{ij}^{e} + \varsigma_{ij}) \leq 0 \tag{2.28}$$

where the structure is placed under applied pressure p, an elastic stress field σ_{ij}^{e} will exist, combined with any self-equilibrated residual stress field ς_{ij}, shakedown will occur as long as an additional condition has been met (dimensional scale parameter is λ). The other condition is that a combination of elastic and residual stress does not exceed the yield condition at any point in the material, i.e. $f(\sigma_{ij}) = 0$.

From understanding the von Mises and Tresca yield stress criteria, Hertzian subsurface stress and surface contact theory along with Melan's theorem, the lower bound shakedown limit of frictionless rolling or sliding line contact is determined as explained by Williams [95]. In summary, by removing the self-equilibrating residual stresses which equal zero and defining the Tresca criterion for which the yield stress must not exceed,

$$\frac{1}{4}\left\{\left(\sigma_x - \rho_y\right) - \sigma_z\right\}^2 + {\tau_{xz}}^2 \leq k^2 \tag{2.29}$$

the lower bound shakedown limit, P_s, can be defined,

$$P_s/k \geq 4 \tag{2.30}$$

where σ_x and σ_y are the stresses in the x and y direction respectively, ρ_y is the residual stress in the x direction and τ_{xz} is the shear stress in the x direction.

Koiter's theorem provides the upper and kinematic shakedown theorem. Mathematically it is more complicated than Melan's theorem. The theorem states that an elastic-perfectly plastic structure will fail due to progressive plastic flow if any kinematically admissible plastic strain rate cycle and any external loads within prescribed limits can be obtained, which therefore defines the upper bound shakedown limit [161]. As described the lower bound shakedown theorem for frictionless rolling or sliding contact, the upper shakedown limit has been defined by Williams [95],

$$P_s/k \leq 4 \tag{2.31}$$

Finally and more recently, ***Ponter's theorem*** considers a kinematic hardening model of material to achieve shakedown by a combination of residual stresses and displacement of the yield locus centre [164],

$$\frac{P_s}{P_Y} = \left(\frac{4}{3.1}\right)^2 = 1.66 \tag{2.32}$$

where P_s and P_Y are the shakedown limit and first yield respectively. Following on from the definition of the shakedown theorems, continuing with the formulation of frictionless rolling or sliding line contact and based on the von Mises yield criterion, Williams states,

> *"A load 66% greater than that which will cause yield on its first application can be carried safely, that is without subsequent yield, in situations of repeated loading."* [95].

By including the surface friction within the shakedown analysis a shakedown map has been developed for rolling and sliding line contact (Figure 2.21a), as well as for point and elliptical contacts (Figure 2.21b).

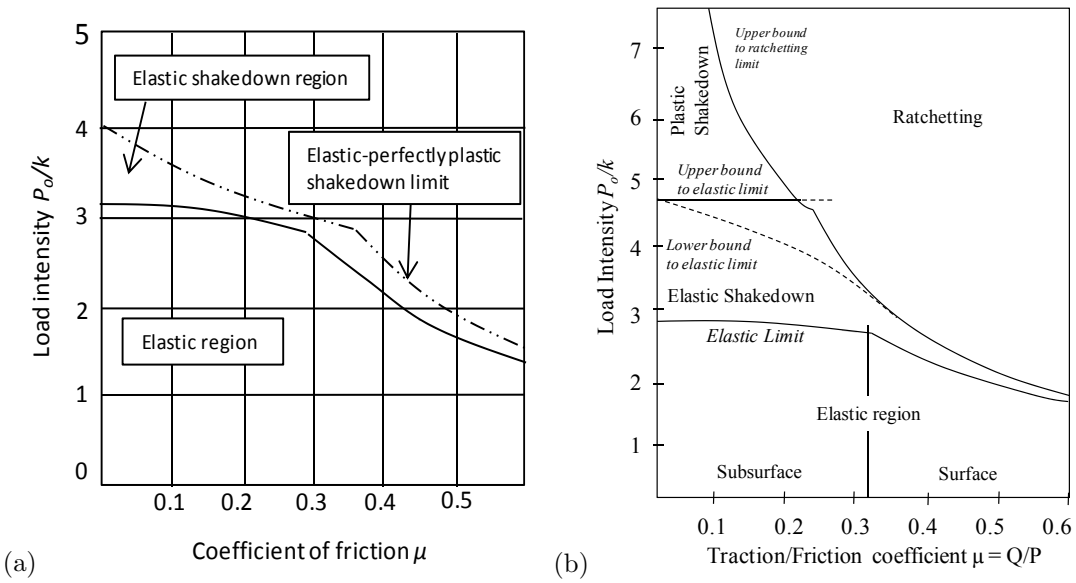

Figure 2.21. Shakedown maps for (a) rolling or sliding line contact [95] (b) point and elliptical contacts [164]

The indications of surface and subsurface regions define the areas where the maximum energy accumulation would occur under rolling and sliding contact. Although the shakedown map in Figure 2.21a is based on cylindrical contact, Johnson [94] states the commonality between

elliptical contact profiles under normal and tangential loading conditions for general non-conforming bodies in contact, including spherical bodies. Through manipulation of the maximum theoretical contact pressure equations presented and discussed in the literature review, for equivalent values of elasticity and poisons ratio, the maximum contact pressure for a cylinder in cylindrical socket $p_{o,s}$ and sphere in spherical socket $p_{o,c}$ are:

$$p_{o,s} = 0.918 \cdot K_D{}^{-2/3} \tag{2.33}$$

$$p_{o,c} = 0.798 \cdot K_D{}^{-2/3} \tag{2.34}$$

where variation of the diameter of body 1, D_1, and the diameter of body 2, D_2, and hence change of equivalent diameter, K_D, on the maximum contact pressure is shown.

2.5.3. Shakedown of Asperity Contact

There are no topological bearing surfaces which are perfectly smooth in reality [96]. The discussions on shakedown and its application to hip implant devices have thus far been referred to on the global component level; however it can also be applied at the asperity level. For non conforming contact, the initial contact of asperities and plastic deformation of asperities leading to wear suggests a shakedown process. Justification of asperity contact for hip replacement or resurfacing devices must be made. By specifically referring to CoCrMo hip resurfacing devices, a smooth surface finish provides desirable contact conditions; this statement is made without mentioning the controversies regarding an optimum level of surface roughness in promoting joint implant lubrication. The average surface roughness R_a, maximum profile peak height R_p, and skewness R_{sk}, along with standard deviation were obtained using a ProSim 10-station hip simulator provided by Smith and Nephew Orthopaedics, Leamington Spa (Figure 2.22). Five Birmingham Hip Resurfacing (BHR) devices were subjected to ISO standard hip simulator testing at 5 million cycles. From the results presented, the surface roughness and maximum peak profile both increased after 5 million cycles, although the results do not provide the surface roughness values within the edge loaded region of the bearing

components. Larger surface roughness values would be expected in the edge loading (stripe wear) region.

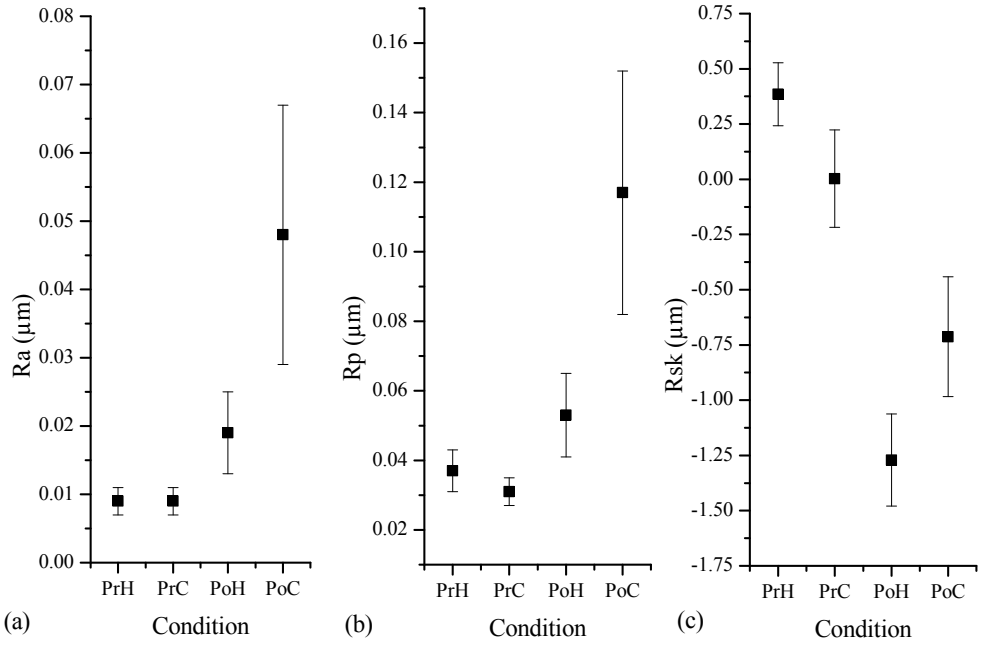

Figure 2.22. Birmingham Hip Resrfacing device pre-tested head (PrH), pre-tested cup (PrC), post-tested head (PoH) and post-tested cup (PoC) (a) R_a (b) R_p and (c) R_{sk} (± standard deviation)

The definition of a 'rough surface' has been provided by Williams [165], it appears that hip bearing surfaces can constitute to being referred to as a rough surface, especially after a few million cycles. The surface roughness being a crucial part of the performance of the materials under sliding and rolling contact, in engineering practice it is often assumed to be one value for the whole surface area of the material before contact occurs i.e. post manufacturing of the devices. Surface parameter values can be established from using experimental techniques, typically known as surface profiling. Specifically for ASTM-F75 CoCrMo material the roughness average has been stated within literature to be 0.011 µm ± 0.001 for CoCrMo [166]. From this value and tolerance limit, it maybe argued that the theory of rough surfaces is not relevant, however, based on the demands expected to be placed upon such devices in the future and current results (Figure 2.22), these assessments should not be ignored.

The application of shakedown theory to asperity contact has been most comprehensively covered in the literature by Kapoor et al. [167-169] and Bhushan [170]. To reduce the problem

complexity, a theoretical assumption was made that all asperities in contact with a surface plane are equal in radius, z_a,

$$R_a = z_a \tag{2.35}$$

where R_a is the roughness average. For the purpose of the analysis the value of area of contact A_i can be calculated,

$$A_i = \pi z_a \delta_a \tag{2.36}$$

where the asperity deformation is given by δ_a (Figure 2.23). Following on from these calculations the load on each asperity L_a in multiple asperity contact can be calculated from

$$L_a = \frac{4E^*}{3} z_a{}^{1/2} \delta_a{}^{3/2} \tag{2.37}$$

By knowing the total number of asperities N_a the total load L_t can also be calculated

$$L_t = \left(\frac{4}{3\pi^{3/2}}\right)\left(\frac{N_a E^* A_i{}^{3/2}}{z_a}\right) \tag{2.38}$$

As shown in Figure 2.23, the global load would be split between the asperities, therefore an asperity contact analysis can be conducted. Bhushan [170] has expanded on Hertz contact theory to apply these principles to asperity contact. Although this research by Bhushan [170] assumes that the asperities are spherical in shape, the heights of the asperities, z, follow a Gaussian distribution $\Phi_h(z)$,

$$\phi_h(z) = \frac{1}{(2\pi)^{1/2}\sigma_a} \exp(-z^2 / 2\sigma_a^2) \tag{2.39}$$

where the mean is zero and standard deviation is σ_a.

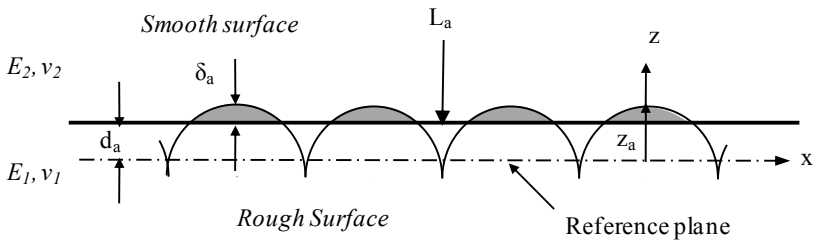

Figure 2.23. Contact of rough surface against a smooth plane surface

The radius of circular micro asperity contact a_a, overlap between the two asperity profiles δ_a and the mean hertzian contact pressure for micro contact σ_m can all be obtained:

$$a_a = \left(\frac{3L_a r_a}{4E^*} \right)^{1/3} \tag{2.40}$$

$$\delta_a = \left(\frac{9{L_a}^2}{16 r_a E^{*2}} \right)^{1/3} \tag{2.41}$$

$$\sigma_m = \frac{2}{3\pi} \left(\frac{6 L_a E^{*2}}{{r_a}^2} \right)^{1/3} \tag{2.42}$$

where r_a is the reduced asperity radius.

If the contact pressure is less than the calculated shakedown pressure then the component will not undergo plastic flow, likewise if the asperity contact pressure is less than the asperity shakedown pressure, then the asperity will not undergo plastic flow. By looking at this from a slightly different perspective, if the largest asperity shakedown pressure is greater than or equal to the asperity shakedown pressure then plasticity flow of the asperity will occur. The knock on effect is that the load placed upon other asperities will increase, therefore plastic flow could occur on more asperities.

The final area to be discussed are the plasticity index theorems, which are summarised by Stachowiak and Batchelor [48]. The general form of the plasticity index is provided by the Greenwood and Williamson model [48] which is used to predict elastic or plastic deformation based on the hardness of the deforming material H_v. By considering the average surface roughness and root mean square roughness, the plasticity index Ψ_{GW} can be determined based on Greenwood and Williamson's formulation [48] of plasticity index,

$$\psi_{GW} = \left(\frac{E^*}{H_{VP}} \right) \left(\frac{\sigma_a}{r_{GW}} \right)^{1/2} \tag{2.43}$$

where H_{VP} is the hardness of the deforming surface in units of Pascal and r_{GW} is the asperity radius. If $\psi_{GW} < 1$ then elastic deformation would occur under contact and if $\psi_{GW} > 1$ then plastic deformation would occur. The shakedown plasticity index Ψ_s is given by

$$\psi_s = \left(\frac{E^*}{p_S}\right)\left(\frac{\sigma_h}{z}\right)^{1/2} \tag{2.44}$$

based on the asperity shakedown pressure p_s for contact surfaces.

2.6. Literature Review Summary and Research Justifications

Despite the extensive amount of research being carried out for hip implant contact and tribological performance, the serious problems identified for orthopaedic hip implant products mean that new and improved methods, strategies and amalgamated topics must be researched to reduce the problems and failure of these medical devices in the future. This is why the key concepts of contact mechanics, computational and numerical methods, experimental techniques, biomechanics of the hip, wear mechanisms and shakedown have all been covered within the literature review.

This literature review has further substantiated the value, motivation and importance of the research carried out in this project. The significance of problems focused on within this project continues to drive the requirement for improving computational methods for solving cyclic hip implant contact and wear problems. However, to ensure successful problem solving techniques are developed, a strong foundation in the subject of contact mechanics was required by researching past and current literature of computational and numerical methods. Without this research, no further improvements or problem solving techniques could be established which justifies the reason for covering this within this literature review. From this research, the biomechanics and the latest developments in experimental testing methods must be studied to establish appropriate boundary conditions of computational models and correct use of theoretical methods. Without this knowledge and pushing for advancements in finding solutions to the problems, achieving the aims and objectives of the project becomes even more challenging. Finally, the previous topics covered within the literature review led on to researching tribology and shakedown to study and simulate the wear of hip implant devices

using methods and obtaining results beyond that of any research carried out in the past. The complexities and challenges of developing tribological simulations using the finite element method and the direct application of models to solve the biotribology problems dealt with in this project will be discussed within the following chapters. These challenges were an important driver for striving to contribute to knowledge within this area, leading to improved problem solving methods and results which can contribute to more reliable and better performing hip implant devices in the future.

The outcomes from this chapter helped to drive the methodological development to meet the aims and objectives set for the project. This can be summarised as taking the subjects of contact mechanics, wear mechanisms and shakedown theory to collectively be used to develop numerical and computational models to study the surface interactions of hip implant devices, especially under normal, edge loading and severe loading conditions. Advanced programming methods provide a framework for merging the work completed in this project for future problem solving and promotion of further research.

Chapter 3 – Methodology

Following on from the literature review in chapter 2, techniques have been used and developed to meet the aims and objectives stated in chapter 1. These include computer aided engineering and numerical methods as well as theoretical models. Experimental methods have also been used where time, resources and equipment availability permitted.

A number of finite element models were developed in this study including different bearing diameters to model both hip resurfacing and hip replacement devices. Firstly, a simple deformable body on rigid body contact model (model A) was developed for specific geometric comparison studies and analysis. In this model hip resurfacing components were backed and fully tied to rigid parts. Moving on from model A, the elasticity of attached bone was considered for the simulation of models B, C and D. A summary of all models is provided in section 3.4. Summary of models. For all models, it was assumed that full contact and bonding was maintained between the top surface of the acetabular cup and acetabulum and likewise between the bottom surface of the femoral head component and femur. Perfect sphericity of the cup and femoral head were also assumed. The finite element modelling techniques were used to analyse the stresses and strains, along with them being used to conduct wear simulations and shakedown analysis.

3.1. Modelling Boundary Conditions and Definition

3.1.1. Hip Replacement and Resurfacing Devices

The hip replacement and resurfacing devices were introduced and discussed within chapters 1 and 2. These two implant options are distinguished by the schematic provided in chapter 2

(Figure 2.3). As the problems dealt with in this project were related to both types of implant devices, they have both been included within the methodology and analysis work. As previously mentioned, in order to narrow down the scope of the project, two nominal bearing diameters were considered, the hip replacement bearing diameter, D_{rp} = 32 mm, and the hip resurfacing bearing diameter, D_{rs} = 50 mm, with a range of different parameters modelled. In this project different radial clearances were modelled. Udofia and Jin published a MoM hip resurfacing study [171] presenting results that a reduction in radial clearance between bearing surfaces provide the greatest effect on reducing the contact pressure distribution between hip implant components. The hip resurfacing device model was based on an assembly consisting of both the femoral component and acetabular cup made from Cobalt Chromium Molybdenum (CoCrMo).

3.1.2. Hip Implant Material Properties

The following material properties for medical grade CoCrMo used by two finite element studies published within the literature are summarised in Table 3.1. The published data provided in the form of a stress-strain curve for 'as cast', HIPed (hot isostatically pressed) and wrought material is provided in Figure 3.1a, for the numerical analysis carried out these material's properties were used along with a density value of 8.345 × 10^{-6} ± 0.250 mm/kg^3 where applicable [162, 172]. Further information and tribological test results of the different CoCrMo manufacturing process forms have been provided by Cawley et al. [76].

Table 3.1. Cobalt chrome material properties

Mechanical Property	**McNie et al. [135]**	**Yildiz et al. [173]**
E (GPa)	230	234
ν	0.3	0.3
σ_Y (MPa) – cast / forged	220 / 500	*np*
Plastic tangent modulus (GPa)	7	*np*
G_{xy}, G_{xz}, G_{yz}	*np*	90

np = not provided

The pre-manufacture process used for material preparation of the Birmingham Resurfacing device and indeed the majority of resurfacing and replacement devices is a cast process. This

refers to the material in a condition with no surface finish, coating or machining. At most, the overflows, flash and runners would be removed following the casting process.

To initially simplify the analysis the following assumptions could be made for the material properties: isotropic, homogenous and linear elastic. There is currently no study within the literature which assumes cobalt chrome molybdenum to be a perfectly-plastic material. However, for ductile materials an idealisation was made which defines the material to have elastic-perfectly plastic material properties. The transition from elastic to perfectly-plastic properties occurs at the yield point of the stress-strain curve and this assumes that the material does not harden under loading conditions.

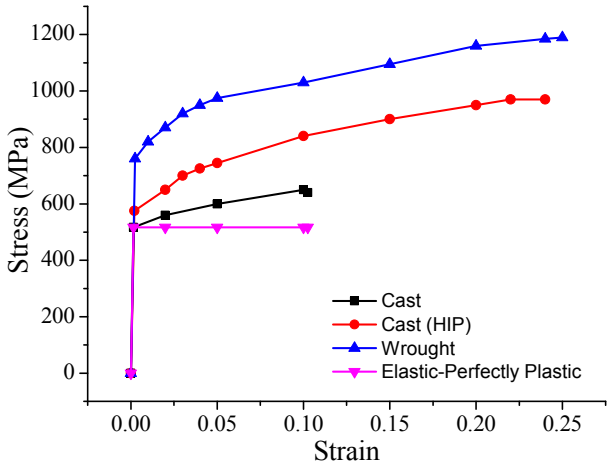

Figure 3.1. (a) Stress-strain curves of ASTMF75 cobalt chrome [162]

For the assessment of asperity shakedown in the contact zone, the root mean square (RMS) roughness of the head and cup is required. For CoCrMo, this value was obtained from the literature as $\sigma_a = 0.013$ µm [174]. To determine the plasticity index for the contact surfaces, the hardness of the deforming material is also required (H_v) which for CoCrMo is 350 ± 20 [175], this unitless constant can be converted to a constant with the units MPa (H_{VP}) by multiplying by 9.807 which is provided by the ISO/TR 10108:1989 standard [176].

3.1.2.1. Isotropic and Kinematic Hardening Models

The material models were essential to modelling the cyclic analysis according to shakedown principles. The isotropic hardening material model is based on the yield stress and plastic

strain material model without the consideration of strain-rate or temperature dependent data, as these are assumed to not be relevant in this problem. For isotropic hardening, the yield function is provided in the following form (3.1):

$$f(\sigma) = \sigma^0(\varepsilon^{pl}, T) \tag{3.1}$$

where σ^0, ε^{pl} and T are the equivalent uniaxial stress, work equivalent plastic strain and temperature respectively. An isotropic hardening model does not consider the Bauschinger effect and the model is based on the yield surface expanding in the stress space. The model is mostly suited to problems which involve very high plastic strains and slowly reversing plastic strains. Although the isotropic hardening model may not provide the most appropriate model for solving the problems discussed, it is the simplest model to obtain initial results. For the consideration of more realistic hardening models the kinematic hardening models were used where the yield surface translates rather than dilates as the yield surface does in the isotropic hardening model.

3.1.3. Bone Materials and Models

Following completion of the literature review, no standardised bone models were found for modelling the hip joint to solve problems such as those dealt with in this project. Computer aided design hardware and software exist to simplify the bone geometry from raw DICOM scanned data obtained from CT (computed tomography) or MRI (magnetic resonance imagining) scans. The simplification and quality of the remodelling would however be subject to the engineer performing the modifications. The need for model processing and refinement is shown in Figures 3.2a-3.2d. Without any surface smoothing following masking of the raw DICOM data leads to a model with high levels of surface roughness. These models can not practically be combined with implant devices for finite element analysis. As the number of iterations of surface smoothing increases the images show a more realistic representation of the true bone shape.

Even with surface smoothing, the geometrical complexity of the femur can be demonstrated using the advanced computer aided design package 'Autodesk Inventor' where the maximum and minimum radius of a scanned femoral head femur sample was 6.7mm and 0.8mm respectively.

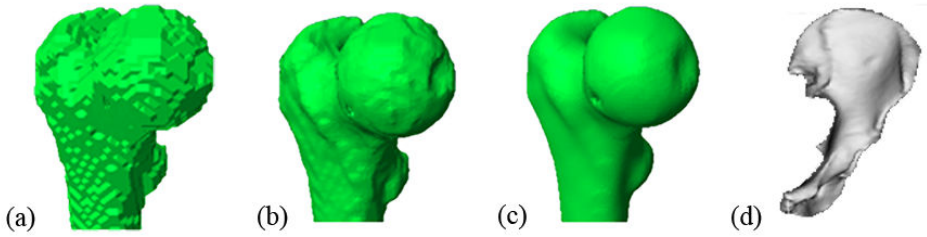

Figure 3.2. DICOM scan of femur with (a) 0 (b) 5 (c) 20 iterations (d) Scanned slices of iliac post processed to full 3D model using scanned data software

Following on from the intricacies of dealing with bone samples and geometries the next step was to apply appropriate material properties. The precedence of bone modelling has already been discussed within chapter 2 – literature review, in which a range of material modelling methods were reviewed. An analysis was carried out to assess the effect and sensitivity of contact stresses due to the geometry and material properties of the surrounding bone which is presented in chapter 4.

3.1.3.1. Medical Imaging and Processing for Finite Element Analysis

To build implanted joint finite element models, use of high quality MRI and CT techniques for accurate imaging is required [177]. These are the two most widely and commonly used methods for obtaining scanned bone data from patients. The CT scanner uses X-rays (ionizing radiation) to obtain images by measuring the amount of X-ray which has been absorbed by the object or part of the body it is scanning. An MRI uses non-ionizing radio frequency signals to obtain images and works by magnets of the machine causing the protons (located in the nucleus) of the hydrogen atoms to change direction, the movement of this new orientation is measured by the scanner. Whilst either option can be used for patients without a metallic implant, CT scanners are recommended for patients with a metallic implant, such as a hip

replacement or resurfacing device, due to the magnetic fields imposed by the MRI scanner. For the scope of this project, no in-depth study was carried out to assess the relative accuracies of the CT and MRI scanning techniques. It is accepted that the resolution capabilities would be sufficiently available and provide adequate accuracy for this study. In addition to this, the scanned data post processing software and computer aided design packages used within this project both contain algorithms to geometrically modify and prepare surfaces e.g. by using Recursive Gaussian filters. This helps to remove 'jagged' edges caused by combining multiple section surface scans into one model and compensate for any lack in resolution or 'noise' of the scanned data. Image clarity is more of a concern if segmentation of the model is required.

A number of mathematical algorithms are implemented into medical image processing tools. The image processing tools allow for scanned data to be prepared for finite element analysis, these processing tools include: background image interpolation, masking, segmentation, morphological filters, Boolean operations, binarisation filter smoothing and recursive Gaussian filters. One of the most widely used and arguably most important is the Hounsfield unit HU (which is also the method used in this project). The Hounsfield unit is a measure of the tissue densities from the patient scanned data. The Hounsfield unit is calibrated with reference to the Hounsfield unit of water being 0 and air being -1000. This is calculated from knowing the linear attenuation coefficients of water μ_{water} and the scanned data μ_x. The Hounsfield unit,

$$HU = 1000 \times \left(\frac{\mu_x - \mu_{water}}{\mu_{water}} \right) \tag{3.2}$$

is then calculated.

3.1.3.2. Homogenous Material Models

The simplest material model and minimum application for solving the finite element stiffness matrix was based on the definition of the material elastic modulus and Poisson's ratio. Therefore, with this bone material model the material is assumed to be homogenous as well as

isotropic. By considering the isotropic case, the stress and strain relationship was defined,

$$\begin{Bmatrix} \varepsilon_{11} \\ \varepsilon_{22} \\ \varepsilon_{33} \\ \gamma_{12} \\ \gamma_{13} \\ \gamma_{23} \end{Bmatrix} = \begin{bmatrix} 1/E & -\nu/E & -\nu/E & 0 & 0 & 0 \\ -\nu/E & 1/E & -\nu/E & 0 & 0 & 0 \\ -\nu/E & -\nu/E & 1/E & 0 & 0 & 0 \\ 0 & 0 & 0 & 1/G & 0 & 0 \\ 0 & 0 & 0 & 0 & 1/G & 0 \\ 0 & 0 & 0 & 0 & 0 & 1/G \end{bmatrix} \begin{Bmatrix} \sigma_{11} \\ \sigma_{22} \\ \sigma_{33} \\ \sigma_{12} \\ \sigma_{13} \\ \sigma_{23} \end{Bmatrix} \tag{3.3}$$

where the shear modulus, G, is given by $G = E / 2(1 + \nu)$, E is the elastic modulus, ν is the Poisson's ratio, ε_{ij} is the strain, γ_{ij} is the shear strain and σ_{ij} is the stress.

The literature review showed this material model to be a simplification of the human bone material properties, and the bone models varied from patient to patient. Therefore, an assessment was conducted to determine the bone model sensitivity, stiffness and stresses of the bone model based on its material properties. This will also help to confirm the level of concern regarding patient specific material property parameters on the contact mechanics under normal, severe and edge loading conditions. To assess the affect of mesh density and material properties, an analysis was also conducted on a bone model to compare the stress and deflection results based on the mesh density.

Literature has shown the variation of material's properties could be a factor of bone model size, geometry, gender and size of the patient. Therefore, this process could have been repeated for each set of bone models for patient specific modelling. This would however be a time consuming process and one which could be avoided through material model assessments and sensitivity studies. Therefore, a parametric study was carried out varying the elastic modulus of the femur and pelvic bone models. Firstly, the same elastic modulus was applied to both femur and pelvis, which was varied between 3 GPa to 25 GPa. Following on from this, a separate segmented bone model assembled with femoral head and acetabular cup components was used to vary the elastic modulus of the femur and pelvis independently between the values of 3 GPa and 30 GPa.

3.1.3.3. Greyscale Material Models

The complexity of the bone model material properties were increased through the application of properties from the greyscale values. The material properties were based on the greyscale data obtained from the computed tomography human body scan, i.e. directly from DICOM scanned data. The mass density, Young's modulus and Poisson's ratio were calculated using defined equations. By using this method, each finite element was allocated a material property based on the greyscale value in Hounsfield units *HU*. The bone density ρ_b is described as a linear function of the element parent voxel greyscale, *GS*,

$$\rho_b = a_b + b_b \cdot GS \tag{3.4}$$

where the value of a_b and b_b refer to the slope and y-intercept respectively. The background information of the equation has been discussed and assessed in detail recently by Pettersen [178]. The basis of the equation is formed from the research conducted which relates the bone composition obtained from computed tomography scans to define the mechanical properties. The technique presented by Pettersen describes how the *HU* value (Figure 3.3) was obtained from the greyscale value recorded by the CT bone scanning process. The values in (3.4) are not universal constants which can be applied to every problem. An assumption was made such that the value of a_b for the pelvis will be the same as that for the femur, however this assumption was challenged and the sensitivity of these constants on the contact stresses of the hip implant devices were assessed. The different bone densities measured (BMD) for the femur and pelvis were presented and discussed by Wilkinson [179], which provides results to compare the pelvic and femur BMD. Wilkinson [179] points out that gender, scanning methodology and changes in bone density over the trial period had a negligible effect on the results. On the contrary, the value of b_b does vary depending on the region of the body. Therefore as a starting point, an average value of bone apparent density (1175 kg/m^3) was obtained from the

literature presented by Pettersen. A linear density relationship was also studied by Rao et al. [180], where the value of a_b and b_b was defined as 0.523 kg/m^3 and 1000 kg/m^3 respectively.

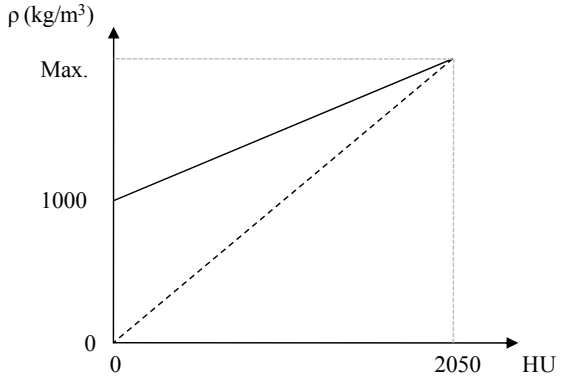

Figure 3.3. Relationship between apparent density and the Housfield number (HU)

Following the definition ρ_b, the elastic modulus of the bone E_b can also be represented as a function of the density

$$E_b = a' + b' \rho^{c'} + d' \rho^{e'} \tag{3.5}$$

where the variables a', b', c', d' and e' are user defined constants. From one of the most cited works in this area by Carter and Hayes [181], the elastic modulus of both trabecular and cortical bone can be approximated to be the cube of the apparent bone density ρ_{ap}. A more detailed review of other mechanical bone property definitions can be found in the review completed by Doblare et al. [182]. The work from Carter and Hayes [181] has inspired the definition of the elastic modulus E_b' (MPa)

$$E_b' = 3790 \times \rho_{ap}{}^3 \tag{3.6}$$

which were obtained using empirical methods [183].

Separate cited literature from Wirtz et al. [184] presents the elastic modulus of both cortical bone and cancellous bone in the axial and transverse load directions. By rewriting Equation (3.6) in a more general form

$$E_b = a_B \times \rho_{ap}^{C'} \tag{3.7}$$

where the parameters have been summarised in Table 3.2.

Table 3.2. Elastic modulus as a function of density for cortical and cancellous bone in the axial and transverse load directions

	Axial load direction		**Transverse load direction**	
	a_B	$\mathbf{C}'$	a_B	$\mathbf{C}'$
Cortical bone	1904	1.64	1157	1.78
Cancellous bone	2065	3.09	2134	1.57

Along with defining the elastic modulus, as previously discussed, the final minimum requirement for the finite element calculations is the Poisson's ratio. By reviewing the literature within chapter 2, all finite element studies defined Poisson's ratio as a constant value. Within the literature the values for Poisson's ratio vary for cortical bone between 0.2 to 0.5 with an average of 0.3, and for cancellous bone between 0.01 and 0.35 with an average of 0.12 [184]. However, it was possible in this project to define finite element values of Poisson's ratio based on bone density as a power law from, ν_b, as a function of density,

$$\nu_b = a' + b'\rho^{c'} + d'\rho^{e'} \tag{3.8}$$

as applied when assessing the effects of bone material properties in this project. When developing models with a single value of Poisson's ratio, the value of 0.3 was applied based on the average value for cortical bone. An analysis check was carried out to justify the use of this single value of Poisson's ratio. By using model D-2b (discussed in section 3.2.6. Model D: Two-Dimensional Axisymmetric Models), the contact pressure between the femoral head and acetabular cup was assessed from using bone models with a range of Poisson's ratio from 0.1 to 0.45, the difference in contact pressure was negligible.

3.1.3.4. Orthotropic Bone Material Properties

The methodology and application of greyscale materials models can be somewhat cumbersome; therefore a more effortless way to apply material properties to the bone using the finite element method would be based on the modelling of orthotropic materials,

$$\begin{Bmatrix} \varepsilon_{11} \\ \varepsilon_{22} \\ \varepsilon_{33} \\ \gamma_{12} \\ \gamma_{13} \\ \gamma_{23} \end{Bmatrix} = \begin{bmatrix} 1/E_1 & -\nu_{21}/E_2 & -\nu_{31}/E_3 & 0 & 0 & 0 \\ -\nu_{12}/E_1 & 1/E_2 & -\nu/E_3 & 0 & 0 & 0 \\ -\nu/E_1 & -\nu/E_2 & 1/E_3 & 0 & 0 & 0 \\ 0 & 0 & 0 & 1/G_{12} & 0 & 0 \\ 0 & 0 & 0 & 0 & 1/G_{13} & 0 \\ 0 & 0 & 0 & 0 & 0 & 1/G_{23} \end{bmatrix} \begin{Bmatrix} \sigma_{11} \\ \sigma_{22} \\ \sigma_{33} \\ \sigma_{12} \\ \sigma_{13} \\ \sigma_{23} \end{Bmatrix} \tag{3.9}$$

A set of elastic orthotropic and isotropic material constants have been defined by Couteau et al [185], which have been applied within the finite element material property definitions. This could be applied more readily than the data provided by Cheal et al. [186] which have all been summarised in Table 3.3.

Table 3.3. Elastic constants and Poissons ratio from Couteau et al.* [185] and Cheal et al.** [186]

	Elastic modulus (GPa)			**Shear modulus (GPa)**			**Poisson's ratio**		
Material	E_1	E_2	E_3	G_{12}	G_{13}	G_{23}	ν_{12}	ν_{13}	ν_{23}
Bone*	11.6	12.2	19.9	4.0	5.0	5.4	0.42	0.23	0.23
Cortical bone, diaphysis**	21.9	14.6	11.6	6.99	6.29	5.29	0.21	0.11	0.30
Cortical bone, metaphysic**	17.5	11.7	9.3	5.59	5.03	4.23	0.21	0.11	0.30
Trabecular (cancellous) bone**		0.6			0.25			0.20	
CoCr Alloy**		234.4			90.16			0.3	

The orthotropic directions have been defined as axial (i.e. long axis of the bone), tangential or circumferential and radial which were noted by subscripts 1, 2 and 3 respectively. These values were defined within the finite element material models by specifying engineering constants within the elastic material model. For the femur and pelvic bone models, the orientation must be defined to apply the orthotropic material's properties using commands within the analysis input file.

3.1.3.5. Image Processed Hip Bone and Implant Models

Material properties are defined to the various masks created during the segmentation process. The details of the material model are defined as a constant material modulus of elasticity or material properties based on Hounsfield units as previously discussed. The computer aided design orthopaedic models are combined with the segmented bone model. Finally, the masks are prepared for finite element analysis by meshing and exporting the parts for finite element analysis. As the techniques to manage the bone models are dependent upon the quality and

methodology adopted to obtain the bone scan e.g. CT 64, PET (positron emission tomography) scans or MRI scans, a number of decisions were required to be made for image processing to be carried out on the bone scans. These decisions were made by having a firm understanding of how the bone models are used and the possible sensitivities impacting on the results. In this project the primary focus lies with the contact modelling between the hip implant bearing components through the implanting of these devices within the computational models, therefore micro and nano accurate modelling of the bone models were not necessary.

The following four steps (S.1 to S.4) were carried out to obtain the finished segmented bone model of the femur and pelvis with orthopaedic implant assemblies:

S.1) By using full human body DICOM data, the relevant section of the data were kept, and the data were cropped to remove unnecessary sections of the bone.

S.2) By using confidence growing region techniques a combination of flood fills and manual image processing was carried out to ensure that all the sections of the femur and pelvis were contained within the defined mask.

S.3) Morphological filters and Recursive Gaussian filters were used to smooth the bone model surfaces.

S.4) If required for the model, the hip implant models were combined with the femur and pelvic models. The models were then meshed and exported to Abaqus for further pre-processing before any finite element post processing.

3.1.3.6. Cortical bone and Cancellous Bone Sections

The approach of applying a separate elastic modulus and Poisson's ratio to defined sections of cancellous and cortical bone was investigated.

Table 3.4. Bone section material properties

Bone section	**Elastic Modulus (GPa)**		**Poisson's ratio**	
	Taylor et al.	Udofia et al.	Taylor et al.	Udofia et al.
Cortical Bone	17.0	17.0	0.33	0.3
Cancellous Bone (a)	1.0	0.8	0.33	0.2
Cancellous Bone (b)	0.4		0.33	

This approach was more easily adapted to the two-dimensional axisymmetric model explained further within this chapter. Current literature was used to reference the elastic modulus and

Poisson's ratio values for both cortical and cancellous bone [15] which are given in Table 3.4.

3.1.4. Loading and Angular Rotations

Study experimental work was carried out in a gait laboratory (The University of Warwick, UK) to obtain load data using a ground reaction force plate, which was used to measure the ground reaction forces from a range of human activities. The ground reaction plate is part of a VICON motion capture gait laboratory as shown in Figure 3.4a. These component force data are not typically used as input to finite element simulations. For this requirement far more accurate and realistic tests have been carried out using instrumented *in vivo* hip implants (Figure 3.4b) [187]. Obtaining load data from both methods shown in Figure 3.4 are independent from one another. Further details of using the gait laboratory are provided in Appendix B – Activity Force Plate Loading.

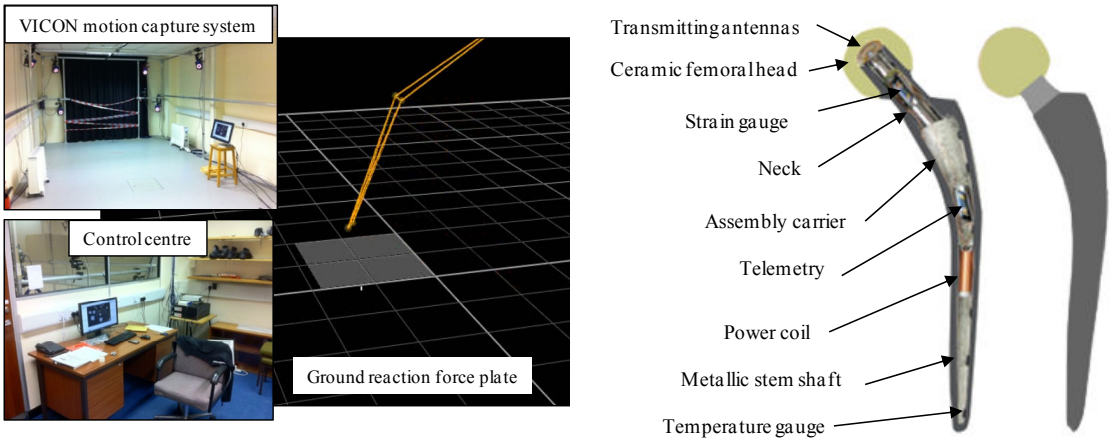

Figure 3.4. (a) VICON motion capure gait laboratory with ground force reaction plate (Gait Laboratory, University of Warwick) (b) instrumented hip implant

Although the methodology above was carried out for research purposes, the gait loading and angular displacement data applied within the finite element models were based on ISO standards. The loading profile was based on the early work of Paul [188], who published work to define the walking cycle, all the work up to more recent gait loading studies were stated by Bergmann et al. [189]. The commonality between these walking gait loading curves is that they contain the same twin-peak curve which occur during the stance phase and a low constant load during the swing phase (Figure 3.5a). Any loading profiles were included within

the modelling by defining amplitudes over the time step. The angular displacement of the hip joint is defined in three directions (Figure 3.5b). The same methodology of applying hip rotations within the experimental simulator studies were applied within the appropriate finite element models. The two most dominate angular displacements in terms of absolute magnitude during the gait cycle are the flexion-extension and inward-outward rotations. Therefore these two rotations were also included within the finite element models where appropriate.

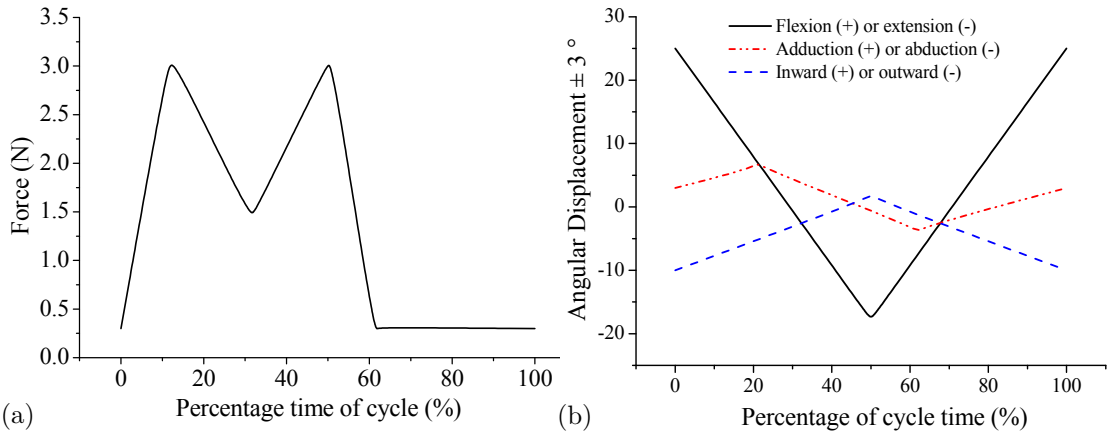

Figure 3.5. ISO standard (a) loading (b) hip joint angular displacement

3.1.5. Modelling Microseparation and Edge Loading

Firstly the kinematical modelling of normal and edge loading is considered in terms of a simplified two-dimensional cross section of the hip implant. A two dimensional model was developed and explained following the research published by Mak et al. (Figure 3.6a) [66]. The size of the acetabular cup in the figure was exaggerated to demonstrate the microseparation model. The bearing centre of the femoral head component is shown by the defined points C_1, C_2 and C_3 (Figure 3.6b). The original x-y axis was rotated by the cup inclination angle θ_i as shown by the axis x'-y'. To begin the analysis, the static position of the hip joint was set so that the bearing centre of the femoral head component was at position C_1, i.e. the distance between point 0 and C_1 would be the radial clearance c, assuming there is no elastic deformation of the implant components. Due to the laxity of the hip joint, it was assumed that point C_1 translates to point C_2 which was located along the y'-axis, and the contact point

between the femoral head and acetabular cup was denoted by microseparation based rim contact c_m (Figure 3.6a). This could occur during the swing phase of walking, jogging, running or indeed any other patient activity. The location of this axis was defined by a superior-inferior axis from the point C_2 and when the femoral head comes into contact with rim of the acetabular cup during heal strike or hip impingement (Figure 3.6b). To define the distance for onset of rim contact s_r, an equation is derived and applied to model microseparation [66],

$$s_r \geq \left(1 + \frac{1}{\tan \theta_i}\right) c \tag{3.10}$$

where θ_i is the cup inclination angle and c is the radial clearance between the acetabular cup and femoral head.

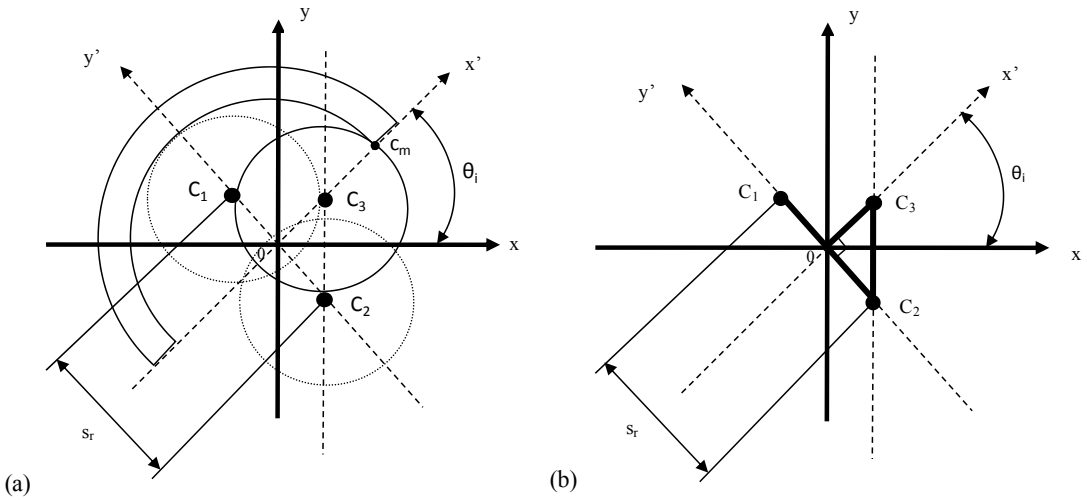

Figure 3.6. (a) 2D microseparation model (b) femoral head displacement leading to edge loading

To back up the importance of developing such theoretical models, fluoroscopy studies have shown that microseparation occurs at the hip joint during gait human activity. However, the current microseparation model only considers one kinematic situation leading to contact, c_m, between the femoral head and the rim of the acetabular cup. This current model leads to contact between the cup and head at a zero degree polar angle i.e. along the y'-axis (Figure 3.7a). However, an additional model shows that under vertical gait loading the acetabular cup makes contact with the femoral head along the y-axis. During each cycle under gait loading, a lateral to medial displacement of the femoral head along the x-axis can be modelled to

represent microseparation leading to acetabular cup rim contact or edge loading. During the swing phase of the walking gait cycle the lateral displacement was applied. However as the hip implant was under a vertical load the displacement was modelled along an angular path θ_m. There is also the possibility of femoral head lateral displacement from the bearing centre position without including any vertical loading (Figure 3.7b). Theoretically, above the centroidal axis of the acetabular cup, the femoral head component could contact the acetabular cup in any direction. However, below the cup centroidal axis, the distance between 0-C_2 can be determined by Equation (3.10). This equation assumes that the microseparation occurs perpendicular to the x'-axis or along with y'-axis, however this may not always occur *in vivo*. Another assumption made was that the relocating ball in cup i.e. the distance travelled from C_2 to C_3, occurred in the vertical direction (along an inferior-superior axis), which is a valid assumption based on contact from the ground at heal strike relocating the head into the cup in the vertical direction.

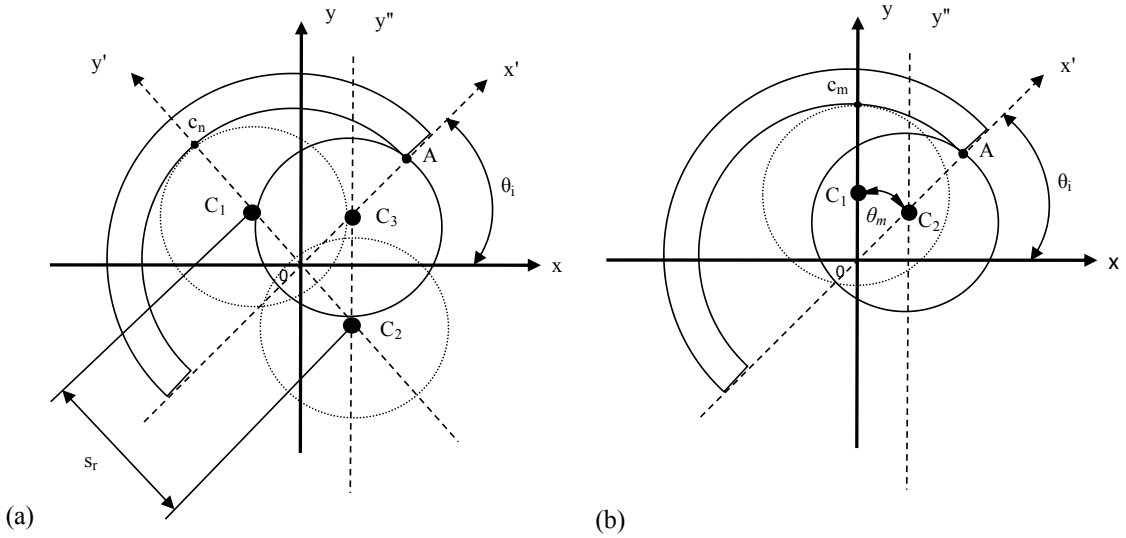

Figure 3.7. Microseparation from (a) vertically loaded hip resurfacing joint (b) rim contact along angular path

All of the microseparation models discussed above were two-dimensional, but it is possible to present the microseparation in three-dimensions. Due to the geometry of the bearing components above the plane, C_p, which intersects the bearing centre and bottom surface of the acetabular cup contact, microseparation could occur at any position within the surface area of

S_m (Figure 3.8). However, outside of this volume, the microseparation would be determined by the laxity of the joint and hip kinematics. The current model assumed that all the microseparation occurred from C_1 to C_2 by a distance of s_r, however it could also occur along the traverse plane by a distance of s_t or sagittal plane by a distance of s_s.

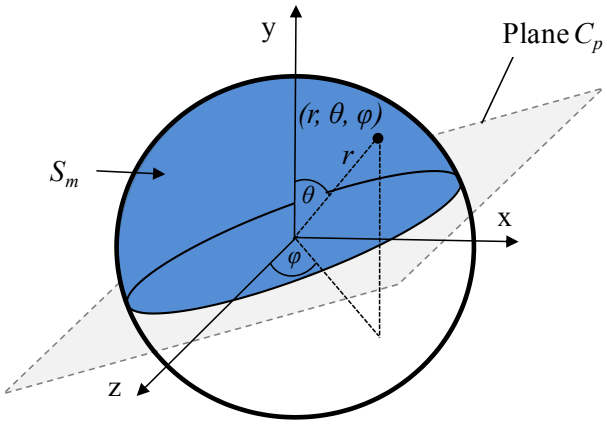

Figure 3.8. Contact between the acetabular cup and femoral head above the plane C_p

By taking into account the microseparation in three-dimensions, displacement in the anterior-posterior direction will be included within the model. Through anterior-posterior displacement, i.e. along the sagittal plane, the displacement would occur due to the swing phase load during gait motion, or by any external forces along this plane due to a number of patient activities. Without the consideration of a rim radius, the displacement of the femoral component was dependent upon the radial clearance between the cup and head. If the femoral component and acetabular cup have coinciding central points and the displacement occurs purely along the anterior-posterior direction without any displacement occurring along the superior-inferior direction, then the femoral component will be displaced a distance of c and edge loading contact will occur above the rim radius of the cup. Although experimental and patient retrievals do not show any stripe wear patterns along the anterior or posterior end of the implant, it is possible that the laxity in this direction could lead to increased adverse effects of edge loading in the lateral-medial direction. In this case the amount of anterversion would not have any effect on the severity of edge loading, especially within the typical installation anteversion angles.

Through the consideration of cup inclination angle, assuming both the femoral component and acetabular cup have initially coinciding central points and the displacement occurs in the anterior-posterior direction without any displacement occurring along the superior-inferior direction, the displacement s_L along the medial-lateral axis will remain constant

$$s_L = \frac{c}{\cos \theta_i} \tag{3.11}$$

where θ_i is the cup inclination angle and c is the radial clearance between the acetabular cup and femoral head.

As long as the centre of the femoral head remains superiorly above the centroidal axis of the acetabular cup, then the contact between the femoral head and acetabular cup will always remain above the cup rim radius, irrespective of the cup rim radius magnitude. By following the model where the femoral component displaces by a distance of s_r (i.e. moves from position C_1 to C_2), and assuming relocation occurring vertically along the inferior-superior direction (i.e. from C_2 to C_3), then contact will also always occur above the rim radius of the acetabular cup. In the extremely unlikely event that $s_r >> c$, then contact below the rim of the acetabular cup radius could occur. However, as current literature has not shown any wear occurring below the rim radius of the acetabular cup, this will not be considered in the analysis.

To simulate the impact loading with the consideration of joint laxity, the vertical loading condition was set to occur over a specific time period. Dynamic explicit modelling allowed for the assessment of contact location and magnitude under relocation due to the action of vertical loading, which has not been modelled in previous studies. To model this condition, the positioning of the hip resurfacing device was initially placed medially and inferiorly in accordance with the 'pure' microseparation model. The equations were extended to determine the medial displacements, D_M, and inferior displacements, D_I, applied in the finite element models:

$$D_M = L_{o-c_2} \cos\theta \tag{3.12}$$

$$D_I = L_{o-c_2} \sin\theta \tag{3.13}$$

where $L_{o\text{-}c2}$ is the distance from 0 to C_2 in the theoretical microseparation model. For the radial displacement of 40 μm and cup inclination angle of 45 ˚, the medial and inferior displacements were both 0.028 mm.

3.2. Finite Element Modelling

This section details the different models that were developed within this project where each model serves a unique purpose as explained below. Both two-dimensional and three-dimensional models were developed along with making full use of the computational hardware available. The modelling definition described is relevant to all of the models A to E covered within this section of the thesis and any specific details will be discussed in each of the appropriate sub sections. The definitions of material models, boundary conditions and loads were discussed within previous sections of the thesis.

A number of computer hardware systems and software programs were used to develop models and solve problems within this project, this includes a custom self-built workstation with the latest Intel Ivy Bridge processor. Detailed descriptions of all the hardware and operating system software packages used in this project have been provided in Appendix D – Computer Hardware and Software.

3.2.1. Finite Element Modelling Methods

Following on from the consideration of linear and non-linear modelling strategies, the methodology of carrying out a static and/or dynamic analysis must be discussed. For a static analysis, the time dependent effects of damping and inertia do not have a significant effect on the response of the structure. The basis of a static analysis is,

$$\{F\} = [K]\{u\} \tag{3.14}$$

where $\{F\}$ is the force vector, $[K]$ is the stiffness matrix of the structure and $\{u\}$ is the displacement vector. Even a nonlinear static analysis can be performed (including contact) assuming that the load is applied gradually to ensure an accurate solution is reached.

In reality, all systems behave dynamically under the action of a load or displacement, however when application of the load or displacement is slow enough, the systems is assumed to be loaded and respond statically as the inertial forces are neglected. The importance of considering both static and dynamic loading for implanted hip joints has been studied in [190, 191]. Both static and dynamic analysis is considered for both linear and non-linear systems; however some limitations in computational techniques may mean that simplifying assumptions are required. The basis of dynamic equilibrium includes inertia effects and is represented by the following equation,

$$M\ddot{u} + I = L_E \tag{3.15}$$

where M, $\ddot{u}$ and I are the mass, acceleration and internal forces of the structure respectively and L_E is the externally applied load, which is based on Newton's second Law of motion ($F = ma$). This equation forms the difference between a static and dynamic analysis where a dynamic analysis includes the inertial effects and internal forces. In terms of a simplistic undamped system such as a spring-mass set-up, for linear dynamics to be applicable then the system must be fully linear along with further criteria defined in the literature [192]. As undamped systems are not valid in reality the analysis should account for a damped influence as a form of energy dissipation. By including the damping term within the dynamic equilibrium equation the following equation is obtained:

$$M\ddot{u} + Ku - C\dot{u} = L_E \tag{3.16}$$

where C and $\dot{u}$ is the damping matrix and velocity of the structure respectively. Through performing a structural dynamic analysis the effects of time varied loading on a structure is determined. Another way to state (3.16) is as follows,

$$\{F(t)\} = M\{\ddot{u}\} + C\{\dot{u}\} + K\{u\} \tag{3.17}$$

where the load vector $\{F\}$ is a function of time t.

Both implicit and explicit methods were used for developing finite element models and carrying out analysis. An explanation of both implicit and explicit methods for engineering problem solving is provided by Harewood and McHugh [193]. For an implicit approach, a solution is obtained by iteration at each increment to obtain a solution to the finite element equations. An explicit solution is determined directly at each increment without iteration or a convergence criterion. Both implicit and explicit solvers are available in the finite element analysis software used in this project, and each solver will be discussed in the more detail below.

The implicit finite element solver determines the unknowns $\{u\}$ and obtains the equilibrium at time t whilst including the effects of damping and inertia. The explicit method includes failure material models, complex contact and impact whilst using less memory and data storage space. The implicit analysis is used for statically and quasi-statically loaded models [194]. For more complex contact conditions such as the laxity based pure microseparation models, the explicit method provides a more efficient solution as the implicit method is required to solve a large number of linear equations. The Abaqus explicit methods work by advancing the kinematic state from a previous increment. By referring back to (3.17), the key components of this equation are the velocity and acceleration. For the implicit method, the mass and damping factors are ignored because the displacement is not a function of time. For the implicit method, the velocities and accelerations are zero, because the derivatives of the displacement are zero. Within this project certain models require very large global stiffness matrices to be inverted, and the computational time and the random access memory size requirement for this is significant. For implicit analysis methods such as the Newton-Raphson method are used to solve the finite element problem. The explicit method considers the

solution to be a function of time, therefore both velocity and acceleration are included which means mass and damping effects are considered. For the explicit method a central difference method time integration scheme is used. The scheme calculates the field variables at the nodal points and the method works by inverting the lumped mass matrix. The basis of the solution works on time step increments. It is not possible to directly solve modal frequencies and mode shapes with the contact conditions modelled within this problem due to nonlinearities and varying values within the stiffness matrix. This can not be dealt with by the finite element method's eigenvalue solvers unless the contact conditions are ignored.

3.2.2. Finite Elements, Meshing and Contact Interactions

The type of elements used (Figure 3.9) is dependent upon the model developed and problem being solved [108]. The number of finite element nodes impacts the accuracy and computational analysis times for solving problems. The formulation of an element is the mathematical theory behind the element's behaviour [110]. For deformation of the finite elements, both a Lagrangian mesh and Eulerian mesh exist to model this change in element geometry. The key difference between the Lagrangian and Eulerian formulations is that Lagrangian allows the nodal points and material points to change position as the material deforms. However, Eulerian formulations allow the material to pass through the nodal points without deformation of the original mesh. A combination of the two is known as Arbitrary Lagrangian-Eulerian (ALE), which is later discussed as it offers a method for mesh ablation when carrying out computational wear simulations.

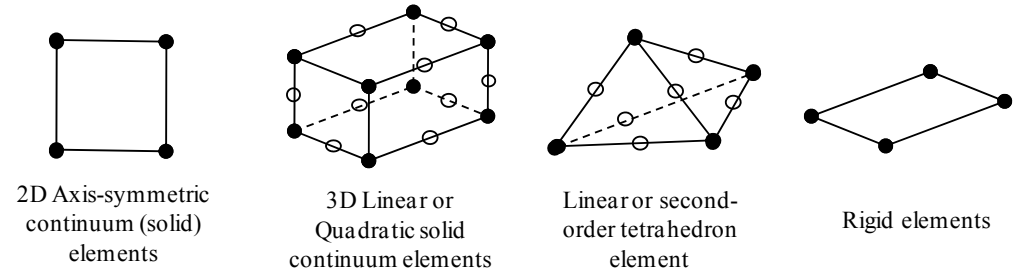

Figure 3.9. Element types

For all the joint implant loading conditions including edge loading, the problem can be modelled using solid continuum elements, which are appropriate for linear and non-linear problems with contact. Generally, linear elements should be used when the 'hard' contact algorithm is used [110] and for stress analysis problems. For contact studies within current literature, no use of tetrahedral elements was cited at the contact surface interaction. Therefore, due to geometrical consistency first order hexahedral elements should be the preferred choice of element types for contact modelling. However, for complex contact geometries modified second-order tetrahedral elements (C3D10M) can be used where it is not possible to use hexahedral elements. The problem with regular second-order 'un-modified' tetrahedral elements (C3D10) is that they have zero contact force at their corner nodes which leads to poor contact pressure predictions and therefore should be avoided. Fully integrated elements will produce more accurate results than reduced integration elements but are more computationally intensive. Incompatible modes for elements are more appropriate for improving the accuracy of results in bending problems, which would be applicable for the stem of the femoral head components.

Inaccurate results can be obtained based solely due to poor meshing especially for modelling complex three-dimensional geometry with elements of high aspect ratios and distorted elements [195]. To aid suitable meshing and reduce the finite element modelling time advanced automatic meshing algorithms were developed since the introduction of the finite element method. However, due to lack of control of the algorithms for use in wear simulations they have been used in combination with manual meshing and seeding definitions.

Following on from the finite element and meshing definitions, careful selection of contact pair surfaces and contact properties must be made. Numerical contact modelling as a whole through the finite element method has provided solutions to contact problems within the orthopaedic device industry. The contact algorithms considered in this thesis are based on

finite sliding interactions. This formulation is especially suitable for hip resurfacing devices under gait motion where large sliding distances relative to the radius of contact are expected. A surface-to-surface discretization method allows for accurate contact between the deformable bodies and would be the preferred choice over node-to-node contact. To consider the friction between the contact surfaces a tangential interaction property is defined based on an isotropic coulomb friction model. This tangential definition models the shear forces between the femoral head and acetabular cup, whereas the normal contact behaviour is modelled as 'hard' contact. This contact formulation provides the foundations for advanced contact analysis between the hip bearing components. When selecting the master contact surface, the larger surface is selected, however if the surfaces are of a similar size then the stiffer body should be selected. If the two surfaces are of a similar size and stiffness then the surface which is modelled with a coarser mesh is selected as the master surface [110].

All finite element analysis was carried out using SIMULIA Abaqus v6.9 to v6.11, which is commercially available and used extensively within academia and industry. Developing a finite element analysis software package specific to the problem being solved within this project was not a viable option. A more sensible methodological approach was to utilise pre-tested and validated software which is refined by experts and technical specialists over many years. The modelling was defined through the CAE (computer aided engineering) environment and input file, which allows for changes to be made in an efficient manner, depending on the modifications being made. The meshing strategies adopted for each model was based on the geometrical complexity of the model and element types required. For the implant devices, the ideal choice of element types were the hexagonal linear order elements, with wedge elements used where hexagonal elements can not be placed within the model. In order to achieve this meshing approach, partitioning of the femoral head and acetabular components was necessary. For the three-dimensional models, C3D8I elements were used (three-dimensional eight-noded

elements enhanced by incompatible modes). These element types were suitable for both contact analysis and stress analysis. Due to the geometrical complexity of the bone models, tetrahedral elements were used, which allows for automatic meshing algorithms to save a significant amount of modelling time over having to manually mesh the components. Part and edge seeding tools were used to define the nodal points on all models, including the bone models. This also allowed for high density and direction biased meshing to be defined in areas where more accurate results were required i.e. in the contact zone.

The coefficient of friction (μ) between the head and cup was modelled nominally as 0.16 based on the friction factor of CoCrMo on CoCrMo in both bovine serum and synovial fluid [119]. Of all material combinations studied by Scholes, Unsworth and Goldsmith [119] this was the largest friction factor value recorded. The coefficient of friction value to be modelled in finite element analysis was shown to have a negligible effect on the contact pressure at low values of friction coefficients [14]. However, as the surface friction coefficient increases during the life of the component the subsurface stresses will also increase [196].

As a form of modelling validation, the constraint penalty work and contact penalty work are checked to ensure they are close to zero, as the analysis problems involve both tie constraints and contact. The problem of modelling normal and microseparation of the hip joint leading to edge loading can be considered as quasi-static (excluding the modelling of laxity based pure microseparation). Due to physical movement of the implant and attached bone bodies, the values of total kinetic energy should not be larger than a small fraction of the total strain energy. Current literature suggests that the dynamic effects of a problem can be considered negligible if the following inequality holds true

$$\frac{E_{KE}}{E_{IE}} \leq 5\% \tag{3.18}$$

where E_{KE} is the kinetic energy and E_{IE} is the strain energy.

Finally, for any dynamic explicit analysis where more complex contact loading occurs by ‘pure’

microseparation, then the energy output provides a good measure of the solution accuracy. Throughout the analysis, the total energy (E_T) should ideally be constant (or close to constant). The results and presence of both artificial energies and real energies should be processed. The kinetic energy (E_{KE}) and strain energy (E_{IE}) should be the dominate energies over the artificial energies such as: artificial strain energy (E_{AE}), damping dissipation (E_{VD}), and mass scaling work (E_{MW}). The total energy balance defined as,

$$E_T = E_{KE} + E_{IE} + E_{VD} + E_{SD} + E_{KL} + E_{FD} + E_{JD} - E_{WK} \tag{3.19}$$

is based on the conservation of energy (first law of thermodynamics) and is in terms of time rates. The following terms also appear in the energy equation (3.19): energy dissipated by automatic stabilization (E_{SD}), loss of kinetic energy at impact (E_{KL}), energy dissipated through frictional effects (E_{FD}), electrical energy dissipation due to electrical current flow (E_{JD}) (zero in this problem) and external work (E_{WK}).

A combination of post processing methods were used and developed to obtain the stress, strain, contact and other results. Although the von Mises stress criterion is known to provide more accurate stress predictions than the Tresca criterion, initial assessments conducted for the problems during the methodology stages showed the results between the two criteria to be very similar. Therefore, in terms of stress criterion only the von Mises stress results are studied.

3.2.3. Model A: Three-Dimensional Hip Implant Rigid Backed Models

The most efficient way to assess the effect of changes to the three dimensional implant devices without the influence of the femur or pelvic bones was to develop a three-dimensional model backed by analytical rigid components. The use of analytical rigid components as opposed to discrete rigid components meant that the backing components were modelled geometrically using arcs and lines and not linear edged elements. Therefore, when a variation of the model

was used to specifically analyse the acetabular cup, then a more continuous contact stress and pressure profile was obtained.

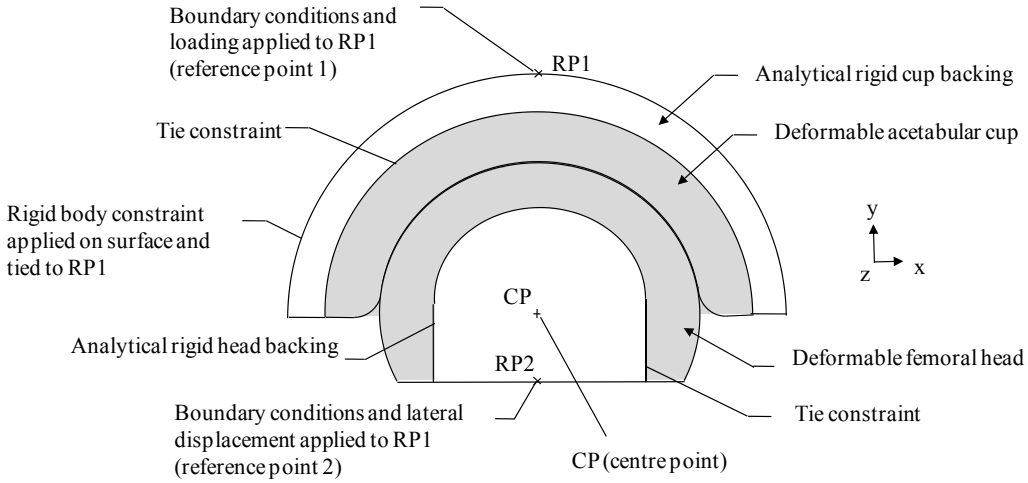

Figure 3.10. Rigid backed 3D hip finite element model (Model A-1)

Both the acetabular cup and femoral head were tied to a rigid cup holder and rigid femoral head holder respectively, as shown in Figure 3.10 which is referred to as model A-1. The reference points (RP1 and RP2) allowed for more flexibility in defining the kinematic and kinetic boundary conditions as opposed to applying boundary conditions on the component surfaces. As rigid backed components were used in model A, there is no consideration of the elasticity of the pelvis or femur. However, it has proved to be less computationally intensive than more complicated models which is very useful for carrying out parametric studies. Carrying out analysis with this model was also efficient for performing comparative implant modelling of the hip device.

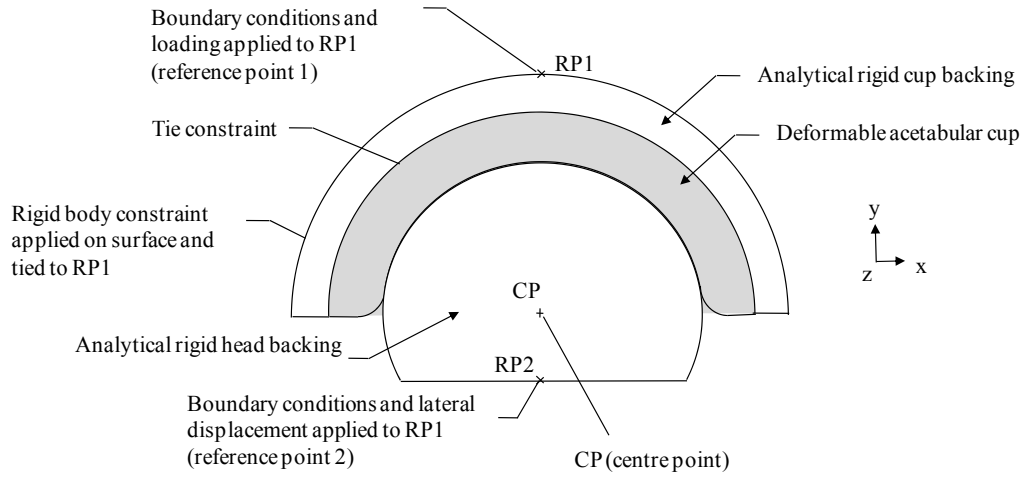

Figure 3.11. Rigid backed 3D hip FE model without deformable femoral component (Model A-2)

A modified version of the model, defined as model A-2, was used to analyse the effect of 'pure microseparation on the acetabular cup. Therefore, to minimise the computational analysis run times and work within the stiffness matrix constraints as far as hardware would allow, the deformable femoral head component was replaced with an analytical rigid component (Figure 3.11).

As discussed in the literature review, the analysis conducted using Abaqus standard (implicit solver) often requires displacement control to be established before a contact force is applied. The explicit finite element solver is used to model impact under normal and edge loading conditions where equilibrium is not required to be established. Under these conditions pure microseparation conditions are modelled and contact established under impact loading. It had been suggested in the literature that cup positioning plays a crucial role in the severity of edge loading wear on hip replacements and resurfacing devices. Model A-2 is used to conduct a contact analysis on the acetabular cup through a range of cup inclination angles (Figure 3.12a) and anteversion angles (Figure 3.12b). For hip implant modelling, the use of 8-noded brick elements allow for an efficient use of elements and nodes over 10-noded quadratic tetrahedral elements. The use of hexahedral elements (C3D8I) and wedge elements (C3D6) are shown in Figure 3.13a, for the same global seeding size, the number of C3D10M tetrahedral nodes and elements was over five times the number used for the hexahedral and wedge model (Figure 3.13b).

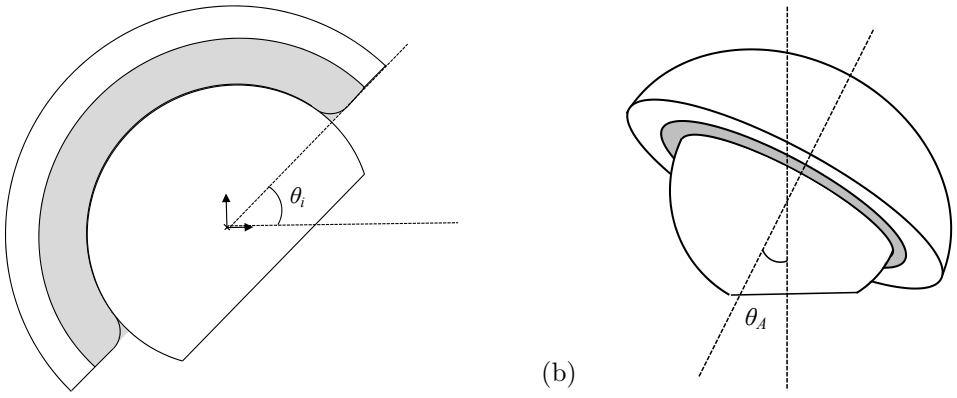

(a) (b)

Figure 3.12. (a) Cup inclination angle (b) cup version angle

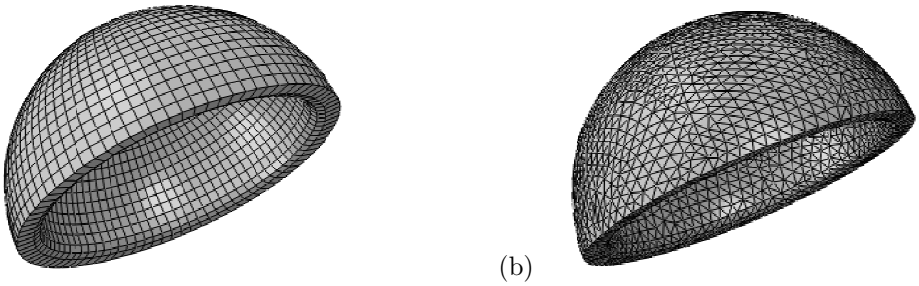

(a) (b)

Figure 3.13. Acetabular cup model with (a) hexahedral brick and wedge elements and (b) tetrahedral elements

Further justification for selecting hexahedral linear elements over tetrahedral quadratic elements was explained within section 3.2.2. Finite Elements, Meshing and Contact Interactions. Initial modelling and assessments using both methods had shown that with model partitioning, the preferred use of hexagonal elements was possible for the implant devices. Based on the recommendations of element types, the use of quadratic elements for the contact mechanics studied within this project meant that the computational analysis was simply too inefficient and therefore the preferred option of using hexahedral elements was focused on. Mesh methodology studies carried out during this project revealed the vast increase in total CPU (central processing unit) and wallclock time of analysis post-processing when using quadratic tetrahedral elements, compared with linear hexahedral elements of the same part seeding size. This further justified the use of these element types within the contact analysis.

3.2.4. Model B: Segmented Hip Resurfacing Device Models

Although model A provides a firm basis for studying the contact mechanics of hip implant devices and microseparation in three dimensions, a more anatomically realistic model is required for further contact analysis. Therefore model B was developed for further contact modelling of hip resurfacing devices. A methodology was developed and defined from the stages of taking DICOM bone scans or bone models to carrying out contact analysis, wear simulations and shakedown assessments (Figure 3.14). The DICOM bone model scans have been obtained from biomedical research community portals and open source computer aided

design model databases. The modelled bone sizes were checked [197], to ensure the bone models are representative of real specimens.

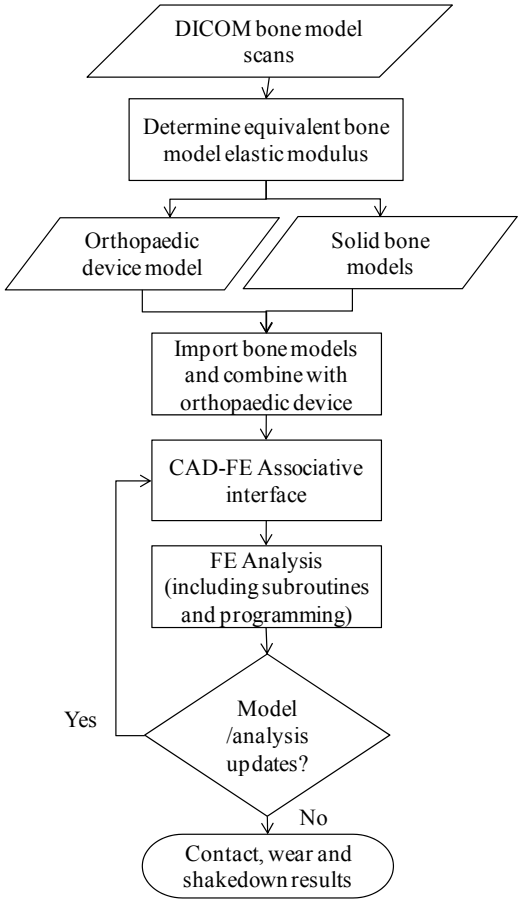

Figure 3.14. Computational development and modelling strategy

The first step of the proposed process requires use of DICOM bone scans or bone models, the bone models are then converted to solid models which is achieved using current computer aided design software packages. For this process SolidWorks (Dassault Systèmes SolidWorks Corp.) computer aided design packages were used with a number of advanced modules. To obtain a solid bone model the *Scanto3D* module was used which required importing the bone model as an STL (stereolithography) file format. This file format type was originally invented for rapid prototyping. The surface of the model is defined as a series of connected triangular surfaces which are each defined by three points and a surface normal. These points and surface normal are defined within a file to be imported into computer aided engineering software packages for further processing and analysis (Figure 3.15a). The model at this stage is a

triangulated surface representation of the bone model. The *Scanto3D* module allows for the surfaces to be smoothed during the process of creating a solid model from the surface data.

At this stage both the pelvis and femur are solid models and the next step is to determine the equivalent bone material properties using the methodology discussed in this chapter. The femoral head and acetabular cup component are modelled as separate components. The model of the 3D hip joint resurfacing device are developed following standard geometry described by Udofia et al. [14], as shown in Figure 3.16a and Figure 3.16b. The nominal dimensions for the model are summarised in Table 3.5. To assess the effect of the underside design of the femoral component on the contact mechanics, an analysis is carried out to assess a common design of the femoral head component (Figure 3.15b).

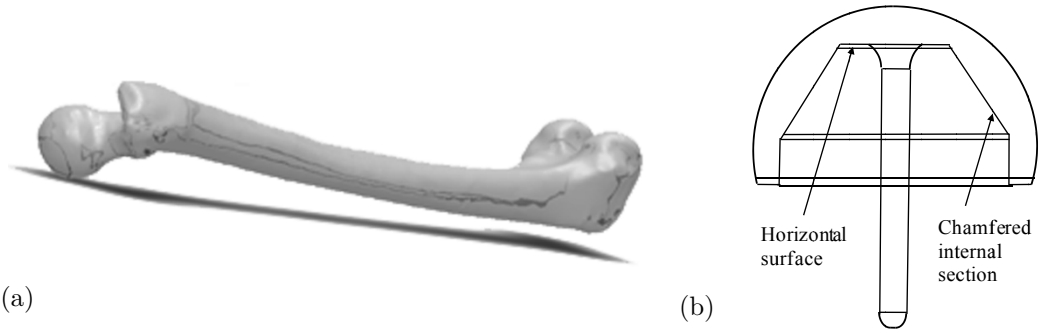

Figure 3.15. (a) Femur solid model from STL surface coodinate data (b) alternative femoral head component underside design (model D-2a)

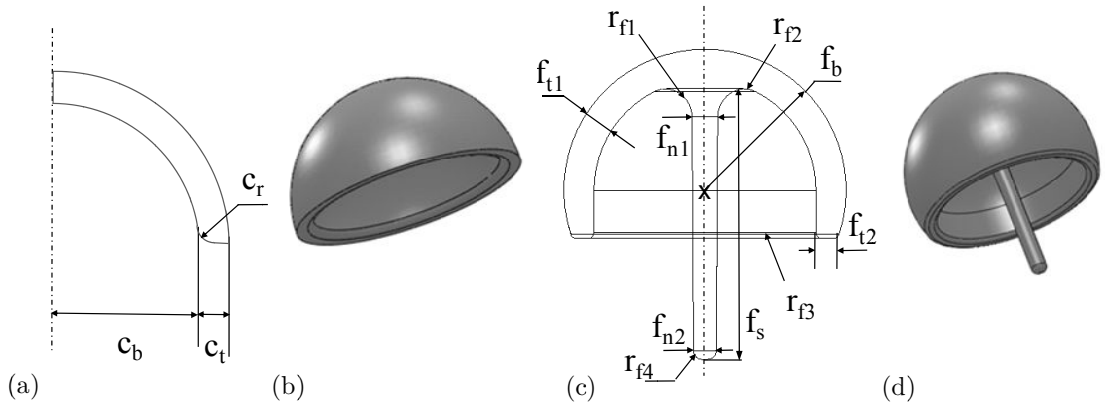

Figure 3.16. Hip implant models with nominal dimensions (a) acetabular cup 2D cross section (b) acetabular cup 3D model (c) femoral head 2D cross section (model D-2b) (d) femoral head 3D model

Following segmentation of the bone models, all components were imported into two separate computer aided design component assembly files. One assembly file combines the acetabular cup with the pelvic section, and the other combines the femoral head component with the

femur section. Boolean negation operations were used to remove bone model material which were taken up by the bearing components, as would occur during surgical implantation.

Table 3.5. Hip resurfacing device nominal model dimensions

Component	**Dimension**	**Nominal value (mm)**
Acetabular Cup	Cup bearing radius (c_b)	25.04
	Cup thickness (c_{tk})	5.0
	Cup rim radius (c_r)	2.0
Femoral Head	Head bearing radius (f_b)	25.0
	Head bearing thickness (f_{t1})	5.3
	Head bearing base thickness (f_{t2})	3.8
	Stem bearing diameter (f_{n1})	2.3
	Stem base diameter (f_{n2})	2.0
	Stem bearing radius 1 (r_{f1})	5.0
	Stem bearing radius 2 (r_{f2})	5.0
	Head radius (r_{f3})	1.0
	Stem base radius (r_{f4})	1.5

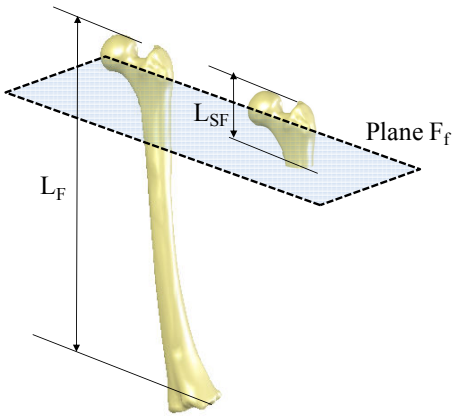

Figure 3.17. Full femur model to segmented femur model

From the solid femur model the length of femur segmentation L_{SF} was defined to be within the range $0.13L_F \leq L_{SF} \leq 0.16L_F$, where L_F is the total length of the femur model and the cutting plane surface of the femur is defined as plane F_f (Figure 3.17). The femur length was measured directly from the computer aided design model from end to end. With the femur in the scanned vertical position, the femoral head had been inserted into the assembly where the angle of inclination (θ_i) was set from the x-axis. To define the insertion positioning of the femoral head into the femur, the cross section of the femoral head component was used as a template (Figure 3.18a) against the cross section of the femur as carried out by surgeons on x-ray scans from patients before any implantation is carried out (Figure 3.18b).

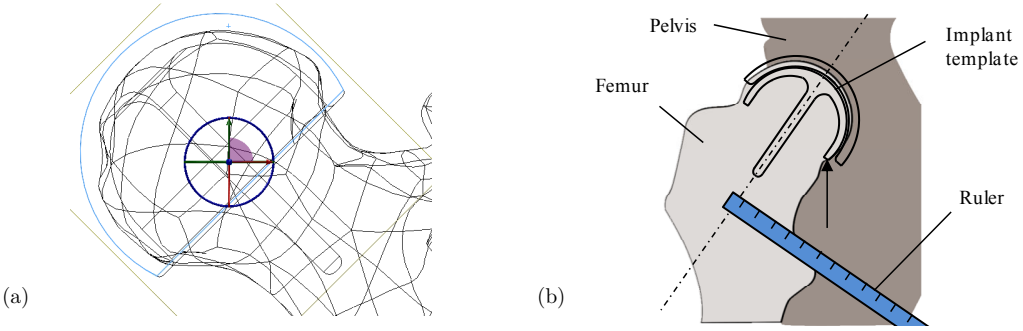

Figure 3.18. (a) Templating during computed aided modelling (b) templating the femoral head and acetabular cup components during surgical implantation

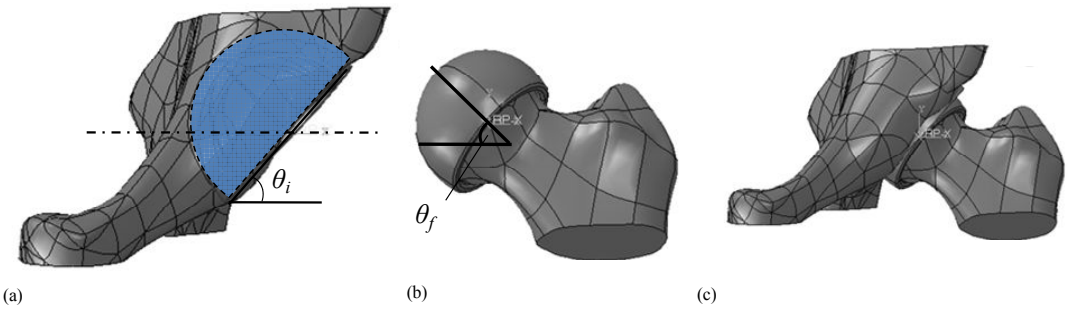

Figure 3.19. (a) Pelvis and cup sub-assembly (b) femoral head and femur sub-assembly (c) segmented hip resurfacing assembly model

A similar templating methodology was used for the pelvic model (Figure 3.19a), however a more in-depth measurement system was required. The femur and femoral head sub-assembly is shown in Figure 3.19b and the segmented hip resurfacing assembly is shown in Figure 3.19c. The segmented dimensions for the pelvic section Pel_{h1} and Pel_{h2} were defined from the datum axis parallel to the x-axis along the centre of the acetabulum. The datum point was measured based on the superior and inferior extremities of the acetabulum, where DP_I is the distance from the acetabulum centre point to the inferior end point, DP_S is the distance from the acetabulum centre point to the superior end point. By assuming $DP_I = DP_S$, i.e. the centre of the acetabulum lies directly between the superior and inferior extremities of the acetabulum, then a radius r_{acetab} from this centre point can be defined. Therefore the dimensions of Pel_{h1} and Pel_{h2} were both defined as shown in (Figure 3.20) and defined as,

$$Pel_{h1} = Pel_{h2} = r_{acetab} + (r_{acetab} \times 0.1) \tag{3.20}$$

An associated computer aided design interface was setup between the computer aided design and the finite element analysis models. This application was used to import both assemblies

for carrying out finite element analysis which allowed for rapid alterations to be made to the computer aided design model and assemblies. This was all achieved whilst keeping the integrity of the finite element model definitions such as boundary conditions, loads and contact interaction properties. This worked by defining a port number and working directory for the parts and assemblies.

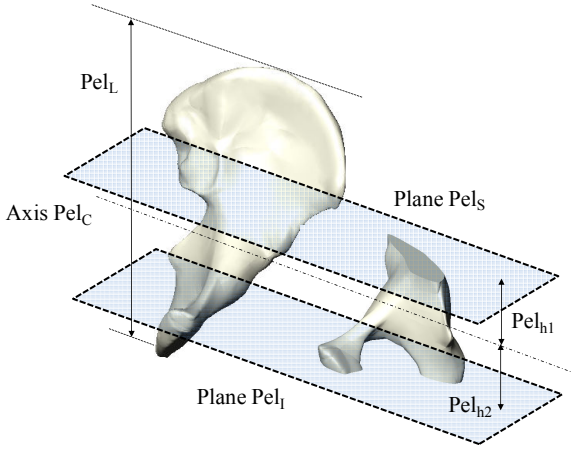

Figure 3.20. Full pelvic model to segmented pelvic model

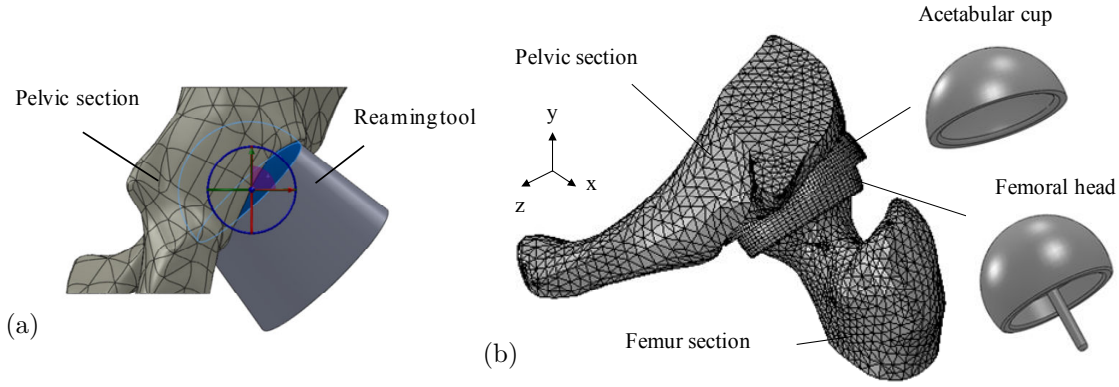

Figure 3.21. (a) Reaming of the acetablum before cup implantation (b) segmented hip finite element model (model B-1)

A reaming tool was used to remove excess surrounding bone around the acetabulum (Figure 3.21a) as would be used during the implantation of the acetabular cup during surgery. This was especially required when implanting an anteverted acetabular cup. The next step in the process was to build up the finite element assembly model (Figure 3.21b) with definition of the meshing, elements, materials, boundary conditions and loads.

In terms of vertical loading conditions, the ISO standard states a maximum of 3000N to be used during experimental simulator testing, however, no reference is made to the reason of

such a value. Bergmann [198] has discussed how such a value has been used for many years during a recent conference. From direct *in vivo* hip joint force measurements obtained by Bergmann et al. [19], the maximum load during the normal walking cycle is shown to be just below 2500 N which is also the maximum loading adopted by Udofia et al. [14] for finite element studies. However a more recent study explains how previous research such as those discussed in this thesis may underestimate the vertical loads acting on the hip joint. Along with the ISO vertical loading of 3000 N (F_I), a vertical load (F_y) of 3900 N was applied based on the high peak loads shown to occur during the walking cycle more recently by Bergmann et al. [187], however a stumbling load (F_s) of 11000 N was also considered as these high vertical loads have been highlighted to occur *in vivo* [187]. Apart from the definition of ISO vertical loading, all other values were obtained directly from *in vivo* patient force measurements.

3.2.4.1. Hip Rotation Modelling

The ISO hip angular rotation data has been discussed within chapter 2 and this chapter simulates the walking cycle during *in vitro* studies. The same approach and data can be used for the computational modelling. The choice of opting for 2 out of the 3 rotational directions i.e. flexion-extension and inward-outward rotation was based on two reasons. Firstly due to the limitations of the computational modelling techniques this decision helps to simplify the analysis, secondly the literature review shows wear rate results from two axis simulator studies match *in vivo* wear rates more closely than wear rates from three axis simulator studies. The start position of the femoral component angular displacement were set at $t = 0$. The flexion-extension and inward-outward angular displacement values were $\phi_{FE_s} = 25\left(\frac{\pi}{180}\right)(rad)$ and $\phi_{IO_s} = -10\left(\frac{\pi}{180}\right)(rad)$ respectively. The values at the angular displacement at the furthest points are $\phi_{FE_f} = -18\left(\frac{\pi}{180}\right)(rad)$ and $\phi_{IO_f} = 2\left(\frac{\pi}{180}\right)(rad)$. For experimental testing there is a tolerance of $\pm\ 3^\circ$ for each angular rotation displacement, however for the numerical model only nominal values were used. The data were tabulated (Table 3.6) to be applied during the

hip wear simulations. The data were interpolated if not directly available from the ISO standard.

Table 3.6. Application of angular displacement of the hip joint for finite element modelling

Axis Rotation	**Time, % of cycle ± 1 %**	**0**	**21**	**50**	**62**	**100**	**displacement**
	Time (FE INPUT)	**0**	**0.21**	**0.5**	**0.62**	**1**	**range**
X Axis	Angle of flexion (+) / extension (-) ± 3 °	25.0	6.940	-18.0	-7.680	25.0	
X Axis	Angle of flexion (+) / extension (-) ± 3 ° (from zero)	0.0	18.060	43.0	32.680	0.0	43.0
X Axis	Angle of flexion (+) / extension (-) Radians	0.436	0.121	-0.314	-0.134	0.436	
X Axis (FE)	Angle of flexion (+) / extension (-) Radians	0.0	0.315	0.751	0.570	0.0	0.751
X Axis (FE AMP)	**Angle of flexion (+) / extension (-) Radians**	**0.0**	**0.420**	**1.0**	**0.760**	**0.0**	
Z Axis	Angle of adduction (+) / abduction (-) ± 3 °	3.0	7.0	-0.780	-4.0	3.0	
Z Axis	Angle of adduction (+) / abduction (-) ± 3 ° (from zero)	0.0	4.0	-3.780	-7	0	11
Z Axis	Angle of adduction (+) / abduction (-) Radians	0.052	0.122	-0.014	-0.070	0.052	
Z Axis (FE)	Angle of adduction (+) / abduction (-) Radians	0	0.070	-0.066	-0.122	0	0.19
Z Axis (FE AMP)	**Angle of adduction (+) / abduction (-) Radians**	**0**	**0.364**	**-0.344**	**-0.636**	**0**	
Y Axis	Angle of inward (+) / outward (-) ± 3 °	-10	-4.96	2	-0.88	-10	
Y Axis	Angle of inward (+) / outward (-) ± 3 ° (from zero)	0	5.04	12	9.12	0	12
Y Axis	Angle of inward (+) / outward (-) Radians	-0.175	-0.087	0.035	-0.015	-0.175	
Y Axis (FE)	Angle of inward (+) / outward (-) Radians	0.000	0.088	0.209	0.159	0.000	0.209
Y Axis (FE AMP)	**Angle of inward (+) / outward (-) Radians**	**0**	**0.42**	**1**	**0.76**	**0**	

3.2.5. Model C: Full Femur and Pelvic Hip Resurfacing Model

To justify the validity of the segmented hip implant model (model B) for contact analysis, the model details are kept the same, and a direct comparison made between having a full and segmented pelvic and femur model. For the full hip resurfacing contact model (Figure 3.22), the back surface of the Ilium (pelvis) is defined as providing displacement control within the first step of the analysis, then switching to load control the same surface of the ilium is fully constrained. The load is then applied at the lower extremity of the femur i.e. below the medial and lateral condyle. The load is applied as a concentrated load to a reference control point with the definition of a kinematic coupling constraint located at the inferior end of the femur

i.e. the model surfaces of the medial condyle, lateral condyle, medial epicondyle, intercondylar fossa, adductor tubercle and lateral epicondyle.

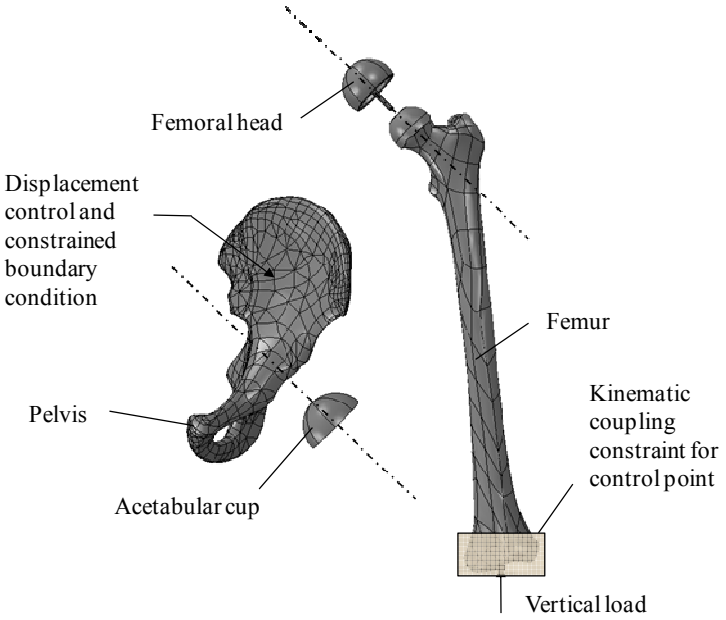

Figure 3.22. Full hip joint model

3.2.6. Model D: Two-Dimensional Axisymmetric Models

A two dimensional model provides many advantages over three dimensional modelling, including the reduction of model development and analysis run times. This does however, require simplifying the geometry of the pelvic and femur models as well as compromising the positioning of the hip implant components. Both the acetabular cup and femoral head components must be assembled without any inclination angle, such as that included within models A, B and C. Having both components at a zero degree inclination angle would not be possible during implantation *in vivo*. Another key limitation of this type of modelling approach is that microseparation and edge loading can not be analysed.

The development of the two-dimensional model was inspired by the research conducted by Udofia et al. [14] and Mak and Jin [89]. The two-dimensional axisymmetric models were developed for specific analysis to be conducted. Model D-1 (Figure 3.23a) was developed to analyse the bearing diameters, stem designs, effect of the inlay and represents a hip replacement device. Model D-2 is a hip resurfacing device model (Figure 3.23b), which was

developed to analyse the subsurface stresses of each of the components along with the contact stresses. Due to the computational efficiency of the two-dimensional model a cyclic shakedown analysis was conducted for the hip resurfacing model.

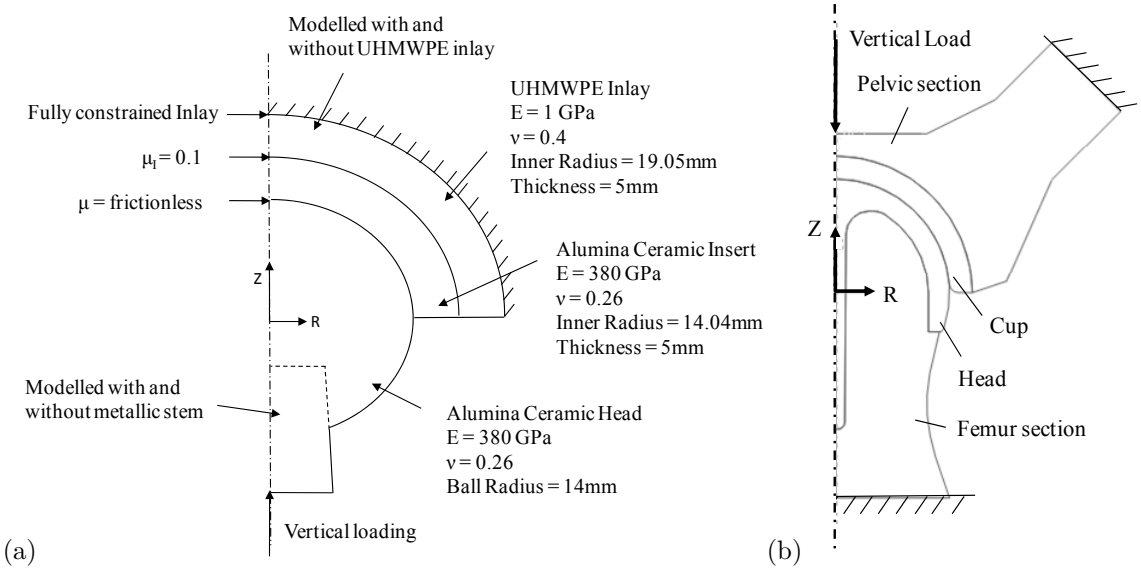

Figure 3.23. 2D axisymmetric models (a) hip replacement model (model D-1) (b) hip resurfacing model (model D-2b)

For both models different vertical loading conditions were applied to analyse the effect of vertical loading on the surface and subsurface stresses. For the hip replacement model, a ceramic insert was modelled along with a polymer inlay and metallic stem. The coefficient of friction between the inlay and insert was set nominally as 0.1. The coefficient of friction between the metallic stem and ceramic head was set nominally as 0.2. These coefficient of friction values represented an unbonded state between the components. Between the insert and head i.e. the bearing components, frictionless contact was assumed based on a fully lubricated contact surfaces and to maintain consistency with the previous literature. To further justify the validity of this assumption, low values of CoC friction coefficients are refereed to in the literature [199]. The stresses of both frictionless contact and contact with a friction coefficient of 0.02 [199] were checked using model D-1, there was a negligible difference between the stresses of both models. For the hip resurfacing two-dimensional axisymmetric model, a kinematic tie constraint was applied between the top surface of the acetabular cup

and bottom surface of the pelvic section. Another kinematic tie constraint was applied between the bottom surface of the femoral head and top surface of the femur section.

The cyclic analysis for model D-2b was conducted using tabulated amplitudes within a time step to apply the load in a cyclic manner. Then through a combination of enveloping, combining and plotting data through the use of operators, the stress-strain curves was plotted. To obtain a correlation of the uniaxial stress-strain curve for the material both the von Mises stress and equivalent plastic strain were considered, as these provide a scalar measurement of the stress and strain respectively. However, for the cyclic analysis a combination of the elastic and plastic states needs to the considered, therefore, the maximum principal stresses and strains were used.

An additional model was developed using the same geometry from model D-2b, with an orphan mesh created to apply separate cortical and cancellous material properties to the femur and pelvis sections. This is referred to as model D-2c where cortical bone material properties were applied to the surface elements and the cancellous bone properties were applied to the interior elements. The material properties were obtained from the literature [14] and discussed in chapter 2.

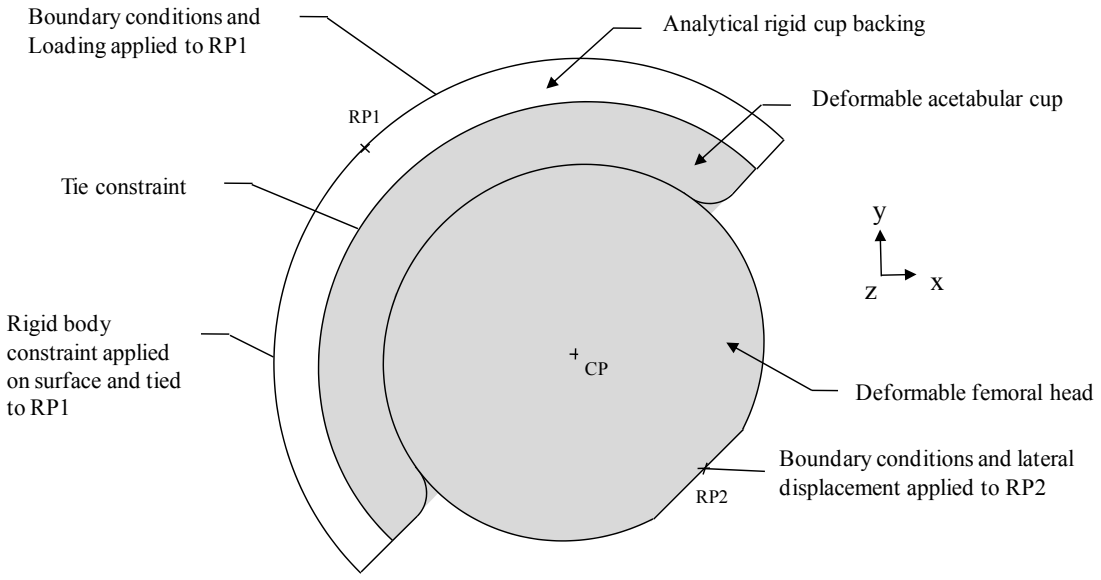

Figure 3.24. Three dimensional fully deformable validation model (model E-1)

3.2.7. Model E: Hip Bearing Comparative Models

Finite element hip bearing models were developed to be compared to the work carried out by Mak et al. [67]. A comparison was required mainly for the normal and edge loading contact stress. The model definition is provided in Figure 3.24 and Figure 3.25 with more detailed parameter data provided in Table 3.7.

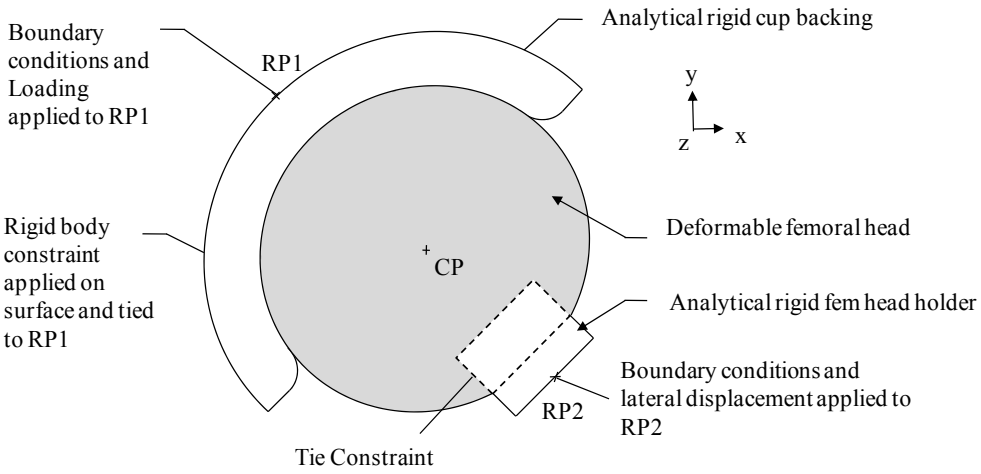

Figure 3.25. Three dimensional deformable cup and rigid head valiation model (model E-2)

Table 3.7. Comparative model parameters

Parameters	Model E-1	Model E-2	Mak et al. 2010
Head model	Deformable	Rigid	Not specified
Cup model	Deformable	Deformable	Deformable
Head diameter (mm)	28	28	28
Cup internal dia. (mm)	28.04	28.04	28.04
Radial clearance (µm)	40	40	40
Radius (mm)	2.5	2.5	2.5
No. elements	21376 (cup) 82944 (head)	21376 (cup)	52800 (total)
Element types	C3D8I & C3D6	C3D8I & C3D6	Not specified
Microseparation (edge load µm)	250 (In lateral direction)	250 (In lateral direction)	250 (In lateral direction)
Material	Alumina	Alumina	Alumina
Elastic modulus (GPa)	380	380	380
Poisson's ratio	0.26	0.26	0.26
Vertical load (N)	2500	2500	2500
Contact model	Normal: hard contact Tangential: frictionless contact	Normal: hard contact Tangential: frictionless contact	Normal: not specified Tangential: frictionless contact
Convergence study	Conducted for hip resurfacing model	Conducted for hip resurfacing model	Only completed under centred contact conditions

3.2.8. Asperity Contact Modelling

As previously discussed, a third body contact analysis is important for modelling abrasive wear debris between two surfaces in contact. The 2D static model has a thickness of 10mm

and the materials are based on CoCrMo. Four-noded plane strain elements were used with surface-to-surface contact and friction coefficient of 0.16 between the contact surfaces. The model analysis includes geometric non-linearity.

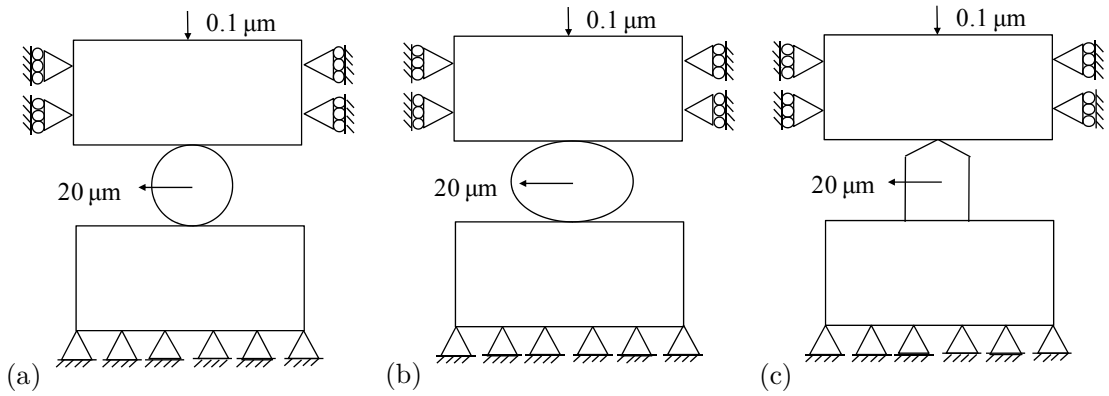

Figure 3.26. Finite element asperity contact modelling (a) circular (b) oval (c) needle

The circular wear debris is 0.1mm in diameter (Figure 3.26a) and the upper and lower surfaces (i.e. acetabular cup and femoral head surfaces) are modelled with a section of 0.6 mm x 0.2 mm. Both oval asperity's (Figure 3.26b) and 'needle' like asperity's (Figure 3.26c) are modelled for a comparative study to be carried out. The oval debris major and minor axes length's are denoted by b_d and a_d respectively. The oval debris is modelled with a b_d/a_d ratio of 1:1.5 and the needle asperity model has a pointed edge at a 30° inclination angle. A high density mesh is used for the wear debris models.

3.3. Wear Modelling

For wear modelling, two separate approaches are taken. For improving the current processes and methodologies published within the literature, specific areas are focused on to find ways of improving on past and current wear simulations. This first approach requires the development and use of a block-on-block contact model. For these wear simulations user subroutines are developed using Fortran programming. The subroutine works in conjunction with the Abaqus post-processing solver to determine the wear depth and volumetric wear of the slave contact surface. This is achieved by calculating the sliding distances of each nodal point during the

loading and sliding cycle. The contact pressures are read during each increment and the wear coefficient is defined within the subroutine. Therefore, through a combination of the data obtained during the analysis and the definition of a wear coefficient there is enough information to apply the Archard wear model.

The second unique approach is to develop a scripting interface using the dynamic programming language Python. The reasons it is more suited to conducting wear simulations of hip bearing devices will be discussed further within this section. The scripting interface is used to establish the sliding distances, contact pressures and combine this with a wear coefficient to apply the Archard Wear model to the hip bearing surfaces.

As it is not possible to conduct experiments to study the wear coefficients between bearing components, the literature was used to establish a basis of wear coefficient values. Two dimensional wear coefficients are presented by Liu et al. [10], which cover the wear up to 1 million cycles ($1.13 \times 10^{-8}\ mm^3\ N^{-1}\ m^{-1}$) and beyond 1 million cycles ($1.20 \times 10^{-9}\ mm^3\ N^{-1}\ m^{-1}$). As previously discussed, the first value covers the wear rate during the bedding-in period and the second value covers the wear during a steady state period.

3.3.1. Metal-on-Metal Contact Model

A combination of history and field output requests from the Abaqus post-processor allows for the linear wear to be recorded based on the common block data which calculates the wear at the end of every increment. Therefore, the cumulative total linear wear is recorded and subsequent updates made to the finite element model. As diffusive, adhesive or oxidative wear are not modelled directly within the analysis, it is assumed that no material becomes embedded into the contact opposing contact surface. Therefore, the wear simulations are based on a reduction of part volume during cyclic contact loading. This calculation in volume reduction is specific and linked to the change in volume totalled for all the elements of the specified element set. The metal-on metal model is provided in Figure 3.27.

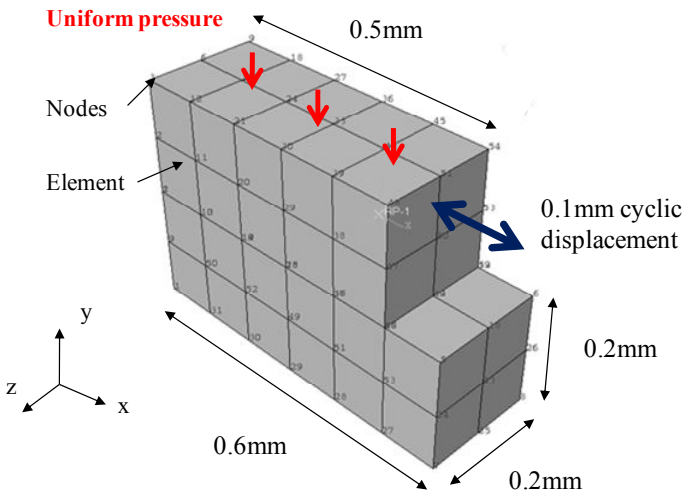

Figure 3.27. Block metal-on-metal wear model

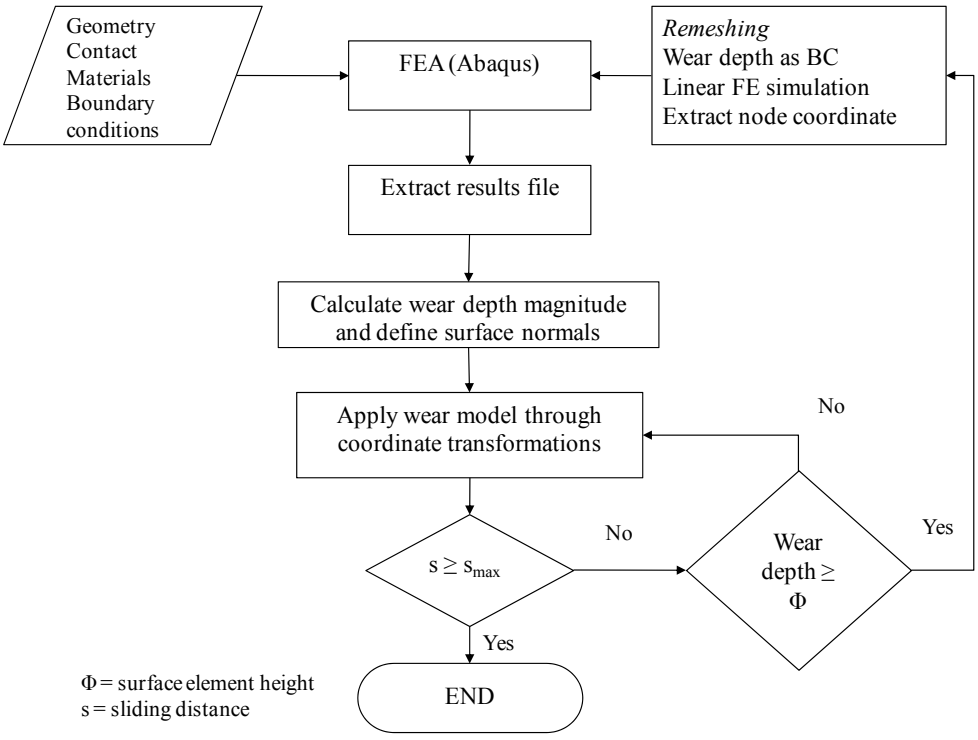

Figure 3.28. Wear model process

Multiple user defined subroutines are developed based on UMESHMOTION (to control mesh ablation) and UFIELD (to obtain wear field variables) inspired from the use in previous studies [200-203]. The UMESHMOTION subroutine controls the mesh ablation through the use of adaptive remeshing techniques, or more specifically ALE (Arbitrary Lagrangian Eulerian) adaptive remeshing. Therefore an approach between Eulerian and Lagrangian is used to control the mesh distortion and simulate material loss [192]. The definition of both approaches has been discussed within chapter 2. The process flow chart of the adaptive re-

meshing process is described in Figure 3.28, however a more detailed presentation of the process is provided in Appendix E – Wear Modelling Subroutines and Scripts.

Following definition of the finite element model the pre-processor is run in combination with the Fortran subroutine. The subroutine calls a number of utilities to support the purpose of the subroutine, including utilities to retrieve part information, node numbers, contact pressures, coordinates and contact slip magnitudes. By obtaining these data and results during the analysis and defining the wear function with the subroutine, the wear model is applied and wear depth of each node calculated. The code is made more efficient by only considering the application of the wear on a node during an increment if the contact pressure is greater than zero, which has not been previously considered in literature. After the wear depth is applied at the end of an analysis increment, the subroutine would repeat if the maximum number of analysis increments has not been reached. The other condition tested is if the wear depth of the contact surface element has been exceeded during the wear simulations. If so, the remeshing of the part is required through adaptive meshing. When the total number of step increments has been reached i.e. at the end of the step and defined cycle. To reduce the number of remeshing processes required the linear wear depth is multiplied by N, which is the number of cycles before any mesh updates are made, this has been set as 250,000 cycles for this analysis.

The methodology of calculating the sliding distance during the hip contact motion is studied using the subroutine. The two methods assessed are the use of CSLIP which requires constant contact to be maintained between the two bearing surfaces in contact, and the other method is the calculation of sliding distances using the nodal coordinates, COORD. The adaptive mesh constraint is specified as displacement control and applied to the slave contact surface.

Following calculation of the wear value, the values are applied to directly update the local coordinate system for each node which has a contact pressure value greater than zero. The

direction of the wear ablation is set in the normal direction to the contact surface at each node defined in the adaptive mesh domain. If the node within adaptive mesh domain lies within the interior of the part, then the local coordinate system variable which is aligned to the node tangent will be set to the identity matrix. If the node lies on the edge, then the direction of the wear will be arbitrary and the direction needed to be defined. Overall, the approaches adopted were based on the literature review conducted, capabilities of engineering software available as well as the finite element modelling and programming techniques developed.

3.3.2. Scripting Interface Wear Model

A Python scripting mechanical wear model was developed and like the linear wear models conducted using Fortran subroutines, the Python scripting method is also based on the constitutive wear equations from the Archard wear law. The scripting procedure makes use of the powerful and flexible scripting capabilities of Abaqus, where a detailed description is provided in Appendix E – Wear Modelling Subroutines and Scripts. The scripting interface can be summarised in the following key points:

- A segmented implant model with hip loadings and angular displacements.
- During each increment the contact pressure, nodal coordinates and contact sliding distances were recorded and the results printed to file.
- The wear was calculated at each increment, the total wear was multiplied by the number of cycles being remeshed, *N*.
- Finite element remeshing followed nodal linear wear depth calculations.
- The total cumulative nodal and volumetric wear was calculated and the results presented.

For manual calculation of the sliding distances as an additional form of numerical check and validation, the coordinates of nodal points during the kinematic motion of the hip at each increment were recorded. As a general expression, for i_i and i_{i-1} where i is the analysis increment, the sliding distance between each increment is defined by

$$d_{c_i} = \sqrt{(u'_i - u'_{i-1})^2 + (v'_i - v'_{i-1})^2 + (w'_i - w'_{i-1})^2} \tag{3.21}$$

where u', v' and w' are the sliding distances in the x, y and z direction respectively.

This provides the linear distance that the node has translated by between increments, and so a small correction can be applied to obtain more accurate values of sliding distances. By knowing the relationship between arc length and base length the sliding distance values can be calculated. If the linear length d_c is the chord length which makes a central angle θ_a, then the arc length a_c can be determined by

$$a_c = r\theta_a = 2r \arcsin(d_c / 2r) \tag{3.22}$$

where r is the radius of the curvature.

The sliding distance through an arc length and chord length is calculated between two points of n_{ci} (current increment nodal position) and n_{ci-1} (previous increment nodal position) as shown in Figure 3.29.

The nodal coordinates are required to be transformed and rotated back to the part nodal position for the reassembly of the proceeding cyclic wear iteration. Therefore, transformation and rotation matrices are required to be applied to each of the nodal coordinates [204, 205] about the x-axis (3.23), y-axis (3.24) and z-axis (3.25):

$$R_x = \begin{bmatrix} x' \\ y' \\ z' \end{bmatrix} = \begin{bmatrix} 1 & 0 & 0 \\ 0 & \cos\omega_r & -\sin\omega_r \\ 0 & \sin\omega_r & \cos\omega_r \end{bmatrix} \begin{Bmatrix} x \\ y \\ z \end{Bmatrix} \tag{3.23}$$

$$R_y = \begin{bmatrix} x' \\ y' \\ z' \end{bmatrix} = \begin{bmatrix} \cos\varphi_r & 0 & -\sin\varphi_r \\ 0 & 1 & 0 \\ \sin\varphi_r & 0 & \cos\varphi_r \end{bmatrix} \begin{Bmatrix} x \\ y \\ z \end{Bmatrix} \tag{3.24}$$

$$R_z = \begin{bmatrix} x' \\ y' \\ z' \end{bmatrix} = \begin{bmatrix} \cos\kappa_r & -\sin\kappa_r & 0 \\ \sin\kappa_r & \cos\kappa_r & 0 \\ 0 & 0 & 1 \end{bmatrix} \begin{Bmatrix} x \\ y \\ z \end{Bmatrix} \tag{3.25}$$

where ω_r is the angle of rotation about the x-axis which is the flexion-extension direction, and the transformation coordinates are x', y′ and z′. The inward-outward rotation occurs about the y-axis which is given by φ_r and the abduction-adduction would occur about the z-axis (κ_r).

By combining the rotation of the coordinates in all directions, the composite rotation matrix is given by $R' = R_x R_y R_z$

$$R' = \begin{bmatrix} x' \\ y' \\ z' \end{bmatrix} = \begin{bmatrix} \cos\varphi\cos\kappa & \cos\omega\sin\kappa + \sin\omega\sin\varphi\cos\kappa & \cos\omega\sin\kappa - \sin\omega\sin\varphi\cos\kappa \\ -\cos\varphi\sin\kappa & \cos\omega\cos\kappa - \sin\omega\sin\varphi\sin\kappa & \sin\omega\cos\kappa + \cos\omega\sin\varphi\sin\kappa \\ \sin\varphi & -\sin\omega\cos\varphi & \cos\omega\cos\varphi \end{bmatrix} \begin{Bmatrix} x \\ y \\ z \end{Bmatrix} \tag{3.26}$$

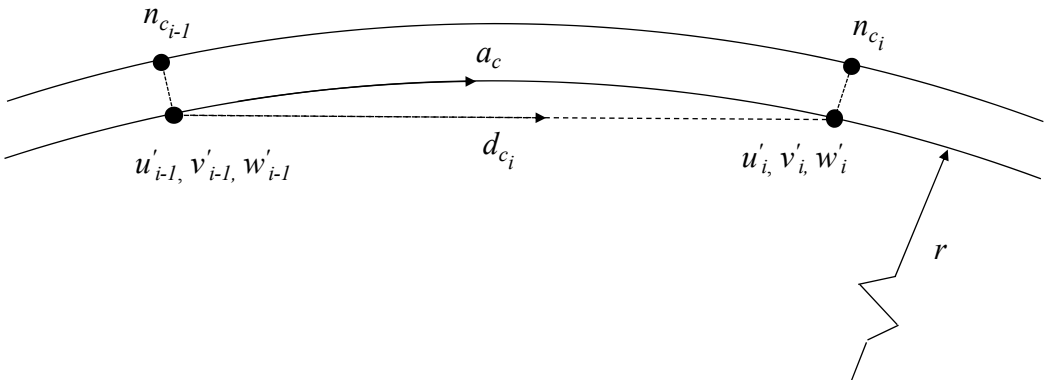

Figure 3.29. Chord and arc length

These rotations are based on a direction in the anti-clockwise direction, however if the rotation is to occur in the clockwise direction then the rotation angles become $-\omega_r$, $-\varphi_r$ and $-\kappa_r$.

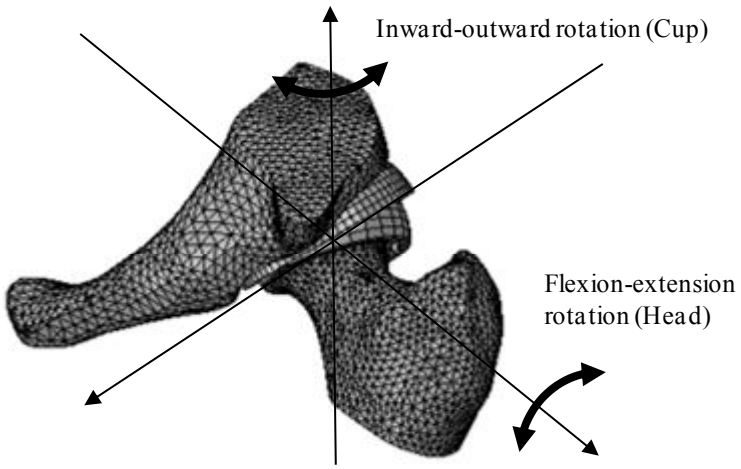

Figure 3.30. Hip resurfacing wear model

Following justification and validity of using a hip and pelvis model rather than a more computationally intensive full hip and pelvis model, the segmented model strategy was used to conduct mechanical hip resurfacing device wear simulations (Figure 3.30). The inward-outward rotation was applied to the acetabular cup and the flexion-extension was applied to the femoral head. The wear simulation process using the Python scripting method is shown in Figure 3.31.

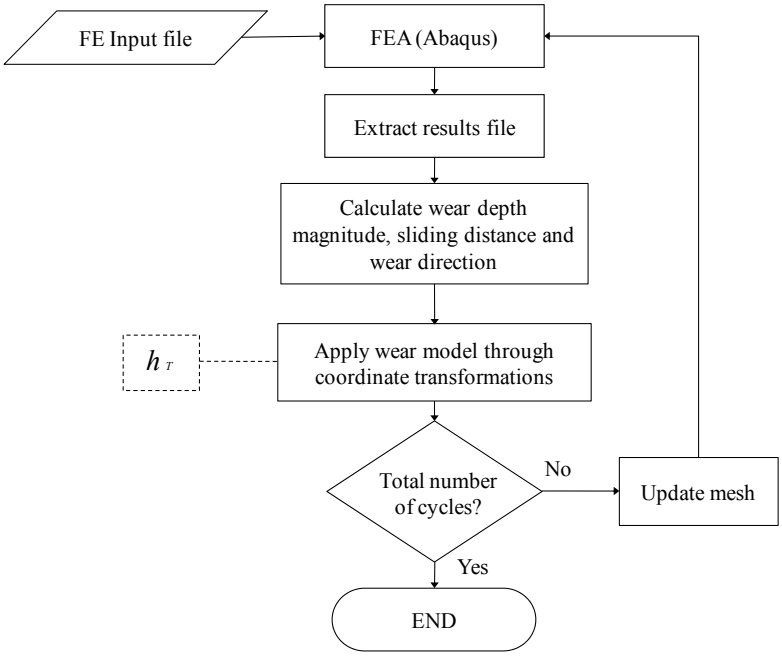

Figure 3.31. Python scripting wear simulation process

For the proposed mechanical wear simulations and number of cycles the total wear depth is calculated for each node on the bearing surface

$$h_I = \sum_{i=1}^{n} k_w p_i (s_i - s_{i-1}) \tag{3.27}$$

where h_I is the total wear depth calculated over the total number of increments n for the analysis at each node of the bearing surface. The total volumetric wear over the testing period is given by h_T,

$$h_T = \sum_{I=1}^{m} h_I \tag{3.28}$$

where m is the total number of operating cycles.

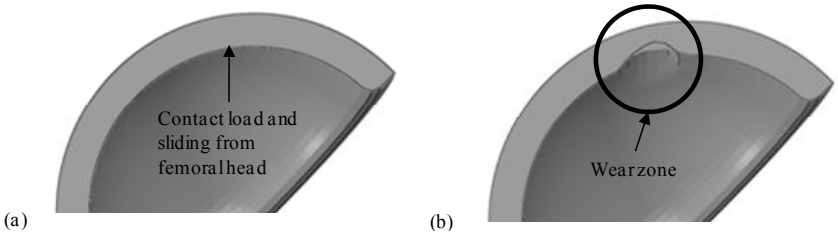

Figure 3.32. Acetabular cup (a) before wear at zero cycles (b) following the wear algorthim application

An initial assessment was carried out to ensure the coding method executes correctly (Figure 3.32), and the mesh ablates in accordance with the contact pressure, sliding distance and wear coefficient value (exaggerated for the method validation).

3.4. Summary of models

This section provides a summary of all the finite element models A-E developed (Table 3.8).

Table 3.8. Sumary of finite element models A-E

Title	Model	Summary
Model A: Three-dimensional Hip Implant Rigid Backed Model	A-1	3D Deformable head and cup model with rigid backed components (no bone)
	A-2	3D Deformable cup model with rigid backed components (no bone)
Model B: Segmented Hip Resurfacing Device Model	B-1	3D Deformable head, cup and bone model with segmented pelvic and femur sections
	B-2	3D Repeated process from B-1, with additional bone geometry and alternative implantation positioning
Model C: Full Femur and Pelvic Hip Resurfacing Model	C	3D Deformable head, cup and bone model with full pelvic and femur models (validation for model B-1 and model B-2)
Model D: Two Dimensional Axisymmetric Model	D-1	2D axisymmetric hip replacement model
	D-2a	2D axisymmetric hip resurfacing model with alternative femoral head component underside design
	D-2b	2D axisymmetric hip resurfacing model with curved femoral head component underside design
	D-2c	2D axisymmetric hip resurfacing model with cortical and cancellous bone sections
Model E: Hip Bearing Comparative Models	E-1	3D deformable head and cup validation model
	E-2	3D deformable cup and rigid head validation model

3.5. Research Software Solutions - HIPprog

The aim of HIPprog is to take the solutions and analyses conducted in this research project then amalgamate a software program and toolbox for solving further engineering problems such as those covered in this project. It is designed and set in such a way to ensure that the software can be developed, adapted and changed as the engineering processes improve along with more efficient software. As there is currently no software package which incorporates such tools and engineering analysis options, it was important to set out clear aims and objectives for the software. The software needs to be based on an operating system which is used by research communities. It must also be adaptable to be used on other operating systems other than the specific operating system it was developed to be used on. The software solution utilises open source software to promote research and development for future research and problem solving without a vast restriction on commercial licensing. This is why the use of

software platforms such as SMath Studio has been used for paper based calculations, which was developed on the Microsoft .NET Framework, which outputs Extensible Markup Language (XML) files. This strategy not only makes the calculations easy to perform and update based on the input variables, but also to be easily accessible and developed by engineers without the need for specialised knowledge or skills of a particular advanced software solution or programming. The current and future demands for studying and comparing the impacts of various life activities, loading conditions and variations in operating conditions over the life of a hip implant device was discussed previously within this thesis. The software solution therefore provides a platform for such studies to work towards standardisation and improving the efficiency of problem solving in the future, as per the aims and objectives of this project.

A number of software programming packages have been considered and tested, and it was concluded that a .NET framework would meet the aims and objectives discussed above. Through the use of the .NET framework a very user friendly GUI (graphical user interface) is developed and linked to other software and engineering programs (Appendix F – HIPprog Process Flow). There are a few key and unique features of using the object oriented .NET framework. Due to the language integration with the .NET framework, sections of code in the different languages can be combined into the software solution (with certain limitations and constraints) [206]. With the extensive development toolbox and Windows programming development tools, efficient software development and debugging is carried out. The .NET framework could also be extended and further developed to be used on handheld devices and other non-PC based devices such as tablets. The primary programming language selected for all of the development of HIPprog was Visual Basic .NET (vb.NET), which is known to be "the world's most widely used rapid application development (RAD) package" [207]. The vb.NET framework was developed through Microsoft's Visual Studio environment.

Chapter 4 – Results

Following on from the development and explanation of the methodology in chapter 3, the results will be presented in this chapter.

4.1. Model A: Three-Dimensional Hip Implant Rigid Backed Model Results

The first observation from the analysis conducted was the difference in contact pressure distribution between normal and edge loading conditions. Even when different vertical loading condition magnitudes were applied under normal loading conditions the contact pressure distribution remained circular with closely matching b/a ratios. Under vertical loading conditions, the location of the contact pressure was determined by the positioning of the hip implant components. When lateral displacement of the femoral component was included as a boundary condition, the contact pressure profile was contrasting to that when microseparation was not considered.

For Model A-1, where both the acetabular cup and femoral head components were deformable and backed by analytical components the contact pressure and von Mises stress were assessed under normal and edge loading conditions. Based on the walking gait peak vertical load of 3900 N the maximum contact pressure was 101 MPa without consideration of microseparation. The von Mises stress and contact pressure increased to a maximum of 616 MPa and 923 MPa respectively when edge loading (250 μm lateral displacement) was applied in combination with the peak load as shown on the edge of the acetabular cup (Figure 4.1a). By considering a lateral reaction force of 500 N (in line with experimental simulator test methods) without any vertical load led to a maximum contact pressure of 564 MPa, von Mises stress of 456 MPa and

maximum principal stress of 431 MPa. Mesh convergence studies were conducted to ensure appropriate mesh densities were used. However computational limitations were an important consideration when running any of the analyses.

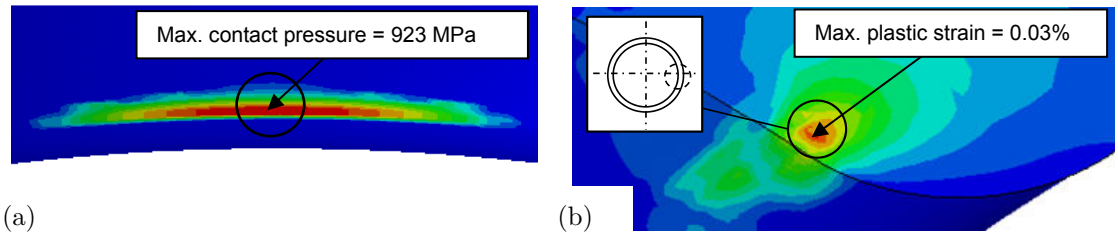

Figure 4.1. (a) Rigid backed edge loading contact pressure distribution (b) plastic strain during edge loading conditions

The simulation conducted on this model considered one cycle of edge loading, even though edge loading is understood to be a cyclic occurrence as previously discussed. When the edge load was considered as a direct lateral displacement, plastic strain was found in the material according to the analysis. The yield stress of material was exceeded due to these edge loading conditions. The maximum plastic strain was 0.03% (Figure 4.1b) as shown on the cross section of the acetabular cup in the rim edge loaded region.

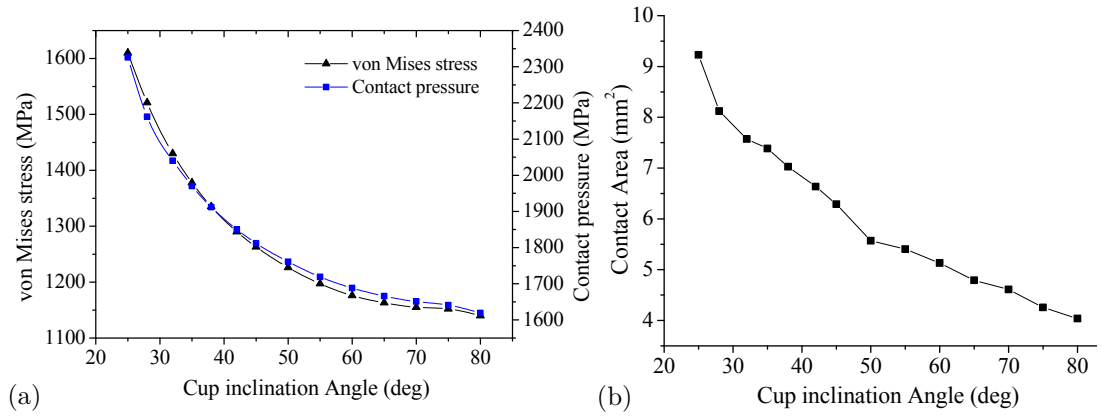

Figure 4.2. (a) Maximum von Mises stress and contact pressure (b) contact area under varying cup inclination angle

The results presented and discussed above were based on a nominal cup inclination angle of 45 ° with no anteversion or retroversion angle. By changing the inclination angle and anteversion angle, the effect on contact pressure, von Mises stress and contact area was assessed using model A-2. The results for maximum contact pressure, von Mises stress and contact area at varying cup inclination angles and anteversion angles are provided in Figure

4.2a and Figure 4.3a. The total contact area under varying cup inclination angle and anteversion angle are provided in Figure 4.2b and Figure 4.3b.

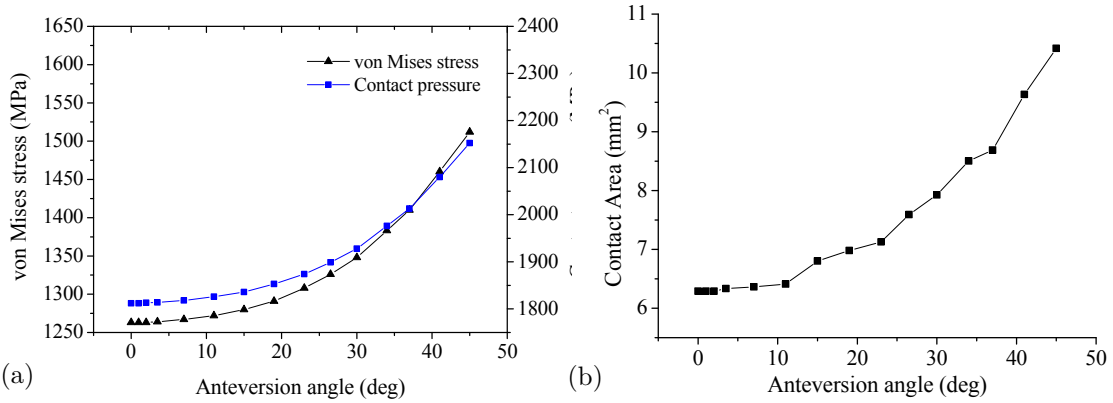

Figure 4.3. (a) Maximum contact pressure and von Mises stress (b) contact area under varying anteversion angle

The results so far have covered the modelling of microseparation which applied to model A-1 and model A-2 by lateral displacement, however as discussed previously within chapter 3 the microseparation kinematics of 'pure' microseparation was also modelled to understand the effects of such possible kinematic occurrences within the orthopaedic implanted hip joint. The laxity of the hip joint following the microseparation model was discussed in the methodology section. By running a dynamic explicit model and applying a vertical load of 3900N, relocation of the hip joint was observed. At a cup inclination angle of 45°, contact initially occurred at the rim of the acetabular cup. The maximum contact pressure observed was 341 MPa and no contact occurred below the rim of the acetabular cup i.e. on the rim radius (Figure 4.4). As expected the contact pressure was symmetrical about the centre of the contact and decreased from the centre of contact. As the distance from the top of the rim radius increased the contact pressure also reduced.

Under pure microseparation conditions, the contact pressure against cup inclination angle was assessed. When the cup inclination angle increased to 60° the maximum contact pressure increased to a 646 MPa. The contact stress distribution occurred at the top of the rim radius when the cup inclination angle was 45°.

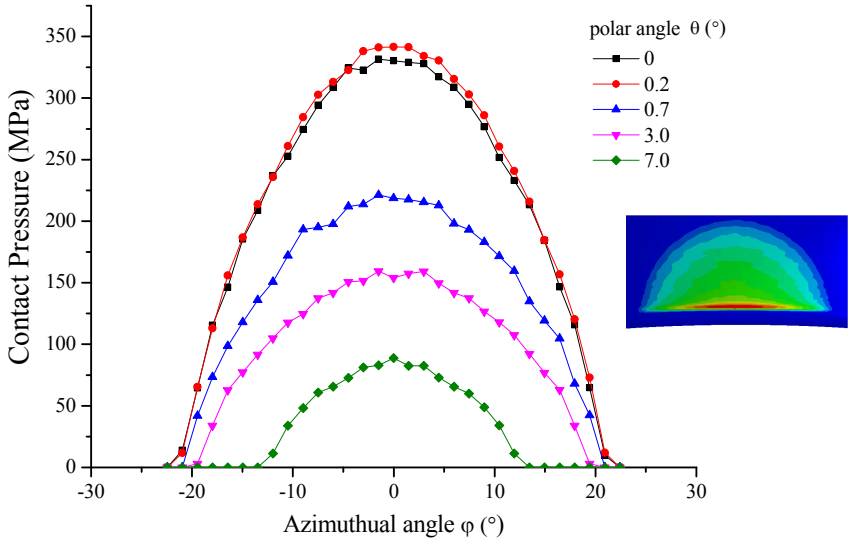

Figure 4.4. Edge loading contact pressure by 'pure' microseparation at a cup inclination angle of 45 ˚

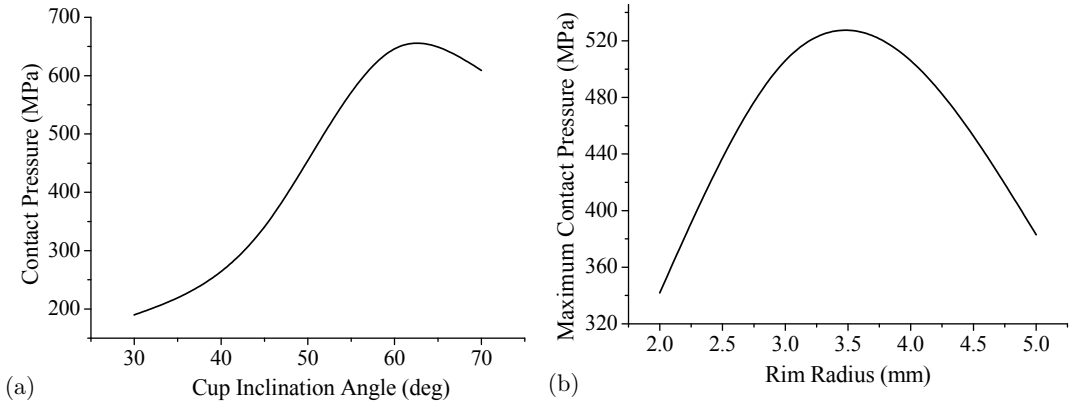

Figure 4.5. Maximum contact pressure against (a) cup inclination angle (b) different rim radius magnitudes

For a cup inclination angle of 30 ˚, the maximum contact pressure of 190 MPa occurred at θ_i = 17 ˚. When the cup inclination angle was modelled at 70 ˚, the maximum contact pressure observed was 609 MPa, occurring at the rim of the acetabular cup (Figure 4.5a). This was based on an acetabular cup with a rim radius of 2.0 mm. Although previous studies have attempted to predict the contact pressure at the rim of the acetabular cup using the finite element method, none of them have considered the contact pressure at varying cup radius caused by different kinematical situations leading to rim contact. The affect of cup radius magnitude were assessed under pure microseparation conditions and results are provided in Figure 4.5b.

4.2. Model B: Segmented Bone Hip Implant Models Results

Following on from the explanation of the methodology in chapter 3, the results for model B-1 and model B-2 i.e. the segmented bone hip implant models are presented within this section. As expected the contact pressure results between the femoral head and acetabular cups were the same, however, the contact surface and subsurface stresses varied between the bearing components. Under vertical loading F_I, without any microseparation or edge loading, the maximum contact pressure was 18 MPa. When the vertical load F_y was applied to the same model, the maximum contact pressure increased to 22 MPa. The contact pressure distribution was more unpredictable than the profile observed for model A-1 and A-2. The two-dimensional and three-dimensional contact pressure distribution is provided in Figure 4.6a and Figure 4.6b.

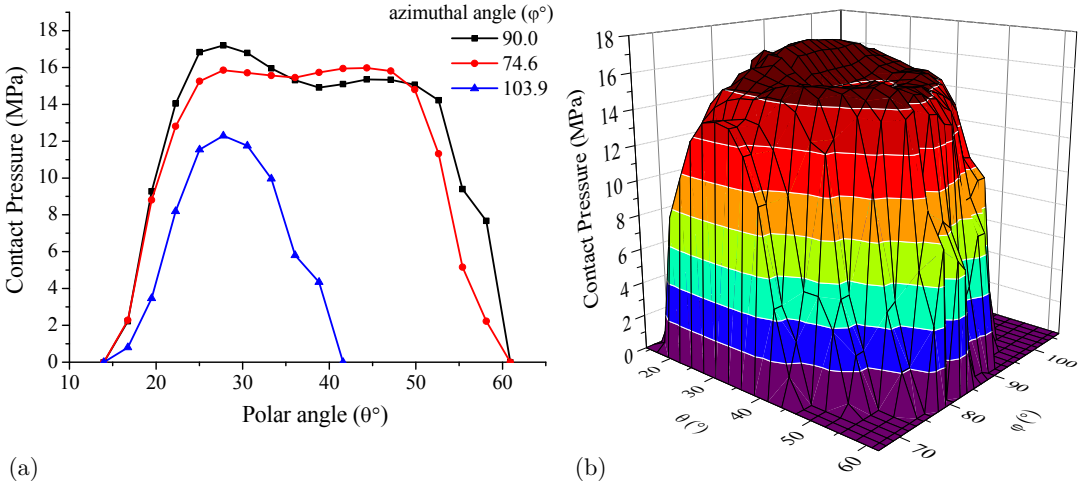

(a) (b)

Figure 4.6. (a) Contact pressure under vertical loading against the polar angle at different azimuthal angles (b) suface contact pressure distribution

Similarly, the two-dimensional contact pressure distribution for the acetabular cup rim under lateral displacement edge loading conditions is provided in Figure 4.7a, and the three-dimension plot is provided in Figure 4.7b. Following the assessment of normal and edge loading factors summarised in Appendix A – Normal and Edge Loading Factor, a selection process was carried out and a number of those factors were assessed for hip resurfacing implant bearings.

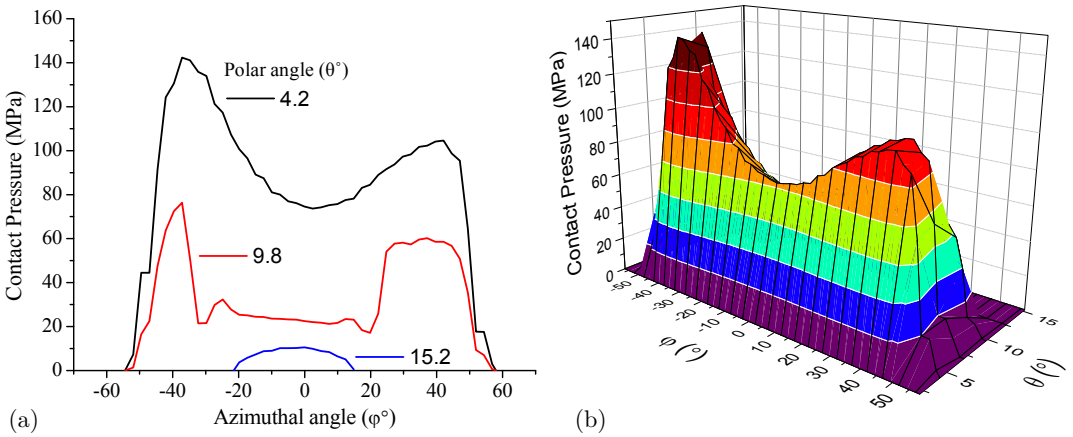

Figure 4.7. (a) Contact pressure under lateral displacement causing edge loading against the polar angle at different azimuthal angles (b) edge loaded contact pressure distribution

Assessments were conducted under flexion-extension cycles through the consideration of ISO gait loading. The maximum contact pressure under varying anteversion angle was plotted (Figure 4.8). As there was negligible difference of contact pressure under different anteversion angles, no further results were presented.

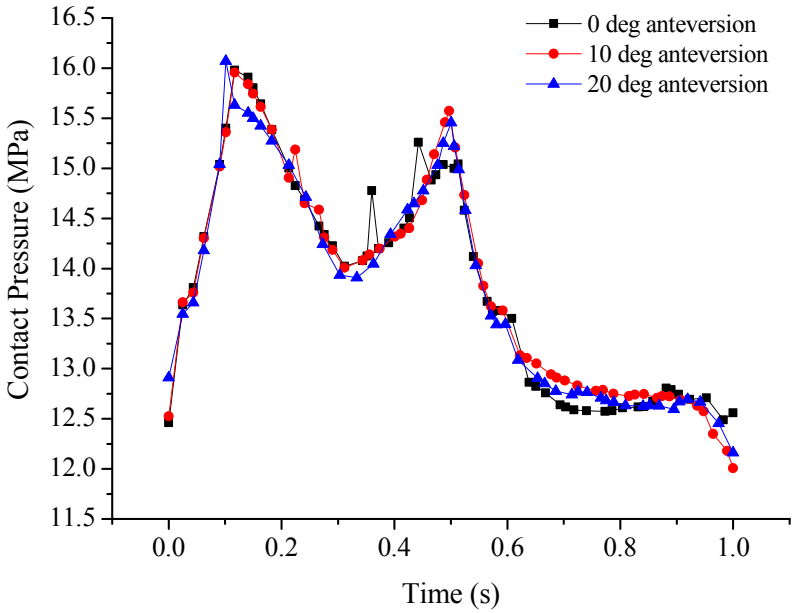

Figure 4.8. Maximum contact pressure against anteversion angle

An assessment was carried to assess the impact of surface coefficient on the contact pressures, stresses and shear stresses (Figure 4.9 to Figure 4.12). It is important to note that, these assessments did not consider any microseparation conditions or edge loading.

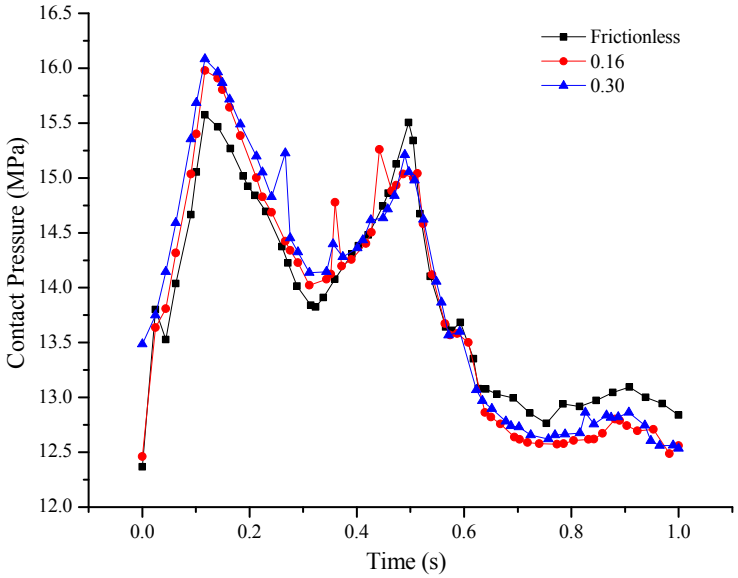

Figure 4.9. Maximum contact pressure against coefficient of friction

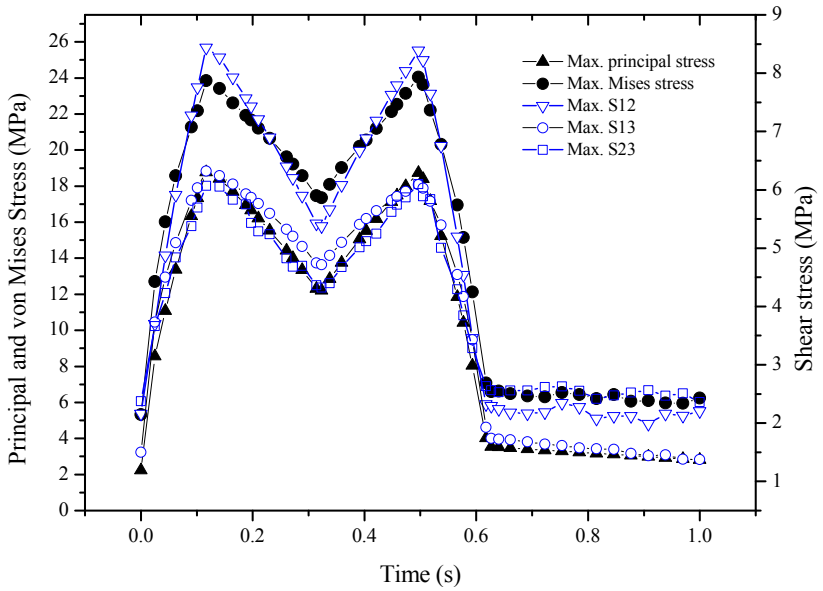

Figure 4.10. Acetabular cup maximum shear stress with frictionless contact

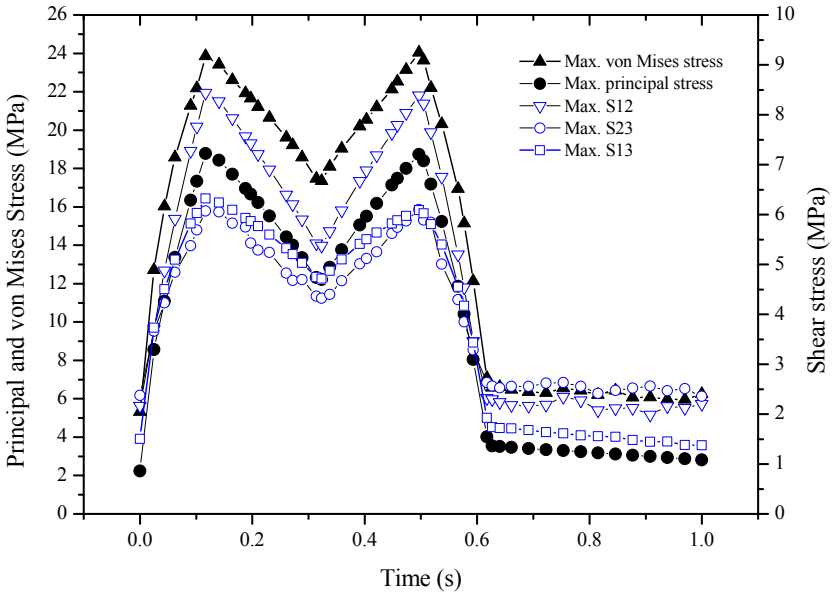

Figure 4.11. Acetabular cup maximum shear stress with surface coefficient of 0.16

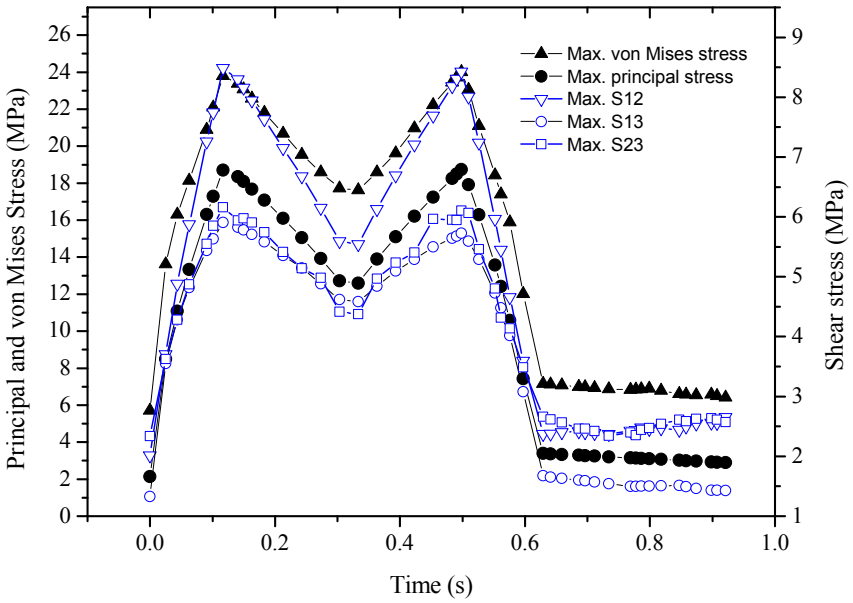

Figure 4.12. Acetabular cup maximum shear stress with surface coefficient of 0.30

The results presented in Figure 4.13 provide the maximum contact pressures when lateral displacements of 200 µm and 500 µm were applied.

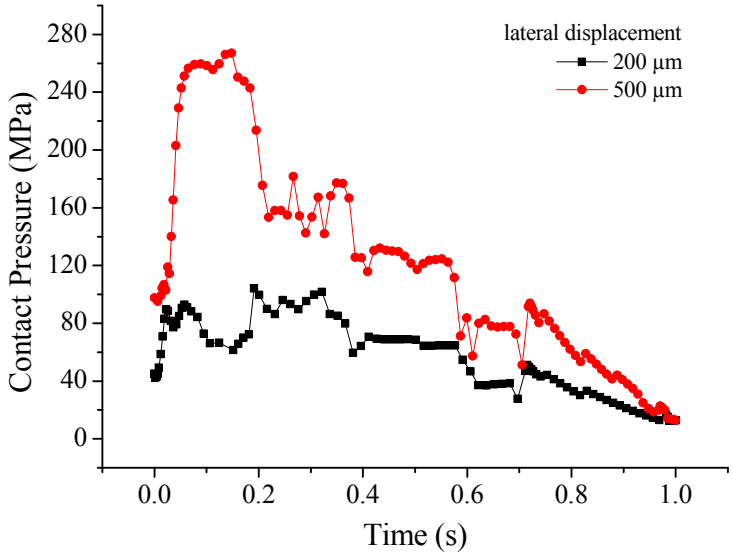

Figure 4.13. Maximum contact pressure against edge loading lateral displacement

Although the assumption was made that the lateral displacement of microseparation occurred during the swing phase load in line with current experimental simulator strategies which include microseparation, both ISO loading and constant peak loading were modelled separately using the same model for comparative purposes (Figure 4.14).

From $t = 0$ to $t = 1$ s, normal loading conditions were modelled, the ISO gait loading profile was observed during this time period and for the peak loading condition the load was ramped

linearly, to the maximum peak load at $t = 1$ s. The highlighted points N_I and N_p are the contact areas under ISO and peak loading conditions without microseparation. However M_I and M_p are the contact areas under ISO and peak loading conditions with microseparation. Normal contact conditions occurred between $t = 0$ to $t = 1.0$ s where no microseparation was applied. From $t = 1.0$ to $t = 2.0$ s lateral microseparation conditions were included within the time step, where full edge loading conditions occurred at $t = 2.0$ s.

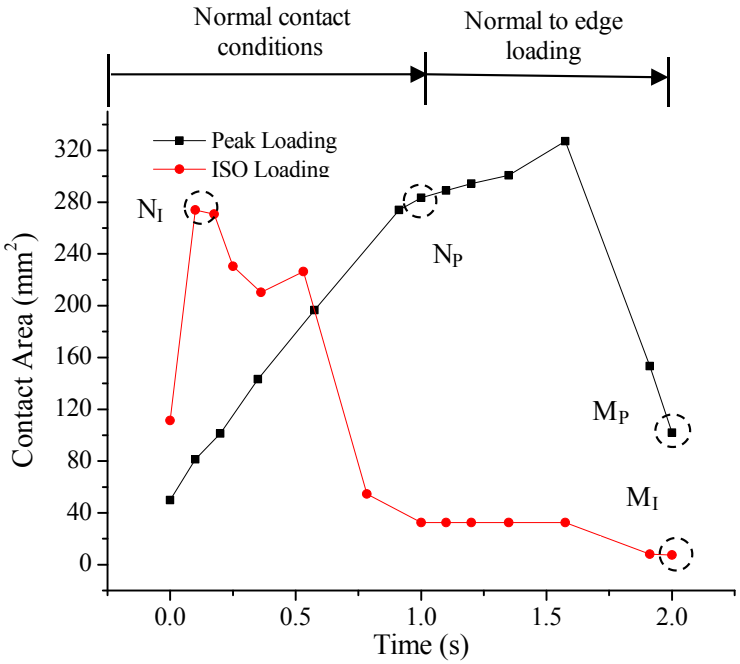

Figure 4.14. Total contact area between the femoral head and acetabular cup under normal and edge loading conditions

The ISO loading profile was observed by the variation of contact area over the analysis time step. A different contact area profile was obtained by applying a peak load in combination with the lateral sliding of the femoral head component. The non-zero contact area at the $t = 0$ was due to the initial contact established by displacement control.

The process described in Figure 3.14 from the beginning of the process through to completion was carried out using femur and pelvic bone models. The same specimen bone models were used, however larger values of L_{SF}, Pel_{h1} and Pel_{h2} were used, where $0.4Pel_L/2 \leq Pel_{h1}$, $Pel_{h1} \leq 0.5Pel_L/2$, $0.4Pel_L/2 \leq Pel_{h2}$, $Pel_{h2} \leq 0.5Pel_L/2$ and $0.17L_F \leq L_{SF} \leq 0.20L_F$. Under these model

conditions (defined as model B-2), the maximum contact pressure was 22 MPa under vertical loading of 3900 N, which very closely matched the maximum contact pressure of model B-1.

The hip implant flexion-extension model was developed and run through both the static implicit and dynamic implicit solvers. For the static implicit model the kinetic energy was zero, therefore all of the external work done would be converted into internal work. The energy dissipated through frictional effects, internal energy, work done and total energy are presented for the model when establishing contact through displacement control ($t = 0$ to $t = 1$ s), a load is then ramped from $t = 1$ s to $t = 2$ s (Figure 4.15). Before the 5th increment of the analysis, no contact had been established and the total energy was kept approximately constant (at zero). Regarding the strain rate effects of the material, these are insignificant based on the loading rates and material properties modelled in this study, therefore no further assessment on this was carried out. From the results, the artificial energies discussed in Chapter 3 – Methodology were zero, and therefore negligible compared with the dominate energies. In addition to this, during this quasi-static analysis, the value of kinetic energy remained within a small fraction of the value of strain energy throughout the analysis.

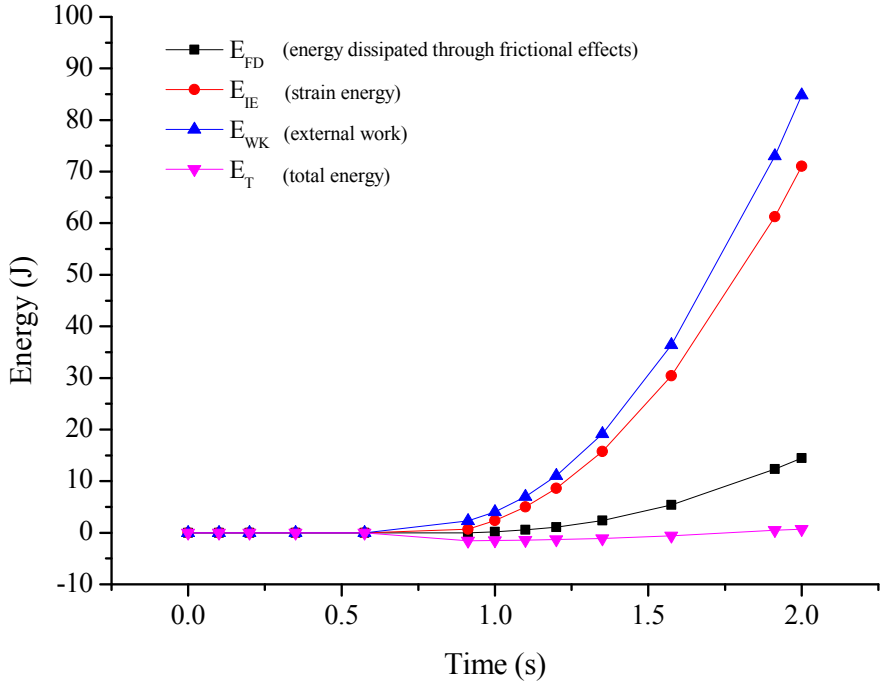

Figure 4.15. Energy during vertical loading hip implant contact analysis

The amount of analysis being conducted in this project was extensive; therefore the more efficient the analysis runs could be, the quicker results could be obtained. Model B-1 was used to compare the analysis run times with and without the use of the Intel® Hyper-threading (HT) technology activated through the BIOS (Basic Input/Output System). The analysis run time without HT (4 physical cores) was 4479s, while with HT (4 physical cores plus 4 hyperthreaded cores) the run time of the same input file took 4691s to complete. The notion of processor core effects on analysis run times led to the assessment of a model under different numbers of processing cores, and the results are provided in Figure 4.16.

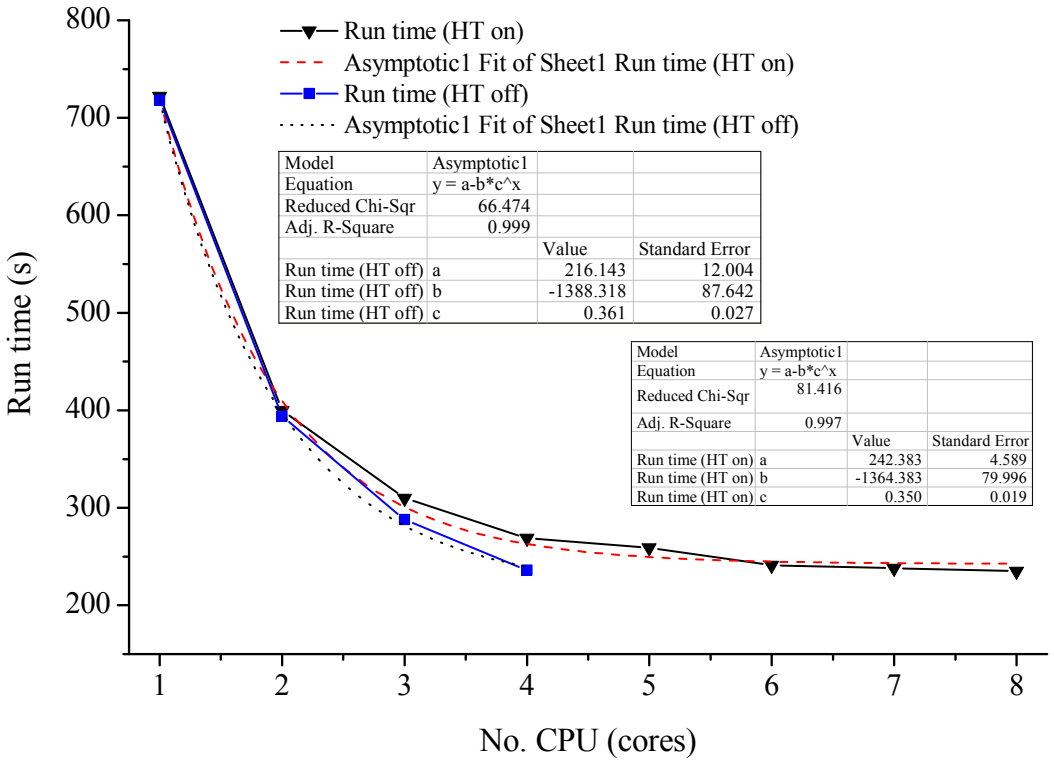

Figure 4.16. Effect of processor cores on analysis run completion times

The curve fitting for run times with HT on and off was successfully achieved with an exponential asymptotic decrease for both curves. The R-squared values for the curve fit of both HT on and off were 0.997 and 0.999 respectively. Of all curve fittings plots assessed, the exponential asymptotic equation and curve provided the best-fit and closest R-squared value (coefficient of determination) to 1, therefore this was chosen to fit the data. To extend the study of computational performance for this problem, further work was carried out. Analysis

run times in relation to the number of nodes, elements and degrees of freedom were established during validation of the finite element models, and the results are presented in section 4.5. Finite Element Model Validation.

4.2.1 Bone Material Modelling Results

Six material mapped femur models labelled as Fe1 to Fe6 were analysed (three of the models are shown in Figure 4.17). The assessment was carried out based on the Fe6 being the reference model which all other models are compared to. The maximum stresses and deflections were obtained and the results along with the number of nodes are provided in Table 4.1 and plotted (Figure 4.18).

Table 4.1. Assessment of hip bone model material properties

Ref.	**Max. von Mises stress (MPa)**	**Relative max. von Mises stress**	**Max. deflection (mm)**	**Relative max. deflection**	**No. of nodes**	**Relative no. of nodes**
Fe1	26.5	0.19	5.45	1.0	6714	0.05
Fe2	25.2	0.18	5.25	1.0	9806	0.08
Fe3	29.8	0.21	5.23	1.0	14797	0.12
Fe4	45.4	0.32	5.25	1.0	21563	0.17
Fe5	78.6	0.56	5.27	1.0	47744	0.38
Fe6	139.7	1.0	5.22	1.0	124954	1.0

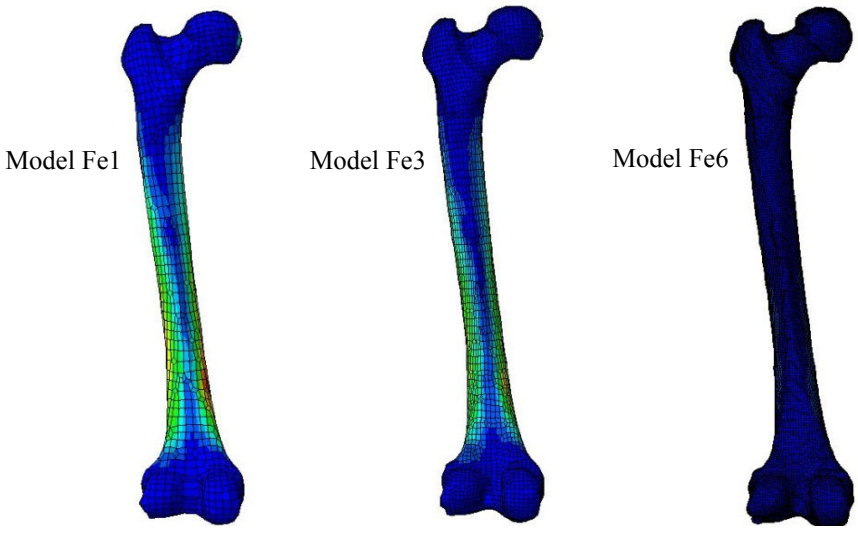

Figure 4.17. The varying mesh densities of mapped material bone models

Following on from this, an “equivalent” elastic modulus for each of the femur and pelvis models were obtained. Through a combination of interpolation and 'trial and error', the equivalent elastic modulus has been obtained for the femur E_{BF} and pelvis E_{BP} by assessing the

stiffness of the bone models. Based on this assessment and models used, the equivalent femur and pelvic bone elastic moduli were 12.3 GPa and 6.1 GPa, respectively.

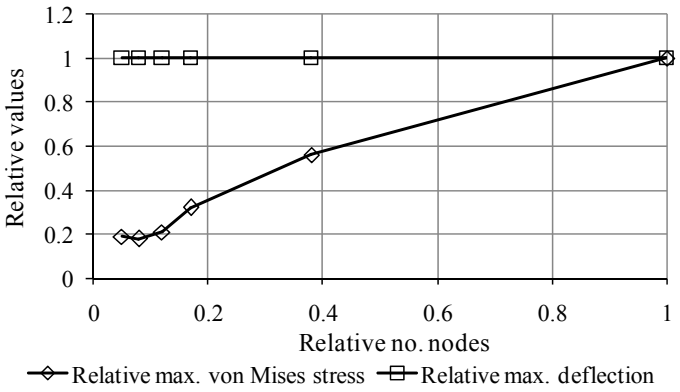

Figure 4.18. Relative maximum von Mises stress and deflection

The maximum contact pressure and stress against the femur and pelvic bone elastic modulus is provided in Figure 4.19. The difference between the contact pressure magnitude of the graphs provided in Figure 4.19 and Figure 4.20 was due to the two different segmented models being used. Although both sets of results were based on the same bone model data, loading conditions and implant devices, there were some differences between the models. Model B-1 had zero degree anteversion and model B-2 was developed with 15 ° of anteversion, also the bone segmentations dimensions differed.

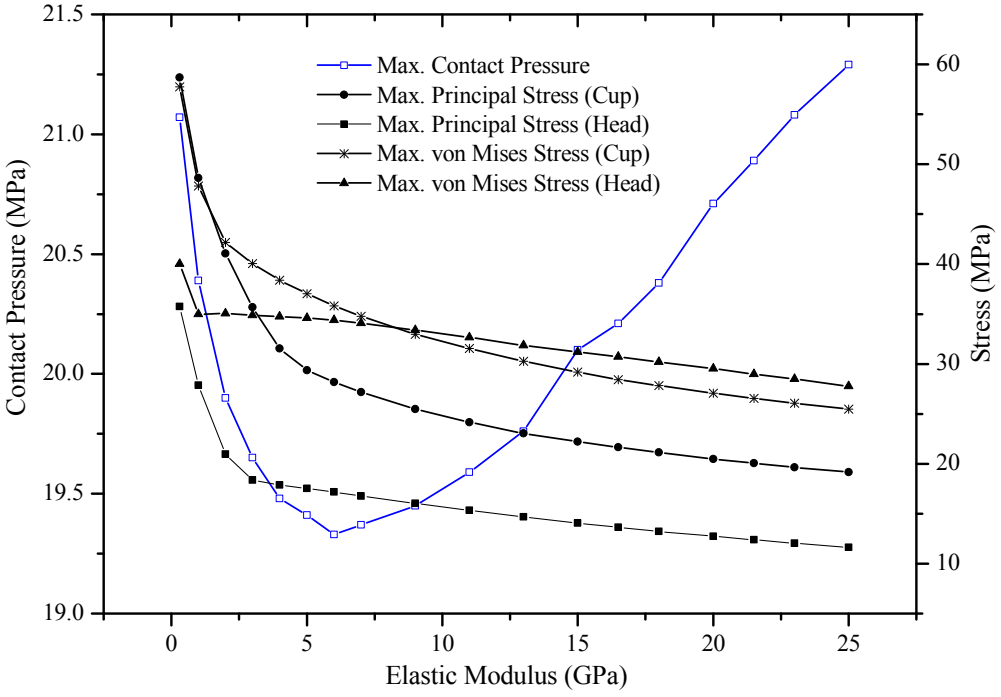

Figure 4.19. Variation of maximum contact pressure and stress against bone elastic modulus (Model B-1)

The contact pressure distribution for each of the models followed the same trend as presented and discussed within this results section, therefore detailed contact pressure and stress distribution plots were not required. By applying the orthotropic bone model described in chapter 3, an assessment was conducted to obtain the contact pressure and von Mises stress results based on the orthotropic bone material model defined by Couteau et al. [185]. Even when modelling these orthotropic material properties, the contact pressure remained the same as when equivalent isotropic bone modulus values were modelled. The contact pressure profile and maximum value was 18 MPa when orthotropic material properties were applied.

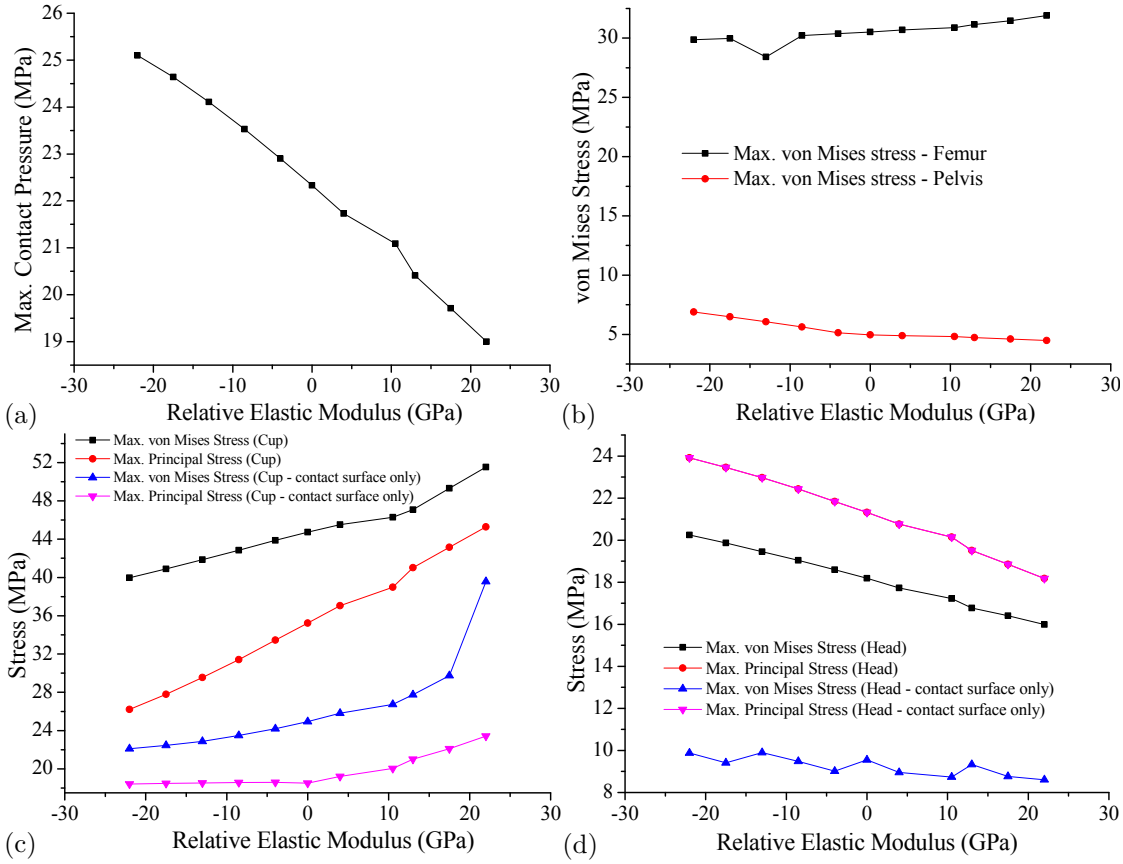

Figure 4.20. Relative bone elastic modulus against (a) contact pressure (b) max. von Mises stress of the femur and pelvic sections (c) max. von Mises stress and principal stress of acetabular cup (d) max. von Mises stress and principal stress of femoral head (Model B-2)

4.3. Model C: Full Hip and Pelvis Hip Implant Model

By applying both F_y (vertical load) and F_s (stumbling load) to the full hip and pelvic model assembly, the contact pressures between the bearing implant components were obtained.

When a 3900 N load was applied the maximum contact was 17 MPa, however when the stumbling load of 11000 N was applied, the maximum contact pressure was 19 MPa.

The maximum von Mises stress for the femur occurred approximately at the centre of the long axis of the bone on the medial side, which suggests a bending of the femur under vertical loading. The value of von Mises stress in this region was 12 MPa, and even less was observed for principal stresses. For the pelvic bone model, the von Mises and principal stresses did not exceed 1.5 MPa. When lateral sliding of the femur was applied to the lower extremity of the femur to simulate edge loading contact, no rim contact was observed.

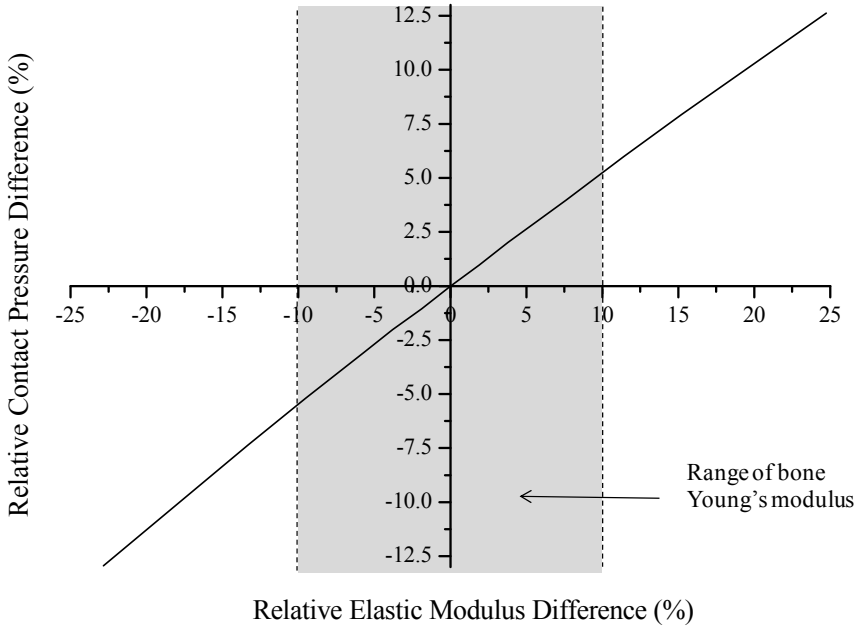

Figure 4.21. Relative elastic modulus diference against relative contact pressure difference with range of bone Young's modulus (Rho et al. [180])

Through the application of a greyscale material bone model assembly and comparing this to a homogeneous and isotropic material bone model assembly, the contact pressures between the femoral head and acetabular cup were within 0.25% when the bone model maximum displacement under an x, y, z vector load was within 0.5%. The relationship between relative elastic modulus as a percentage is provided in Figure 4.21. The range of young modulus obtained by using ultrasonic methods by Rho et al. [180] is highlighted in the plot. The energy results from the dynamic explicit analysis are provided in Figure 4.22a and Figure 4.22b.

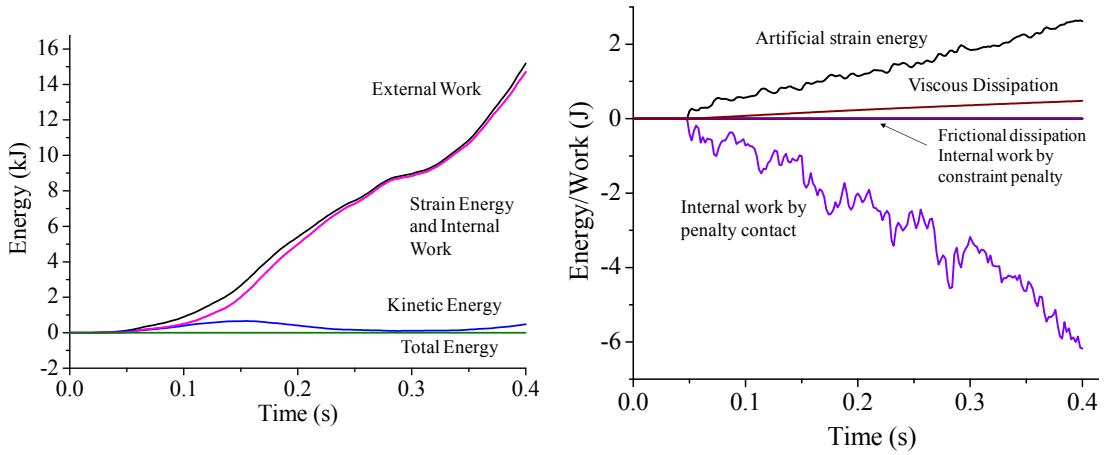

Figure 4.22. (a) External work, strain energy, kinetic energy and total energy (b) artificial energies, penalty and contact internal work

4.4. Model D: 2D Axisymmetric Hip Implant Models

As previously discussed, by developing two-dimensional axisymmetric models, the subsurface of the implant devices and backed material could be assessed efficiently in detail and accurately considering the computational hardware and software limitations. The results obtained using Model D-1, Model D-2a and Model D-2b are presented and discussed within this section.

4.4.1. Backing and Loading Conditions

The stress distribution of the femoral head, inlay and insert were assessed, with the maximum stress of 61 MPa being observed below the surface of the acetabular cup (Figure 4.23). In addition to this, the contact pressure was 101 MPa off the axis of symmetry. The analysis was based on a radial clearance of 0.04 mm, insert thickness of 4.96 mm, inlay thickness of 5 mm and maximum vertical loading of 2500 N. The results were compared to the research conducted by of Mak et al. [88, 89].

The method of load application was investigated to clarify the effects of applying the vertical force as a concentrated load or uniformly distributed pressure load (Figure 4.24). The assessment for the inclusion of an acetabular inlay cup was also conducted and the results are provided in Figure 4.25. From the investigations and research by Mak et al. [89], comparative models were developed. As well as comparing results to previous studies, further assessments

were carried out on the models with and without a stem and a cup inlay. The comparisons and results are summarised in Table 4.2.

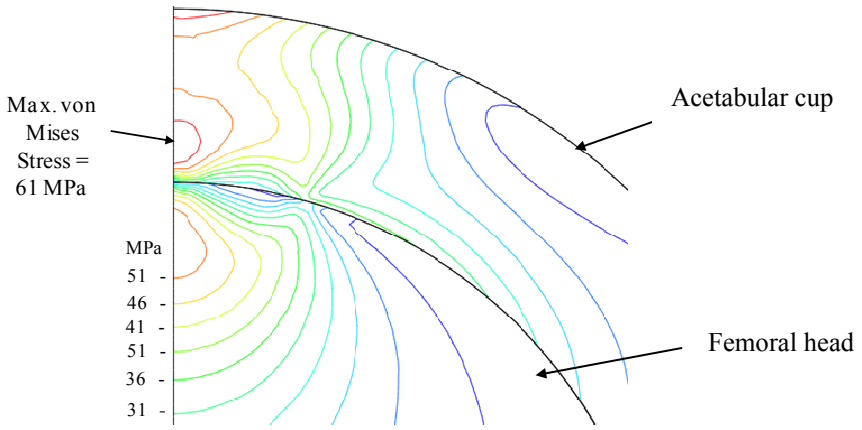

Figure 4.23. Hip joint bearing prosthesis contact analysis: von Mises stress under maximum load

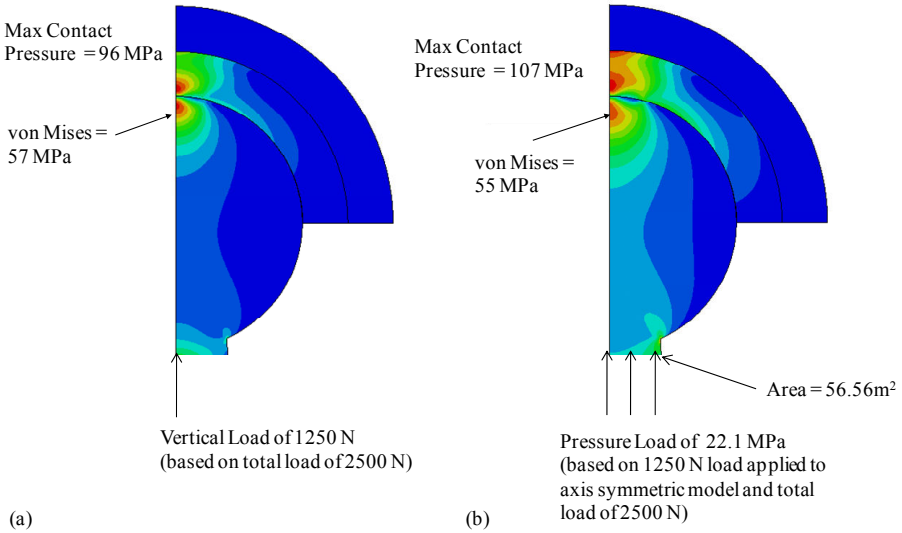

Figure 4.24. The von Mises stress, contact pressures and stress distributions by (a) applying concentrated load (b) applying uniformly distributed pressure load.

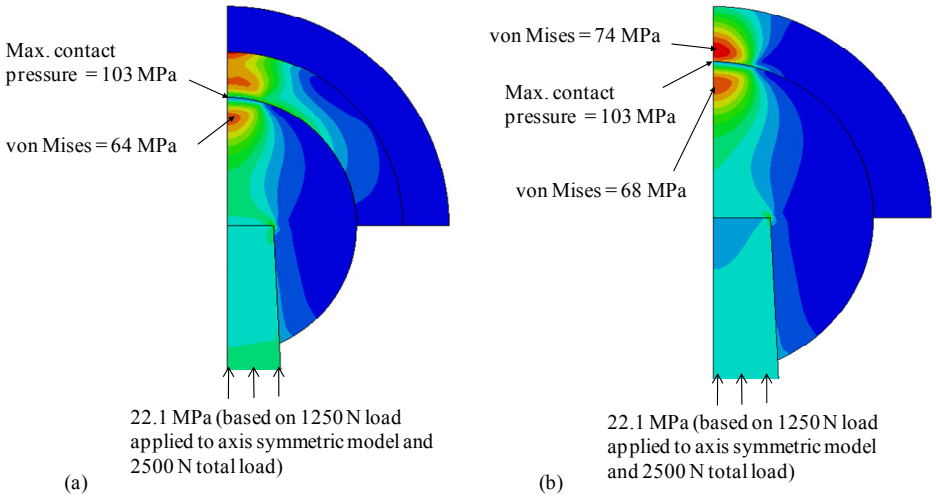

Figure 4.25. Hip bearing model with the inclusion of (a) stem with inlay backing (b) stem with no inlay backing

Table 4.2. Two dimensional axisymmetric hip bearing model results

Part	Model with stem?[a]	Model with inlay? [a]	Max. von Mises stress	Max. contact pressure
Head[b]	Y	Y	57.8 MPa	80 MPa
Head[b]	np	np	np	94.1 MPa
Head	N	Y	55 MPa	96 MPa
Head	Y	Y	56 MPa	83 MPa
Head	Y	N	68 MPa	103 MPa
Cup[b]	Y	Y	57.8 MPa	80 MPa
Cup	N	Y	57 MPa	96 MPa
Cup	Y	Y	56 MPa	83 MPa
Cup	Y	N	74 MPa	103 MPa
Inlay[b]	Y	Y	4.61 MPa	np
Inlay	Y	Y	1.6 MPa	3.6 MPa
Inlay	N	Y	0.86 MPa	1.8 MPa

[a] Y = yes, N = no, np = (result not provided)

[b] Results published by Mak et al. [88, 89]

4.4.2. Hip Joint Resurfacing Device

The hip resurfacing model (model D-2) was extremely useful for providing a model for assessing the surface and subsurface stresses, as well as for assessing the component under cyclic loading and conducting a shakedown assessment. Firstly, by comparing model D-2b with the alternative femoral head design (D-2a) the difference in contact pressure was negligible under vertical loading conditions; the difference between the maximum contact pressures was less than 2%. Using these computationally efficient models meant that direct comparisons of different vertical loading magnitudes could be carried out and the results analysed. By conducting the 2D axisymmetric cyclic analysis using model D-2b, the stress-strain relationship (Figure 4.26a) was predicted to remain within the elastic region under normal loading conditions. The loading curve shows the first 6 loading cycles.

The subsurface von Mises stress as well as the directions of the stress vectors for the maximum principal stresses can be observed on the subsurface of both the acetabular cup and femoral head components (Figure 4.26b) under F_I (ISO), F_y (normal) and F_s (stumbling) vertical loading conditions. The locations of maximum von Mises stresses are highlighted which occurred below the surface of contact in all but one of the cases. It was only when a stumbling

load F_s was applied that the maximum von Mises stress occurred at the base of the head component. The maximum values of von Mises stress, shear stress and x, y principal stress are provided in Table 4.3. A cyclic analysis has been completed and the maximum contact pressure plotted against cycle time for an isotropic elastic-plastic material model for the application of 3900N and 11000N vertical loading Figure 4.27. An arbitrary loading frequency of 10Hz was used during the cyclic analysis. The contact pressure results to compare the cortical and cancellous sectioned model (model D-2c) to the equivalent bone sectioned model (model D-2b) were obtained. There was a 10% difference in contact pressure between the two models.

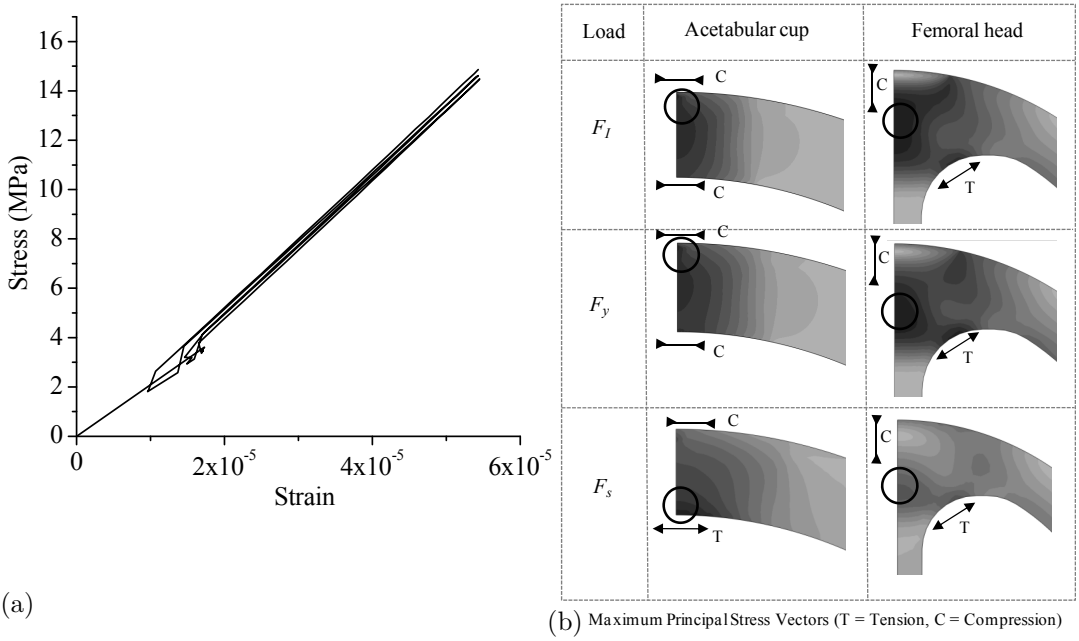

Figure 4.26. 2D-axisymmetric (model D-2) (a) cyclic stress-strain curve during normal loading (b) von Mises stress distributions under vertical load

Table 4.3. Stresses under vertical loads (model D-2b)

Load	Max. von Mises stress (σ) MPa	Max. shear stress (τ_{xy}) MPa	Principal Stress (σ_x) MPa	Principal Stress (σ_y) MPa
		Acetabular Cup		
F_1	34	3.4	-19.8	-49.6
F_y	45	4.6	-25.5	-64.5
F_s	125	14.5	-69.6	-139.9
		Femoral Head		
F_1	15	7.2	-37.1	-32.1
F_y	21	9.5	-49.7	-39.8
F_s	66 (107)[a]	27.4	-135.2	-160.1

[a]107 MPa predicted at the base of the femoral head stem

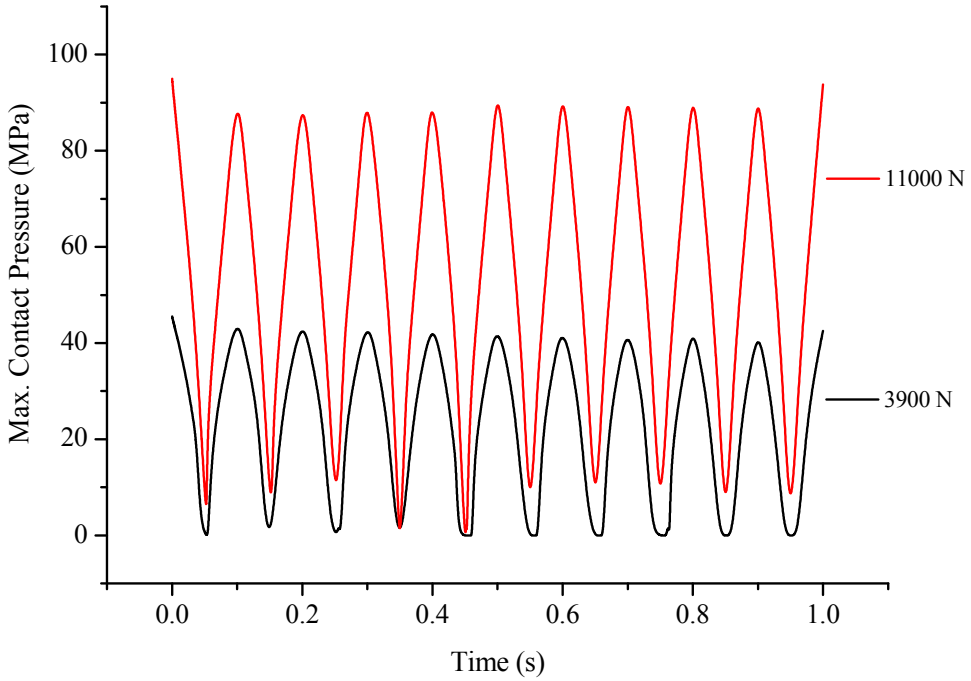

Figure 4.27. Cyclic analysis of 3900N and 11000N vertical loading with isotropic and elastic-plastic material model (10 cycles)

4.5. Finite Element Model Validation

A combination of finite element model validation, comparisons with literature and theoretical models were carried out where time and computing power permitted.

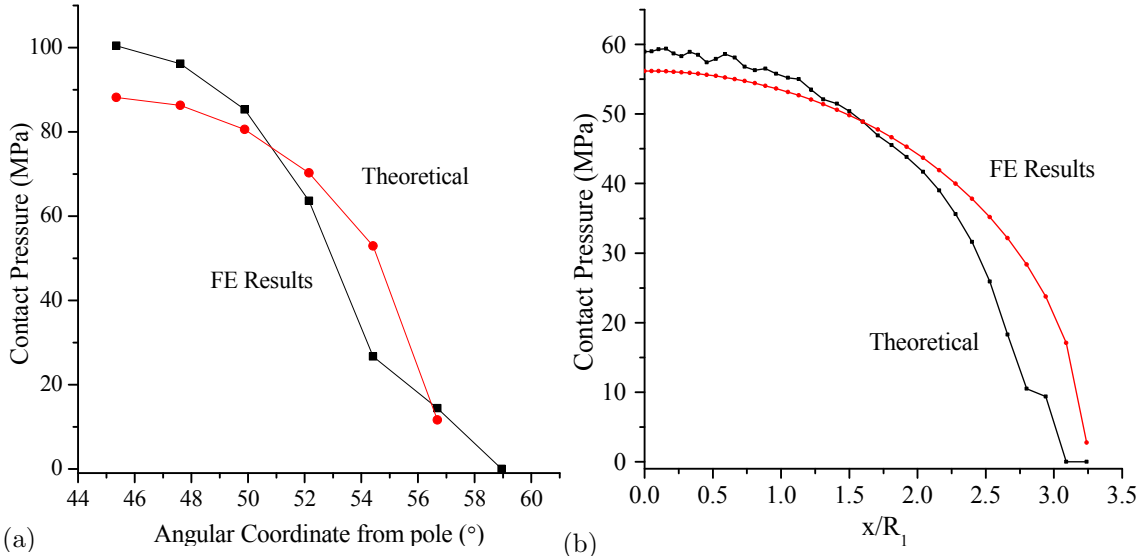

Figure 4.28. Comparison between adapted Hertzian and FE contact pressure (a) normal loading with cup inclination angle (b) normal loading with no inclination angle

The contact pressure distribution between the adapted Hertz contact model for a ball-in-socket joint and finite element models are shown in Figure 4.28. Both hip resurfacing model B-

1 (Figure 4.28a) and basic ball-in-socket joint model A-1 (Figure 4.28b) were compared to theoretical contact pressures under vertical loading conditions (2.12) as defined and discussed in chapter 2.

4.5.1. Model E: Comparative Model Results

By using the models discussed within chapter 3, the contact pressures and von Mises stresses are presented. For model E-1, under centred contact conditions the maximum von Mises and contact pressures were 30 MPa and 41 MPa respectively. Under edge loading conditions the maximum von Mises and contact pressures were 137 MPa and 307 MPa respectively. Three-dimensional plots of the contact pressure distribution for model E-1 under centred and edge loading conditions is provided in Figure 4.29 and Figure 4.30.

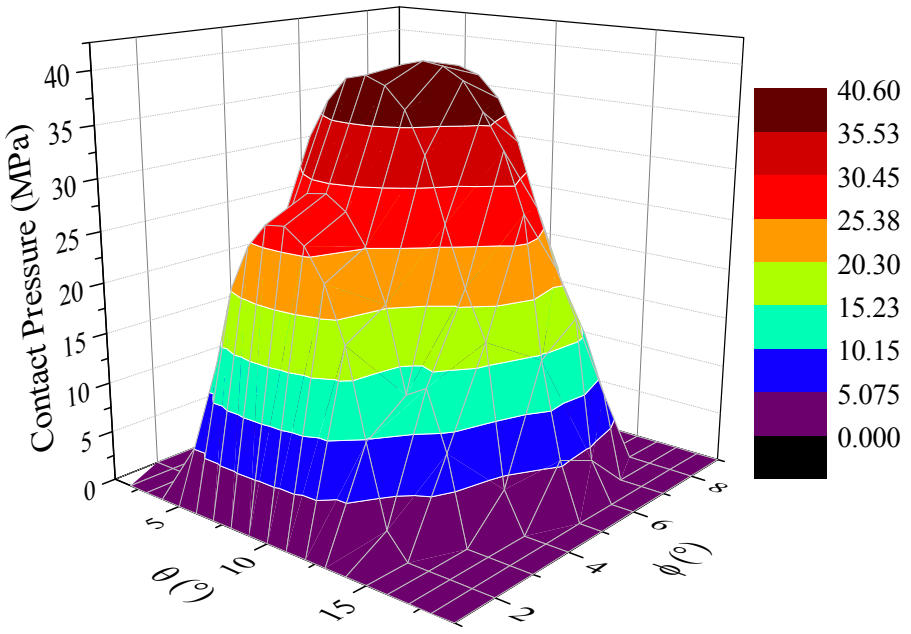

Figure 4.29. Contact pressure distribution under centred contact conditions (model E-1)

The same process and methodology was used to obtain contact pressure results under edge loading conditions for model E-2 (Figure 4.31). Under edge loading conditions the maximum von Mises and contact pressures were 256 MPa and 417 MPa respectively. The results have been summarised and compared directly to the results presented by Mak et al. [67] (Table 4.4).

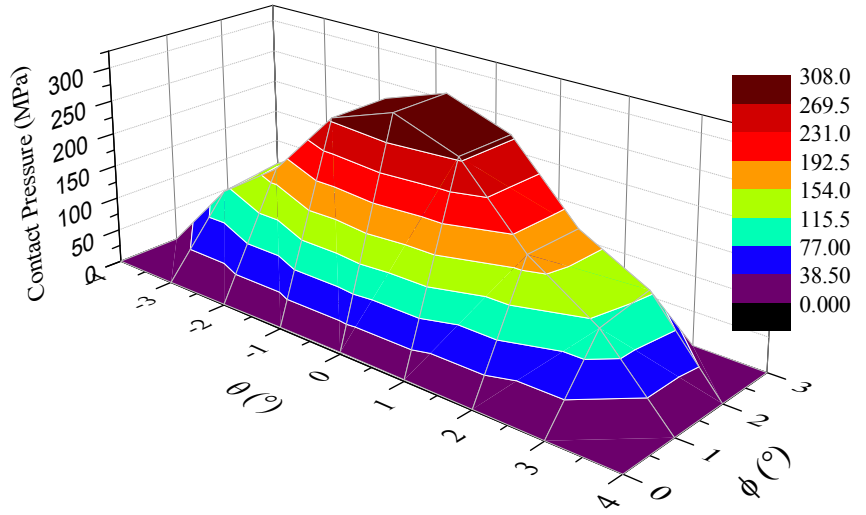

Figure 4.30. Contact pressure distribution under edge loading conditions (model E-1)

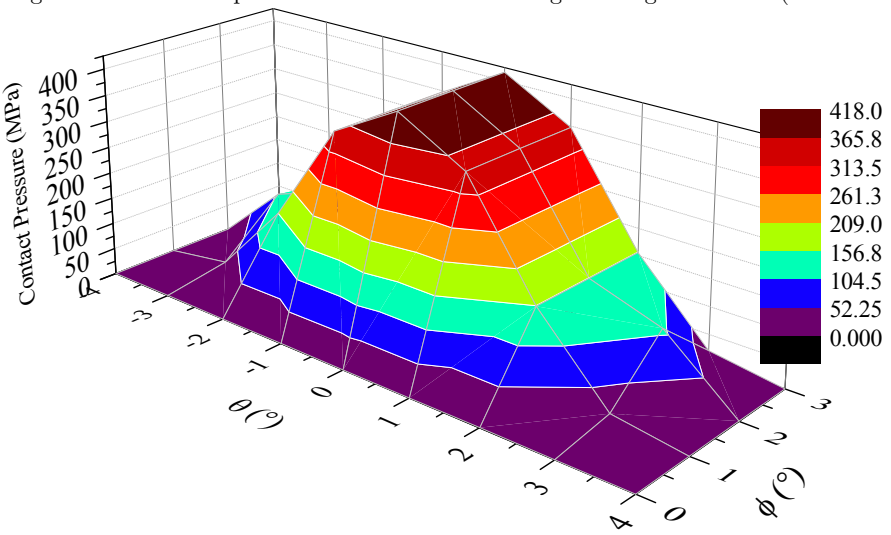

Figure 4.31. Contact pressure distribution under edge loading conditions (model E-2)

Table 4.4. Results comparison with Mak et al.

Parameters	Model E-1	Model E-2	Mak et al. (2010)
	Centred Contact		
Max. von Mises stress (MPa)	30	47	Not specified
Max. contact pressure (MPa)	41	61	81.6
	Edge Loading		
Max. von Mises (MPa)	183	256	646
Max. contact pressure (MPa)	307	417	437

4.5.2. Normal and Edge Loading Mesh Convergence

All convergence studies were based on the hip bearing contact models discussed so far, initially no edge loading was considered. By increasing the number of finite element nodal points (i.e. increasing the nodal seeding) equally on both hip implant bearing components, the mesh density was increased for each analysis run. The modelling details for the convergence study under normal loading conditions, including the analysis run completion times are provided in

Table 4.5. The convergence of the von Mises stress (Figure 4.32a) and contact pressures (Figure 4.32b) are plotted as well as the analysis run times provided (Table 4.6). Obtaining convergence is relatively effortless for centred contact conditions under a vertical load. However more computational effort was required for completion of convergence studies under edge loading conditions (Table 4.7).

Table 4.5. Convergence study without edge loading (vertical load of 3900 N)

Run	Seed	No. of elements in edge contact zone - Cup	No. of elements in edge contact zone - Head	No. of Nodes		No. of Elements		Total number of Nodes	Total Elements
				Cup	Head	Cup	Head		
1	4	6	4	1250	927	720	584	2177	1304
2	3	7	6	2947	1803	2048	1280	4750	3328
3	2	8	8	7395	5636	5544	4224	13031	9768
4	1	18	16	49398	39507	42336	33782	88905	76118
5	0.75	21	20	103943	93848	92064	83720	197791	175784

Unlike the seeding strategy used for the convergence analysis under normal loading conditions, the mesh density for the edge loading convergence study was completed by increasing the number of elements across the circumference of the acetabular cup and femoral head component in the edge loaded zone, as well as using biased based seeding.

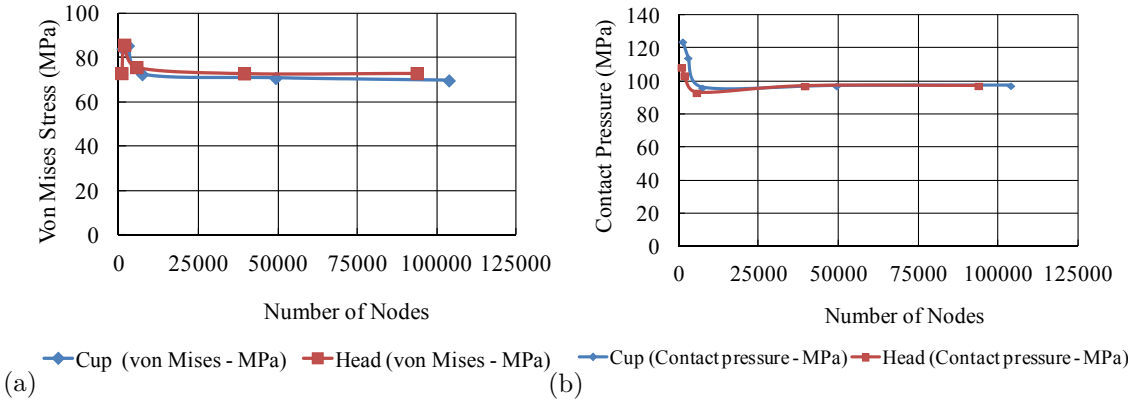

Figure 4.32. Convergence plot for cup and head (a) von Mises stress (b) contact pressure

The convergence of the von Mises stress (Figure 4.33a) and contact pressures (Figure 4.33b) were plotted against the number of elements in the edge loading zone. This was due to the nodal point definitions of edge seeding method used on the rim of acetabular cup rather than simple part seeding for the normal loading convergence study presented above. The zone

specific edge node seeding was defined to increase the number of elements within the edge loading zone. This was completed whilst keeping within the maximum allowable degrees of freedom defined by the stiffness matrix size limitations due to the amount of computer memory available for the analysis.

Table 4.6. Number of nodes and analysis run times

Total number of nodes	Analysis run time (s)
2177	55
4750	145
13031	373
88905	3879
197791	32613

Table 4.7. Convergence study including edge loading (vertical load of 3900 N)

Run	No. of elements in edge contact zone (approx) - Cup	No. of elements in edge contact zone (approx) - Head	Run time (s)	Total Nodes	Total Elements
1	**30**	**18**	12462	102475	94143
2	**100**	**22**	38641	183626	170600
3	**60**	**40**	20281	156728	145937
4	**100**	**60**	49790	238269	222536

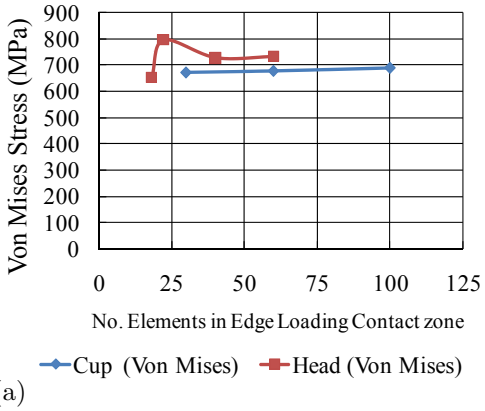

(a)

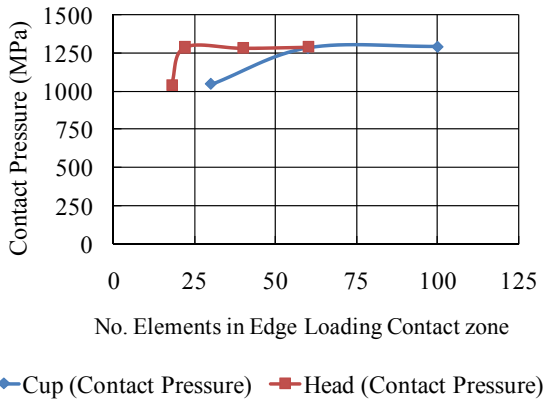

(b)

Figure 4.33. Convergence plot for cup and head (including edge loading) (a) von Mises stress (b) contact pressure

Throughout the engineering study and literature review, it was not uncommon to develop rigid on deformable body contact models to assess the contact between bearing components. This methodology was used to obtain contact results as a further convergence model was developed using a rigid body on deformable body to investigate the accuracy of contact stresses within the edge loaded region of the acetabular cup. The results are provided in Figure 4.34.

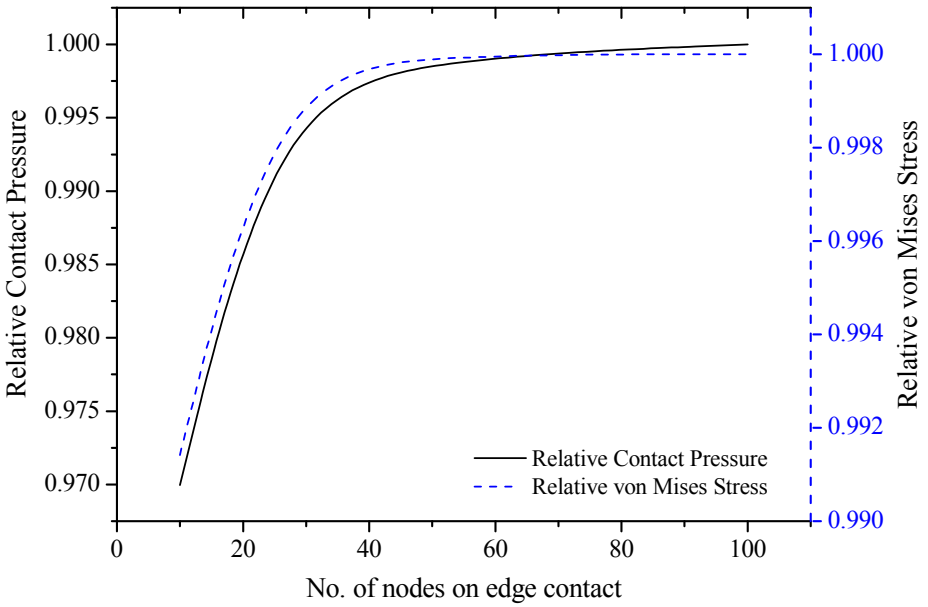

Figure 4.34. Rigid body on deformable cup edge contact mesh convergence study with contact pressure and von Mises stress against no. of nodes across the circumference of the edge contact zone.

4.6. Wear Modelling Results

The results for the wear models discussed within chapter 3 will be presented within this section. Firstly the block-on-block model technique using the user defined subroutines (section 3.3.1. Metal-on-Metal Contact Model) are discussed followed by the wear simulation results obtained using the Python scripting method (section 3.3.2. Scripting Interface Wear Model).

4.6.1. Simple Block Wear Model Results

The simulation for the block wear model was carried out for 15 million cycles (mc). To ensure results were numerically accurate, a node was chosen arbitrarily and the results were assessed in detail. According to tribological experimental simulator testing results discussed within the literature review a simple comparison of volumetric wear rates were made.

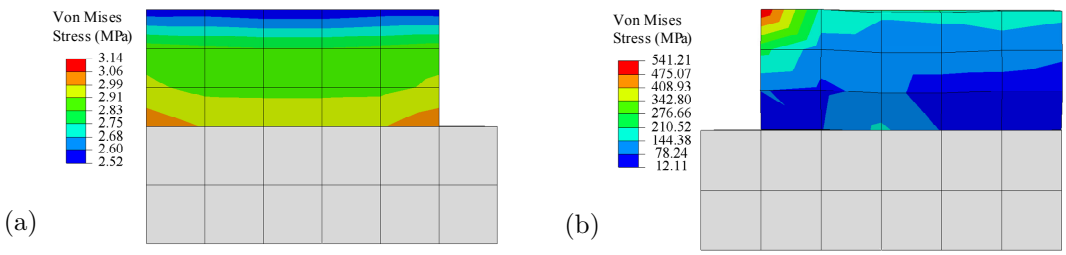

Figure 4.35. Stress distribution of sliding block (a) before wear (b) after 15 million cycles of sliding (with abalation of mesh within contact zone)

From the literature review, the volumetric wear per cycle could be as small as 4.2×10^{-6} mm^3, and therefore 2.1 mm^3 volumetric material loss over the first half a million cycles (assuming a linear relationship between the number of cycles and volumetric wear). For the simple block model, a load of 0.3 N was sufficiently large to establish and maintain contact between the two surfaces, however small enough to avoid excessive element distortions and convergence problems. Using the method discussed within chapter 3, the total volumetric material loss was 1.6×10^{-6} mm^3 per cycle (Figure 4.35).

4.6.2. Hip Implant Device Rigid Backed Wear Model

The logical progression from the block-on-block model was the application of the wear simulation technique to the rigid backed hip implant model (model A-1), as discussed in chapter 3.

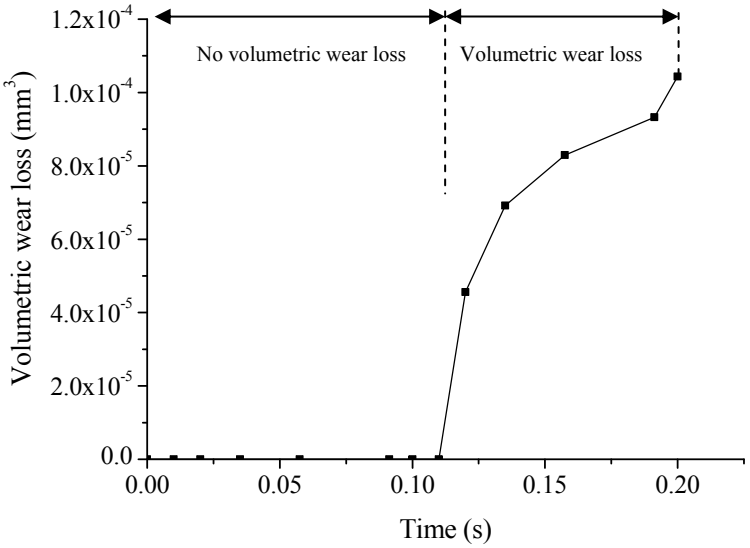

Figure 4.36. Volumetric wear loss of acetabular cup over 250,000 cycles

Using the coding developed for plotting linear wear as a field output within the analysis post processor, the surface linear wear was obtained for the first 250,000 cycles. The volumetric wear loss of material over the 250,000 cycles was incrementally shown at the end of each analysis increment. For the first 250,000 cycles, the total volumetric wear was observed as 1.0×10^{-4} mm^3 (Figure 4.36).

4.6.3. Python Scripting Wear Modelling

The next step on conducting wear simulations were based on using the Python scripting methodology discussed in chapter 3. The mechanical wear prediction for the volumetric material loss due to mechanical wear under flexion-extension and internal-external rotation and ISO gait loading conditions were recorded for both the acetabular cup and femoral head simultaneously, which had not been obtained from the same analysis in previous studies. By determining the contact sliding distance directly from the output database (CSLIP), based on a wear coefficient of 4.2×10^{-9} mm^3/Nm the wear was 82 mm^3/mc (million cycles) for the femoral head and 109 mm^3/mc for the acetabular cup. When a lower long term wear coefficient value was applied to the wear model obtained from the literature (1.0×10^{-10} mm^3/Nm), the volumetric wear rates were reduced to 1.5 mm^3/mc for the femoral head and 2.6 mm^3/mc for the acetabular cup. A comparison between using CSLIP and calculating the sliding distance from the coordinates (COORD) was carried out; the difference between using each method for the same segmented hip resurfacing model under angular displacement for one million cycles was 3.5%.

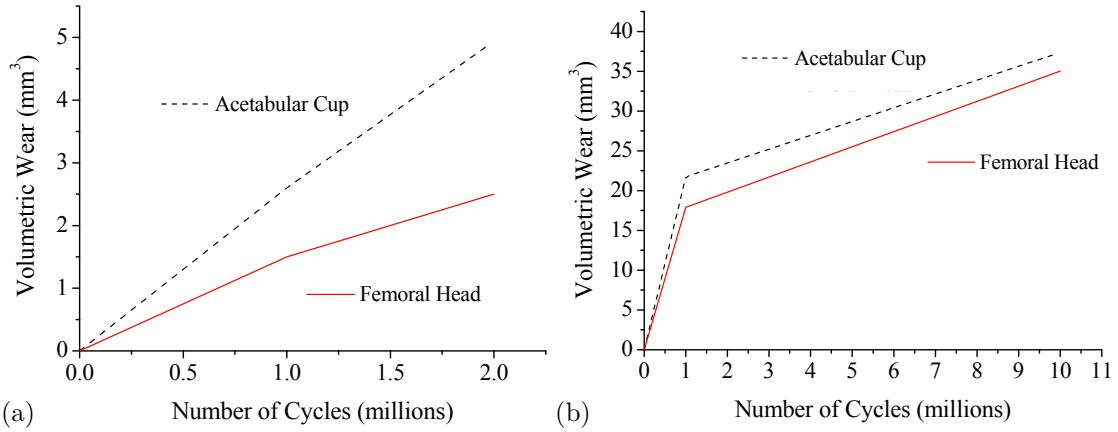

Figure 4.37. Femoral head and acetabular cup volumetric wear (a) over 2 million cycles (b) over 10 million cycles including variation of wear coefficient

By using the long term wear coefficient defined within the literature the volumetric wear was simulated for 2 million cycles for both the acetabular cup and femoral head and the results plotted in Figure 4.37a. For this analysis the wear coefficient was kept constant, however when a long term wear simulation of 10 million cycles was carried out after 1 million cycles the

wear coefficient value was changed to reflect long term wear (Figure 4.37b). The volumetric wear loss of the femoral head against wear coefficient value was obtained (Figure 4.38), where each value was recorded after 1 million cycles.

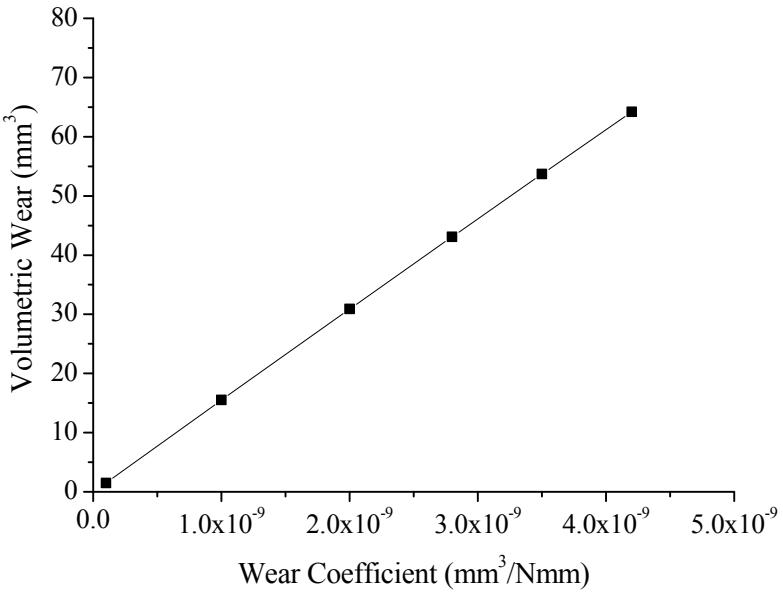

Figure 4.38. Volumetric wear loss of the femoral head at different wear coefficient values

4.7. Asperity Contact Results

The results for the circular (Figure 4.39a) and needle (Figure 4.39b) asperity under compression without any sliding contact is provided. The differences in von Mises stress magnitude and distribution are shown by the results plotted below. To ensure convergence was obtained for the needle like asperity a small radius was required to avoid excessive element distortion and discontinuities.

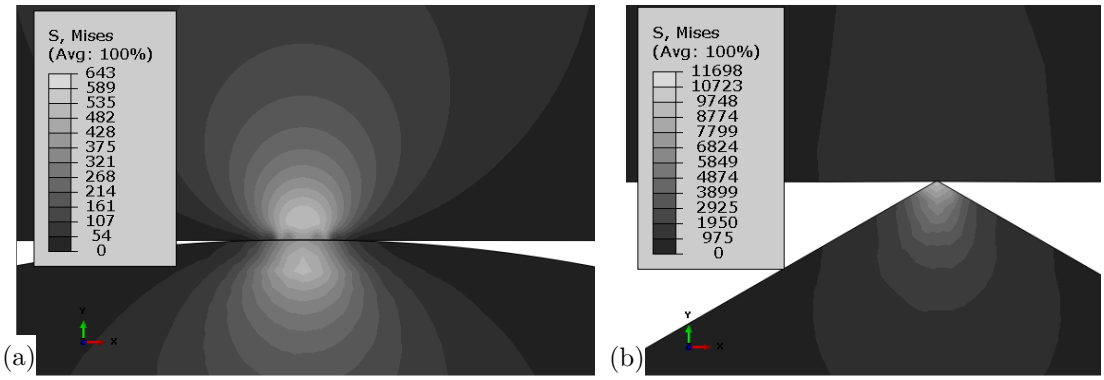

Figure 4.39. von Mises stress (a) circular asperity before sliding (b) needle asperity before sliding

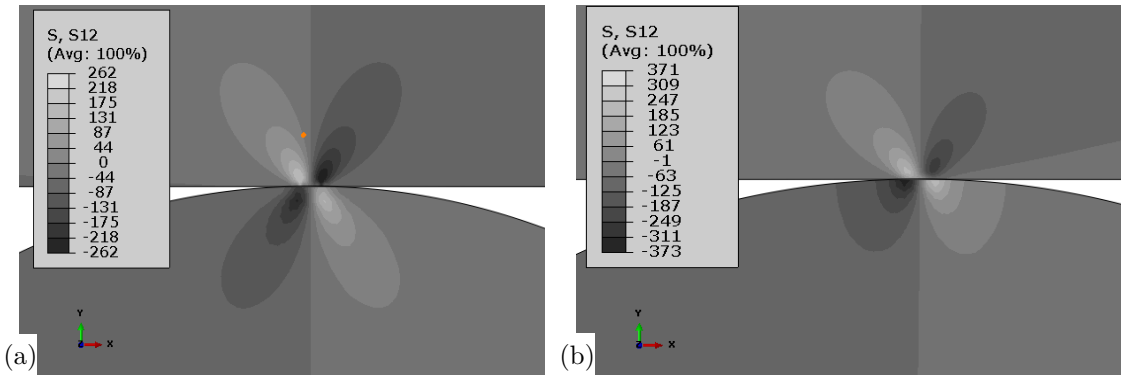

Figure 4.40. Shear stress of circular asperity (a) before 20 µm of sliding contact (b) after 20 µm of sliding contact

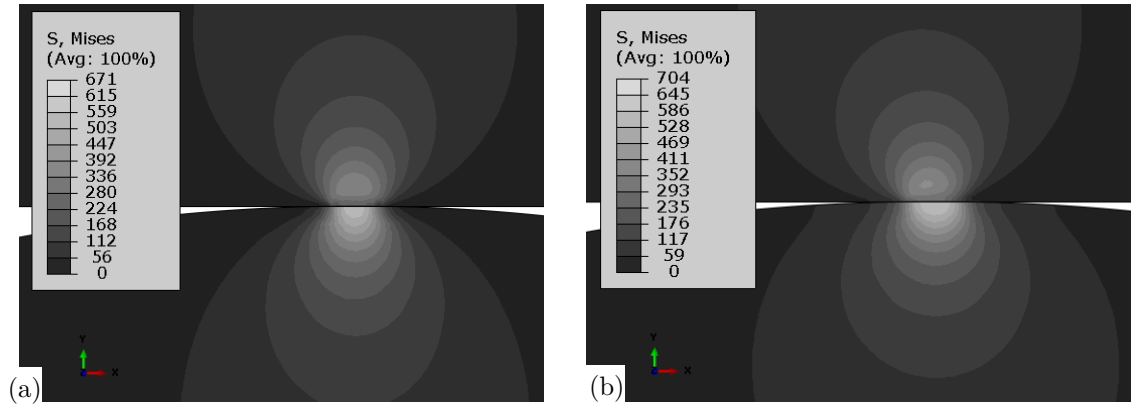

Figure 4.41. Oval asperity von Mises stress (a) before 20 µm of sliding contact (b) after 20 µm of sliding contact

The shear stress under compression loading for the circular asperity is shown in Figure 4.40a, and the shear stresses were observed to increase dramatically after 20 µm sliding contact (Figure 4.40b). The shear stress distribution becomes asymmetrical about the centre of contact following sliding contact. When an oval asperity was modelled (Figure 4.41a) the von Mises stress was shown to increase over that observed for the circular asperity. The stress increased further after contact sliding was applied to the model as well as a change in the stress distribution. When linear elastic cortical bone material properties were applied to the circular debris model the maximum von Mises stress of 110 MPa on the CoCrMo material section occurred at a depth of $0.003 \times h_a$, where h_a is the CoCrMo section height.

4.8. Theoretical Models and Lubrication Theory Application

From the maximum contact pressure results obtained using the finite element method and theoretical models of the contact pressure distribution, theoretical contact pressure

distribution plots were provided for both normal and edge loading contact. By obtaining the maximum contact pressure and contact radius from the finite element analysis results, the theoretical contact pressure distribution under normal conditions were plotted (Figure 4.42a). The result below was based on observing a maximum contact pressure $P_{o,n}$ and corresponding contact radius a_n under normal loading conditions. From the contact pressure under normal loading conditions,

$$P_N = \left(1 - \frac{r_n^{\,2}}{a_n^{\,2}}\right)^{n_n} \cdot P_{o,n} \tag{4.1}$$

and assuming Hertz contact for both normal and edge loading contact i.e. the constants $n_n = n_e = ½$, then the pressure distribution was obtained as the distance from the centre of contact, r_n varied. The advantage of using this technique is the reduction in time taken to assess the contact pressure at specific locations compared with the time taken to intricately analyse data within the contact area using finite element model results. For theoretical contact pressure distribution plot (Figure 4.42b) within the edge loaded region, P_E,

$$P_E = \left(1 - \left(\frac{x_e}{a_e}\right)^2 - \left(\frac{y_e}{b_e}\right)^2\right)^{n_e} \cdot P_{o,e} \tag{4.2}$$

the maximum contact pressure $P_{o,e}$ and elliptical contact dimensions a_e and b_e were obtained from finite element studies, where the values of x_e and y_e are defined as $-a_e \leq x_e \leq a_e$ and $-b_e \leq y_e \leq b_e$. All the plots shown in Figure 4.42 are produced using matplotlib in IPython.

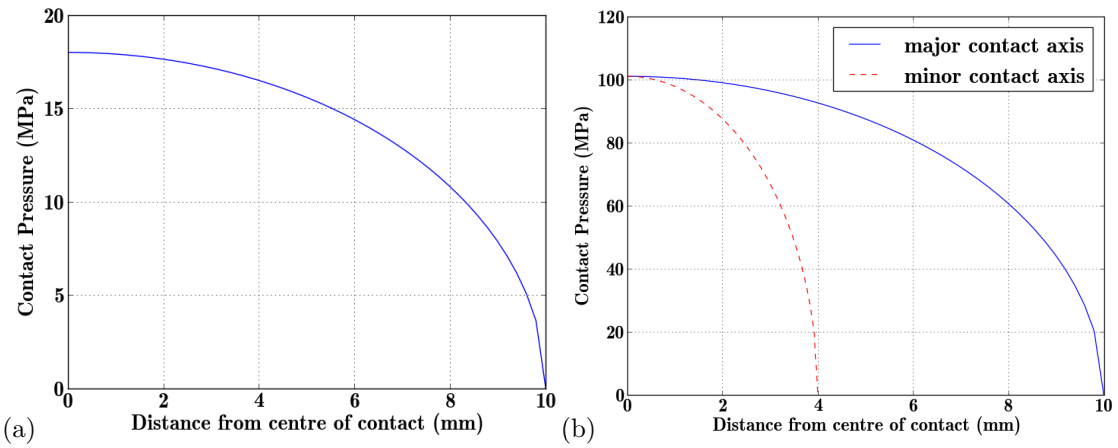

(a) (b)

Figure 4.42. (a) Normal loading contact pressure distribution (b) edge loading theoretical contact

In terms of theoretical models, close agreements were observed between the Hertzian contact models and finite element analysis under normal/centred loading conditions, therefore this provided a comfortable level of confidence in the numerical results obtained so far. Edge loading and lubrication 'live' calculation sheets were developed and used to carry out engineering calculations quickly and efficiently, this is provided in Appendix G – Edge Loading and Lubrication Calculations. From the defined inputs, within the calculation sheet, the onset of rim contact against cup inclination angle was plotted which provided an inverse tan plot. In addition to this, by defining a constant cup inclination angle of 45 ° the onset of rim contact was plotted as a linear relationship against varying diametral clearance between the acetabular cup and femoral head. Following on from the theoretical edge loading calculations, the minimum lubrication film's thickness and lambda ratio were calculated based on the bearing contact parameters, sliding velocity and fluid viscosity. It was however out of the scope of this study to link these results to further develop the wear simulation models.

4.9. Shakedown and Cyclic Analysis of Hip Bearing Implants and Materials

From the live calculations sheets provided in Appendix H – Contact and Shakedown Analysis, the equivalent contact modulus between the bearing surfaces was calculated based on the Poisson's ratio and elastic modulus of each implant. The main material of both the acetabular cup and femoral head assessed during this project was the CoCrMo ASTM F75 grade. The equivalent contact modulus calculated for this material was 115 GPa. By defining the nominal diameters of both the femoral head components and acetabular cup the dimensional coefficient K_D was calculated to be 31.3 m, therefore both the radius of contact and maximum contact stresses could be obtained. For a 500 N load, which is typically applied within experimental simulator studies with microseparation, the radius of contact and maximum compressive stress were 7.4 mm and 17.4 MPa. However when considering a stumbling load of 11000 N, the

values increased to 20.8 mm and 48.7 MPa respectively. Based on shakedown maps for line and circular contact [95, 208], and a friction coefficient of 0.16 the hip bearing implant components were predicted to remain in an elastic state under contact loading as long as the load intensity P_o/k did not exceed 3 (Figure 4.43), where P_o and k are the maximum contact pressure and material shear yield strength respectively. The value of material shear yield strength in simple shear, k, calculated from

$$k=\sqrt{3}\cdot\sigma_Y \tag{4.3}$$

is defined in the literature [208], where σ_Y is the material yield stress. Based on theoretical shakedown maps and considering the maximum contact pressure observed, the load intensity $\sigma_{c,max}/k$ was predicted to be between 0.87 and 2.6, where $\sigma_{c,max}$ is the maximum contact pressure. This load intensity remains within the elastic region of the shakedown map and does not fall within the predicted elastic shakedown regions of the shakedown maps (Figure 4.43).

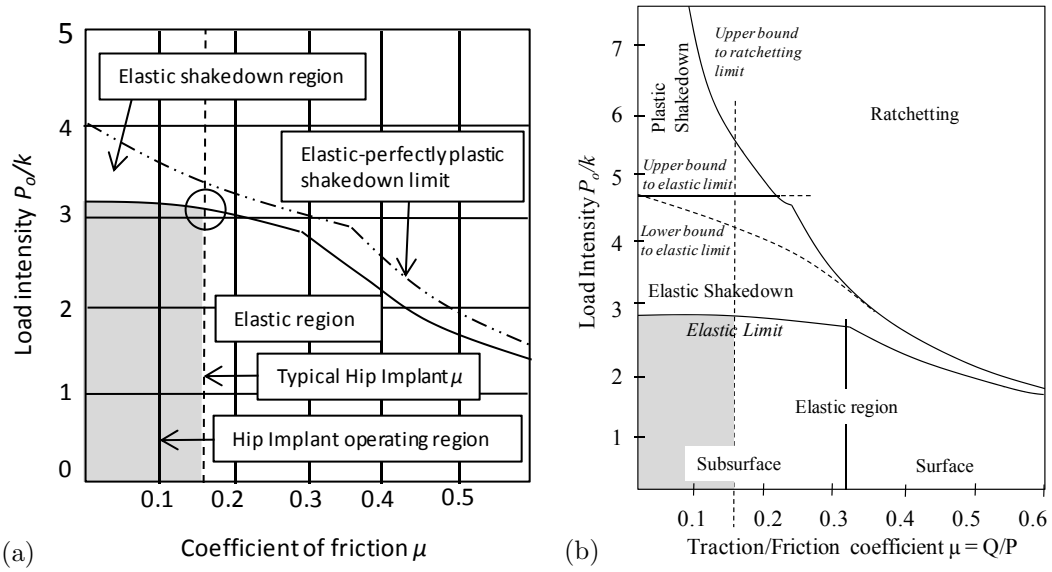

Figure 4.43. Hip Implant life operating region (a) shakedown map for line contact [95] (b) shakedown map for point and elliptical contact

The results presented above, covers the shakedown analysis of the hip bearing components on a global level. On the asperity level, further calculations were carried out. Based on the asperity shakedown model presented by Bhushan [170], and assuming the values of surface roughness declared within chapter 3. The contact area on the asperity was calculated with the

assumption that all asperities on the contact surface were of equal size. From this assumption the load on the asperity W_i was calculated to be 7×10^{-6} N. An in depth study of the number of asperities could not be conducted during this research project; therefore, the total load on the contact surface area was difficult to predict with any justifiable means. However, from the prediction of asperity load, the mean Hertzian contact pressure for micro contact, σ_m, was determined to be 3.5×10^{10} N, as well as the radius of circular micro contact area, a_a, and interface between two asperity profiles, δ_a, which were both 10^{-9} m in terms of order of magnitude. These were useful calculations, as current literature and understanding of shakedown theory shows that, if the asperity contact pressure is less than the asperity shakedown pressure then the asperity will not undergo plastic flow under cyclic loading.

A further assessment of the normalised asperity behaviour was carried out based on the theory defined and explained within chapter 2 and chapter 3. Following a normal distribution of asperities, the interference of asperities was assumed with the values of I_h and I_d. This defined the upper integral limit, I_h, and lower integral limit, I_d, of the surface asperity probability density function (PDF). By calculating this value, the normalised nominal shakedown pressure against the shakedown plasticity index in relative sliding was referred to. Then the prediction of the asperities undergoing plastic flow (above the h/σ lines) or elastic shakedown (below the h/σ) was made. The shakedown asperity plasticity index for repeated sliding was calculated to be 3.6.

Chapter 5 - Discussion

Each of the results using the methodology described in chapter 3 provided techniques to obtain the unique results presented and discussed in chapter 4. These results contribute to meeting the overall aims and objectives of the project. The results from each of the methods used will be discussed independently before providing more general discussions on all the results obtained.

The magnitude of stresses and contact pressures observed may appear large for model A, however the rigidity of backing components increased the results by at least a factor of 5 over the results obtained using models B, C and D. For bearing contact analysis, the maximum stress was observed below the surface of the material as predicted by Hertzian theory for surfaces in contact with a coefficient less than 0.3. The maximum plastic strain was also observed below the surface of the rim under edge loading conditions, however this was observed only in model A and only under very severe edge loading conditions. No plasticity was observed in models B, C and D. For model A, the total contact area under edge loading conditions was 2.7 times less than under central/normal contact conditions. This was an important finding as the contact patch dimensions directly affects the linear wear, as does the contact pressure according to the Archard wear model used to study wear of the bearing surfaces. The Archard wear model in combination with the finite element solver provided a basis for modelling the wear of the bearing surfaces.

5.1. Model A: Three-dimensional Rigid Backed Model

Model A provided a useful model for assessing the contact between the femoral head and

acetabular cup under specific edge loading conditions modelled within this project. Initially, the contact pressure under central loading contact was assessed through the application of a peak vertical load. The radial contact pressure was symmetric about the centre of contact, regardless of the radial position of the contact central axis.

When edge loading was applied in combination with a peak vertical load, the maximum contact pressure and stress distribution changed considerably. By applying a lateral sliding displacement in-line with experimental simulator testing methodology discussed within chapter 2, the contact pressure increased by a factor as large as 9.1. This was considerably larger than the contact pressure under central loading conditions and perhaps was an unrealistic prediction at first glance. This was caused by a considerably large lateral force of over 4480N, which was even larger than the peak vertical load applied. This result instigated more in-depth edge loading and microseparation modelling and led to questioning of the past methodology and assumptions. For comparative purposes, the reaction forces under lateral sliding of the femur and femoral head component leading to rim contact was investigated further. As previously discussed, the lateral sliding within experimental simulator studies led to a maximum lateral force of 500 N. Due to the time increments of the analysis being small relative to the total step time, the contact pressure was interpolated to obtain the maximum contact pressure when at lateral reaction force of 500 N was applied. When this boundary condition was applied, the contact pressure increased by a factor of 5.6 over the contact pressure observed under a vertical peak load. The maximum von Mises stress and maximum principal stress were predicted to remain within the material's elastic region, and therefore not exceed the yield of the material. It was no surprise that a negligible amount of plastic strain was observed to occur at the subsurface of the material under edge loading conditions.

One of the most studied parameters within the literature was the cup inclination angle, with the nominal angle of 45° being the target. On the other hand, the analysis of varying

anteversion angle was not as extensively covered within the literature. When investigating the cup inclination angle and anterversion angle, the changes in contact pressures, stresses and contact areas were observed. Both the contact pressure and contact area decreased as the cup inclination angle increased. This finding seems to contradict the observation of cup inclination angle increasing the wear rate of hip bearing surfaces as reported from patient retrievals and experimental studies. This further suggested that the lateral displacement method used to model microseparation and edge loading may not fully simulate the kinematics and kinetics of the problem accurately using the computational method.

The affect of varying the anteversion on the contact pressure and stress had more of an impact than initially anticipated. The methodology used led to results which supported the current recommendation of cup anteversion angle for patient implantation. The lowest values of contact pressure and stress occurred at low values of anteversion. The reduction in contact area as the cup inclination angle increased did not lead to an increase in contact pressure as discussed in the literature review. This was due to the microseparation being a fixed value of lateral displacement rather than a specific load magnitude.

The modelling of microseparation was carried out in two distinct and separate ways. This was achieved by modelling both lateral sliding and 'pure' microseparation then assessing the contact stress, subsurface stress, strain and shakedown. Laxity of the joint was simulated based on a theoretical microseparation model which provided further explanation of the increasing wear rates as observed from *in-vitro* studies and patient retrievals. Both types of microseparation simulation models showed an increase of contact stress by at least a factor of 2 over normal or centrally loaded hip resurfacing devices, depending on a number of factors including the anteversion of the acetabular cup and load magnitude. This level of contact stress increase compares closely to the level of wear rate increase from *in vitro* experimental simulator studies which included microseparation.

By applying 'pure' microseparation conditions, the finite element method was used to assess the affects of contact pressure and stress. This therefore extended previous modelling and studies of hip implant device edge loading. Laxity of the joint occurred when there was no contact between the femoral head and acetabular cup and the centre point of the acetabular cup did not coincide with the centre point of the femoral head. The centre point of the femoral head was moved to a specified distance relative to the acetabular cup in the inferior-medial direction for the left hip or in the inferior-lateral direction for the right hip. Following laxity of the joint and relocation by a vertical load to re-engage the hip joint using an explicit finite element solver, initial contact occurred on the rim of the acetabular cup. The magnitude of the contact pressure was larger than under normal loading conditions; however the value was less than that observed when lateral displacement control edge loading was applied as the boundary condition. This methodology led to lower values of contact pressure and a symmetric pressure distribution about the centre of contact. As the cup inclination angle increased the contact pressure also increased, which agreed with the trend observed from *in vivo* and *in vitro* retrievals. Along with this finding, the importance of acetabular cup rim radius was observed from the contact pressure results under 'pure' microseparation.

5.2. Model B: Segmented Hip Device Models

As expected the maximum contact pressure and stress values reduced over those observed from model A due to the elasticity of the bone backed model material properties and reduced model rigidity. Initial results showed the maximum contact pressure to be located off the centre of the contact, which differed to the more predictable contact pressure profile observed for the results in model A. The maximum contact pressure under vertical loading conditions applied to model B-1 occurred towards the posterior end of the cup. The contact pressure distribution under lateral displacement edge loading also differed to that observed in model A. The maximum contact pressure of 142 MPa did not occur at the centre of contact (i.e. contact

radius equal to zero). In all contact cases, the initial non-zero value of contact pressure occurred at $t = 0$. This was due to displacement control being used to establish equilibrium before the application of load control.

As with model A, under maximum vertical loading conditions, no edge loading or rim contact was observed. When edge loading was simulated by a lateral displacement, the occurrence of the off centre maximum contact pressure was caused by a combination of peak load and lateral displacement. In the case where ISO gait loading was considered, the amount of contact between the head and cup was significantly less than in the case where constant peak loading was modelled along with normal and edge loading. The contact area between the bearing components with microseparation at peak loading and ISO loading conditions were denoted by M_p and M_I respectively. In addition to this, the contact area between the bearing components without microseparation at peak loading and ISO loading conditions were denoted by N_p and N_I respectively. The contact area profiles and magnitudes are clear to see from Figure 4.14, where a varying contact area profile was observed when an ISO loading profile was applied. However, a steady state increase in contact area was observed as the contact load was increased during the application of peak loading conditions. The contact area for both types of loading conditions was reduced when microseparation was applied.

As discussed in chapter 2, previous literature suggests that the magnitude of vertical loading has negligible effect on the contact pressures between the hip bearing components, however the results from model B have shown that increasing vertical load magnitude by 30%, i.e. from F_I to F_y, increased the maximum contact pressure by 22%, which leads to a proportional increase in wear according to the wear theories referred to and used in this project.

Non-symmetric contact pressures and magnitudes were due to the influences of bone geometry and as expected the contact pressure increased when a larger lateral displacement was applied (from 200 μm to 500 μm). Modelling development following the methodology proposed in

Figure 3.14 was repeated to ensure that this was not caused by any errors with the modelling (referred to as model B-2), however the same results were obtained.

For model B-1, when a lateral displacement was applied in combination with a peak vertical load the maximum contact pressure increased by a factor of 7.9 over the maximum contact pressure observed under vertical loading. This increase in contact pressure above the rim of the acetabular cup was caused by a 907 N lateral reaction force as a result of applying the lateral displacement boundary condition of 250 µm. Although the reaction force at the rim of the cup was lower than that observed for model A, this is still larger than the lateral force applied in experimental *in vitro* simulator studies.

Following the calculation and study of edge loading factors, further analysis considered the flexion-extension profile in line with ISO standards and experimental simulator testing methodologies. When assessing the effect of varying the anteversion angle under ISO gait loading conditions and flexion-extension hip rotations, no effect on the contact pressure was observed. The cup diametral clearance was also increased from 80 µm to 150 µm, however, this had very little effect on the contact pressure magnitudes and the contact profiles were almost matching. The variation of shear stress occurred in line with variation of ISO loading, where the maximum shear stress of 8.5 MPa was present on the surface of the acetabular cup, at the time of peak vertical loading. Varying the surface coefficient of friction had a negligible effect on the surface shear stresses under ISO loading and component sliding contact simulations.

The importance of checking the energy results of any implicit or explicit analysis was discussed and justified. The energy results and assessments provided an additional level of confidence in the results obtained during this project using the finite element method, especially with regards to the complexity of modelling sliding contact.

The profile of the maximum contact pressure throughout the time step was representative of the variation in vertical load throughout the single gait cycle. Reducing the cup rim radius

had no effect on reducing the maximum contact pressure throughout the gait cycle as no rim contact was observed without the inclusion of microseparation. The fixation area between the cup and pelvis also did not have a considerable effect on the results. Less than a 1% difference of the average maximum contact pressure was observed when the contact fixation area between the superior surface of the acetabular cup and inferior surface of the pelvis acetabulum was increased by 15%. The total edge load magnitude was applied in the first step of the analysis and therefore the maximum edge load was present at the beginning of the subsequent step, which in this case was the flexion-extension cycle. This type of kinematic and kinetic condition meant that the maximum contact pressure distribution did not follow the gait cycle loading profile applied in the analysis. As the edge load was removed the femoral head was free to relocate under the application of the ISO gait vertical loading. The combined effect of a maximum edge load and the application of the gait cycle meant that the maximum contact pressure occurred between the cycle time 1 s to 1.6 s which was within the region of the loading cycle where more than 10% of the vertical loading occurs and the peak loads occurred at 10% and 50% of the cycle time.

From the contact pressures of model A and model B under normal vertical loading with the application of an edge load, the average edge load factor was determined to be 5.6. This means that an edge load can increase the maximum contact pressure to around 5.6 times greater than the maximum pressure observed under normal/vertical loading conditions. This includes the analysis where the edge loading was modelled with a lateral displacement and an analysis where the edge loading was observed through a pure separation of the joint, i.e. laxity of the joint leading to relocation by the application of a vertical load causing acetabular cup rim contact.

Model B-2 was also used to assess the performance of using the computer's central processing unit (CPU) with hyperthreading technology when using the Abaqus postprocessor. Such

results had not been previously published within the literature. A 5% increase in analysis run time occurred as a result of using hyperthreading technology and allocating all cores and threads available to the post-processor. This was due to the delays caused by scheduled data processing through threads when hyperthreading was enabled, which is a problem not just specific to floating point units (FPU). Further results using a smaller three-dimensional hip model had shown that the negative effects of hyperthreading only became prominent for larger models. The results of analysis run times and the number of processor cores activated showed a consistent reduction in run times as the number of cores and threads were increased for both hyperthreaded and non-hyperthreaded analysis runs. There was a negligible difference between running the analysis with and without hyperthreading for the smaller models. By maintaining the same allocation of software and hardware settings, the effect of analysis run times due to the number of nodes is shown.

In this project, a number of techniques have been studied and developed to apply different material properties to the bone models. These include simple isotropic models with single values of elastic modulus, to more complicated greyscale based material properties. The variation of bone model elastic modulus material properties changed the contact by as much as 24%, this was however with the consideration of 'extreme' relative values of bone material properties between the femur and pelvis sections. The maximum von Mises stresses of the pelvic and femur sections varied by different amounts through these material model studies. The maximum von Mises stress of the femur and pelvis varied by as much as 35% and 7% respectively.

5.3. Model C: Full Hip and Pelvis Implant Model

When conducting the analysis with the consideration of a full femur and pelvic model, the contact pressure and stress results were comparable to model B. This further justified the validity of using a more computationally efficient three dimensional segmented model for

contact analysis. Two-dimensional axisymmetric studies were conducted in the past which also provided further justification of a segmented model, however no study in the past had confirmed this validity with a more computationally complex three dimensional approach using the conditions modelled in this study. As with both model A and model B, no rim contact was observed under normal gait loading and angular displacement conditions. When the larger vertical loads were applied to the full bone backed models, increasing the vertical load by 280% led to a 10% increase in contact pressure. No further studies were carried out using model C as the computational efficiency and confirmed validity of model B meant no further results were required from using model C.

5.4. Model D: Two-dimensional Axisymmetric hip joint

One of the key advantages of the two dimensional models, was that they provided the basis for comparative work against other studies conducted and published within the literature. This was the initial aim of carrying out investigations using two dimensional axisymmetric models. An important question raised by biomedical communities was regarding the benefits of an acetabular cup inlay or insert between the acetabular cup and acetabulum. It was clear from the results obtained using model D-1, that the polymeric inlay material provided no advantage in reducing the contact pressures and stresses of the implant components. In addition to this assessment, as the application of a vertical load was important in developing contact and mechanical models within this project, the methodology of applying the load needed to be justified. The options available were to apply the vertical force as a concentrated load or distributed load. The results show that the contact pressures and stress distributions differed by applying the load in a different way. As expected, by applying a concentrated load there was a high stress concentration at the base of the femoral head component along the axis of symmetry. Direct comparisons were made to the results published by Mak et al. [88, 89],

however, further modelling combinations were considered in this project from that completed in previous studies.

From model D-2b under normal cyclic loading conditions, the stress-strain curves showed the loading and unloading of the implant material remained in the elastic region with no hysteresis occurring, as expected when using the isotropic model. The largest difference between the two-dimensional and three-dimensional models was the impact of vertical loading magnitude on the stresses of the bone models. There was a considerable difference in subsurface, internal stresses and load vectors of the femur and pelvic models when F_I (ISO vertical loading), F_y (normal vertical loading) and F_s (stumbling vertical load) where applied. For the implant components, the maximum stresses occurred a considerable distance away from the subsurface of the femoral head component. The depth from the subsurface of the maximum stress was at least $f_{tI}/2$, where f_{tI} is the head bearing thickness. For the acetabular cup, the maximum stress occurred at the superior surface when F_I and F_y were applied. When the stumbling load was applied, the maximum stress occurred at the interface surface of contact between the bearing components.

5.5. Model E: Finite Element Model Validations and Theory

Although a number of attempts were made to replicate the results obtained by Mak et al. [67] there still remained a level of disparity between the results in this study and the results from the study by Mak et al. Through this study it was observed that the sensitivity of the rigid backed models were very high, especially if a low mesh density is applied within the edge loading contact zone. It has not been stated how the total of 52,800 elements were distributed on the model from Mak et al.'s study, however, the mesh appears to visually match the models developed in this study, where only 21376 elements were used for the cup model. These factors along with the other unknowns highlighted in Table 3.7 led to the difference between results obtained. The closest comparable results were between the contact pressures obtained for

model B (417 MPa) and the contact pressure obtained by Mak et al. at the rim of the cup (437 MPa). Following on from this, the normal and edge loading convergence studies provided validity for the results obtained. It was observed that convergence was relatively easier to obtain for normal/centred contact than it was for edge loading contact. When modelling deformable-on-rigid body contact, the justification for using a lower number of contact elements than in deformable on deformable body contact in the edge loaded zone was valid as the rigid femoral component master surface offered a perfect analytical spherical contact surface over a meshed surface. This reduced the occurrences of contact overclosure and result discontinuities. The finite element mesh convergence study showed that at least 16 nodes within the radius of the contact zone were required for accurate results in the central/normal loading contact. For edge loading contact occurring at the rim of the acetabular cup, at least 60 nodes (275% increase in the number of nodes required) were required across the major axis of the elliptical contact zone.

Fortunately, the historical development of contact theory has been such that comparisons could be made directly with finite element studies to provide further validation of the results. The positive correlation and comparison between the numerical and theoretical results provided further supporting evidence for the validity of the results. By combining the use of finite element results and theoretical models, the options for assessing and analysing the contact pressure profiles under normal and edge loading conditions were increased.

5.6. Wear Modelling and Simulations

The first method of studying the wear between contact surfaces using the finite element method was based on the use of subroutines with an Intel Fortran complier. Unfortunately, the limitations of using this technique in combination with the Abaqus were not documented within the literature; therefore, a significant allocation of the time was spent on understanding the limitations of this methodology. However, this was not wasted research, as further

understanding and documentation of the process and methodology could lead to firm strategies and standardisation for wear simulation techniques in the future. The limitations of the methodology based on the study conducted and results obtained will be discussed below within this section.

For the subroutine method, to record the contact pressure field output values using the GETVRMATAVGNODE utility, one part in contact was required to be a master surface and the other as the slave surface. Therefore, the wear of both components could not readily be modelled simultaneously if the guidelines of defining slave and master surfaces were to be followed correctly. The other limiting factor was that the user defined subroutine UMESHMOTION could only be used with the Abaqus Standard solver, therefore no explicit analysis could be conducted in combination with the wear simulations using this subroutine technique. It should be noted that the CSLIP (finite element analysis output result for contact sliding distance) variable was only valid if contact was maintained between the surfaces, if contact was not maintained then the contact slip variable would be reset to zero. One of the biggest challenges from a programming perspective of using the subroutine method was the inconsistency of using common blocks. The use of common blocks is the past and current standard in Abaqus subroutines for passing variables which are stored in temporary memory hardware locations. As new programming standards have been released for Fortran, modules have recently replaced common blocks to solve the problem of losing data during analysis runs, however they could not be used with current Abaqus subroutines. Another key limitation of this technique, was that only a single processing core could be allocated to the analysis in combination with the subroutine due to the conflicts with common blocks. The slave adjustment and surface smoothing algorithms used for surface-to-surface contact to establish analysis convergence could not be used with the subroutines and adaptive meshing techniques. Therefore, viscous damping was used to control the instability of the contact problem.

However, due to the uncertainties in result accuracies this was the least preferred option over using displacement control to establish contact before switching to load control. Although the viscous damping parameters reduce as the analysis increments increase and are minimised at the end of the step, the contact solution would be less accurate using this technique. The solution was less accurate because of the viscous damping term being subtracted from the applied load as well as the internal load being subtracted from the applied load to equal zero. Results showed that it was possible to ablate the mesh under contact loading based on the application of Archard's wear law. This resulted in obtaining the low levels of volumetric material loss due to sliding contact for both the metal-on-metal block model and the wear simulations using a modified version of model A-1. The extent of the limitations for using this methodology led to the development of a newly proposed method for conducting segmented hip implant contact wear simulations using a modified version of model B-1. Despite some of the challenges associated with using the constructs of the Abaqus and Python scripting interface, the new methodology offered a number of advantages over the previous wear simulation methods used and discussed. Node sets were required to be used instead of surface sets (as shown in the object oriented code below) which were less easily selectable in the Abaqus CAE environment,

odb.rootAssembly.instances['TOP_PART-1'].nodeSets['CONTACT_NODE_SET']

Although surface sets could not be used directly to obtain node sets, to overcome this problem a separate node set was selected from the surface by selecting the nodes with a defined angle. Then a field output request could then be defined to obtain the output data from the relevant sections.

For the mechanical wear simulations a cyclic ISO loading profile was applied in combination with flexion-extension and inward-outward rotations. Assumptions were made between the numerical and experimental strategies to simplify the model. The dimensional wear coefficients

from current literature provided material and application specific values to be applied to the Archard wear model.

From the literature review carried out, the volumetric wear rates from experimental simulator studies can be compared against the results obtained in this study. From all experimental simulator studies reviewed, the range of volumetric wear after 1 million cycles was between 0.8 – 25 mm^3, however some studies have reported *in vitro* wear rates as excessive as 100 mm^3 over 1 million cycles [209]. When conducting wear simulations using a long term cyclic wear coefficient, the volumetric wear was significantly less at 1-3 mm^3 per million cycles for both the femoral head and acetabular cup. This low level of volumetric material loss occurred when more than 1 million cycles was modelled i.e. using a long term wear coefficient. Therefore, the volumetric wear rates observed from computational simulations were comparable to those from experimental simulator studies.

5.7. Shakedown, Cyclic and Asperity Contact Analysis

The finite element contact results presented within the previous chapter have provided the opportunity to study shakedown of the hip implant devices. Based on the von Mises criterion, the elastic limit of a bearing component was exceeded. This occurred at the subsurface of the material where the maximum Hertz pressure exceeded $p_o = 3.10 \times k$, where k was the yield stress in simple shear. It must be noted that this only occurred for model A during severe lateral sliding microseparation conditions. The detailed subsurface assessments of von Mises and shear stress was possible due to the computational efficiency of applying a high number of nodal points on the two-dimensional axisymmetric model.

The original shakedown map introduced by Johnson and Jeffries [210] define the shakedown limits in rolling and sliding contact. From the maximum contact pressure, calculated value of k and value of load intensity, under central and edge loading conditions, the hip implant components of models B-D were all predicted to remain within the elastic region of a contact

shakedown map. This is a 'safe' region for the components to be operating in. Therefore, in terms of the hip resurfacing device's response to loading and based on line, point and elliptical contact shakedown maps; elastic shakedown, plastic shakedown or ratchetting behaviour would not be observed during normal contact conditions, edge loading or stumbling load conditions.

When considering both cyclic gait loading and high stumbling loads no plasticity was observed in models B-F, therefore in reality it was predicted that material plasticity would not occur under normal, edge loading or extreme stumbling load conditions. In addition to assessing the plasticity and fracture, fatigue assessments are an important consideration for any cyclically loaded component, however through this study it was deemed that fatigue strength along with fracture toughness of cobalt chromium is significantly larger than bone. The fracture toughness of cobalt-chromium-molybdenum could be up to 50 times greater than for bone [211]. This high fracture toughness would much sooner cause femoral neck fracture [212, 213] before fracture or fatigue failure of the metal-on-metal device. Even by considering the large range of the hip implant device materials properties shown in Chapter 3 and severe loading such as stumbling as well as edge loading, high cycle fatigue is not a threat to the structural or surface integrity, especially in comparison to the problem caused by plastic deformation of asperities and wear debris.

The distinction between different debris geometries along with the effect of von Mises stress and shear stress on the two dimensional hip implant sections for both the surface and subsurface were observed from the finite element results. The shear stress increased following contact sliding of the debris model and the bone debris caused a maximum stress on the CoCrMo sections to decrease by 83%, compared with the stress when modelling metallic debris.

The literature discussed within chapter 2 and methodology in chapter 3 discussed the importance of understanding asperity effects on surface damage and wear of hip bearing surfaces. In this study, the asperity contact analysis offered a comparative assessment between circular, oval and needle like asperities, which were reviewed to be recorded from patient retrievals and *in vitro* studies. The differences in von Mises stress and shear stress between the circular and oval asperities was negligible compared with the results obtained for the needle like asperity.

Chapter 6 – Conclusions

A combination of computational, numerical and theoretical techniques were developed and used to form the basis of studying the contact mechanics, wear and shakedown of hip resurfacing devices. The finite element method was used to build contact models, further develop numerical mechanical wear techniques from previous studies and assess the application of shakedown theory to normal and edge loaded hip joint resurfacing devices under different loading conditions.

6.1. Finite Element Modelling of Hip Implant Devices

Each computational model developed provided either a solution or a form of validation to the problem studied in this project. The following conclusions were reached for the assessment of cup inclination angle and anteversion angle:

- The corresponding contact on the femoral head component was dependent upon the anteversion angle of the implanted cup, however anteversion did not affect the contact profile on the rim of the acetabular cup.
- The contact pressure and contact area profiles matched as the cup inclination angle and anteversion angle varied. This justified the importance of accurate edge load modelling to obtain realistic results comparable to those seen *in vivo* and *in vitro*.

The following points have been observed for edge loading and microseparation:

- The effect of edge loading was significant and agrees with the level of damage observed from stripe wear on *in vitro* and *in vivo* retrievals.

- For all three dimensional models, the plastic strains and stresses were shown to be above the rim radius of the acetabular cup as observed from patient retrievals and experimental testing which consider microseparation conditions.
- The results at the rim of the acetabular cup were heavily dictated by the method of simulating edge loading conditions using computational techniques.
- The modelling and boundary conditions significantly affected the stress and contact results obtained.
- The differences between normal contact results in this study against stress and contact pressure results obtained previously in the literature were less than the differences of results under microseparation conditions.

Through hip implant finite element modelling the conclusions are as follows:

- Both the segmented implant model geometry and variation of material properties meant that the sensitivity of these two important modelling parameters did not significantly affect the contact mechanics between the bearing implant devices, especially when analysing three-dimensional models.
- The results of the proposed modelling process were repeatable even with variation in the implant coordinates, locations and bone model segmentation geometries. Therefore, the scope for studying the contact mechanics and wear of hip resurfacing devices is possible without the need for complex density based material models.
- An equivalent bone modulus could be used without accurate refinement as the affect on producing varied contact pressures was not significant to varying the contact pressure results for realistic variations and bone elastic material properties.

Validation and verification of the finite element results can be summarised as follows:

- The justification and validation in opting for a segmented three dimensional hip implant model (model B) was confirmed as the contact results under normal loading conditions

matched that of the full hip model (model C).

- The methods of validation including energy results, mesh convergence studies and model verification checks, provided some confidence in the validity of the results obtained.
- Two dimensional axisymmetric modelling showed good comparison to the work previously completed in the literature.
- By using a combination of finite element analysis and equations based on theory, solutions were derived and applied to both normal and edge loading contact efficiently for specific subject based cases.
- Overall, there was no benefit of using Hyperthreading technology to reduce the computational analysis run times.

Finally, it was observed that the theoretical calculations compared closely with the results obtained in this study and the results in the literature for normal loading conditions. Throughout the analysis and convergence studies, obtaining an accurate solution under normal contact vertical loading was simpler and less computationally intensive than a solution under rim contact (i.e. microseparation leading to edge loading).

6.2. Wear Modelling of Hip Implant Devices

The Archard wear model in combination with the FE solver provided a basis for predicting the wear of the bearing surfaces. The methodological approach adopted in this study ensured that numerical and process checks could be performed at every step to ensure that the developed simulations provided traceable results. The modelling constraints for carrying out wear simulations with two deformable segmented parts in contact meant that simplifying assumptions were made in order to simulate the wear between devices.

The current limitations of using finite element based wear modelling techniques in combination with user defined subroutines meant that only wear analysis with the Abaqus standard product could be conducted. The combination of advanced user defined subroutines,

implicit methods and adaptive meshing techniques meant that contact modelling aids, including the removal of slave surface overclosure and automatic smoothing could not be used as this provided difficulty in controlling the element ablation. Therefore, to obtain a acceptable accuracy in the contact zone with the level of computing power available, compromises were made to simplify the wear simulations.

The points and benefits of the wear simulations are summarised:

- For simultaneous wear modelling of the femoral head and acetabular cup, explicit methods could only be realised if an alternative wear modelling method and technique was developed. This was just one of the benefits of developing unique and newly proposed hip implant wear simulations using a dynamic scripting language which directs the kernel through an interpreter.
- The scripting method allowed for mesh ablation to be applied on the surfaces of the acetabular cup and femoral head components from the same analysis output data, which had not been covered within previous hip resurfacing implant studies.

6.3. Cyclic Analysis and Shakedown of Hip Implant Devices

Based on the assumptions made in this study and the modelling conditions used to simulate normal and edge loading occurring on hip joint resurfacing devices, predictions showed that although cyclic loading was present during the operation of the hip resurfacing devices under operating conditions; elastic shakedown, plastic shakedown or rachetting was not predicted to occur. The cobalt-chrome device material was predicted to remain operating within the elastic region. Following on from the global shakedown analysis for the hip implant, shakedown at an asperity level was also carried out. In summary, building a framework using this theory on a practical level for this problem became very complex with a number of assumptions required.

Chapter 7 – Summary

7.1. Summary of Contributions

From this study, the research extended current knowledge, understanding and methods used to study the problem of normal loading, edge loading and severe contact of hip implant devices. The results showed that the amalgamation and links between various topic areas all strongly contributed to solving the problem.

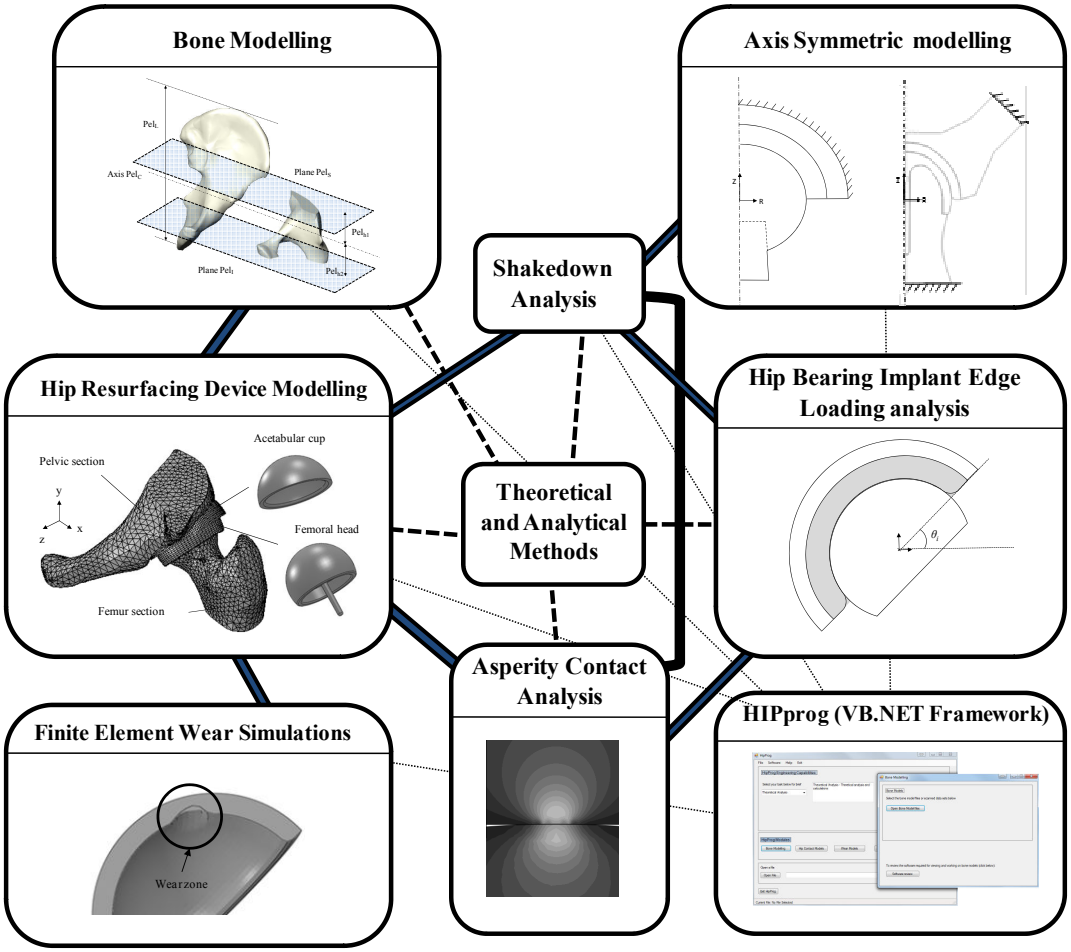

Figure 7.1. Hip implant solution based engineering amalgamation

Although a number of areas were covered within this project, the relationship and importance of covering as well as linking these areas were discussed. A clear way to present the methodological consolidation and linking all the topics covered within this project is

shown in Figure 7.1. This also shows the important relationships between the various areas studied.

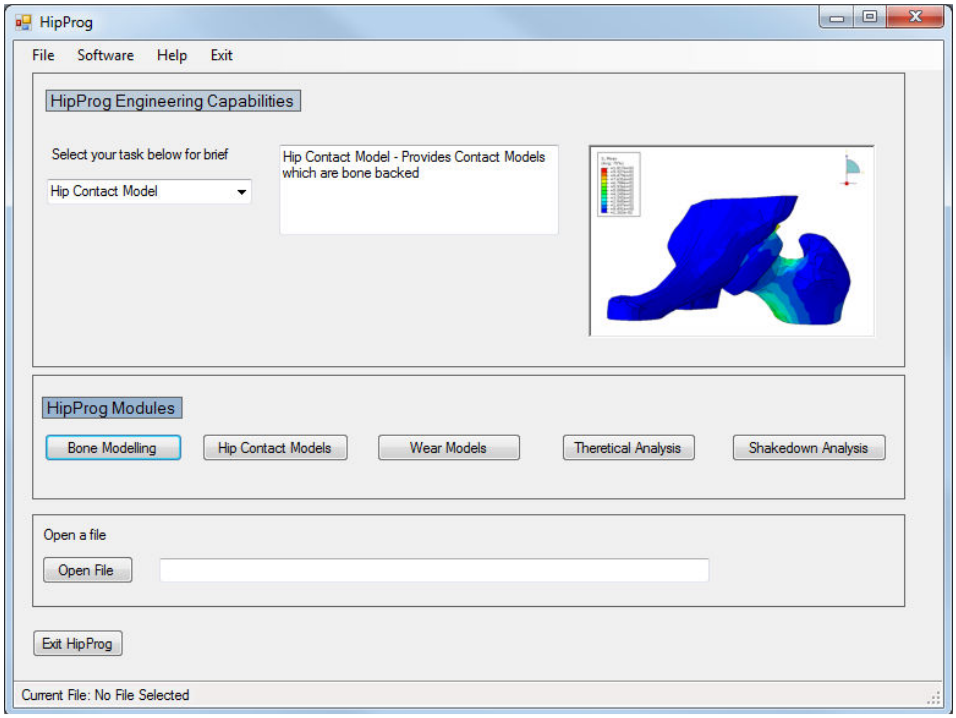

Figure 7.2. HIPprog Graphical User Interface

In addition to this, the following points highlight the key achievements and contributions of the project:

- Advanced implicit and explicit finite element modelling of hip implant devices under normal, edge loading and severe loading conditions. With the development of different models to assess specific problem areas, along with the assessment of differences in contact stresses of the hip implant devices under these conditions.
- Quantified the severity of edge loading on hip resurfacing devices against normal loading conditions.
- Use of explicit methods to simulate edge loading conditions from hip joint laxity leading to acetabular cup rim contact under vertical gait loading (i.e. heal strike).
- Validation of finite element models and comparisons to theoretical models.
- Assessment of different materials models for bone and sensitivity of properties on the contact mechanics of hip implant devices.

- Comparison of the contact mechanics of typical third body debris contact between hip implant devices.
- Development of cyclic hip resurfacing wear models using Archard's Wear Law to simulate the wear of both the femoral head and acetabular cup simultaneously, based on ISO gait loading and angular displacements.
- Shakedown assessments of hip implant devices at the global and asperity levels.
- Amalgamation of the methods developed in this project to promote further work and research (Figure 7-2).

7.2. Further Work

The aims and objectives of this research were to focus on specific problems which have occurred in the past and continue to occur, as explained in chapter 1 and chapter 2. There is certainly scope for further research to be conducted in a number of areas. The majority of further work recommendations are based on the development of more advanced wear models with the incorporation of lubrication models. Within this project the Archard wear model was used, however this did not consider all the complex wear mechanisms and lubrication between orthopaedic devices discussed within the literature review. The total number of increments to update the finite element could also be reduced to update the mesh more regularly. The wear simulations could also be developed to consider more variation in dimensional wear coefficient throughout the cyclic life of the bearing components.

Despite the progress made during this project, further work is required to develop theoretical and computational models to more accurately simulate and assess the effects of real patient specific consequences of edge loading and microseparation on hip resurfacing devices. The kinematics of these conditions during human joint motion should be considered in more depth if simulations are to more accurately and realistically model these problems. For this to be achieved, strong collaboration between the medical and engineering communities are

essential. It is also important for engineers to have a strong understanding of human anatomy and the biological processes involved, not only to design safer and more successful implants, but also as a source of inspiration for future designs. Overall, using a combination of techniques and theoretical models has shown to be beneficial in developing numerical analysis of hip resurfacing devices under specific conditions.

References

[1] F. Nebeker, "Golden accomplishments in biomedical engineering," in *IEEE Engineering in Medicine and Biology Magazine* vol. 21, ed, 2002, pp. 17-47.

[2] D. Dowson, "New joints for the Millennium: wear control in total replacement hip joints," *Proceedings of the Institution of Mechanical Engineers, Part H: Journal of Engineering in Medicine,* vol. 215, pp. 335-358, 2001.

[3] G. M. Direct. (9th December 2008). *Global Markets Direct: The Future of the Orthopedic Devices Market to 2012*. Available: http://www.the-infoshop.com/press/labd78480_en.shtml

[4] GlobalData. (June 2011). *Hip Replacement Implants - Global Pipeline Analysis, Competitive Landscape and Market Forecasts 2017*. Available: http://www.researchandmarkets.com/research/46d1ca/hip_replacement_im

[5] F. Liu, I. J. Udofia, Z. M. Jin, F. Hirt, C. Rieker, P. Roberts, *et al.*, "Comparison of contact mechanics between a total hip replacement and a hip resurfacing with a metal-on-metal articulation," *Proceedings of the Institution of Mechanical Engineers Part C-Journal of Mechanical Engineering Science,* vol. 219, pp. 727-732, Jul 2005.

[6] C. Matthews, *Engineers' data book*, 2nd ed. Bury St Edmunds: Professional Engineering, 2000.

[7] L. Blunt, P. Bills, X. Jiang, C. Hardaker, and G. Chakrabarty, "The role of tribology and metrology in the latest development of bio-materials," *Wear,* vol. 266, pp. 424-431, Feb 2009.

[8] J. D. Enderle, J. D. Bronzino, and S. M. Blanchard, *Introduction to biomedical engineering*, 2nd ed. Burlington MA; London: Elsevier Academic Press, 2005.

[9] S. Williams, A. Schepers, G. Isaac, C. Hardaker, E. Ingham, D. van der Jagt, *et al.*, "The 2007 Otto Aufranc Award - Ceramic-on-metal hip arthroplasties - A comparative in vitro and in vivo study," *Clinical Orthopaedics and Related Research,* pp. 23-32, Dec 2007.

[10] F. Liu, I. Leslie, S. Williams, J. Fisher, and Z. Jin, "Development of computational wear simulation of metal-on-metal hip resurfacing replacements," *Journal of Biomechanics,* vol. 41, pp. 686-694, 2008.

[11] R. L. Huston, *Principles of biomechanics*. Boca Raton: CRC Press, 2009.

[12] G. J. Tortora, *Principles of human anatomy*, 11th ed. Hoboken, NJ: J. Wiley, 2009.

[13] E. Sariali, V. Veysi, and T. Stewart, "(i) Biomechanics of the human hip - consequences for total hip replacement," *Current Orthopaedics,* vol. 22, pp. 371-375, 2008.

[14] I. J. Udofia, A. Yew, and Z. M. Jin, "Contact mechanics analysis of metal-on-metal hip resurfacing prostheses," *Proceedings of the Institution of Mechanical Engineers Part H-Journal of Engineering in Medicine,* vol. 218, pp. 293-305, 2004.

[15] M. Taylor, K. E. Tanner, M. A. R. Freeman, and A. L. Yettram, "Cancellous bone stresses surrounding the femoral component of a hip prosthesis: an elastic-plastic finite element analysis," *Medical Engineering & Physics,* vol. 17, pp. 544-550, 1995.

[16] F. Linde, I. Hvid, and F. Madsen, "The effect of specimen geometry on the mechanical behaviour of trabecular bone specimens," *Journal of Biomechanics,* vol. 25, pp. 359-368, 1992.

[17] A. Yew, Z. M. Jin, A. Donn, M. M. Morlock, and G. Isaac, "Deformation of press-fitted metallic resurfacing cups. Part 2: finite element simulation," *Proceedings of the Institution of Mechanical Engineers Part H-Journal of Engineering in Medicine,* vol. 220, pp. 311-319, 2006.

[18] M. Dalstra, R. Huiskes, and L. Vanerning, "Development and Validation of a 3-Dimensional Finite-Element Model of the Pelvic Bone," *Journal of Biomechanical Engineering-Transactions of the Asme,* vol. 117, pp. 272-278, 1995.

[19] G. Bergmann. (2010, 14 June). *Orthoload - Loading of Orthopedic Implants*. Available: http://www.orthoload.com

[20] H. Jiang, "Static and Dynamic Mechanics Analysis on Artificial Hip Joints with Different Interface Designs by the Finite Element Method," vol. 4, pp. 123-131, 2007.

[21] G. Wu and Z. Ladin, "Limitations of quasi-static estimation of human joint loading during locomotion," *Medical and Biological Engineering and Computing,* vol. 34, pp. 472-476, 1996.

[22] E. F. Rybicki, F. A. Simonen, and E. B. Weis Jr, "On the mathematical analysis of stress in the human femur," *Journal of Biomechanics,* vol. 5, pp. 203-215, 1972.

[23] F. P. Beer, E. R. Johnston, and J. T. DeWolf, *Mechanics of materials*, 3rd ed. Boston; London: McGraw-Hill, 2002.

[24] J. G. Bowsher, T. K. Donaldson, P. A. Williams, and I. C. Clarke, "Surface Damage After Multiple Dislocations of a 38-mm-Diameter, Metal-on-Metal Hip Prosthesis," *Journal of Arthroplasty,* vol. 23, pp. 1090-1096, Oct 2008.

[25] T. Tateiwa, I. C. Clarke, G. Pezzotti, L. Sedel, T. Kumakura, T. Shishido, *et al.*, "Surface micro-analyses of long-term worn retrieved "Osteal (TM)" alumina ceramic total hip replacement," *Journal of Biomedical Materials Research Part B-Applied Biomaterials,* vol. 83B, pp. 562-570, Nov 2007.

[26] I. C. Clarke, D. D. Green, P. A. Williams, K. Kubo, G. Pezzotti, A. Lombardi, *et al.*, "Hip-simulator wear studies of an alumina-matrix composite (AMC) ceramic compared to retrieval studies of AMC balls with 1-7 years follow-up," *Wear,* vol. 267, pp. 702-709, Jun 2009.

[27] W. L. Walter, G. M. Insley, W. K. Walter, and M. A. Tuke, "Edge loading in third generation alumina ceramic-on-ceramic bearings," *Journal of Arthroplasty,* vol. 19, pp. 402-413, Jun 2004.

[28] A. A. Stans, M. W. Pagnano, W. J. Shaughnessy, and A. D. Hanssen, "Results of total hip arthroplasty for Crowe Type III developmental hip dysplasia," *Clinical Orthopaedics and Related Research,* pp. 149-157, Mar 1998.

[29] I. J. Leslie, S. Williams, G. Isaac, E. Ingham, and J. Fisher, "High Cup Angle and Microseparation Increase the Wear of Hip Surface Replacements," *Clinical Orthopaedics and Related Research,* vol. 467, pp. 2259-2265, 2009.

[30] J. E. Nevelos, E. Ingham, C. Doyle, A. B. Nevelos, and J. Fisher, "The influence of acetabular cup angle on the wear of "BIOLOX Forte" alumina ceramic bearing couples in a hip joint simulator," *Journal of Materials Science-Materials in Medicine,* vol. 12, pp. 141-144, 2001.

[31] S. Williams, I. Leslie, G. Isaac, Z. M. Jin, E. Ingham, and J. Fisher, "Tribology and wear of metal-on-metal hip prostheses: Influence of cup angle and head position," *Journal of Bone and Joint Surgery-American Volume,* vol. 90A, pp. 111-117, 2008.

[32] R. A. Poggie, T. R. Turgeon, and R. D. Coutts, "Failure analysis of a ceramic bearing acetabular component," *Journal of Bone and Joint Surgery-American Volume,* vol. 89A, pp. 367-375, Feb 2007.

[33] A. Hatton, J. E. Nevelos, A. A. Nevelos, R. E. Banks, J. Fisher, and E. Ingham, "Alumina-alumina artificial hip joints. Part I: a histological analysis and characterisation of wear debris by laser capture microdissection of tissues retrieved at revision," *Biomaterials,* vol. 23, pp. 3429-3440, 2002.

[34] R. Bader, R. Scholz, E. Steinhauser, S. Zimmermann, R. Busch, and W. Mittelmeier, "The influence of head and neck geometry on stability of total hip replacement - A mechanical test study," *Acta Orthopaedica Scandinavica,* vol. 75, pp. 415-421, 2004.

[35] R. L. Barrack, R. L. Thornberry, M. D. Ries, C. Lavernia, and E. Tozakoglou, "The effect of component design on range of motion to impingement in total hip arthroplasty," *Instr Course Lect,* vol. 50, pp. 275-80, 2001.

[36] P. J. Firkins, J. L. Tipper, E. Ingham, M. H. Stone, R. Farrar, and J. Fisher, "Influence of simulator kinematics on the wear of metal-on-metal hip prostheses," *Proceedings of the Institution of Mechanical Engineers Part H-Journal of Engineering in Medicine,* vol. 215, pp. 119-121, 2001.

[37] S. Kinkel, N. Wollmerstedt, J. A. Kleinhans, C. Hendrich, and C. Heisel, "Patient Activity after Total Hip Arthroplasty Declines with Advancing Age," *Clinical Orthopaedics and Related Research,* vol. 467, pp. 2053-2058, Aug 2009.

[38] F. W. Preston, "Theory and design of glass polishing machines," vol. 11, pp. 214-256, 1927.

[39] D. Dowson, F. C. Wang, W. Z. Wang, and Z. M. Jin, "A predictive analysis of long-term friction and wear characteristics of metal-on-metal total hip replacements," *Proceedings of the Institution of Mechanical Engineers Part J-Journal of Engineering Tribology,* vol. 221, pp. 367-378, 2007.

[40] "ISO 14242-1:2002 - Implants for surgery -- Wear of total hip-joint prostheses -- Part 1: Loading and displacement parameters for wear-testing machines and corresponding environmental conditions for test," 3rd ed, 2002.

[41] S. Affatato, A. Spinelli, M. Zavalloni, C. Mazzega-Fabbro, and A. Viceconti, "Tribology and total hip joint replacement: Current concepts in mechanical simulation," *Medical Engineering & Physics,* vol. 30, pp. 1305-1317, Dec 2008.

[42] R. L. Barrack, C. Barak, and H. B. Skinner, "Concerns about ceramics in THA," *Clinical Orthopaedics and Related Research,* pp. 73-79, Dec 2004.

[43] J. J. Yoo, Y.-M. Kim, K. S. Yoon, K.-H. Koo, W. S. Song, and H. J. Kim, "Alumina-on-Alumina Total Hip Arthroplasty. A Five-Year Minimum Follow-up Study," *Journal of Bone and Joint Surgery,* vol. 87, pp. 530-535, 2005.

[44] S. Williams, D. Jalali-Vahid, C. Brockett, Z. M. Jin, M. H. Stone, E. Ingham*, et al.*, "Effect of swing phase load on metal-on-metal hip lubrication, friction and wear," *Journal of Biomechanics,* vol. 39, pp. 2274-2281, 2006.

[45] S. Williams, T. D. Stewart, E. Ingham, M. H. Stone, and J. Fisher, "Metal-on-metal bearing wear with different swing phase loads," *Journal of Biomedical Materials Research Part B-Applied Biomaterials,* vol. 70B, pp. 233-239, Aug 2004.

[46] P. S. Walker and B. L. Gold, "Tribology (Friction, Lubrication and Wear) of All-Metal Artificial Hip Joints," *Wear,* vol. 17, pp. 285-&, 1971.

[47] S. Soderberg, U. Bryggman, and T. McCullough, "Frequency-Effects in Fretting Wear," *Wear,* vol. 110, pp. 19-34, 1986.

[48] G. W. Stachowiak and A. W. Batchelor, *Engineering tribology*, 3rd ed. Amsterdam; Boston: Elsevier Butterworth-Heinemann, 2005.

[49] G. Bergmann, F. Graichen, A. Rohlmann, N. Verdonschot, and G. H. van Lenthe, "Frictional heating of total hip implants. Part 1. measurements in patients," *Journal of Biomechanics,* vol. 34, pp. 421-428, 2001.

[50] A. Neville, A. Morina, T. Liskiewicz, and Y. Yan, "Synovial joint lubrication - does nature teach more effective engineering lubrication strategies?," *Proceedings of the Institution of Mechanical Engineers, Part C: Journal of Mechanical Engineering Science,* vol. 221, pp. 1223-1230, 2007.

[51] G. Willmann, "Improving bearing surfaces of artificial joints," *Advanced Engineering Materials,* vol. 3, pp. 135-141, 2001.

[52] A. Wang, A. Essner, V. K. Polineni, C. Stark, and J. H. Dumbleton, "Lubrication and wear of ultra-high molecular weight polyethylene in total joint replacements," *Tribology International,* vol. 31, pp. 17-33, Jan-Mar 1998.

[53] L. A. Knight, S. Pal, J. C. Coleman, F. Bronson, H. Haider, D. L. Levine, *et al.*, "Comparison of long-term numerical and experimental total knee replacement wear during simulated gait loading," *Journal of Biomechanics,* vol. 40, pp. 1550-1558, 2007.

[54] J. F. Archard, "Contact and Rubbing of Flat Surfaces," *Journal of Applied Physics,* vol. 24, pp. 981-988, 1953.

[55] S. Andersson, *Wear Simulation, Advanced Knowledge Application in Practice, Igor Fuerstner (Ed.)*: InTech, 2010.

[56] D. Dowson, C. Hardaker, M. Flett, and G. H. Isaac, "A hip joint simulator study of the performance of metal-on-metal joints: Part II: Design," *The Journal of Arthroplasty,* vol. 19, pp. 124-130, 2004.

[57] F. Liu, Z. Jin, P. Roberts, and P. Grigoris, "Importance of Head Diameter, Clearance, and Cup Wall Thickness in Elastohydrodynamic Lubrication Analysis of Metal-On-Metal Hip Resurfacing Prostheses," *Proceedings of the Institution of Mechanical Engineers, Part H: Journal of Engineering in Medicine,* vol. 220, pp. 695-704, 2006.

[58] C. L. Brockett, S. Williams, Z. M. Jin, G. Isaac, and J. Fisher, "A comparison of friction in 28 mm conventional and 55 mm resurfacing metal-on-metal hip replacements," *Proceedings of the Institution of Mechanical Engineers Part J-Journal of Engineering Tribology,* vol. 221, pp. 391-398, 2007.

[59] P. Grigoris, P. Roberts, K. Panousis, and Z. Jin, "Hip resurfacing arthroplasty: the evolution of contemporary designs," *Proceedings of the Institution of Mechanical Engineers Part H-Journal of Engineering in Medicine,* vol. 220, pp. 95-105, 2006.

[60] P. Roberts, P. Grigoris, H. Bosch, and N. Talwaker, "Resurfacing arthroplasty of the hip," *Current Orthopaedics,* vol. 19, pp. 263-279, Aug 2005.

[61] Z. M. Jin, S. Meakins, M. M. Morlock, P. Parsons, C. Hardaker, M. Flett, *et al.*, "Deformation of press-fitted metallic resurfacing cups. Part 1: experimental simulation," *Proceedings of the Institution of Mechanical Engineers Part H-Journal of Engineering in Medicine,* vol. 220, pp. 299-309, 2006.

[62] I. Udofia, F. Liu, Z. Jin, P. Roberts, and P. Grigoris, "The initial stability and contact mechanics of a press-fit resurfacing arthroplasty of the hip," *Journal of Bone and Joint Surgery-British Volume,* vol. 89B, pp. 549-556, 2007.

[63] J. Y. Lazennec, L. M. Jennings, J. Fisher, and B. Masson, "Two Ceramic Bearing Surfaces with a Self Adjusting cup: A New Application of Delta Ceramics to reduce the Risk of Dislocation and Subluxation," *Bioceramics and Alternative Bearings in Joint Arthroplasty,* pp. 61-66, 2005.

[64] L. M. Jennings, J. Fisher, T. D. Stewart, B. Masson, and J. Y. Lazennec, "Wear simulator study of the tripolar all ceramic hip prosthesis," *Bioceramics and Alternative Bearings in Joint Arthroplasty,* pp. 307-308, 2006.

[65] M. M. Mak and Z. M. Jin, "Effect of acetabular cup position on the contact mechanics of ceramic-on-ceramic hip joint replacements," *Bioceramics 16,* vol. 254-2, pp. 639-642, 2004.

[66] M. M. Mak, A. A. Besong, Z. M. Jin, and J. Fisher, "Effect of microseparation on contact mechanics in ceramic-on-ceramic hip joint replacements," *Proceedings of the Institution of Mechanical Engineers Part H-Journal of Engineering in Medicine,* vol. 216, pp. 403-408, 2002.

[67] M. Mak, Z. Jin, J. Fisher, and T. D. Stewart, "Influence of Acetabular Cup Rim Design on the Contact Stress During Edge Loading in Ceramic-on-Ceramic Hip Prostheses," *The Journal of Arthroplasty,* vol. 26, pp. 131-136, 2011.

[68] K. Holmberg, H. Ronkainen, A. Laukkanen, and K. Wallin, "Friction and wear of coated surfaces -- scales, modelling and simulation of tribomechanisms," *Surface and Coatings Technology,* vol. 202, pp. 1034-1049, 2007.

[69] H. A. McKellop, "The lexicon of polyethylene wear in artificial joints," *Biomaterials,* vol. 28, pp. 5049-5057, Dec 2007.

[70] J. J. Kauzlarich and J. A. Williams, "Archard wear and component geometry," *Proceedings of the Institution of Mechanical Engineers Part J-Journal of Engineering Tribology,* vol. 215, pp. 387-403, 2001.

[71] H. C. Meng and K. C. Ludema, "Wear models and predictice equations: their form and content," *Wear,* vol. 181, pp. 443-457, 1995.

[72] H. W. A. Wiskott and U. C. Belser, "Lack of integration of smooth titanium surfaces: a working hypothesis based on strains generated in the surrounding bone," *Clinical Oral Implants Research,* vol. 10, pp. 429-444, Dec 1999.

[73] S. Williams, M. Butterfield, T. Stewart, E. Ingham, M. Stone, and J. Fisher, "Wear and deformation of ceramic-on-polyethylene total hip replacements with joint laxity and swing phase microseparation," *Proceedings of the Institution of Mechanical Engineers Part H-Journal of Engineering in Medicine,* vol. 217, pp. 147-153, 2003.

[74] C. G. Figueiredo-Pina, Y. Yan, A. Neville, and J. Fisher, "Understanding the differences between the wear of metal-on-metal and ceramic-on-metal total hip replacements," *Proceedings of the Institution of Mechanical Engineers Part H-Journal of Engineering in Medicine,* vol. 222, pp. 285-296, 2008.

[75] P. J. Firkins, J. L. Tipper, E. Ingham, M. H. Stone, R. Farrar, and J. Fisher, "A novel low wearing differential hardness, ceramic-on-metal hip joint prosthesis," *Journal of Biomechanics,* vol. 34, pp. 1291-1298, 2001.

[76] J. Cawley, J. E. P. Metcalf, A. H. Jones, T. J. Band, and D. S. Skupien, "A tribological study of cobalt chromium molybdenum alloys used in metal-on-metal resurfacing hip arthroplasty," *Wear,* vol. 255, pp. 999-1006.

[77] (2012, September 13). *Birmingham Hip Resurfacing System.* Available: http://global.smith-nephew.com/us/14635_14638.htm

[78] J. Fisher, X. Q. Hu, J. L. Tipper, T. D. Stewart, S. Williams, M. H. Stone, *et al.*, "An in vitro study of the reduction in wear of metal-on-metal hip prostheses using surface-engineered femoral heads," *Proceedings of the Institution of Mechanical Engineers Part H-Journal of Engineering in Medicine,* vol. 216, pp. 219-230, 2002.

[79] I. J. Leslie, S. Williams, C. Brown, J. Anderson, G. Isaac, P. Hatto, *et al.*, "Surface Engineering: A Low Wearing Solution for Metal-On-Metal Hip Surface Replacements," *Journal of Biomedical Materials Research Part B-Applied Biomaterials,* vol. 90B, pp. 558-565, 2009.

[80] S. C. Scholes, S. M. Green, and A. Unsworth, "The wear of metal-on-metal total hip prostheses measured in a hip simulator," *Proceedings of the Institution of Mechanical Engineers Part H-Journal of Engineering in Medicine,* vol. 215, pp. 523-530, 2001.

[81] A. A. Besong, Z. M. Jin, and J. Fisher, "Importance of pin geometry on pin-on-plate wear testing of hard-on-hard bearing materials for artificial hip joints," *Proceedings of the Institution of Mechanical Engineers Part H-Journal of Engineering in Medicine,* vol. 215, pp. 605-610, 2001.

[82] Y. Yan, A. Neville, D. Dowson, S. Williams, and J. Fisher, "Tribo-corrosion analysis of wear and metal ion release interactions from metal-on-metal and ceramic-on-metal contacts for the application in artificial hip prostheses," *Proceedings of the Institution of Mechanical Engineers Part J-Journal of Engineering Tribology,* vol. 222, pp. 483-492, 2008.

[83] Y. Yan, A. Neville, D. Dowson, and S. Williams, "Tribocorrosion in implants - assessing high carbon and low carbon Co-Cr-Mo alloys by in situ electrochemical measurements," *Tribology International,* vol. 39, pp. 1509-1517, 2006.

[84] Z. M. Jin, P. Firkins, R. Farrar, and J. Fisher, "Analysis and modelling of wear of cobalt-chrome alloys in a pin-on-plate test for a metal-on-metal total hip replacement," *Proceedings of the Institution of Mechanical Engineers Part H-Journal of Engineering in Medicine,* vol. 214, pp. 559-568, 2000.

[85] J. E. Shigley and C. R. Mischke, *Mechanical engineering design*, 6th ed. Boston: McGraw Hill, 2001.

[86] R. J. Roark and W. C. Young, *Roark's formulas for stress and strain*, 6th ed. New York; London: McGraw-Hill, 1989.

[87] J. T. Mottram and C. T. Shaw, *Using finite elements in mechanical design*. London: McGraw-Hill, 1996.

[88] M. M. Mak and Z. M. Jin, "Analysis of contact mechanics and lubrication in ceramic-on-ceramic hip joint replacements," *Bioceramics 14,* vol. 218-2, pp. 531-534, 2002.

[89] M. M. Mak and Z. M. Jin, "Analysis of contact mechanics in ceramic-on-ceramic hip joint replacements," *Proceedings of the Institution of Mechanical Engineers Part H-Journal of Engineering in Medicine,* vol. 216, pp. 231-236, 2002.

[90] A. Buford and T. Goswami, "Review of wear mechanisms in hip implants: Paper I - General," *Materials & Design,* vol. 25, pp. 385-393, 2004.

[91] G. B. Cornwall, J. T. Bryant, and C. M. Hansson, "The effect of kinematic conditions on the wear of ultra-high molecular weight polyethylene (UHMWPE) in orthopaedic bearing applications," *Proceedings of the Institution of Mechanical Engineers Part H-Journal of Engineering in Medicine,* vol. 215, pp. 95-106, 2001.

[92] A. Yew, M. Jagatia, H. Ensaff, and Z. M. Jin, "Analysis of contact mechanics in McKee-Farrar metal-on-metal hip implants," *Proceedings of the Institution of Mechanical Engineers Part H-Journal of Engineering in Medicine,* vol. 217, pp. 333-340, 2003.

[93] A. Yew, M. Jagatia, H. Ensaff, and Z. M. Jin, "Analysis of contact mechanics in McKee-Farrar metal-on-metal hip implants," vol. 217, pp. 333-340, 2003.

[94] K. L. Johnson, *Contact mechanics*. Cambridge: Cambridge University Press, 1985.

[95] J. A. Williams, "The influence of repeated loading, residual stresses and shakedown on the behaviour of tribological contacts," *Tribology International,* vol. 38, pp. 786-797, 2005.

[96] T. A. Stolarski, *Tribology in machine design*: Industrial Press, Incorporated, 1990.

[97] R. Huiskes and E. Y. S. Chao, "A Survey of Finite Element Analysis in Orthopedic Biomechanics - The 1st Decade," *Journal of Biomechanics,* vol. 16, pp. 385-409, 1983.

[98] O. L. A. Harrysson, Y. A. Hosni, and J. F. Nayfeh, "Custom-designed orthopedic implants evaluated using finite element analysis of patient-specific computed tomography data: femoral-component case study," *BMC Musculoskelet Disord,* vol. 8, p. 91, 2007 Sep 2007.

[99] T. Hansen, "Virtual Medical Device Simulation using ABAQUS," presented at the 2005 ABAQUS User's Conference, 2005.

[100] N. H. Kim, D. K. Won, D. Burris, B. Holtkamp, G. R. Gessel, P. Swanson, *et al.*, "Finite element analysis and experiments of metal/metal wear in oscillatory contacts," *Wear,* vol. 258, pp. 1787-1793, 2005.

[101] D. Kluess, R. Souffrant, W. Mittelmeier, A. Wree, K. P. Schmitz, and R. Bader, "A convenient approach for finite-element-analyses of orthopaedic implants in bone contact: Modeling and experimental validation," *Computer Methods and Programs in Biomedicine,* vol. 95, pp. 23-30, Jul 2009.

[102] F. H. Dar, J. R. Meakin, and R. M. Aspden, "Statistical methods in finite element analysis," *Journal of Biomechanics,* vol. 35, pp. 1155-1161, Sep 2002.

[103] A. J. Petrella, "A General Adhesive Wear Simulation to Predict Long-Term Function of Total Joint Replacements," *ABAQUS User's Conference,* 2002.

[104] S. Pal, H. Haider, P. J. Laz, L. A. Knight, and P. J. Rullkoetter, "Probabilistic computational modeling of total knee replacement wear," *Wear,* vol. 264, pp. 701-707, 2008.

[105] A. C. Jones and R. K. Wilcox, "Finite element analysis of the spine: Towards a framework of verification, validation and sensitivity analysis," *Medical Engineering & Physics,* vol. 30, pp. 1287-1304, Dec 2008.

[106] A. A. Besong, R. Lee, R. Farrar, and Z. M. Jin, "Contact mechanics of a novel metal-on-metal total hip replacement," *Proceedings of the Institution of Mechanical Engineers Part H-Journal of Engineering in Medicine,* vol. 215, pp. 543-548, 2001.

[107] D. D. D'Lima, N. Steklov, B. J. Fregly, S. A. Banks, and C. W. Colwell, "In Vivo Contact Stresses during Activities of Daily Living after Knee Arthroplasty," *Journal of Orthopaedic Research,* vol. 26, pp. 1549-1555, Dec 2008.

[108] S. I. Heisler, *The Wiley engineer's desk reference : a concise guide for the professional engineer*, 2nd ed. New York; Chichester: Wiley, 1998.

[109] L. Kang, A. L. Galvin, Z. M. Jin, and J. Fisher, "A simple fully integrated contact-coupled wear prediction for ultra-high molecular weight polyethylene hip implants," *Proceedings of the Institution of Mechanical Engineers Part H-Journal of Engineering in Medicine,* vol. 220, pp. 33-46, 2006.

[110] "Abaqus 6.10 Documentation," *user's manual,* vol. Hibbitt, Karlsson & Sorensen Inc., Rhode Island, USA, 2010.

[111] C. M. Roarty and N. M. Grosland, "Adaptive meshing technique applied to an orthopaedic finite element contact problem," vol. 24, pp. 21-9, 2004.

[112] Z. M. Jin, S. M. Heng, H. W. Ng, and D. D. Auger, "An axisymmetric contact model of ultra high molecular weight polyethylene cups against metallic femoral heads for artificial hip joint replacements," *Proceedings of the Institution of Mechanical Engineers Part H-Journal of Engineering in Medicine,* vol. 213, pp. 317-327, 1999.

[113] T. A. Maxian, T. D. Brown, D. R. Pedersen, and J. J. Callaghan, "A sliding-distance-coupled finite element formulation for polyethylene wear in total hip arthroplasty," vol. 29, pp. 687-692, 1996.

[114] S. M. Kurtz, J. A. Ochoa, C. B. Hovey, and C. V. White, "Simulation of initial frontside and backside wear rates in a modular acetabular component with multiple screw holes," *Journal of Biomechanics,* vol. 32, pp. 967-976, 1999.

[115] K. L. Ong, S. Rundell, I. Liepins, R. Laurent, D. Markel, and S. M. Kurtz, "Biomechanical Modeling of Acetabular Component Polyethylene Stresses, Fracture Risk, and Wear Rate following Press-Fit Implantation," *Journal of Orthopaedic Research,* vol. 27, pp. 1467-1472, Nov 2009.

[116] T. A. Maxian, T. D. Brown, D. R. Pedersen, and J. J. Callaghan, "Adaptive finite element modeling of long-term polyethylene wear in total hip arthroplasty," *Journal of Orthopaedic Research,* vol. 14, pp. 668-675, 1996.

[117] J. J. Callaghan, D. R. Pedersen, R. C. Johnston, and T. D. Brown, "Clinical biomechanics of wear in total hip arthroplasty," *Iowa Orthop J,* vol. 23, pp. 1-12, 2003.

[118] C. Brockett, S. Williams, Z. M. Jin, G. Isaac, and J. Fisher, "Friction of total hip replacements with different bearings and loading conditions," *Journal of Biomedical Materials Research Part B-Applied Biomaterials,* vol. 81B, pp. 508-515, 2007.

[119] S. Scholes, A. Unsworth, and A. Goldsmith, "A frictional study of total hip joint replacements," *Physics in Medicine and Biology,* vol. 45, pp. 3721-3735, Dec 2000.

[120] I. C. Gebeshuber, "Engineering at the interface revisited," *Proceedings of the Institution of Mechanical Engineers Part C-Journal of Mechanical Engineering Science,* vol. 223, pp. 65-70, Jan 2009.

[121] R. Crockett, "Boundary Lubrication in Natural Articular Joints," *Tribology Letters,* vol. 35, pp. 77-84, Aug 2009.

[122] J. Katta, Z. M. Jin, E. Ingham, and J. Fisher, "Biotribology of articular cartilage - A review of the recent advances," vol. 30, pp. 1349-1363, Dec 2008.

[123] J. D. Bronzino, *The biomedical engineering handbook*, 3rd ed., 2006.

[124] B. J. Hamrock and D. Dowson, "Elastohydrodynamic Lubrication of Elliptical Contacts for Materials of Low Elastic-Modulus I - Fully Flooded Conjunction," *Journal of Lubrication Technology-Transactions of the Asme,* vol. 100, pp. 236-245, 1978.

[125] C. L. Brockett, P. Harper, S. Williams, G. H. Isaac, R. S. Dwyer-Joyce, Z. Jin, *et al.*, "The influence of clearance on friction, lubrication and squeaking in large diameter metal-on-metal hip replacements," *Journal of Materials Science-Materials in Medicine,* vol. 19, pp. 1575-1579, 2008.

[126] C. Chevillotte, R. T. Trousdale, Q. S. Chen, O. Guyen, and K. N. An, "The 2009 Frank Stinchfield Award "Hip Squeaking'' A Biomechanical Study of Ceramic-on-ceramic Bearing Surfaces," *Clinical Orthopaedics and Related Research,* vol. 468, pp. 345-350, Feb 2010.

[127] C. Restrepo, J. Parvizi, S. M. Kurtz, P. F. Sharkey, W. J. Hozack, and R. H. Rothman, "The noisy ceramic hip: Is component malpositioning the cause?," *Journal of Arthroplasty,* vol. 23, pp. 643-649, Aug 2008.

[128] P. A. Williams and I. C. Clarke, "Understanding polyethylene wear mechanisms by modeling of debris size distributions," *Wear,* vol. 267, pp. 646-652, 2009.

[129] G. I. Howling, P. I. Barnett, J. L. Tipper, M. H. Stone, J. Fisher, and E. Ingham, "Quantitative characterization of polyethylene debris isolated from periprosthetic tissue in early failure knee implants and early and late failure Charnley hip implants," *Journal of Biomedical Materials Research,* vol. 58, pp. 415-420, 2001.

[130] F. C. Wang, Z. M. Jin, H. M. J. McEwen, and J. Fisher, "Microscopic asperity contact and deformation of ultrahigh molecular weight polyethylene bearing surfaces," *Proceedings of the Institution of Mechanical Engineers Part H-Journal of Engineering in Medicine,* vol. 217, pp. 477-490, 2003.

[131] M. Manaka, I. C. Clarke, K. Yamamoto, T. Shishido, A. Gustafson, and A. Imakiire, "Stripe wear rates in alumina THR - Comparison of microseparation simulator study with retrieved implants," *Journal of Biomedical Materials Research Part B-Applied Biomaterials,* vol. 69B, pp. 149-157, May 2004.

[132] T. Yamamoto, M. Saito, M. Ueno, T. Hananouchi, Y. Tokugawa, and K. Yonenobu, "Wear analysis of retrieved ceramic-on-ceramic articulations in total hip arthroplasty: Femoral head makes contact with the rim of the socket outside of the bearing surface," *Journal of Biomedical Materials Research Part B-Applied Biomaterials,* vol. 73B, pp. 301-307, May 2005.

[133] R. Pourzal, R. Theissmann, S. Williams, B. Gleising, J. Fisher, and A. Fischer, "Subsurface changes of a MoM hip implant below different contact zones," *Journal of the Mechanical Behavior of Biomedical Materials,* vol. 2, pp. 186-191, Apr 2009.

[134] V. Saikko and H. G. Pfaff, "Low wear and friction in alumina/alumina total hip joints - A hip simulator study," *Acta Orthopaedica Scandinavica,* vol. 69, pp. 443-448, Oct 1998.

[135] C. M. McNie, D. C. Barton, J. Fisher, and M. H. Stone, "Modeling of damage to articulating surfaces by third body particles in total joint replacements," *Journal of Materials Science-Materials in Medicine,* vol. 11, pp. 569-578, 2000.

[136] E. Rabinowicz, *Friction and wear of materials*, 2nd ed. New York; Chichester: Wiley, 1995.

[137] D. Najjar, A. Behnamghader, A. Iost, and H. Migaud, "Influence of a foreign body on the wear of metallic femoral heads and polyethylene acetabular cups of total hip prostheses," *Journal of Materials Science,* vol. 35, pp. 4583-4588, 2000.

[138] C. M. McNie, D. C. Barton, E. Ingham, J. L. Tipper, J. Fisher, and M. H. Stone, "The prediction of polyethylene wear rate and debris morphology produced by microscopic asperities on femoral heads," *Journal of Materials Science-Materials in Medicine,* vol. 11, pp. 163-174, 2000.

[139] L. Que and L. D. T. Topoleski, "Third-body wear of cobalt-chromium-molybdenum implant alloys initiated by bone and poly(methyl methacrylate) particles," *Journal of Biomedical Materials Research,* vol. 50, pp. 322-330, 2000.

[140] T. De Baets, W. Waelput, and J. Bellemans, "Analysis of third body particles generated during total knee arthroplasty: Is metal debris an issue?," *Knee,* vol. 15, pp. 95-97, Mar 2008.

[141] M. Mirghany and Z. M. Jin, "Prediction of scratch resistance of cobalt chromium alloy bearing surface, articulating against ultra-high molecular weight polyethylene, due to third-body wear particles," *Proceedings of the Institution of Mechanical Engineers Part H-Journal of Engineering in Medicine,* vol. 218, pp. 41-50, Jan 2004.

[142] T. Shishido, K. Yamamoto, S. Tanaka, T. Masaoka, I. C. Clarke, and P. Williams, "A study for a retrieved implant of ceramic-on-ceramic total hip arthroplasty," *Journal of Arthroplasty,* vol. 21, pp. 294-298, Feb 2006.

[143] J. L. Tipper, A. Hatton, J. E. Nevelos, E. Ingham, C. Doyle, R. Streicher*, et al.*, "Alumina-alumina artificial hip joints. Part II: Characterisation of the wear debris from in vitro hip joint simulations," *Biomaterials,* vol. 23, pp. 3441-3448, 2002.

[144] C. Brown, J. Fisher, and E. Ingham, "Biological effects of clinically relevant wear particles from metal-on-metal hip prostheses," *Proceedings of the Institution of Mechanical Engineers Part H-Journal of Engineering in Medicine,* vol. 220, pp. 355-369, 2006.

[145] C. Brown, S. Williams, J. L. Tipper, J. Fisher, and E. Ingham, "Characterisation of wear particles produced by metal on metal and ceramic on metal hip prostheses under standard and microseparation simulation," *Journal of Materials Science-Materials in Medicine,* vol. 18, pp. 819-827, May 2007.

[146] I. Leslie, S. Williams, C. Brown, G. Isaac, Z. M. Jin, E. Ingham*, et al.*, "Effect of bearing size on the long-term wear, wear debris, and ion levels of large diameter metal-on-metal hip replacements - An in vitro study," *Journal of Biomedical Materials Research Part B-Applied Biomaterials,* vol. 87B, pp. 163-172, 2008.

[147] J. Halling, *Principles of tribology*. London: Macmillan, 1975.

[148] I. M. Hutchings, *Tribology: friction and wear of engineering materials*. London: Edward Arnold, 1992.

[149] J. A. Davidson, "Characteristics of Metal and Ceramic Total Hip Bearing Surfaces and Their Effect on Long-Term Ultra-High-Molecular-Weight Polyethylene," *Clinical Orthopaedics and Related Research,* pp. 361-378, 1993.

[150] P. Dearnley, "A review of metallic, ceramic and surface-treated metals used for bearing surfaces in human joint replacements," *Proceedings of the Institution of Mechanical Engineers, Part H: Journal of Engineering in Medicine,* vol. 213, pp. 107-135, 1999.

[151] L. Costa, P. Bracco, E. B. del Prever, M. P. Luda, and L. Trossarelli, "Analysis of products diffused into UHMWPE prosthetic components in vivo," *Biomaterials,* vol. 22, pp. 307-315, Feb 2001.

[152] M. H. Zhu, Z. B. Cai, W. Li, H. Y. Yu, and Z. R. Zhou, "Fretting in prosthetic devices related to human body," *Tribology International,* vol. 42, pp. 1360-1364, Sep 2009.

[153] W. J. Maloney, M. Jasty, D. W. Burke, D. O. Oconnor, E. B. Zalenski, C. Bragdon*, et al.*, "Biomechanical and Histologic Investigation of Cemented Total Hip Arthroplasties - A Study of Autopsy - Retrived Femurs After Invivo Cycing," *Clinical Orthopaedics and Related Research,* pp. 129-140, 1989.

[154] E. Ebramzadeh, F. Billi, S. N. Sangiorgio, S. Mattes, W. Schmoelz, and L. Dorr, "Simulation of fretting wear at orthopaedic implant interfaces," *Journal of Biomechanical Engineering-Transactions of the Asme,* vol. 127, pp. 357-363, Jun 2005.

[155] D. W. Hoeppner and V. Chandrasekaran, "Fretting in orthopaedic implants: A review," *Wear,* vol. 173, pp. 189-197, 1994.

[156] J. Fisher, D. Dowson, H. Hamdzah, and H. L. Lee, "The Effect of Sliding Velocity on the Friction and Wear of UHMWPE for use in Total Artificial Joints," *Wear,* vol. 175, pp. 219-225, Jun 1994.

[157] S. M. Hsu, M. C. Shen, and A. W. Ruff, "Wear prediction for metals," *Tribology International,* vol. 30, pp. 377-383, May 1997.

[158] I. G. Goryacheva, *Contact Mechanics in Tribology*: Springer.

[159] S. K. Wong, A. Kapoor, and J. A. Williams, "Shakedown limits on coated surfaces," *Thin Solid Films,* vol. 292, pp. 156-163, 1997.

[160] S. Foletti and H. J. Desimone, "Application of shakedown maps under variable loads," *Engineering Fracture Mechanics,* vol. 74, pp. 527-538, 2007.

[161] H. S. Yu and J. B. Burland, *Plasticity and Geotechnics*: Springer, 2006.

[162] *Materials and Coatings for Medical Devices: Cardiovascular*: ASM International, 2009.

[163] J. A. Williams, I. N. Dyson, and A. Kapoor, "Repeated loading, residual stresses, shakedown, and tribology," *Journal of Materials Research,* vol. 14, pp. 1548-1559, Apr 1999.

[164] K. L. Johnson, "The application of shakedown principles in rolling and sliding contact," *Eur. J. Mech., A/Solids,* vol. 11, pp. 155-172, 1992.

[165] J. Williams, *Engineering Tribology*: Oxford University Press, 1994.

[166] A. Kamali, A. Hussain, C. Li, J. Pamu, J. Daniel, H. Ziaee*, et al.*, "Tribological performance of various CoCr microstructures in metal-on-metal bearings the development of a more physiological protocol in vitro," *Journal of Bone and Joint Surgery-British Volume,* vol. 92B, pp. 717-725, May 2010.

[167] A. Kapoor, J. A. Williams, and K. L. Johnson, "The Steady State Sliding of Rough Surfaces," *Wear,* vol. 175, pp. 81-92, Jun 1994.

[168] A. Kapoor, K. L. Johnson, and J. A. Williams, "A model for the mild ratchetting wear of metals," *Wear,* vol. 200, pp. 38-44, Dec 1996.

[169] A. Kapoor, "Wear by plastic ratchetting," *Wear,* vol. 212, pp. 119-130, 1997.

[170] B. Bhushan, "Contact mechanics of rough surfaces in tribology: multiple asperity contact," *Tribology Letters,* vol. 4, pp. 1-35, Jan 1998.

[171] I. J. Udofia and Z. M. Jin, "Elastohydrodynamic lubrication analysis of metal-on-metal hip-resurfacing prostheses," *Journal of Biomechanics,* vol. 36, pp. 537-544, 2003.

[172] T. Kilner, W. M. Laanemae, R. Pilliar, G. C. Weatherly, and S. R. MacEwen, "Static mechanical properties of cast and sinter-annealed cobalt-chromium surgical implants," *Journal of Materials Science,* vol. 21, pp. 1349-1356, 1986.

[173] H. Yildiz, F.-K. Chang, and S. Goodman, "Composite hip prosthesis design. II. Simulation," *Journal of Biomedical Materials Research,* vol. 39, pp. 102-119, 1998.

[174] S. R. Williams, J. J. Wu, A. Unsworth, and I. Khan, "Tribological and surface analysis of 38mm alumina–as-cast Co–Cr–Mo total hip arthroplasties," *Proceedings of the Institution of Mechanical Engineers, Part H: Journal of Engineering in Medicine,* vol. 223, pp. 941-954, 2009.

[175] N. S. Vandamme, L. Que, and L. D. T. Topoleski, "Carbide surface coating of Co-Cr-Mo implant alloys by a microwave plasma-assisted reaction," *Journal of Materials Science,* vol. 34, pp. 3525-3531, Jul 15 1999.

[176] "International Organization for Standardization: ISO/TR 10108:1989," *Steel -- Conversion of hardness values to tensile strength values,* 1989.

[177] P. Diamantopoulos and J. D. Richardson, "Application of an interface system for the development of a three dimensional finite element model of the knee joint using magnetic resonance imaging (MRI) data," in *4th International Symposium on Computer Methods in Biomechanics and Biomedical Engineering*, Lisbon, Portugal, 1999, pp. 437-443.

[178] S. H. Pettersen, "Subject Specific Finite Element Analysis of Bone - for the evaluation of the healing of a leg lengthening and evaluation of femoral stem design," Thesis for the degree of Philosophiae Doctor, Faculty of Engineering Science and Technology, Norwegian University of Science and Technology, 2009.

[179] J. Wilkinson, "Measuring bone mineral density of the pelvis and proximal femur after total hip arthroplasty," *J Bone Joint Surg Br.,* vol. 83-B, No. 2, 2001.

[180] J. Y. Rho, R. B. Ashman, and C. H. Turner, "Young's modulus of trabecular and cortical bone material: Ultrasonic and microtensile measurements," *Journal of Biomechanics,* vol. 26, pp. 111-119, 2// 1993.

[181] D. R. Carter and W. C. Hayes, "Compressive Behavior of Bone as a 2-Phase Porous Structure," *Journal of Bone and Joint Surgery-American Volume,* vol. 59, pp. 954-962, 1977.

[182] M. Doblare, J. M. Garcia, and M. J. Gomez, "Modelling bone tissue fracture and healing: a review," *Engineering Fracture Mechanics,* vol. 71, Sep 2004.

[183] I. Li, H. Li, L. Shi, A. S. L. Fok, C. Ucer, H. Deulin*, et al.*, "A mathematical model for simulating the bone remodeling process under mechanical stimulus," *Dental Materials,* vol. 23, Sep 2007.

[184] D. C. Wirtz, N. Schiffers, T. Pandorf, K. Radermacher, D. Weichert, and R. Forst, "Critical evaluation of known bone material properties to realize anisotropic FE-simulation of the proximal femur," *Journal of Biomechanics,* vol. 33, Oct 2000.

[185] B. Couteau, L. Labey, M. C. Hobatho, J. Vander Sloten, J. Y. Arlaud, and J. C. Brignola, "Validation of a three dimensional finite element model of a femur with a customized hip implant," *Computer Methods in Biomechanics & Biomedical Engineering - 2,* 1998.

[186] E. J. Cheal, M. Spector, and W. C. Hayes, "Role of loads and prosthesis material properties on the mechanics of the proximal femur after total hip arthroplasty," *Journal of Orthopaedic Research,* vol. 10, pp. 405-422, 1992.

[187] G. Bergmann, F. Graichen, A. Rohlmann, A. Bender, B. Heinlein, G. N. Duda*, et al.*, "Realistic loads for testing hip implants," *Bio-Medical Materials and Engineering,* vol. 20, pp. 65-75, 2010.

[188] J. P. Paul, "Paper 8: Forces Transmitted by Joints in the Human Body," *Proceedings of the Institution of Mechanical Engineers, Conference Proceedings,* vol. 181, pp. 8-15, 1966.

[189] G. Bergmann, G. Deuretzbacher, M. Heller, F. Graichen, A. Rohlmann, J. Strauss*, et al.*, "Hip contact forces and gait patterns from routine activities," *Journal of Biomechanics,* vol. 34, pp. 859-871, Jul 2001.

[190] H. F. El'Sheikh, B. J. MacDonald, and M. S. J. Hashmi, "Finite element simulation of the hip joint during stumbling: a comparison between static and dynamic loading," *Journal of Materials Processing Technology,* vol. 143-144, pp. 249-255, 2003.

[191] A. Z. Senalp, O. Kayabasi, and H. Kurtaran, "Static, dynamic and fatigue behavior of newly designed stem shapes for hip prosthesis using finite element analysis," vol. 28, pp. 1577-1583, 2007.

[192] Simulia, "Abaqus 6.9 Online Documentation," ed, 2009.

[193] F. J. Harewood and P. E. McHugh, "Comparison of the implicit and explicit finite element methods using crystal plasticity," *Computational Materials Science,* vol. 39, pp. 481-494, 4// 2007.

[194] J. P. Halloran, A. J. Petrella, and P. J. Rullkoetter, "Explicit finite element modeling of total knee replacement mechanics," *Journal of Biomechanics,* vol. 38, pp. 323-331, 2005.

[195] M. Viceconti, L. Bellingeri, L. Cristofolini, and A. Toni, "A comparative study on different methods of automatic mesh generation of human femurs," *Medical Engineering & Physics,* vol. 20, pp. 1-10, Jan 1998.

[196] J. Farley, "Development of a Computational Method of Low Cycle Fatigue Prediction for Multi-Layer Surfaces under Rolling/Sliding Conatact Conditions," Ph.D. dissertation, School of Engineering and Design, Brunel University, 2008.

[197] D. G. Steele and C. A. Bramblett, *The Anatomy and Biology of the Human Skeleton*: Texas A&M University Press, 1988.

[198] G. Bergmann, "Do ISO tests for knee implants simulate the real loading in patients," presented at the International Conference of the Polish Society of Biomechanics: Biomechanics 2012, Bialystok, Poland, 2012.

[199] E. Sariali, T. Stewart, Z. Jin, and J. Fisher, "258. Consequences of Edge Loading on the Friction Coefficient of Ceramic-On-Ceramic Total Hip Arthroplasty: Application for Squeaking," *Journal of Bone & Joint Surgery, British Volume,* vol. 93-B, pp. 534-534, 2011.

[200] S. Bhattacharya, "Predictive Finite Element Modeling of Artificial Cervical Discs in a Ligamentous Functional Spinal Unit," Ph.D. dissertation, The University of Toledo, 2011.

[201] B. Kanavalli, "Application of User Defined subroutine UMESHMOTION in ABAQUS for simulatiing dry rolling/sliding wear," Master's thesis, Scientific Computing, Royal Institute of Technology (KTH), 2006.

[202] V. Hegadekatte, N. Huber, and O. Kraft, "Finite element based simulation of dry sliding wear," *Modelling and Simulation in Materials Science and Engineering,* vol. 13, pp. 57-75, 2005.

[203] P. Podra and S. Andersson, "Simulating sliding wear with finite element method," *Tribology International,* vol. 32, pp. 71-81, Feb 1999.

[204] H. Goldstein, *Classical mechanics*: Addison-Wesley Pub. Co., 1980.

[205] G. B. Arfken, H. J. Weber, and F. E. Harris, *Mathematical Methods for Physicists: A Comprehensive Guide*: Academic Press, 2012.

[206] J. Liberty, *Programming Visual Basic .Net*: O'Reilly, 2003.

[207] S. Roman, R. Petrusha, and P. Lomax, *VB.NET Language Pocket Reference*: O'Reilly Media, 2002.

[208] A. R. S. Ponter, H. F. Chen, M. Ciavarella, and G. Specchia, "Shakedown analyses for rolling and sliding contact problems," *International Journal of Solids and Structures,* vol. 43, pp. 4201-4219, 2006.

[209] J. K. Lord, D. J. Langton, A. V. F. Nargol, and T. J. Joyce, "Volumetric wear assessment of failed metal-on-metal hip resurfacing prostheses," *Wear,* vol. 272, pp. 79-87, 2011.

[210] K. Johnson and J. Jefferis, "Plastic flow and residual stress in rolling and sliding contact," in *Symposium on Rolling Contact Fatigue*, London, 1962, p. p.50.

[211] R. E. Smallman and R. J. Bishop, "Modern Physical Metallurgy and Materials Engineering - Science, Process, Applications," 6th ed: Elsevier, 1999.

[212] H. Sharma, B. Rana, C. Watson, A. C. Campbell, and B. J. Singh, "Femoral neck fractures complicating metal-on-metal resurfaced hips," *Journal of Bone & Joint Surgery, British Volume,* vol. 87-B, pp. 48-48, 2005.

[213] D. R. Marker, T. M. Seyler, R. H. Jinnah, R. E. Delanois, S. D. Ulrich, and M. A. Mont, "Femoral neck fractures after metal-on-metal total hip resurfacing," *Journal of Arthroplasty,* vol. 22, pp. 66-71, 2007.

Appendix A – Normal and Edge Loading Factors

	Sub-system	Ref.	Factor	Factor Description
Operating	General	O1	Lubrication regime	The lubricating film between the cup and head
		O2	Lubrication fluid properties	The properties of the lubricant
		O3	Hip impingement	Between femoral head and acetabular cup
		O4	Microseparation	Laxity of the hip joint after orthopaedic device implantation leading to microseparation between the joint.
		O5	Implant laxity	Looseness between the femoral head and acetabular cup
		O6	Coefficient of friction	The coefficient of friction between the cup and head
Design	Femoral component	D1a	Femoral Head Diameter	The external diameter of the femoral head component
		D1b	Sphericity	The sphericity of the femoral component
	Cup Component	D2a	Cup Diameter	The internal diameter of the cup component
		D2b	Sphericity	The sphericity of the cup component
		D2c	Cup Rim Design	Radius dimension
	General	D3	Diametral Clearance	The clearance between the femoral head and cup components
Materials	Material selection	MT1a	Femoral Component	The choice of material for the femoral head component
		MT1b	Cup Component	The choice of material for the acetabular cup component
	General	MT2	Material stress-strain relationship	The stress-strain profile of the material including the elasticity and plasticity regions
		MT3	Modulus	The modulus of elasticity of the implant materials
		MT4	Poisson's ratio	Poisson's ratio of the material
		MT5	Material hardening	Material hardening under cyclic loading
		MT6	Material reactions	Reactions to body environments including reactions of the material to joint temperatures and fluid environment properties
Manufac-turing	General	M1	Material defects	Surface and subsurface defects including micro and nano sized cracks.
		M2	Surface finish	Post manufacture surface finish, roughness and asperity profile.
Installation	General	I1	Implant positioning	The position of the implant post installation
		I2	Cup inclination angle	The inclination angle of the cup when installed into the patient
		I3	Pelvis to cup fixation	The fixation rigidity and integrity between the pelvis and cup
		I4	Cup anteversion (or retroversion) angle	Following surgical implantation
		I5	Head to femur fixation	The fixation rigidity and integrity between the femur and head
	Implant rotation and loading	RL1	Flexion-extension profiles	Flexion (+) and extension (-) about the *x*-axis
		RL2	Adduction-abduction	Adduction (+) and abduction (-) about the *z*-axis
		RL3	Inward-outward rotation	Inward (+) and outward (-) rotation and the *y*-axis
		RL4	Axial loading	The loading along the y axis varying during the gait cycle
		RL5	Edge load displacement	The magnitude of the edge load displacement during the gait cycle
	Pelvis	P1	Pelvis geometry	Model of the pelvis
		P2	Pelvis material properties	Material properties including, modulus of elasticity, Poisson's ratio, model assumptions and density based material models
	Femur	F1	Femur geometry	Model of femur
		F2	Femur material properties	Material properties including, modulus of elasticity, Poisson's ratio, model assumptions and density based material models
Modelling	General	MO1	Static, quasi-static or dynamic modelling	Modelling the problem based under static, quasi-static or dynamic loading conditions using an implicit or explicit finite element solver
		MO2	Modelling parameters	Finite element mesh, element types, solver, mesh density
		MO3	Boundary conditions	Assumptions of constraints, applications of loading conditions and rotations
Shake-down	General	S1	Shakedown analysis at global level	Impact of shakedown normal, edge loading and severe loading conditions in relation to global shakedown maps
		S2	Shakedown analysis at asperity level	Asperity contact shakedown analysis based on the asperity height.

Appendix B – Activity Force Plate Loading

B-1. Activities for Force Plate Testing

The main human activity considered within literature is the walking cycle (such as the Paul curve), which is also the main activity applied during experimental hip simulator studies. As well as static loads, more strenuous activities are also considered. Jumping activity on both legs and each leg independently could provide more understanding of dynamic loading conditions. Although the jogging and running speeds and kinematics would be subjective, the disparity would capture the variation expected between patients. A stumbling (lunge type) activity in three directions could be categorised to include: forwards stumbling (0°), semi-sideways forward stumbling (45°), sideways stumbling (90°), semi-sideways backward stumbling (135°) and backwards stumbling (180°). The angles could be measured with the expectance that the angles are accurate to within $\pm 2.5^\circ$, as a higher accuracy than this can not be expected from participants during the stumbling motion (Figure B1). By studying the range of activities measured directly from patients using 'smart implants' at the Julius Wolff Institute, it is felt that the range of activities covered within this proposed experimental plan will cover a range of typical and extreme patient activity cases.

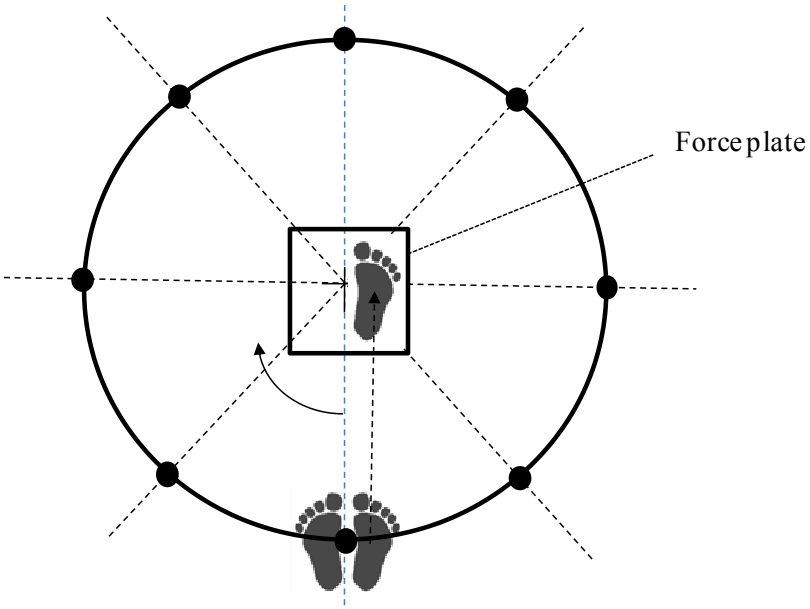

Figure B1. Stumbling motions

Table B1. Passive reflective marker positions

Marker	**Description**
LASI	Lateral anterior superior iliac
MASI	Medial anterior superior iliac
LPSI	Lateral posterior superior iliac
MPSI	Medial posterior superior iliac
LEK	Lateral epicondyle knee
MEK	Medial epicondyle knee
LFI	Lateral fibula inferior
MTI	Medial tibia inferior

The gait lab used during this study had a force plate with sampling rate of 1000 Hz which could withstand a maximum force of 2500N. If a comparison of kinematics is required, then motion sensors can be used with a total of 8 passive reflective markers placed in the positions as detailed in Table B1. All motion capturing can be conducted on one leg for consistency, with the assumption of symmetry between both legs.

B-2. Testing sheet

Date:	
Subject Code:	
Height:	
Weight:	
Age:	

Test procedure

1) If using motion sensors position them on the subject and calibrate.
2) Check the loading test plate is active
3) Conduct the tests shown in Table B2 and record all results in files (tick in table when test complete). Repeat each motion three times i.e. R.1 to R.3.

Table B2. Motion recordings

Ref.	Motion Description	R.1	R.2	R.3
FSL	Forward stumbling (left leg)			
FSR	Forward stumbling (right leg)			
SSSFSL	Semi-sideways stumbling (45 ˚) left leg			
SSSFSR	Semi-sideways stumbling (45 ˚) right leg			
SSFSL	Sideways stumbling (90 ˚) left leg			
SSFSR	Sideways stumbling (90 ˚) right leg			
SSBSL	Semi-sideways backward stumbling (135 ˚) left leg			
SSBSR	Semi-sideways backward stumbling (135 ˚) right leg			
BSL	Backwards stumbling (180 ˚) left leg			
BSR	Backwards stumbling (180 ˚) right leg			
WL	Forward walking (left leg)			
WR	Forward walking (right leg)			
BL	Backward walking (left leg)			
BR	Backward walking (right leg)			
JL	Forward jumping (left leg)			
JR	Forward jumping (right leg)			
JB	Forward jumping (both legs)			
JH	Jumping from height (both legs)			

B-3. Activity Loading

Through a number of activities studied the F_x, F_y and F_z forces could be recorded, however only the force magnitude F_{mag} from a test are shown (Figure B2 to Figure B4).

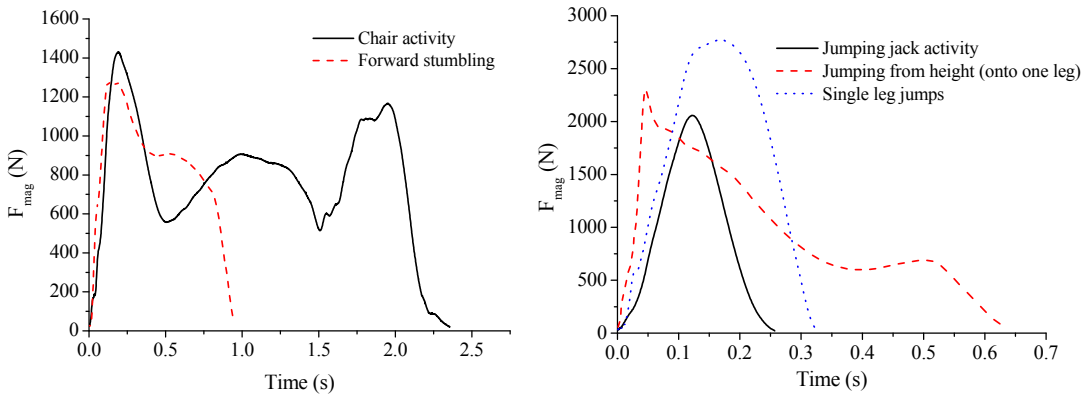

Figure B2. One cycle of (a) chair activity and forward stumbling (b) jumping jack activity, jumping from height onto one leg and single leg jumps

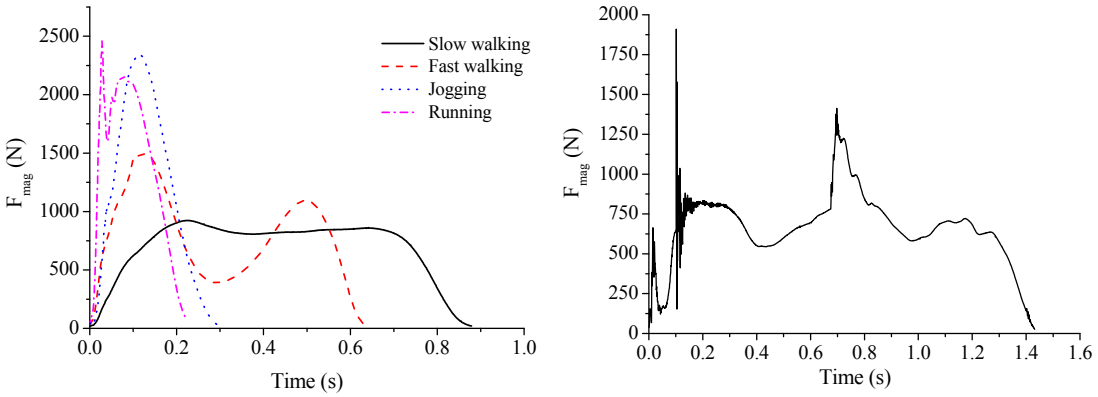

Figure B3. One cycle of (a) slow walking, fast walking, jogging and running (b) step up/step down activity

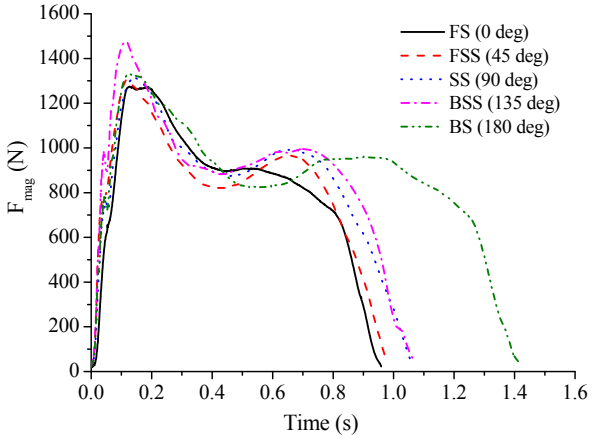

Figure B4. Stumbling force magnitude at defined angles

Appendix C – Lubrication of Hip Implant Devices

The lubricating synovial fluid between articulating joint surfaces is known as a non-Newtonian fluid, where the viscosity of the fluid is not constant [C1, C2]. The ideal combination for high performing lubrication is a healthy articulating joint which has synovial fluid with sufficient viscosity and suitable joint contact speed to enable hydrodynamic lubrication [C3]. Articulating hip joints are expected to experience both sliding and rolling contact, at a speed between 0.03 and 0.3 m/s [C4]. In addition to speed, viscosity is an important property for effective joint lubrication. Medical conditions such as rheumatoid arthritis can lower the viscosity of the synovial fluid and therefore reduce its effectiveness in adequately lubricating the articulating surface. Explanations of cartilage and synovial fluid lubrication are provided by Neville et al. [C4] and Ateshian et al. [C5]. A simplistic explanation of synovial fluid composition is that it contains 85% water and is a dialysate of blood plasma with hyaluronic acid. It contains complex proteins and polysaccharides along with other components [C6].

When considering lubrication, one must emphasise the point of friction and wear being different entities. From a tribological wear and surface damage perspective, the ideal way to control friction and wear for articulating joints is through separating them by a film of lubricant [C7]. Therefore, the purpose of the lubricant is to reduce the wear and friction of the contacting surfaces. For any lubricant to achieve this during high normal contact, edge loading contact or any other loading contact is a difficult task. It is therefore important to understand what possible lubricating regimes may occur between the engineering bearing surfaces. There are five possible lubrication situations between the contact of materials which are: hydrodynamic, elastohydrodynamic, transition from hydrodynamic to boundary lubrication, boundary and dry (i.e. no lubrication) [C2, C6]. The effect of the lubrication regime on the coefficient of friction between bodies in contact can be described by the Stribeck curve (Figure C1). The non-dimensional number is known as the Hersey number (H_s), which is determined from the absolute viscosity (η) with units Pa · s, rotational speed (ω) in revolutions per second (rps) and pressure (Pa) [C8].

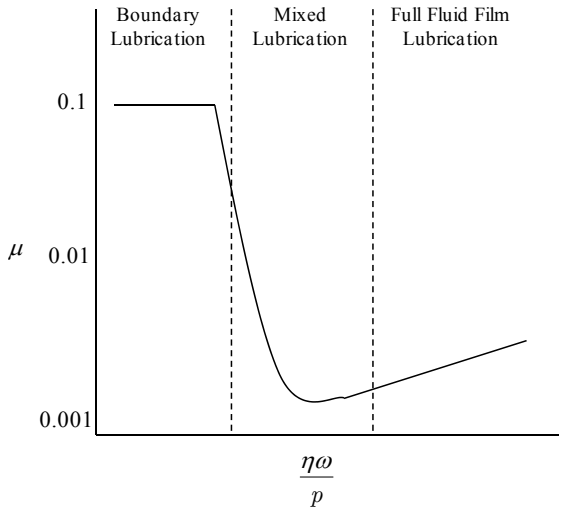

Figure C1. Stribeck curve [C3], [C9]

The concepts of hydrodynamic lubrication, elastohydrodynamic lubrication, microelastohydro-dynamic lubrication, squeeze film lubrication and weeping (or boosted) lubrication for artificial joint implants and the natural joint is summarised by Hall et al. [C10]. The principle of full fluid film lubrication would significantly help to reduce the surface damage and wear, however to obtain full fluid film lubrication with 'hard' bearings (i.e. metal-on-metal) under physiological conditions is very challenging [C11].

Theoretical lubrication models have aided the understanding of achieving full hydrodynamic lubrication between natural and artificial joints. Extensive research by Jin and Dowson provide confidence in the possibility of full hydrodynamic lubrication between artificial hip replacements with high elastic modulus during the walking gait cycle [C12]. However, the theoretical model does have its limitations such as, not considering elastohydrodynamic lubrication (EHL) caused by local elastic deformation of the bearing surfaces. There are a number of numerical methods available for elastohydrodynamic lubrication which includes Newton-Raphson, multi-grid, multi-level multi-integration and fast Fourier transform techniques which are all compared by Gao et al. [C13]. The difficulty and indeed a limitation of these studies is that experimental data was not available for comparisons against theoretical models to be made. Nevertheless, on a practical level it was demonstrated that fluid film lubrication was possible by maintaining a good surface finish of the bearing surfaces [C14]. The lubricating fluid film thickness between the hip bearing surfaces would vary greatly due to different operating conditions. This could therefore explain the large variations in results from hip simulator studies and highlight the need to consider realistic loading and kinematic conditions for studying the tribology of hip joints [C15]. As with the previous studies discussed within this literature review, only the walking cycle is considered and more complex factors such as surface roughness or asperities which could effect the lubrication were not included.

The research for feasible occurrences of elastohydrodynamic lubrication between hip implants and its association with edge loaded hip bearing surfaces have been studied [C16]. It was noted that a very small radial clearance between the bearing surfaces could lead to breakdown of the lubricant films, asperity contact as well as edge loading. Although the finite element contact modelling in this project assumes perfectly spherical bearing surfaces, within literature, an EHL model was developed for non-spherical bearing surfaces of a total hip replacement. Under walking conditions and a sphericity tolerance of ± 6 µm, a 43 % and 17 % change of predicted film thickness and pressure occurred respectively [C17]. A similar study was conducted to assess the impact of geometry changes of the metal-on-metal (MoM) total hip replacement bearing surfaces with EHL [C18]. Out of roundness from the manufacturing process can lead to a smaller lubricant film thickness and larger contact pressure. Based on the theoretical models and simplified assumptions, gradual increases in wear of the surface during running-in phase provides improved conformity, lubrication and therefore reduced wear. An attempt was made to combine the affects of lubrication with surface wear. A mixed lubrication study was completed by Jin et al, to predict the wear of MoM artificial hip joints along with the asperity load sharing ratio [C19]. Although this was only a theoretical study, the results claimed to be comparable to experimental results.

To understand the impact of start-up as well as steady state conditions to implant wear rates, a number of lubrication studies have been carried out. A study by Jin et al. provides a full transient EHL analysis for a simple ball-on-plane model to assess the effect of start-up conditions. The research shows that variation in speed and load during start-up has only a small effect on the predicted lubricant film thickness and a repetitive cyclic lubricant film thickness is established after start-up [C20]. A paper more recently published by Jin et al. provides an analysed EHL model for artificial hip joints under steady state conditions. This is used to study the effect of the acetabular cup anatomical position, 3D loading and motion on the lubrication between the bearing surfaces. A cup inclination of up to 45° which is the nominal cup inclination angle used in this project, has negligible effect on both the predicted lubricant film thickness and pressure under the condition of physiological loading [C21]. Both radial clearance and material backing (i.e. bone and cement) were investigated and these parameters had only a small effect on the predicted lubrication film thickness that occurred [C22]. Although the effect of radial clearance on the contact mechanics of hip resurfacing devices is studied, material backing is less understood. One particular study had used FEM and the finite difference method (FDM) for the study of EHL of MoM hip implants. Acetabular cup backing materials did not affect the predicted contact pressure and bearing surface elastic deformation [C23]. However, it should be noted that only a two dimensional section model was used and only the backing material of the cup was discussed. To complete the discussion on design parameters, head diameter, clearance and wall cup thickness all contributed to promoting EHL between the cup and femoral head [C12], [C24]. According to the study carried out by Liu et al., a reduction in metallic wall thickness and an increase in polyethylene backing thickness led to an increase in predicted film thickness and reduction in hydrodynamic pressure [C25], which is useful literature to provide justification for using polyethylene backed design, however this is only based on theoretical models.

Appendix C References

[C1] Higginso. Gr and R. Norman, "Lubrication of Porous Elastic Solids with reference to functioning of human joints," *Journal of Mechanical Engineering Science,* vol. 16, pp. 250-257, 1974.

[C2] D. Dowson, A. Unsworth, and v. wright, "Analysis of Boosted-Lubrication in Human Joints," *Journal of Mechanical Engineering Science,* vol. 12, pp. 364-369, 1970.

[C3] G. W. Stachowiak, *Engineering Tribology / Gwidon W. Stachowiak, Andrew W. Batchelor*, 3rd ed. Amsterdam; Boston: Elsevier Butterworth-Heinemann, 2005.

[C4] A. Neville, A. Morina, T. Liskiewicz, and Y. Yan, "Synovial joint lubrication - does nature teach more effective engineering lubrication strategies?," *Proceedings of the Institution of Mechanical Engineers, Part C: Journal of Mechanical Engineering Science,* vol. 221, pp. 1223-1230, 2007.

[C5] G. Ateshian and C. Hung, "The natural synovial joint: Properties of cartilage," *Proceedings of the Institution of Mechanical Engineers, Part J: Journal of Engineering Tribology,* vol. 220, pp. 657-670, 2006.

[C6] J. D. Bronzino, *The Biomedical Engineering Handbook*, 3rd ed., 2006.

[C7] D. Dowson, "Engineering at the interface (Reprinted from vol 1, 1959)," *Proceedings of the Institution of Mechanical Engineers Part C-Journal of Mechanical Engineering Science,* vol. 223, pp. 85-101, Jan 2009.

[C8] B. J. Hamrock, S. R. Schmid, and B. O. Jacobson, *Fundamentals of Fluid Film Lubrication*: Taylor & Francis, 2004.

[C9] *The Engineering Handbook / editor-in-chief, Richard C. Dorf*: CRC Press: IEEE Press, 1996.

[C10] R. M. Hall, M. J. K. Bankes, and G. Blunn, "Biotribology for Joint Replacement," *Current Orthopaedics,* vol. 15, pp. 281-290, Aug 2001.

[C11] G. H. Isaac, J. Thompson, S. Williams, and J. Fisher, "Metal-on-metal bearings surfaces: materials, manufacture, design, optimization, and alternatives," *Proceedings of the Institution of Mechanical Engineers Part H-Journal of Engineering in Medicine,* vol. 220, pp. 119-133, 2006.

[C12] Z. M. Jin and D. Dowson, "A full numerical analysis of hydrodynamic lubrication in artificial hip joint replacements constructed from hard materials," *Proceedings of the Institution of Mechanical Engineers Part C-Journal of Mechanical Engineering Science,* vol. 213, pp. 355-370, 1999.

[C13] L. M. Gao, Q. E. Meng, F. C. Wang, P. R. Yang, and Z. M. Jin, "Comparison of numerical methods for elastohydrodynamic lubrication analysis of metal-on-metal hip implants: multi-grid verses Newton-Raphson," *Proceedings of the Institution of Mechanical Engineers Part J-Journal of Engineering Tribology,* vol. 221, pp. 133-140, 2007.

[C14] Z. M. Jin, D. Dowson, and J. Fisher, "Analysis of fluid film lubrication in artificial hip joint replacements with surfaces of high elastic modulus," *Proceedings of the Institution of Mechanical Engineers Part H-Journal of Engineering in Medicine,* vol. 211, pp. 247-256, 1997.

[C15] L. M. Gao, F. C. Wang, P. R. Yang, and Z. M. Jin, "Effect of 3D physiological loading and motion on elastohydrodynamic lubrication of metal-on-metal total hip replacements," *Medical Engineering & Physics,* vol. 31, pp. 720-729, 2009.

[C16] F. Liu, Z. M. Jin, P. Roberts, and P. Grigoris, "Effect of bearing geometry and structure support on transient elastohydrodynamic lubrication of metal-on-metal hip implants," *Journal of Biomechanics,* vol. 40, pp. 1340-1349, 2007.

[C17] F. C. Wang and Z. M. Jin, "Effect of non-spherical bearing geometry on transient elastohydrodynamic lubrication in metal-on-metal hip joint implants," *Proceedings of the Institution of Mechanical Engineers Part J-Journal of Engineering Tribology,* vol. 221, pp. 379-389, 2007.

[C18] F. Liu, Z. M. Jin, F. Hirt, C. Rieker, P. Roberts, and P. Grigoris, "Effect of wear of bearing surfaces on elastohydrodynamic lubrication of metal-on-metal hip implants," *Proceedings of the Institution of Mechanical Engineers Part H-Journal of Engineering in Medicine,* vol. 219, pp. 319-328, 2005.

[C19] Z. M. Jin, "Analysis of mixed lubrication mechanism in metal-on-metal hip joint replacements," *Proceedings of the Institution of Mechanical Engineers Part H-Journal of Engineering in Medicine,* vol. 216, pp. 85-89, 2002.

[C20] D. Jalali-Vahid, Z. M. Jin, and D. Dowson, "Effect of start-up conditions on elastohydrodynamic lubrication of metal-on-metal hip implants," *Proceedings of the Institution of Mechanical Engineers Part J-Journal of Engineering Tribology,* vol. 220, pp. 143-150, 2006.

[C21] F. Wang and Z. Jin, "Elastohydrodynamic Lubrication modelling of Artificial Joints Under Steay-State Conditions," vol. Vol. 127, ed: Journal of Tribology, 2005, pp. pp. 729-739.

[C22] I. J. Udofia and Z. M. Jin, "Elastohydrodynamic lubrication analysis of metal-on-metal hip-resurfacing prostheses," *Journal of Biomechanics,* vol. 36, pp. 537-544, 2003.

[C23] M. Jagatia and Z. M. Jin, "Elastohydrodynamic lubrication analysis of metal-on-metal hip prostheses under steady state entraining motion," *Proceedings of the Institution of Mechanical Engineers Part H-Journal of Engineering in Medicine,* vol. 215, pp. 531-541, 2001.

[C24] F. Liu, Z. Jin, P. Roberts, and P. Grigoris, "Importance of Head Diameter, Clearance, and Cup Wall Thickness in Elastohydrodynamic Lubrication Analysis of Metal-On-Metal Hip Resurfacing Prostheses," *Proceedings of the Institution of Mechanical Engineers, Part H: Journal of Engineering in Medicine,* vol. 220, pp. 695-704, 2006.

[C25] F. Liu, Z. M. Jin, and D. Dowson, "Investigation into the effect of a sandwich acetabular cup upon lubricant film thickness in metal-on-metal total hip replacements," *Proceedings of the Institution of Mechanical Engineers Part J-Journal of Engineering Tribology,* vol. 220, pp. 151-158, 2006.

Appendix D – Computer Hardware and Software

All computer systems for computational modelling were used with a 64-bit Windows 7 operating system, however Linux was used for certain programming tasks.

Analysis system 1	**Laptop (portable workstation)**
Processor:	Intel® Core™ i5 CPU M450 @ 2.40 GHz (2 cores, 4 threads)
Memory:	4.00 GB RAM
Hard drive:	Samsung HN-M101M SATA-II 5400 rpm
Graphics:	ATI mobility Radeon HD 5400 Series

Analysis system 2	**Pre-built workstation**
Processor:	Intel® Core 2 Duo™ E7400 @ 2.80 GHz
Memory:	8.00 GB RAM
Hard drive:	Hitachi HDT721016SLA380 ATA (160 GB)
Graphics:	RDPDD Chained DD

Analysis system 3	**Custom built workstation (see Figure D1)**
Processor:	Intel® Core™ i7 CPU M450 @ 3.50 GHz (overclocked to 4.22 GHz and validated using Prime95 and CPU-Z)
Memory:	32.00 GB RAM
Hard drive:	Seagate ST1000DM005 HD103SJ (1000 GB) and Kingston SVP200S3120G (120 GB) solid state hard drive
Graphics:	Intel® HD Graphics 4000

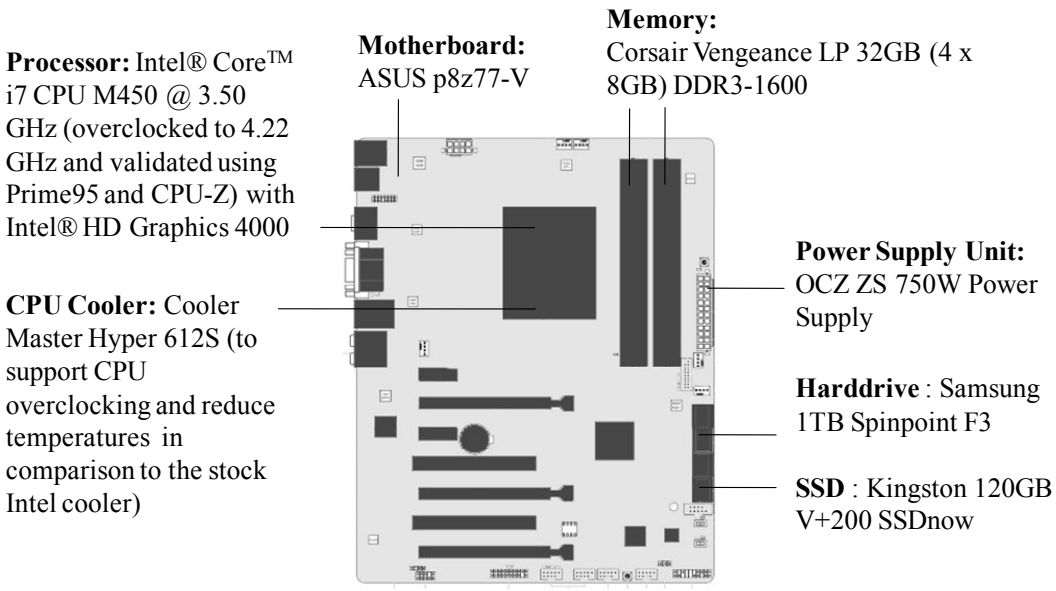

Figure E1. Custom built workstation

Appendix E – Wear Modelling Subroutines and Scripts

E.1. Wear Modelling Subroutine

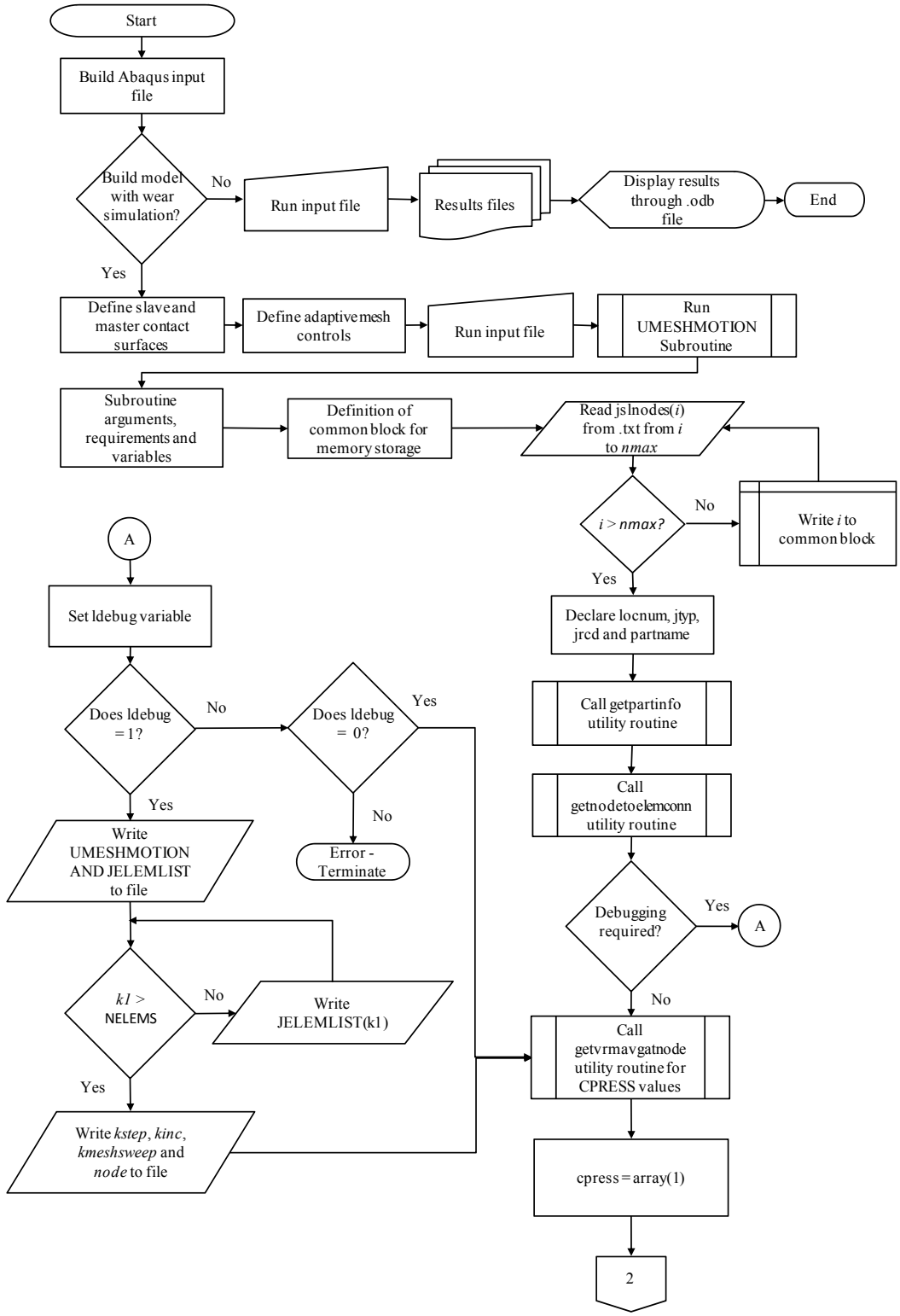

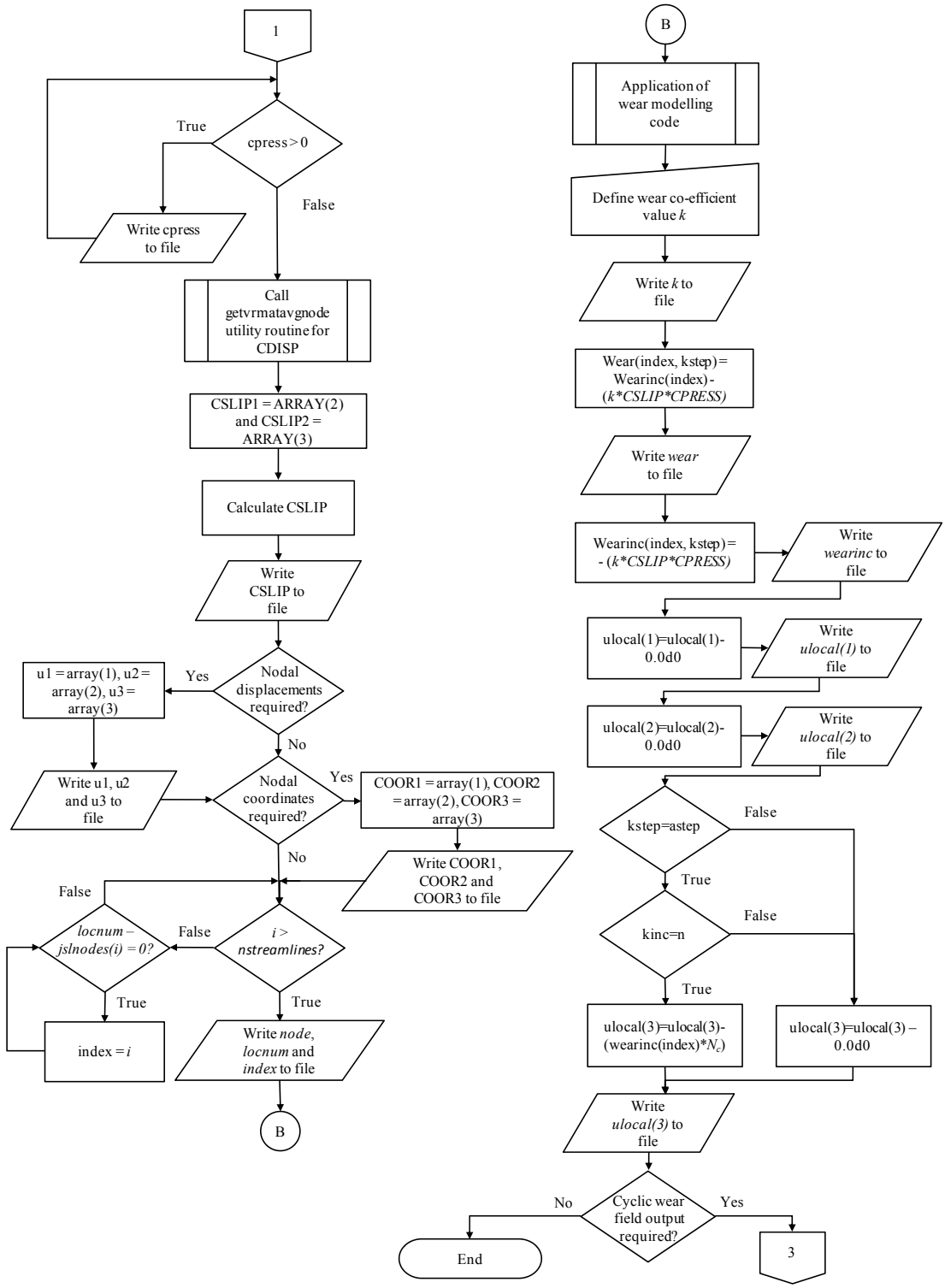
1
True
cpress > 0
False
Write cpress to file
Call getvrmatavgnode utility routine for CDISP
CSLIP1 = ARRAY(2) and CSLIP2 = ARRAY(3)
Calculate CSLIP
Write CSLIP to file
Nodal displacements required?
Yes
u1 = array(1), u2 = array(2), u3 = array(3)
No
Write u1, u2 and u3 to file
Nodal coordinates required?
Yes
COOR1 = array(1), COOR2 = array(2), COOR3 = array(3)
No
Write COOR1, COOR2 and COOR3 to file
False
locnum – jslnodes(i) = 0?
False
i > nstreamlines?
True
index = i
True
Write node, locnum and index to file
B
B
Application of wear modelling code
Define wear co-efficient value k
Write k to file
Wear(index, kstep) = Wearinc(index) - (k*CSLIP*CPRESS)
Write wear to file
Wearinc(index, kstep) = - (k*CSLIP*CPRESS)
Write wearinc to file
ulocal(1)=ulocal(1)-0.0d0
Write ulocal(1) to file
ulocal(2)=ulocal(2)-0.0d0
Write ulocal(2) to file
kstep=astep
False
True
kinc=n
False
True
ulocal(3)=ulocal(3)-(wearinc(index)*Nc)
ulocal(3)=ulocal(3)–0.0d0
Write ulocal(3) to file
No
Cyclic wear field output required?
Yes
End
3

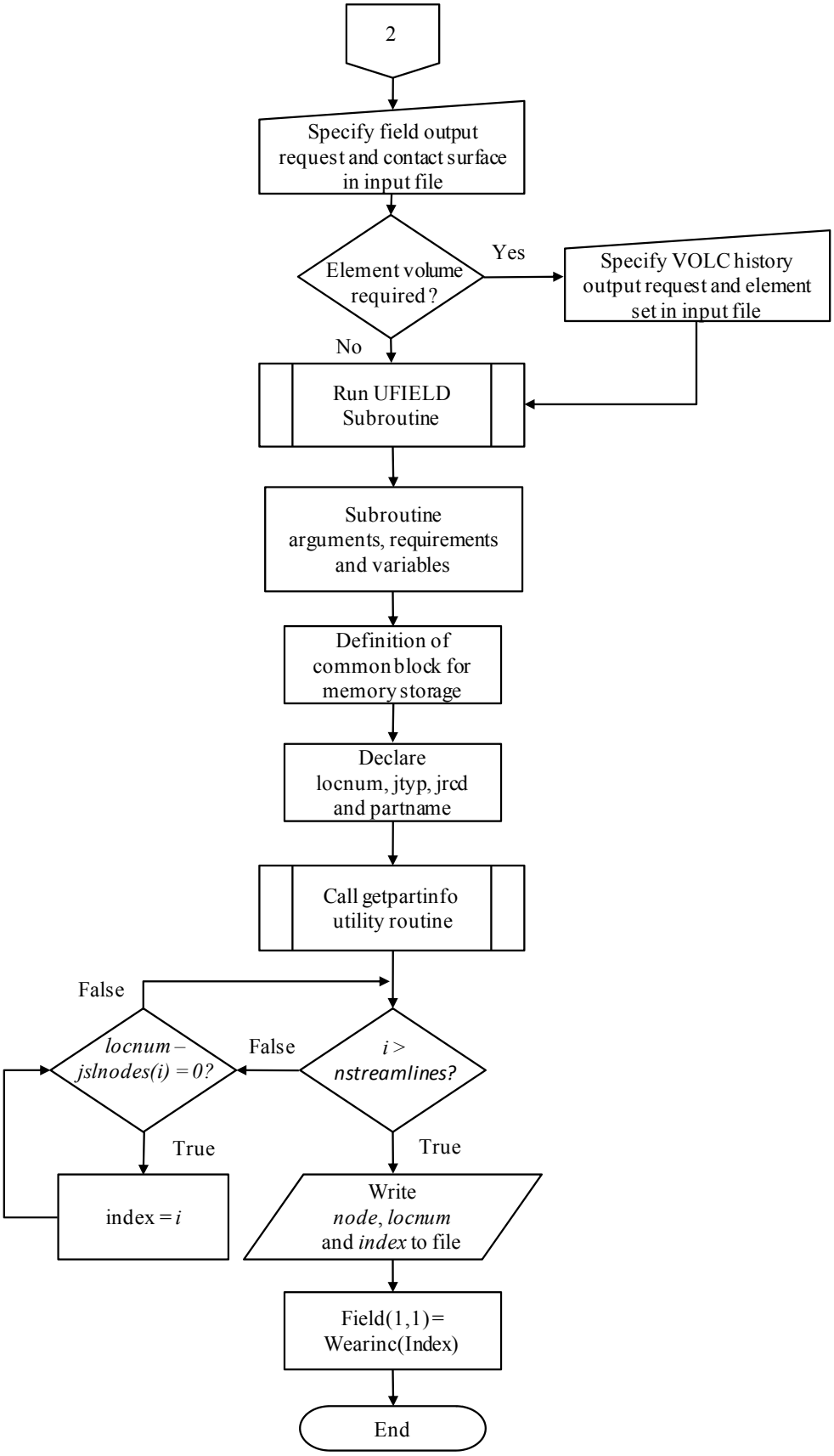
2
Specify field output request and contact surface in input file
Element volume required?
Yes
Specify VOLC history output request and element set in input file
No
Run UFIELD Subroutine
Subroutine arguments, requirements and variables
Definition of common block for memory storage
Declare locnum, jtyp, jrcd and partname
Call getpartinfo utility routine
False
locnum – jslnodes(i) = 0?
False
i > nstreamlines?
True
True
index = i
Write node, locnum and index to file
Field(1,1)= Wearinc(Index)
End

E.2. Block Wear Model Mesh Updates at the End of Each Increment

This code is only applicable to the block-on-block model

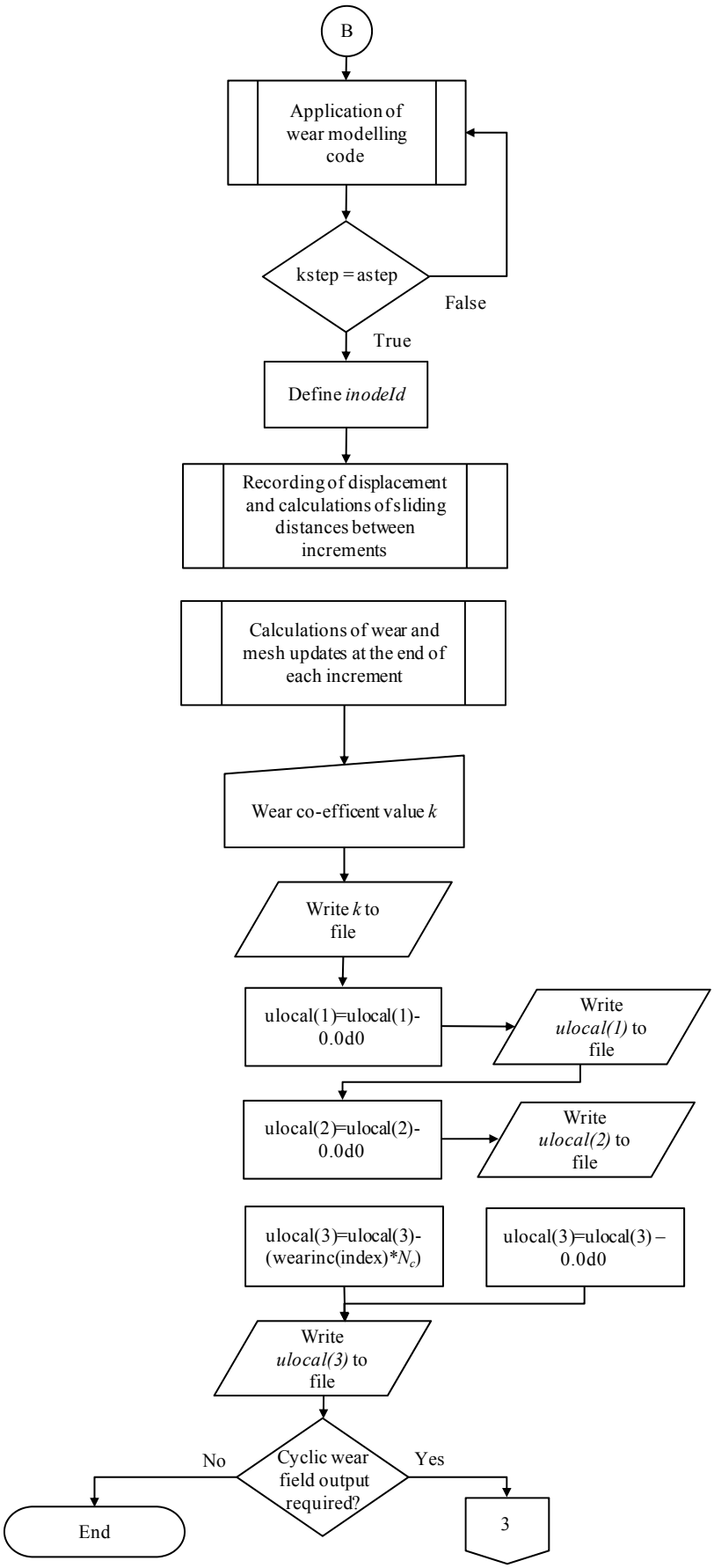

E.3. Hip Implant Wear Modelling Scripts

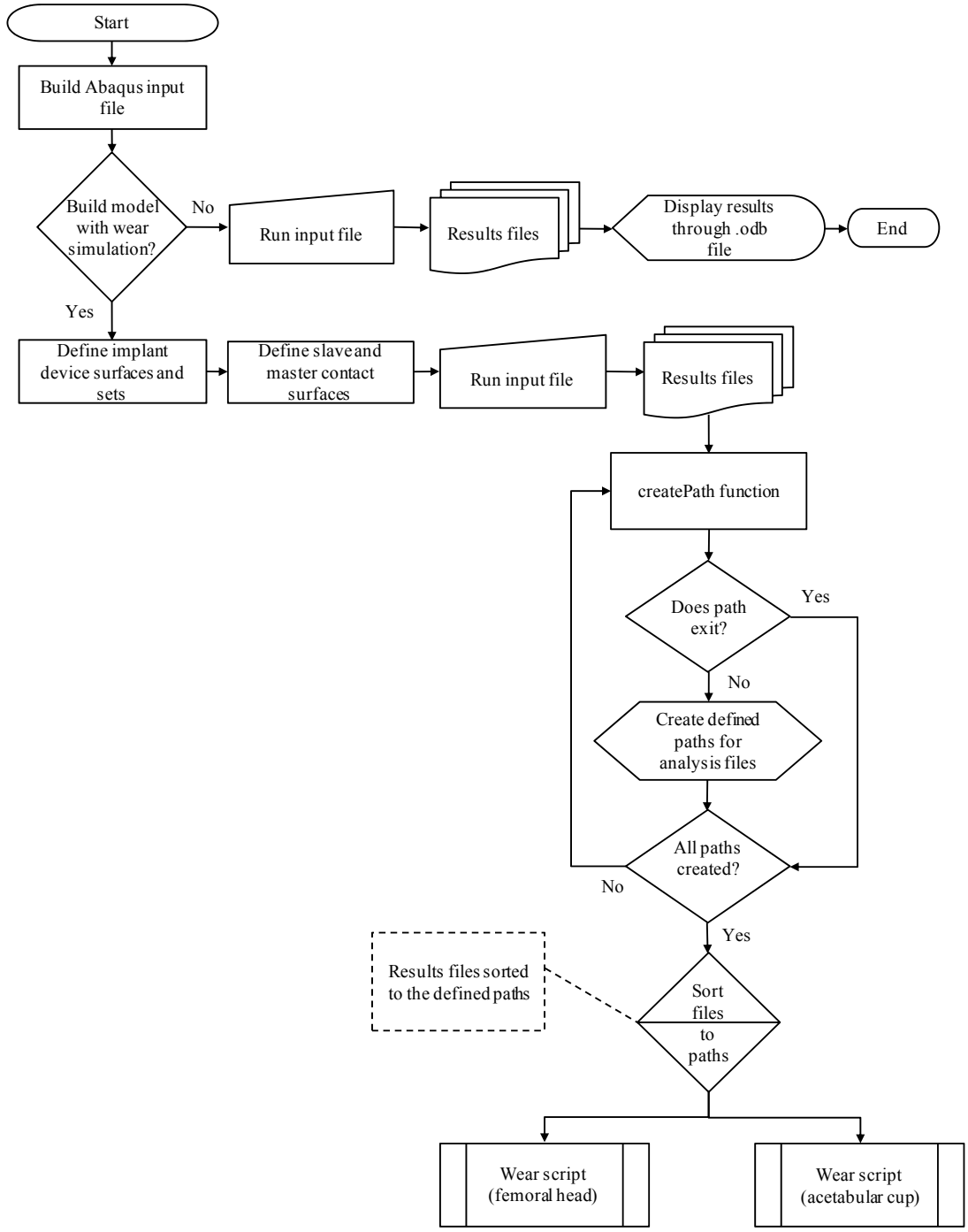

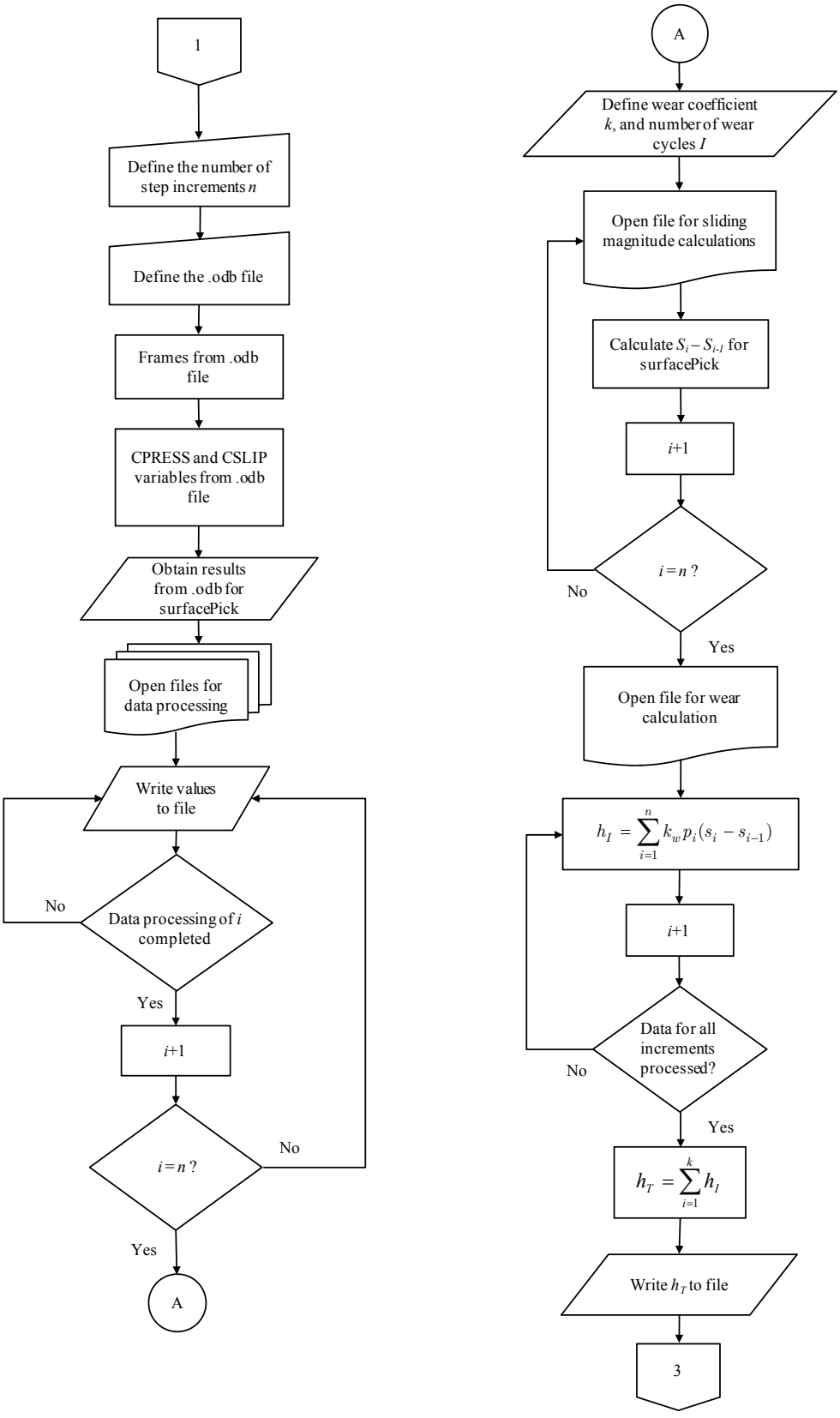
1
Define the number of step increments n
Define the .odb file
Frames from .odb file
CPRESS and CSLIP variables from .odb file
Obtain results from .odb for surfacePick
Open files for data processing
Write values to file
Data processing of i completed
No
Yes
i+1
i=n ?
No
Yes
A
A
Define wear coefficient k, and number of wear cycles I
Open file for sliding magnitude calculations
Calculate $S_i - S_{i-1}$ for surfacePick
i+1
i=n ?
No
Yes
Open file for wear calculation
$h_I = \sum_{i=1}^{n} k_w p_i (s_i - s_{i-1})$
i+1
Data for all increments processed?
No
Yes
$h_T = \sum_{i=1}^{k} h_I$
Write h_T to file
3

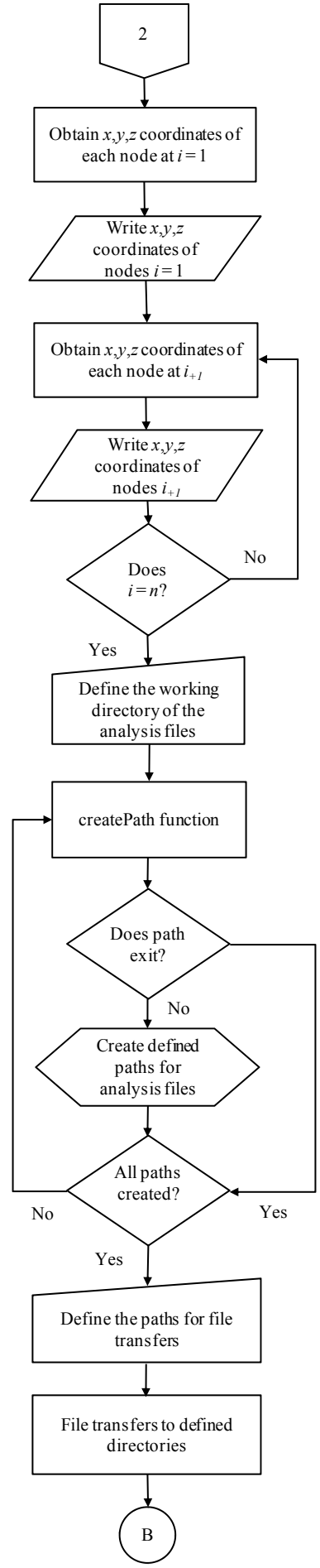
2
Obtain x,y,z coordinates of each node at i = 1
Write x,y,z coordinates of nodes i = 1
Obtain x,y,z coordinates of each node at i+1
Write x,y,z coordinates of nodes i+1
Does i = n?
No
Yes
Define the working directory of the analysis files
createPath function
Does path exit?
No
Create defined paths for analysis files
All paths created?
No
Yes
Yes
Define the paths for file transfers
File transfers to defined directories
B

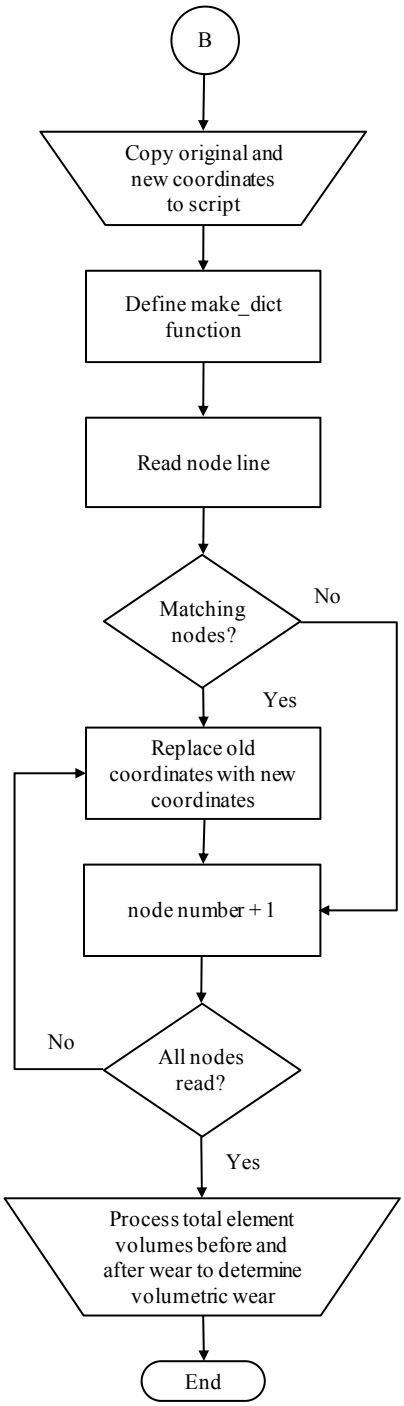
B
Copy original and new coordinates to script
Define make_dict function
Read node line
Matching nodes?
No
Yes
Replace old coordinates with new coordinates
node number + 1
All nodes read?
No
Yes
Process total element volumes before and after wear to determine volumetric wear
End

Appendix F – HIPprog Process Flow

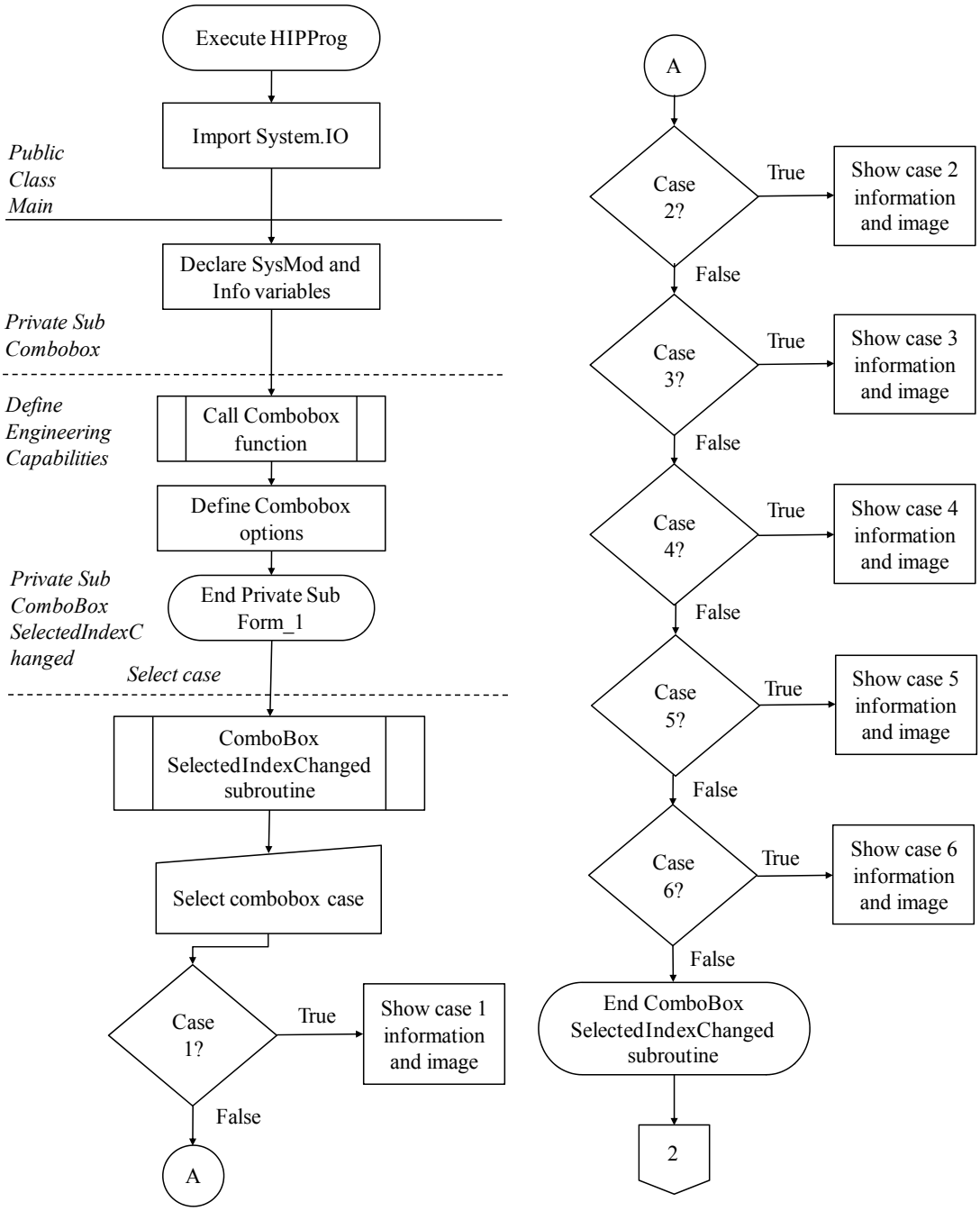

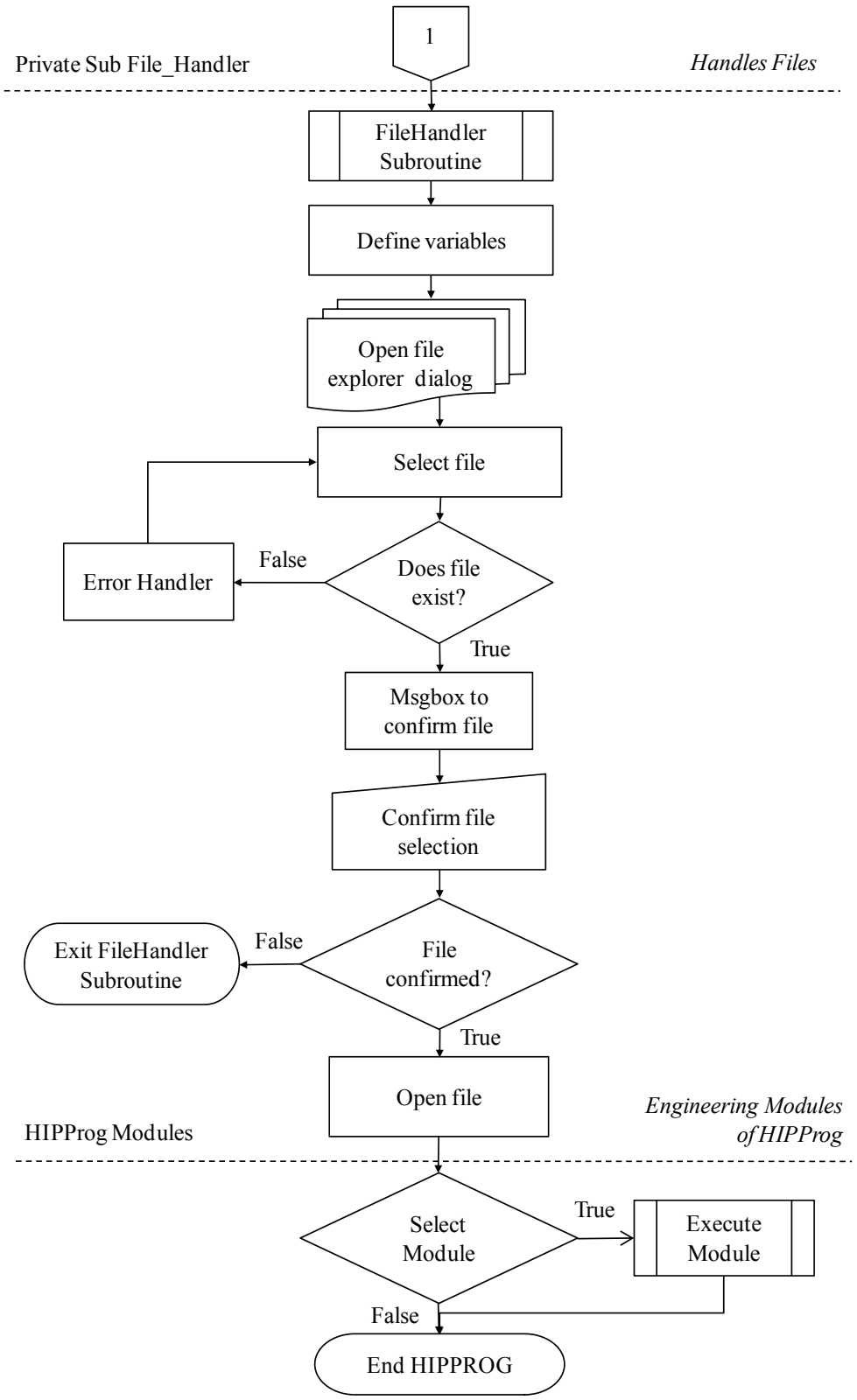
1
Private Sub File_Handler
Handles Files
FileHandler Subroutine
Define variables
Open file explorer dialog
Select file
Error Handler
False
Does file exist?
True
Msgbox to confirm file
Confirm file selection
Exit FileHandler Subroutine
False
File confirmed?
True
Open file
HIPProg Modules
Engineering Modules of HIPProg
Select Module
True
Execute Module
False
End HIPPROG

Appendix G – Edge Loading and Lubrication Calculations

Edge Loading Theoretical Calculation Sheet

Version 1.2

Theoretical Microseperation leading to edge loading

Press F9 to update calculations

Enter the variables in the square boxes to determine the distance for onset of rim contact. [1]

if $\theta_i := 45\ deg$ $\theta_i = 0.79\ rad$

To determine the clearance, define the diametral clearance of both head and cup

$D_c := 50.00\ mm$ $D_h := 50.08\ mm$

if $c := D_h - D_c$ $c = 0.08\ mm$

$$S_i := \left(1 + \frac{1}{\tan(\theta_i)}\right) \cdot c \qquad S_i = 0.16\ mm$$

Define function S1

$$f(\theta_i, c) := \left(1 + \frac{1}{\tan(\theta_i)}\right) \cdot c \qquad S1(\theta_i) := f(\theta_i, c)$$

e.g. $S1(45) = 0.13\ mm$ $S1_{val} := 1, 10 .. 90$ for $i \in 1 .. length(S1_{val})$

$S1_i := S1(S1_{val_i})$

Onset of rim contact s_r s_r (distance to onset of rim contact)

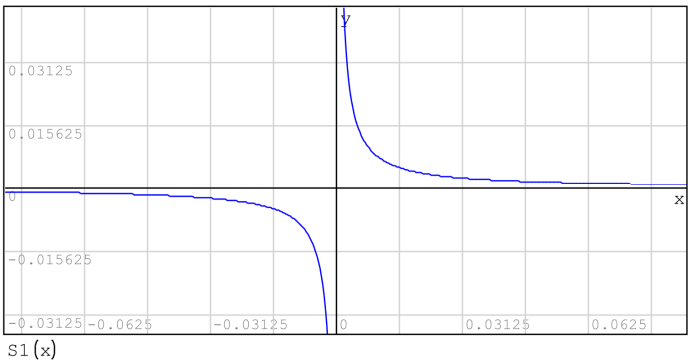

θ_i (cup inclination angle)

$S1(x)$

$S2(c) := f(\theta_i, c)$ $S2_{val} := 0.01, 0.03 .. 0.2$ for $i \in 1 .. length(S2_{val})$

$S2_i := S2(S2_{val_i})$

Onset of rim contact s_r **with varying diametral clearance against constant inclination angle**

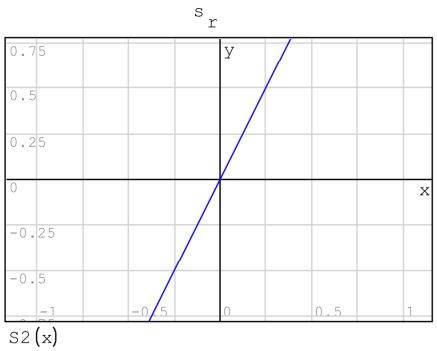

C

$S2(x)$

REFERENCES

[1] Influence of Acetabular Cup Rim Design on the Contact Stress During Edge Loading in Ceramic-on-CeramicHip Protheses, 2010, Mak et al.

Lubrication Theory Calculation Sheet

Version 1.1

Press F9 to update calculations

Enter the variables in the square boxes to conduct lubrication calculations [1]

$R_h := 25\ mm$ $\quad E_h := 210 \cdot 10^9\ Pa$

$R_c := 25.04\ mm$ $\quad E_c := 210 \cdot 10^9\ Pa$

$L := 2500\ N$

R_h *Femoral head radius*

R_c *Acetabular cup radius*

E_h *Elastic modulus of femoral head*

E_c *Elastic modulus of acetabular cup*

L *Load*

Poissons Ratio

$\nu_h := 0.3$ $\quad \nu_c := 0.3$

ν_h Poisson's ratio of femoral head

ν_c Poisson's ratio of acetabular cup

Contact modulus

$$E := \left(2 \cdot \left(\frac{1}{\left(\frac{1-\nu_h^2}{E_h}\right) + \left(\frac{1-\nu_c^2}{E_c}\right)}\right)\right)$$

$E = 2.31 \cdot 10^{11}\ Pa$

Sliding velocity between articulating surfaces

$v := 0.015\ \frac{m}{s}$

Viscosity of the fluid

$\eta := 0.005\ Pa\ s$

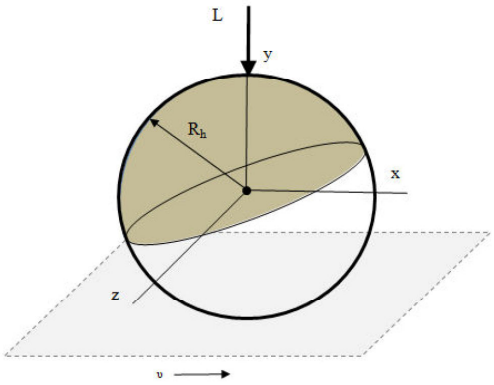

Equivalent radius

$$R_e := \frac{R_c \cdot R_h}{R_c - R_h}$$

$R_e = 15.65\ m$

Minimum film thickness

$$h_{min} := R_e \cdot \left(\left(2.8 \cdot \left(\frac{\eta \cdot v}{E \cdot R_e}\right)^{0.65} \cdot \left(\frac{L}{E \cdot R_e^2}\right)^{-0.21}\right)\right)$$

$h_{min} = 0.09\ \mu m$

Assessment of Lambda ratio

$R_{ah} := 0.011\ \mu m$ $\quad R_{ac} := 0.011\ \mu m$

$$\lambda_1 := \frac{h_{min}}{\left(\left(R_{ah}\right)^2 + \left(R_{ac}\right)^2\right)^{0.5}}$$

$\lambda_1 = 6.03$

R_{ah} surface roughness of femoral head

R_{ac} surface roughness of acetabular cup

$\lambda > 3$ lubrication film exists between surfaces

$\lambda < 1$ boundary lubrication exists

$1 < \lambda < 3$ mixed lubrication exists

REFERENCES

[1] Analysis of fluid film lubrication in artificial hip joint replacements with surfaces of high elastic modulus, Jin et al., 2003.

Appendix H – Contact and Shakedown Analysis

Contact and Shakedown analysis Calculation Sheets

Version 1.1

Enter the variables in the square boxes to conduct contact and shakedown calculations

Press F9 to update calculations

Contents

Section 1. Equivalent or Contact Modulus

Calculations of equivalent contact modulus [1]

$D_h := 0.05008\ m$ $D_c := 0.05\ m$ $E_h := 210 \cdot 10^9\ Pa$ $E_c := 210 \cdot 10^9\ Pa$ $P_g := 3000\ N$

D_h *Diameter of body 1*
D_c *Diameter of body 2*
E_h *Elastic modulus of material 1*
E_c *Elastic modulus of material 2*
P_g *Global Total Load*

Poissons Ratio

$\nu_h := 0.3$ $\nu_c := 0.3$

ν_h *Poissons ratio of body 1*
ν_c *Poissons ratio of body 2*

Contact modulus

$$E := \frac{1}{\left(\frac{1-\nu_h^2}{E_h}\right) + \left(\frac{1-\nu_c^2}{E_c}\right)} \qquad E = 1.15 \cdot 10^{11}\ Pa$$

Section 2. Hertz contact analysis (Global)

Calculations of equivalent contact radius and contact pressure [1]

$$K_D := \frac{D_h \cdot D_c}{D_h - D_c} \qquad K_D = 31.3\ m$$

K_D *Diametral constant*

$$C_E := \frac{1-(\nu_h)^2}{E_h} + \frac{1-(\nu_c)^2}{E_c} \qquad C_E = 8.67 \cdot 10^{-12}\ \frac{m\ s^2}{kg}$$

C_E *Equivalant or contact modulus E*

Radius of circular contact area (Global)

$$a := 0.721 \cdot \left(P_g \cdot K_D \cdot C_E\right)^{\left(\frac{1}{3}\right)} \qquad a = 0.01\ m$$

a_g *Half radius of global contact area*

$a_{tot} := 2 \cdot a \qquad a_{tot} = 0.01\ m$

Maximum compressive stress (Global)

$$\sigma_{cmax} := 0.918 \cdot \left(\frac{P_g}{(K_D)^2 \cdot (C_E)^2}\right)^{\left(\frac{1}{3}\right)} \qquad \sigma_{cmax} = 3.16 \cdot 10^7\ Pa$$

σ_{cmax} *Global maximum compressive stress*

Relative motion of approach along axis of loading

$$y_m := 1.040 \cdot \left(\frac{(P_g)^2 \cdot (C_E)^2}{K_D}\right)^{\left(\frac{1}{3}\right)} \qquad y_m = 2.9 \cdot 10^{-6}\ m$$

y_m *Realative motion of approach along the axis of loading*

Section 3. Global Shakedown contact analysis (FE and material shear yield)

The following sections considers the use of finite element analysis and known values of material yield strength to determine the load intensity on the the shakedown map, based on line and circular contact shakedown maps [2].

$\mu := 0.16$ [3]

μ *Coefficient of friction (global)*

Load intensity

From FE the maximum contact pressure can be determined under both normal and edge loading

$p_o := 1284 \cdot 10^6$ *Pa*

σ_{yt} *Tensile yield strength*

p_o *Contact Pressure*

The material shear yeild strength

k *Shear yeild for shakedown*

τ_y *Shear yeild*

$\tau_y := 0.58 \cdot \sigma_{yt}$ [4]

L_I *Load intensity*

For ASTM F75 'As Cast' Material (CoCrMo) the value of shear yield is

$\sigma_{yt} := 864 \cdot 10^6$ *Pa* [5]

$\tau_y = 5.01 \cdot 10^8$ *Pa*

$k := \tau_y$ $k = 5.01 \cdot 10^8$ *Pa*

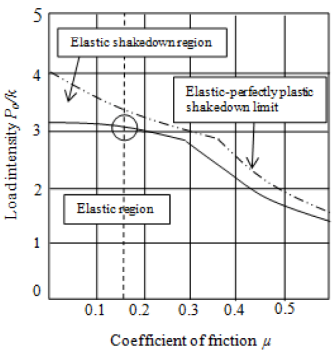

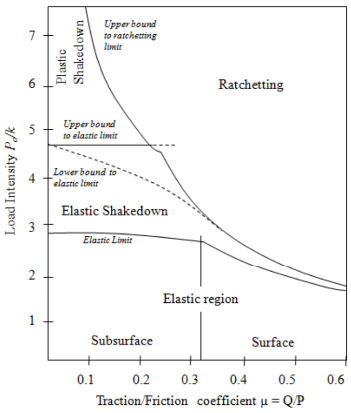

Load intensity

$L_I := \frac{p_o}{k}$ $L_I = 2.56$

Section 4. Asperity Contact Loads

An asperiy contact analysis can be conducted [6].

Assumptions

1) Let z_a be equal to the roughness (R_a) from experimental results.

z *Asperity height (distribution curve - PDF)*

2) Let d_a = 0.5*(z_a)

z_a *Distance from Ref plane of rough surface to top of asperity*

$z_a := 0.011\ \mu m \pm 0.001$

R_a value (average of head and cup) - Determined from Wyco surface profilometer [7]

$d_a := 0.5 \cdot z_a$ $d_a = 5.5 \cdot 10^{-9}$ *m*

By assuming that Ra (Surface roughness) determined from surface profiler is equal to R_a1 (radius of all identical asperities)

$R_a := z_a$

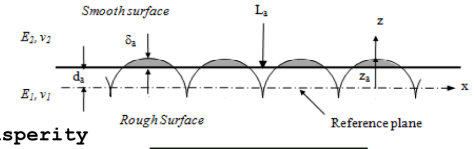

R_a *Roughness average (from surface profiler)*

Area of contact on asperity

$A_i := \pi \cdot R_a \cdot \delta_a$ $\delta_a := (z_a - d_a)$ $A_i = 1.9 \cdot 10^{-16}\ m^2$

A_i *Area of contact on asperity*

Number of asperities per unit area m^2 (determined from surface profiler)

$N_a := 9 \cdot 10^{10}$

N_a *Number of asperities per unit area (obtain from surface profiler)*

The load on each asperity

$L_a := \frac{4 \cdot E}{3} \cdot (R_a)^{\left(\frac{1}{2}\right)} \cdot (\delta_a)^{\left(\frac{3}{2}\right)}$ $L_a = 6.58 \cdot 10^{-6}\ N$

N_1 *Number of asperities per unit area*

L_a *Load on asperity*

The total load is

$$L_t := \left(\frac{4}{3\cdot\pi^{(1.5)}}\right)\cdot\left(\frac{N_a\cdot E\cdot\left(A_i\right)^{\left(\frac{3}{2}\right)}}{R_a}\right) \qquad L_t = 5.92\cdot10^{5}\ N$$

L_t *Total load on surface*

Section 6. Hertz Asperity Contact Analysis

As the global load will be split amongst the asperities:

$L_a = 6.58\cdot10^{-6}\ N$

Assume that the average asperity height R_a (roughness average obtained from inspection) is the uniform radius of curvature peak

Let $R_a = r_a$

$r_a := R_a \qquad r_a = 1.1\cdot10^{-8}\ m$

R_1 *Uniform Radius of curvature peak*

Radius of circular micro contact area

$$a_a := \left(\frac{3\cdot L_a\cdot r_a}{4\cdot E}\right)^{\left(\frac{1}{3}\right)} \qquad a_a = 7.78\cdot10^{-9}\ m$$

a_a *Radius of circular micro contact area*

Interference or overlap between the two asperity profiles

$$\delta_a := \left(\frac{9\cdot L_a^{\,2}}{16\cdot r_a\cdot E^{\,2}}\right)^{\left(\frac{1}{3}\right)} \qquad \delta_a = 5.5\cdot10^{-9}\ m$$

δ_a *Total displacement (Overlap or interference between the two asperity profiles)*

Mean Hertizian contact pressure for micro contact

$$\sigma_m := \frac{2}{3\cdot\pi}\cdot\left(\frac{6\cdot L_a\cdot E^{\,2}}{r_a^{\,2}}\right)^{\left(\frac{1}{3}\right)} \qquad \sigma_m = 3.46\cdot10^{10}\ Pa$$

σ_m *Mean Hertizian contact pressure for micro contact*

Section 7. Plasticty Index

Asperity shakedown pressure

If the asperity contact pressure is less than asperity shakedown pressure then the asperity will not undergo further plastic flow.

Calculation of asperity shakedown pressure

If the largest asperity shakedown pressure is greater than or equal to the asperity shakedown pressure then plasticity flow of the asperity will occur. If the asperity pressure remains below the asperity shakedown pressure than the asperity will remain in an elastic state.

According to Kapoor et al. [8] on the asperity level in the shakedown state:

$p_s := \sigma_m \qquad p_s = 3.46\cdot10^{10}\ Pa$

p_s *Asperity shakedown pressure*

For the interference with assumed values of I_h and I_d.

$I_h := 0.9$ $\qquad$ $I_d := 0.2$

$\delta_m := I_h - I_d \qquad \delta_m = 0.7$

RMS Surface Roughess (this is the standard deviation as S.D is the RMS of the deviations from the mean)

Average of RMS roughness value for head and cup [9]

$\sigma_1 := 0.013\ \mu m$

σ_1 *RMS Roughness*

Plasticity Index

$$\Psi_s := \left(\frac{E}{p_s}\right)\cdot\left(\frac{\sigma_1}{R_a}\right)^{0.5} \qquad \Psi_s = 3.62$$

Ψ_s *Plasticity index*

Greenwood and Williamson model [10]

Hardness of the deforming surface

$H_v := 350 \pm 20$ [11]

H_v *Vickers hardness*

To convert HV to units of Pascal, multiply by 9.807 [12]

$H_{VP} := 9.807 \cdot H_v \ MPa$ $H_{VP} = 3.43 \cdot 10^{9} \ Pa$

$r_{GW} := z_a$ $r_{GW} = 1.1 \cdot 10^{-8} \ m$

r_{GW} *Asperity radius constant (G-W model)*

$\sigma_p := \sigma_1$ $\sigma_p = 1.3 \cdot 10^{-8} \ m$

σ_p *Standard deviation of surface peak height ditribution*

Greenwood and Williamson plasticity index Ψ_{GW}

$$\Psi_{GW} := \left(\frac{E}{H_{VP}}\right) \cdot \left(\frac{\sigma_p}{r_{GW}}\right)^{0.5} \qquad \Psi_{GW} = 36.54$$

If $\Psi_{GW} < 1$ contact involves elastic deformation

If $\Psi_{GW} > 1$ contact involves plastic deformation

Section 8. Normal contact pressure distribution

From finite element analysis obtain the maximum contact pressure and maximum contact radius. This can then be used to calculate the contact pressure at any point within the contact area without the need for model further assessment of the FE model.

$p_{oe} := 18 \ MPa$ $a_n := 10 \ mm$

p_{oe} *Uniformly distributed pressure load (normal loading)*

Define the value of n_p

For uniform pressure: $n_p := 0$

For uniform normal displacement and general pressure: $n_p := -\frac{1}{2}$

For hertz pressure: $n_p := \frac{1}{2}$

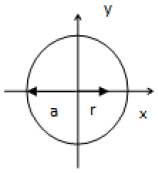

$n_p := \frac{1}{2}$

Define the position from the contact centre point to calculate contact pressure

$r_n := 5 \ mm$

$$P_N := \left(1 - \frac{(r_n)^2}{(a_n)^2}\right)^{n_p} \cdot p_{oe} \qquad P_N = 16 \ MPa$$

P_N *Contact pressure under normal loading conditions*

Section 9. Edge loading contact pressure distribution

From finite element analysis obtain the maximum contact pressure and maximum contact radius. This can then be used to calculate the contact pressure at any point within the contact area without the need for model further assessment of the FE model.

$p_{oe} := 101 \ MPa$ $a_e := 10 \ mm$ $b_e := 4 \ mm$

p_{oe} *Uniformly distributed pressure load (edge loading)*

Define the value of n_e

$n_e := \frac{1}{2}$

Define the position from the contact centre point x_e **and** y_e **to calculate contact pressure**

$x_e := 5 \ mm$ $y_e := 2 \ mm$

$$P_E := \left(1 - \left(\frac{x_e}{a_e}\right)^2 - \left(\frac{y_e}{b_e}\right)^2\right)^{n_e} \cdot p_{oe} \qquad P_E = 71.42 \ MPa$$

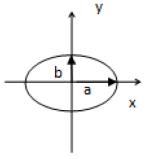

Section 10. Distrbution of asperity heights

Calculation using the probability density function

From optical surface profiler the roughness average can be determined.

$R_a = 1.1 \cdot 10^{-8}\ m$

Therefore,

$\mu_{Ra} := \frac{R_a}{1 \cdot 10^{-6}} \cdot \left(\frac{1}{m}\right)$ Note: μ_Ra becomes unitless value with multiplying by (1/metres)

$\mu_{Ra} = 0.01$ μ_{Ra} Average surface Roughness i.e. height)

The probability density function of the normal distribution (General form)

$$f(z, \sigma_a, \mu_{Ra}) := \frac{1}{\sigma_a \cdot \sqrt{2 \cdot \pi}} \cdot e^{-\frac{(z - \mu_{Ra})^2}{(2 \cdot (\sigma_a)^2)}}$$

The following conditions satisfy a standard normal distribution:

$\mu := 0$ $\sigma := 1$

The probability density function can have any value as long as it is:

$\mu > 0$ $\sigma > 0$

From Kapoor et al. (1994) [8]

$$f(z_1, \sigma_a, \mu_{Ra}) := \frac{1}{\sigma_a \cdot \sqrt{2 \cdot \pi}} \cdot e^{\frac{(-z_1)^2}{(2 \cdot (\sigma_a)^2)}} \quad \text{for} \quad z < h$$

$$\Phi_1(z) \cdot dz := \left(\frac{1}{2}\right) \cdot \left[1 - \operatorname{erf}\left(\frac{h}{2^{0.5} \cdot \sigma_a}\right)\right] \quad \text{for} \quad z := h$$

$\Phi_1(z) := 0$ for $z > h$

$f1(z_1) := f(z_1, \sigma_a, \mu_{Ra})$

To obtain the standard deviation in terms of the probability distribution function (σ):

$U_1 := \int_{-\sigma_a}^{\sigma_a} f1(z_1)\, dz_1$ $U_1 = 0.95$ Therefore: $\sigma_{a1} := U_1$ $\sigma_{a1} = 0.95$

Probability density function

$z_{eg} := -0.03, -0.02 .. 0.03$ for $i \in 1 .. \text{length}(z_{eg})$

$f1_i := f1(z_{eg_i})$

$$z_{eg} = \begin{pmatrix} -0.03 \\ -0.02 \\ -0.01 \\ -3.47 \cdot 10^{-18} \\ 0.01 \\ 0.02 \\ 0.03 \end{pmatrix} \qquad f1 = \begin{pmatrix} 439.92 \\ 100.21 \\ 41.25 \\ 30.69 \\ 41.25 \\ 100.21 \\ 439.92 \end{pmatrix}$$

Based on the probability density function

$$f(z, \sigma_a, \mu_{Ra}) := \frac{1}{\sigma_a \cdot \sqrt{2 \cdot \pi}} \cdot e^{-\frac{(z-\mu_{Ra})^2}{\left(2 \cdot (\sigma_a)^2\right)}}$$

$f2(z) := f(z, \sigma_a, \mu_{Ra})$ $f2(0.03) = 10.55$ $f2(-0.03) = 0.21$

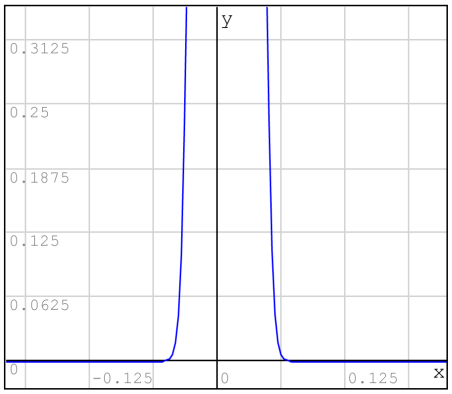

$f2(x)$

$z_{eg1} := -0.03, -0.02 .. 0.03$

for $i \in 1 .. \text{length}(z_{eg1})$

$f2_i := f2(z_{eg1_i})$

$$z_{eg1} = \begin{pmatrix} -0.03 \\ -0.02 \\ -0.01 \\ -3.47 \cdot 10^{-18} \\ 0.01 \\ 0.02 \\ 0.03 \end{pmatrix}$$

$$f2 = \begin{pmatrix} 0.21 \\ 1.79 \\ 8.32 \\ 21.45 \\ 30.6 \\ 24.15 \\ 10.55 \end{pmatrix}$$

$$U_2 := \int_{-3 \cdot \sigma_a}^{3 \cdot \sigma_a} f2(z)\, dz$$

$U_2 = 0.98$

This is representative of a probability density function (as the integral = 1)

REFERENCES

[1] R. J. Roark, Roark's formulas for stress and strain / Warren C. Young, 6th ed. ed. New York, London McGraw-Hill, 1989.
[2] ref. J. A. Williams, "The influence of repeated loading, residual stresses and shakedown on the behaviour of tribological contacts", 2005
[3] S. C. Scholes, A. Unsworth, and A. A. J. Goldsmith, "A frictional study of total hip joint replacements," Physics in Medicine and Biology, vol. 45, pp. 3721-3735, Dec 2000.
[4] E. Oberg, Machinery's Handbook 28th Edition, 2008
[5] Materials and Coatings for Medical Devices: Cardiovascular: ASM International, 2009.
[6] B. Bhushan, "Contact mechanics of rough surfaces in tribology: multiple asperity contact," Tribology Letters, vol. 4, pp. 1-35, Jan 1998.
[7] A. Kamali, A. Hussain, C. Li, J. Pamu, J. Daniel, H. Ziaee, et al., "Tribological performance of various CoCr microstructures in metal-on-metal bearings
[8] A. Kapoor, J. A. Williams, and K. L. Johnson, "The steady-state sliding of rough surface," Wear, vol. 175, pp. 81-92, Jun 1994.
[9] S. R. Williams, J. J. Wu, A. Unsworth, and I. Khan, "Tribological and surface analysis of 38mm alumina-as-cast Co-Cr-Mo total hip arthroplasties," Proceedings of the Institution of Mechanical Engineers, Part H: Journal of Engineering in Medicine, vol. 223, pp. 941-954, 2009.
[10] G. W. Stachowiak, Engineering tribology / Gwidon W. Stachowiak, Andrew W. Batchelor, 3rd ed. ed. Amsterdam ; Boston :: Elsevier Butterworth-Heinemann, 2005.
[11] N. S. Vandamme, L. Que, and L. D. T. Topoleski, "Carbide surface coating of Co-Cr-Mo implant alloys by a microwave plasma-assisted reaction," Journal of Materials Science, vol. 34, pp. 3525-3531, Jul 15 1999.
[12] Gordon England. (13th November 2012). Available: http://www.gordonengland.co.uk/hardness/hvconv.htm

Bibliography

J. D. Bronzino, *The biomedical engineering handbook*, 3rd ed., 2006.

A. J. Cartwright, *Engineering data book*, 5th ed. Coventry : University of Warwick, School of Engineering, 2006.

J. D. Enderle, J. D. Bronzino, and S. M. Blanchard, *Introduction to biomedical engineering*, 2nd ed. Burlington MA; London: Elsevier Academic Press, 2005.

D. M. Etter, *Structured Fortran 77 for Engineers and Scientists*: Benjamin/Cummings, 1993.

I. M. Hutchings, *An engineering data book / edited by J.R. Calvert and R.A. Farrar.*

K. L. Johnson, *Contact mechanics*. Cambridge : Cambridge University Press, 1985.

M. Kutz, *Mechanical Engineers' Handbook*: John Wiley & Sons, 1998.

H. C. Martin and G. F. Carey, *Introduction to finite element analysis, theory and application,* New York; London : McGraw-Hill, 1973.

R. J. Roark and W. C. Young, *Roark's formulas for stress and strain,* 6th ed. New York ; London : McGraw-Hill, 1989.

Z. Shaw, Learn Python The Hard Way, 3rd Edition.

J. E. Shigley and C. R. Mischke, *Mechanical engineering design*, 6th ed. Boston : McGraw Hill, 2001.

G. W. Stachowiak and A. W. Batchelor, *Engineering tribology,* 3rd ed. Amsterdam ; Boston : Elsevier Butterworth-Heinemann, 2005.

K. A. Stroud and D. J. Booth, *Engineering Mathematics*: Industrial Press, 2001.

Timoshenko, S. P. & Goodier, J. N. Theory of Elasticity, New York, McGraw-Hill.

J. J. Tuma and R. A. Walsh, *Engineering mathematics handbook*, 4th ed. London : McGraw-Hill, 1997.